Investigation of Wireless Power Transfer-based Eddy Current Non-Destructive Testing and Evaluation

Lawal Umar Daura
B.Eng, M.Eng

A doctoral thesis submitted for the degree of Doctor of Philosophy

School of Engineering, Newcastle University

(Intelligent Sensing and Communications (ISC) Research Group)

May 2022

CERTIFICATE OF ORIGINALITY

I certify that the work submitted in this thesis is my work except as stated in the acknowledgements. None of this thesis report or part of it has been submitted to any other institution for another degree award. I also confirm that other sources of knowledge used in this thesis have been acknowledged, cited inside the thesis report and adequately credited in the reference list.

The research contributions presented in Chapters 4 and 5 were published and listed in the list of the publication page.

..... (Signed)

Lawal Umar Daura
(140527814)

..... (Candidate)

Acknowledgement

Alhamdulillah, all praise be to Allah, and peace and blessing be upon his prophet Muhammad (S.A.W). I thank Almighty God for making it possible for me to get the PTDF PhD scholarship to study at Newcastle University under high ranking faculties that open my eyes to the world of research. My sincere gratitude to Him for giving me the strength, health, and ability to carry out this research. After that, I would like to acknowledge my parent' contributions for the moral upbringing and financial assistance required for my educational career leading my academic excellence throughout my life. Many thanks to my sponsor, PTDF Nigeria, my parent and my employer, Bayero University Kano.

This thesis would not have been possible without the internal and external guidance, different kinds of support and encouragement from different people, whom I fell short of showing my thankful words physically for their help at various stages of this research work. My first and profound appreciation goes to my research supervisor, Professor Gui Yun Tian, for his endless support and guidance and his given high sense of research belonging to me throughout my study period. His supervision makes it possible to reach this completion stage of my study aim, opening my research to the other world of the electromagnetic non-destructive testing community. Thanks to his devoted time for ensuring I explore my ultimate strength and capability to achieve the best of my study. My warm appreciation also goes to Engr. Y S Adamu, Alh Shamsu Salisu Daura, Prof Junaid of Chemistry Department BUK, Dr Musbahu Muhammad of Centre for Sustainable Engineering, Teeside University, and Dr Isiyaku Abubakar (Sallau), who made my stay worthwhile through their different contribution to support my living condition.

It is worth to me for remembering, thanking and mentioning the names of my fellow Newcastle University colleagues, particularly members of our research team whose decent and demonstrative support helped me a lot. Dr Ruslee Sutthaweekul, Dr Adi Mahmud Jaye Marinda, Dr Mohammed Dahiru Buhari, Dr Denis Ona, Dr Chaoqing Tang, Dr Qiuji Yi, Dr Monica Roopak, Mr Juma Abdulwali, Mr Emmanuel Tashiwa Ibrahim, and Mr Changrong Yan, and so on. I would also like to thank the staff and technicians of Newcastle University who have always helped me with the necessary things I needed, especially Senior Electrical/Electronic Technician Mr Paul Killan. To all the rest, I direct my profound gratitude and sincere thanks.

Lastly, but most importantly, I am indebted to my parent, brothers, wife (Sumayya Ibrahim Dahiru) and children (Farouq Umar, Ibrahim, and Hamza) —the incentive behind my success. To all of them, May Allah reward them abundantly, Ameen.

ABSTRACT

Eddy current testing (ECT) is a non-contact inspection widely used as non-destructive testing and evaluation (NDT&E) of pipeline and rail lines due to its high sensitivity to surface and subsurface defects, cheap operating cost, tolerance to harsh environments, and capability of a customisable probe for complex geometric surfaces. However, the remote field of transmitter-receiver (Tx-Rx) ECT depends on the Tx-Rx coils gap, orientation, and lift-off distance, despite each coil responding to the effect of sample parameters according to its lift-off distance. They bring challenges to accurate defect detection and characterisation by weakening the ECT probe's transfer response, affecting sensitivity to the defect, distorting the amplitude of the extracted features, and responding with fewer feature points at non-efficient energy transfer. Therefore, this study proposed a magnetically-coupled resonant wireless power transfer (WPT)-based ECT (WPTECT) concept to build the relationship between Tx-Rx coil at maximum energy transfer response, including shifting and splitting (resonance) frequency behaviour.

The proposed WPTECT system was investigated in three different studies viz., (1) investigated the multiple resonance point features for detection and characterisation of slots on two different aluminium samples using a series-series (SS) topology of WPTECT; (2) mapped and scanned pipeline with a natural dent defect using a flexible printed coil (FPC) array probe based on the parallel-parallel (PP) topology of WPTECT; and (3) evaluated five different WPTECT topologies for optimal response and extracted features and characterised entire parameters of inclined angular Rolling Contact Fatigue (RCF) cracks in a rail-line material via an optimised topology. Multiple feature extraction, selection, and fusion were evaluated for the defect profile and compared in the study, unattainable by other ECT methods.

The first study's contribution investigated multiple resonances and principal component analysis (PCA) features of the transfer response from scanning (eight) slots on two aluminium samples. The results have shown the potential of the multiple features for slot depth and width characterisation and demonstrated that the eddy-current density is highest at two points proportionate to the slot width. The second study's contribution provided a larger area scanning capability in a single probe amenable to complex geometrical structures like curvature surfaces. Among the extracted individual and fused features for defect reconstruction, the multi-layer feed-forward Deep learning-based multiple feature fusion has better 3D defect reconstruction, whilst the second resonances feature provided better local information than the first one for investigating pipeline dent area. The third study's contribution optimised WPTECT topology for multiple feature points capability and its optimal features extraction at the desired lift-off

conditions. The PP and combined PP and SS (PS-PS) WPTECT topologies responded with multiple resonances compared to the other three topologies, with single resonance, under the same experimental situation. However, the extracted features from PS-PS topology provided the lowest sensitivity to lift-off distances and reconstructed depth, width, and inclined angle of RCF cracks with a maximum correlation, R^2-value of 96.4%, 93.1%, and 79.1%, respectively, and root-mean-square-error of 0.05mm, 0.08mm, and 6.6^0, respectively.

The demonstrated magnetically-coupled resonant WPTECT Tx-Rx probe characterised defects in oil and gas pipelines and rail lines through multiple features for multiple parameters information. Further work can investigate the phase of the transfer response as expected to offer robust features for material characterisation. The WPTECT system can be miniaturised using WPT IC chips as portable systems to characterise multiple layers parameters. It can further evaluate the thickness and gap between two concentric conductive tubes; pressure tube encircled by calandria tube in nuclear reactor fuel channels.

List of Publication

1. **L. U. Daura** and G. Y. Tian, "Characterization of Angular RCF Cracks in a Railway Using Modified Topology of WPT-Based Eddy Current Testing," IEEE Transactions on Industrial Informatics, 2021, Under review.
2. **L. U. Daura**, G. Y. Tian, Q. Yi, and A. Sophian, "Wireless power transfer-based eddy current non-destructive testing using a flexible printed coil array," Philosophical Transactions of the Royal Society A: Mathematical, Physical and Engineering Sciences, vol. 378, no. 2182, p. 20190579, 2020, doi: doi:10.1098/rsta.2019.0579.
3. **L. U. Daura** and G. Y. Tian, "Wireless Power Transfer Based Non-Destructive Evaluation of Cracks in Aluminum Material," IEEE Sensors Journal, vol. 19, no. 22, pp. 10529-10536, 2019, doi: 10.1109/JSEN.2019.2930738.

I dedicated this thesis to my parent, wife, and children

Table of Contents

Table of Contents

List of Figures

List of Tables

Chapter 1. Introduction

In this chapter, a brief background of non-destructive testing and evaluation (NDT&E) of electrically conductive materials, narrowed down to Eddy Current Testing (ECT), including integration of magnetically-coupled resonant Wireless Power Transfer (WPT) to ECT, are presented. The research motivations, aim and objectives, and achievements are also described in this chapter. Finally, an outline of the entire thesis and a summary of the chapters are concluded and presented.

1.1 Research Background

Despite the development of many metal-like structures, metals continue to be used and become exceptional in many vital applications. However, it has some limitations that may lead to structural failure, although it possesses unique properties [1]. The commonly occurring failure in metallic engineering structures arises due to corrosion and fatigue defects, accounting for more than ninety per cent of the frequently occurring failure in engineering structures and aeroplanes [2]. Exposure to external and internal causative factors to the metallic structures while in service or due to ageing causes defects, which weakens its microstructures, leading to imperfection. Non-destructive testing and evaluation (NDT&E) quantitatively assess such weakness in metallic structures; effectively, safely, and reliably whilst the structure is in operation without negatively disturbing its serviceable functions for facilitating preventive maintenance, among others. There are different NDT&E techniques offered for metallic structures inspection like pipelines and railway integrity, including ECT [3-6], electromagnetic acoustic transducers (EMAT) [7, 8], magnetic flux leakage (MFL) [9, 10], ultrasonic techniques [11, 12], and microwave testing [13, 14] among others. Different NDT&E techniques have different capabilities depending on their principles of operation and responses to metallic structures and defects, leading to specific advantages and disadvantages to a particular application. This study explores the advantages of ECT as a prominent NDT&E technique by modifying its probes for addressing the issues related to features capabilities and applies for investigation of some challenging defect characterisation.

ECT has been widely applied to evaluate corrosion and other fatigue defects during an inspection of engineering structures due to its higher operation safety, reasonably inexpensive, and highly responsive testing system than other NDT&E techniques [4]. It has been developing, for decades, from single-frequency [3, 15] to multiple frequencies [16], pulsed [17], and sweep frequency [3, 18] ECT. The response of ECT includes a collection of features for defects and sample parameters and geometry and probe lift-off information. Therefore, it may not be easy

to separate a single influence from the response features. An appropriate evaluation of defect parameters and sample surface properties are needed, especially through a thorough understanding of multiple features influence on the ECT response signal from inspecting the critical part of sample and defect. Assessment of the essential parameters depends on correctly designed operating frequency and probe geometry by considering the defect size and location, sample permeability and conductivity, and optimal lift-off distance.

However, coupled to the mentioned challenges, an inductively coupled transmitter-receiver (Tx-Rx) coils probe of ECT suffers weak induction, leading to weak induced eddy current density, which provides a weaker detection signal. The ECT operation at a lower remote field energy transfer efficiency led to lower detection sensitivity and fewer feature points, which became a challenge to conventional ECT. Therefore, this research integrates magnetically-coupled resonant WPT concepts of charging electric vehicles and ECT technique for modifying the ECT probe to overcome the low energy transfer issue and fewer feature points. The magnetically-coupled resonant WPT-based ECT (WPTECT) technique uses a magnetically coupled resonant behaviour for excitation and sensing units [19]. It explores the scattering transmission (S21) parameters as a performance measure of the transfer response at different frequencies of interest [20]. The magnetically-coupled resonant WPT operates at maximum energy transmission efficiency from a transmitter (Tx) to receiver (Rx) coils as non-radiative WPT for charging electric vehicles based on inductive magnetic resonance behaviour [19]. Furthermore, it provides multiple resonances response when operating in an over-coupled region of operation [21] and has the availability of integrated circuit (IC) chips for signal processing [22]. The magnetically-coupled resonant WPT idea has been applied to Tx-Rx ECT and integrated into this research as a novel WPTECT for sensing application, operating at a sweeping frequency excitation [23, 24].

Compared to other ECT techniques, the novel Tx-Rx WPTECT provides multiple resonance frequency responses for multiple feature points [4, 25], combining the advantages of different WPT topologies and other inductively coupled Tx-Rx ECT methods. Furthermore, it uses sweep frequency excitation for different penetration depths information and variation of defect parameters, which is a challenge to single-frequency ECT [26]. Similarly, it overcomes the issue of shorter testing time with less power in each frequency component as exhibited by multiple-frequency ECT [27]. Compared with pulsed ECT, besides pulsed ECT reduction of measuring time to a minimum and a broad spectrum of frequency components [5], it still suffers coupling variation and response distortion due to non-resonance harmonic frequencies contents. The broad frequency spectrum of pulse excitation produces fundamental and harmonic currents,

which causes some attenuation of the inductively coupled Tx-Rx coils' response and that of induced eddy current in the sample due to the non-resonance frequency components. Of recent, an emerging EC testing explored sweep frequency excitation and natural resonance feature for crack quantification [28], detection of thickness, measurement of permeability and conductivity of materials coating [29-31] and more complex information about the metallic objects detection [30, 32]. The nature of sweep frequency excitation and fixed probe position by this ECT enables testing of complicated areas where scanning is not feasible. However, it is blind to defects location [33] and operates at a decreasing (single resonance) frequency with increasing response magnitude for higher crack depth [28, 29]. In view of the limitations mentioned above by ECT methods, the proposed WPTECT study designed and developed different WPTECT topologies for different investigations of material and defect non-destructively to harness the advantages compared to conventional ECT.

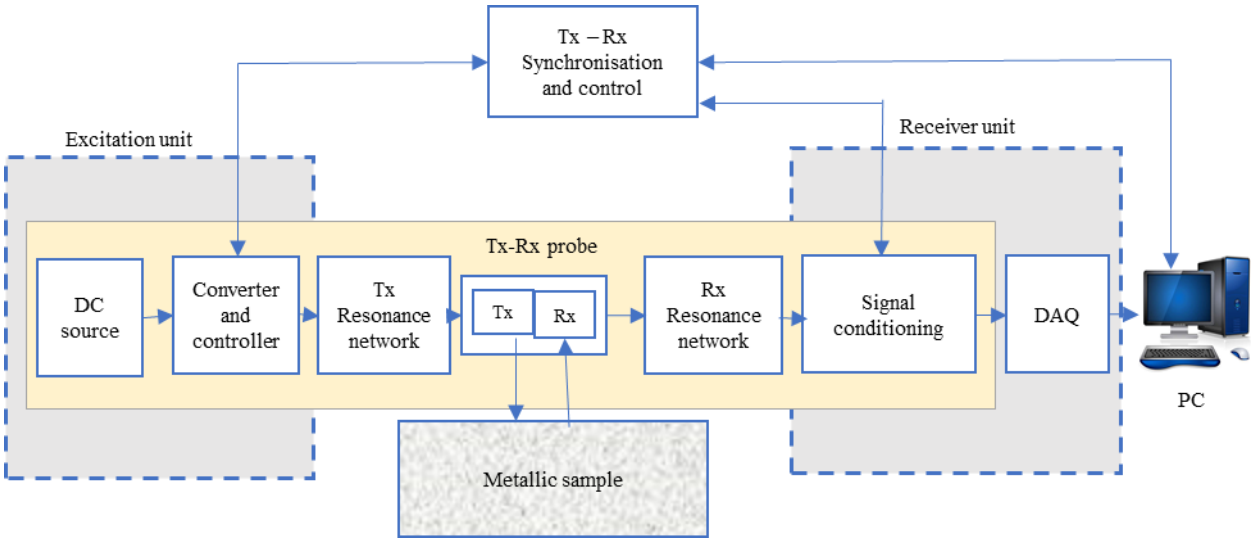

Figure 1.1 Block diagram of WPTECT system

The novel WPTECT has been applied in this research for eddy current NDT&E application because of its maximum energy transfer and capability of multiple resonance behaviour [21]. Figure 1.1 shows a general block diagram of the integrated system of WPT-based ECT, including metallic sample and personal computer (PC) for the data capturing and processing. The unique behaviour of WPTECT encourages optimum eddy-current generated field from the metallic sample due to a maximum induced eddy current, based on Faraday's law of electromagnetic induction and Lenz's law, resulting from the optimum flux generated by the Tx coil. The DC source and converter are the ac source to the Tx resonance network block. The resonance network consists of compensation reactance (inductor or capacitor) and the Tx inductance to form a frequency-controlled Tx resonance network. Similarly, the Rx inductance, together with the Rx resonance network, forms another frequency-controlled Rx network. The

Rx response is the data acquisition (DAQ) output, but the influences of sample and defect affect the two coils. Therefore, a transfer response is adopted in this research because it combines the input and output dynamic behaviour of the WPTECT system at the same time.

The challenge to defect study depends on the complex relationship of WPTECT transfer response and the influence of sample and defect parameters. The transfer response based on sweeping frequency gives different depth information because of the skin depth issue in a conduction sample [34]. The resonance points pose the maximum sensitivity deviation to any disturbance of the dynamic behaviour of the WPTECT system. In contrast, the shape of the response statistically depends on the defect parameters in addition to the Tx-Rx parameters. Therefore, the resonance points and shape of the response analysis are the features to explore for the defect analysis in this study.

In this study, the designing and development of WPTECT have been undertaken as a novel idea in the history of ECT. It investigates multiple feature extraction using inexpensive and simple Tx-Rx planar spiral coils connected to compensating capacitors for magnetically-coupled resonant WPT. The extracted features from the multiple resonances and statistical analysis of the response shape quantified the depths and widths of the cracks. Therefore, the platform magnetically-coupled resonant WPT approach is valuable for improving an ECT probe on comprehensive quantitative NDT&E through multiple feature extraction and mapping to defect parameters. Similarly, the magnetically-coupled resonant WPT and flexible coil array have been integrated by this study to inspect a pipeline sample with a natural dented area due to metal loss and corrosion. Multiple feature extraction, selection, and fusion through correlation and deep learning analysis have been evaluated to reconstruct the 3D dented-area. Furthermore, because of the problems associated with the variation of response for different topologies of WPTECT, the system response and features optimisation have been undertaken. Finally, the optimised topology has been applied in this study to characterise the challenging parameters of inclined angular cracks due to rolling contact fatigue in a railway.

1.2 Research Motivation

Eddy-current testing (ECT) applies for non-destructive testing and evaluating defects in a pipeline, railway, and other metallic structures because of its non-invasive behaviour, more straightforward operation, and inexpensive components. Despite the fact that various modified ECT probes have different performances, the stability and precision of the excitation signal and energy-efficient response signal are challenging factors to the probe's accuracy and stability. The electrical variables generated by an ECT probe are affected by noise agents due to the

inherent sample parameters, lift-off and other external factors. The noise agents usually significantly impact the response signal, leading to a signal conditioning circuit requirement before connecting to a laboratory instrument or accurate digitisation by the miniaturised device's, analog-to-digital (ADC) converter. The attempts to achieve maximum output information for ECT probe signal conditioning include the use of signal filtering and amplification, Wheatstone bridges for impedance measurement and transformer for inductive coupling. However, the conventional ECT probe and their signal conditioning circuits operate at a non-resonance Tx-Rx coils behaviour, which causes weak energy transfer leading to lower sensitivity and responsiveness to defect parameters.

Being a higher response sensitivity to defect parameters is synonymous with maximum energy transfer operation. Therefore, the motivation here is to maximise the energy transfer for improving defect detectability that guarantees safer structural operation. Maximum power transfer has recently been developed for non-radiative magnetically-coupling resonant WPT by a group of researchers from the Massachusetts Institute of Technology (MIT) [19], primarily for a wireless charge of Electric Vehicles [19, 35, 36], triggers several wireless communications and sensor innovations. The maximum energy transfer (MET) by the WPT has the potential of frequency splitting behaviour [37] and the availability of an integrated circuit for its easier signal processing [22]. These are the motives for integrating WPT and ECT for sensing application, though the ECT techniques rely on the remote field rather than the MET between Tx-Rx [6, 38]. Therefore, regardless of the Tx-Rx coupling strength, the variables in the Tx and Rx coils are concurrently affected by the induced eddy current field, which depends on the sample and defect parameters. Consequently, MET enhances the interaction of sample conditions and each of the Tx and Rx coils for optimal response and features.

From the application point of view, cracks and corrosions in engineering structures dominate the sources of structural failures with the highest significant percentage compared to other defects [2]. Ignoring such causes of defects in engineering structures resulted in the loss of human lives and properties, leading to substantial financial penalties reaching 4-5% of national incomes of industrialised countries [39]. In a particular case, the recent development of high-speed train construction and operation positively expands the transportation sector and transportation infrastructure sustainability. However, the train rail exposes to intermittent sliding and rolling contact fatigue (RCF) due to repeated stresses at the wheel-rail contact because of increasing transportation volume. The worst rail line failure due to RCF consequences is caused by multiple cracks initiation from the surface by crushing away the rail surface and eventually propagating at an inclined angle to the surface [40, 41]. It has been a

leading cause of rail breaks, causing fatal loss of life and properties in many parts of the world [41, 42]. Therefore, timely and efficient characterisation of RCF cracks in a railway facilitates preventive maintenance, averting rail breaks and safeguarding the operation of high-speed trains.

Furthermore, the challenging factor here is characterising the RCF crack geometric parameters such as crack opening width, depth and inclined angle at a measurement result. Previous quantitative NDT&E studies quantified one crack parameter at a measurement result while other parameters were unconsidered or assumed to be unchanged as in refs. [40, 43-47]. However, in real NDT&E applications, the system response is simultaneously influenced by the entire parameters, depth, width, and inclined angle of the crack. In view of this, the study considers the application of novel WPTECT to efficiently assess railway structure for facilitating preventive maintenance and eventually safeguarding the operation of high-speed trains.

From another application point of view, complex curved structures like pipelines present non-uniform lift-offs, which is a challenge to NDT&E of a defect. The problem is worsened for detecting underground pipe defects due to the protection of the pipe surface by compressed sand in addition to the coating material. The presence of dented area in the pipeline causes confined significant stresses in the dented area, including fatigue stress, which affects the pipeline carrying capacity. Also, the pig cannot pass through the pipeline for inner inspection which leads to pipeline failure based on dent severity in the near or long run, which threatens the pipeline's safer operation [48]. In particular, the dent due to natural corrosion and metal loss appeared as a surface defect, whereas the ECT is the best candidate for surface inspection. However, the pipeline sample has a curvature surface, making lift-off non-uniform. In this motive, integration of a unique flexible coil probe amenable to curvature surface as the probe of WPTECT has been considered for corroded dent area evaluation in such a complex geometric sample.

This study's applied WPTECT topologies have a distinct frequency response and quality factor, depending on the designed circuit elements parameters [35]. The response uniqueness obstructs the accuracy of extracted features for quantifying the defect and other materials' properties, including electrical conductivity and materials geometry. Therefore, it is worthy of understanding the different topologies of WPTECT and assessing an optimal topology, response, and features for enhancing the sensitivity to other defect parameters. Hence, comparing different WPTECT topologies for optimal response to defect and material for

quantitative non-destructive evaluation (QNDE) is another motive for studying different WPTECT topologies and their response optimisation.

1.3 Aims and Objectives

This research aimed to design, develop, and investigate a novel wireless power transfer-based eddy current testing for defect evaluation in metallic structures based on non-destructive testing and evaluation. The research improves the existing ECT probe applications for responding with multiple feature points at maximum energy transfer. The investigation of a novel, magnetically-coupled resonant wireless power transfer approach maps the multi-feature points at maximum energy transfer to different defect parameters for quantitative NDT&E as a novel idea in the history of ECT. The following objectives are set out for accomplishing the aim of the study:

1. To investigate the integration of magnetically-coupled resonant wireless power transfer systems (WPT) concept and ECT by designing, developing, and evaluating a model of the laboratory setup for quantitative non-destructive testing and evaluation of different samples' defects parameters.
2. To investigate the new features extraction strategy system based on multiple feature points from the multiple resonance response and compare with the set of features from the response shape for different defect parameters quantification.
3. To design, develop and investigate a flexible printed coil array probe using the WPT concept to improve ECT probe because of its advantages in mapping and scanning a sample with a complex geometrical shape such as curvature of pipeline and defect.
4. To devise a means of evaluation for selecting, extracting, and fusing defect detection and characterisation features on investigating complex geometric samples with defects.
5. To compare the response of different WPTECT topologies and optimise their features for optimal quantification of challenging parameters of rolling contact fatigue defect in a rail line material.

1.4 Proposed Research Methodology

The research has designed and implemented an NDT&E system that integrates the concept of wireless power transfer (of charging electric vehicles) and an eddy current testing to improve energy transfer and the capability of multiple features. Experimental studies supporting theoretical models are used in this research to implement the three independent studies. In each of the studies, the design and selection of sample and defect study, measurement and

instrumentation, system response, and features processing for the defect assessments are discussed in this section.

The conceptual ideas were firstly conducted by designing and developing WPTECT to investigate the detection and quantification of depths and widths parameters of defects in aluminium samples. The samples and defects were prepared in this study to mimic real-world situations in terms of their sizing comparable to industrial structures with known crack parameters for comparison with the extracted features. Then the transfer response of the WPTECT system to the samples and defects were measured as the response signal data for feature extraction and other processing. MATLAB numerical simulation software was used for signal data processing, feature extraction via samples with cracks. Similarly, other features were extracted using principal components analysis from the shape of the system transfer responses. Then, extracted features from the resonance points and principal components analysis were mapped and compared with the dedicated defect parameters.

After the first designed model case study, the designed WPTECT system was then modified and applied to investigate and reconstruct the dented area in a pipeline sample using a flexible printed coils (FPC) array as another modified probe. The FPC array was fabricated on polyimide film with a trace of micro-thickness and line spacing, which give advantages for spatial resolution and sensitivity enhancement to different geometric shapes, including curvature in a pipeline. The FPC array consists of four layers with Tx covering the top and bottom layers, while the Rx coils are distributed in the two middle layers. The arrangement allows the Tx coil-induced magnetic field to be evenly distributed across the Rx array considerably. The multiple feature extraction, selection, and fusion were investigated and compared for dented area reconstruction.

Optimisation of WPTECT topologies, response and features was finally carried out. The optimised topology was used to characterise inclined Rolling Contact Fatigue (RCF) cracks in a rail line material as it's a challenging defect. Topologies optimisation was conducted because the earlier studies were based on SS and PP topologies of WPTECT, respectively, while different topology has unique transfer response and quality factor expression. In this investigation, a carbon steel sample was used because it has the permeability and conductivity influences and the geometrical nature of the sample. Also, crack and no-crack points were considered for the response comparison based on sensitivity at varying lift-off distances.

Furthermore, features from the optimal topology were also evaluated to suppress the influence of lift-off and sample permeability by finding an optimal lift-off level. Lastly, the optimal topology was applied to characterise the incline angular RCF crack in a railway

material. Also, features extraction, selection, and mapping to the crack parameters for QNDE were numerically investigated using MATLAB® software.

1.5 Research Achievements

Compared to other ECTs, the contributions of this novel WPTECT include the design and evaluation of a magnetically coupled multiple resonance transmitter-receiver (Tx-Rx) probe operating at sweep frequency excitation for different layer information at a certain lift-off point. Different layer information eases permeability separation as ECT depends on conductivity and offers permeability invariant phenomenon at certain lift-off [49]. The contribution to ECT includes designing and developing a Tx-Rx probe operating at maximum energy transmission and potentially having a transfer response with multiple feature points. Due to multiple resonances, the responded multiple feature points provide multiple parameter information such as depth, width, orientation, and inclined angle of defects.

The whole research project investigates the designing, developing and evaluating WPTECT system for an NDT&E application. This research achievement comprises (1) Integration of magnetically-coupled resonant WPT and ECT into a novel WPTECT; (2) WPTECT application to NDT&E of artificial cracks' parameters; (3) Integration of FPC array to WPTECT for complex geometrical structure (pipeline) application for corroded dent area reconstruction; (4) Investigation of RCF cracks in railway material and (5) Optimisation of WPTECT topology and its features for QNDE. Along with implementing the stated five achievements, new sets of features have been developed based on resonance points and another statistical analysis of the response shape from the principal component analysis. The achieved extracted features were compared, including their fusion, for defect characterisation in the application of pipeline defect investigation and assessment of fatigue cracks in a railway material. These achievements are centred around three independent pieces of research mentioned below**.**

(a) Integration of WPT and ECT for sensing application

In this research, the design and development of WPTECT model investigation have been achieved using the series-series topology of WPTECT because of its higher current at the resonance point, leading to higher induced eddy current and higher flux linking the receiver coil. Furthermore, it investigated multiple feature extraction for slot detection and quantification using the WPT concept. The response from scanning two aluminium samples was analysed based on resonance points and the shape of the system response as features. The extracted features from the resonance frequency points and statistical approach demonstrated that the eddy-current density is highest around the slot and each slot width (depth) depends on

the width (peak) of each extracted feature spanning before and after the slot. Initial results of the first WPTECT model investigation have been published in the IEEE sensors journal, which is in line with the mandate of this research deliverables and given by reference [24].

(b) Modified probe for the reconstruction of the dented (corroded) area in a pipeline:

This research contributed to the new concept of WPTECT probe modification and its evaluation technique for inspecting a complex geometric sample, especially where scanning is non-viable. In this research, WPT, sweep frequency, and flexible printed coils array are integrated to reconstruct the dented area in a pipeline due to natural corrosion and metal loss using the parallel topology of WPTECT. The parallel topology circuit has a higher transfer function response to metal and defects with less sensitivity to noise influence due to its current source nature and higher input and out impedance at the resonance point. The research investigated multiple feature extraction, selection, and fusion, which then characterised and mapped 3D natural dent-area on a pipeline sample [23]. The features from the multiple resonant points and principal components analysis of the two resonant areas were considered for correlation analysis, feature selection, and fusion. The deep learning-based multiple feature fusion outperforms canonical correlation analysis feature fusion and other non-fused 3D dented area reconstruction features. The achievement of these results has been published in the Philosophical Transactions of the Royal Society A (Theme issue: Advanced electromagnetic non-destructive evaluation and smart monitoring). It investigated the dual resonance response of S21 for multiple feature extraction, selection, fusion, and mapping to the 3D dent-area parameter for reconstruction and characterisation [23].

(c) WPTECT topologies, response, and feature optimisation:

In this study, a comparison of different WPTECT topologies for achieving multiple resonances, including preferred features extraction for characterisation of inclined angular RCF cracks, has been investigated. The results show that parallel topology and combined parallel/serial topology provide multiple resonances for multiple feature points within the operating frequency range. The multiple peak frequency of the WPTECT response is more affected by the lift-off distance. In contrast, the response magnitude is affected by both sample's conductivity and permeability and lift-off distance. The depth, width, and inclined angle of RCF cracks were capably characterised by the extracted features of the combined topology of WPTECT in a measurement result contrary to other techniques. The combined topology establishes the capability of the multiple-resonance response of WPTECT on responding to eddy current losses in the sample and defect characterisation compared with other ECT

methods. Part of the results of this achievement is under review at IEEE Transactions on Industrial Informatics journal.

1.6 Thesis Outline

The thesis has divided into seven chapters. The first three chapters are the introduction, literature review, and research methodology. The three contributions have appropriately spread into chapters four, five, and six, but the whole thesis conclusion and recommendations are summarised in chapter 7. Below is the breakdown of each chapter's summary.

Chapter 2 presents an in-depth literature review of electromagnetics NDT&E techniques, including the advantages and disadvantages of each technique. It furthermore offers a background review of WPT linking to the theoretical background of the ECT and its consideration for probe improvement. The chapter explores some existing challenges and problems of ECT and integrates the potentials of magnetically-coupled resonant WPT to address them, and finally, it concludes by summarising the significant achievements.

Chapter 3 revisits the essentials of theoretically and experimentally integrating inductive Tx-Rx ECT probe and its performance for multiple resonance capability based on different topologies of magnetically-coupled resonant WPT. It also comes up with the research methodology that includes multiple features extraction, selection, fusion and comparison based on the three studies: first WPTECT designed model investigation, application and topology optimisation for eddy current non-destructive testing and evaluation. The merit of the chapter is the layout procedures linking magnetically-coupled resonant WPT and ECT for energy-efficient NDT&E inspection with multiple features capabilities at higher sensitivity.

Chapter 4 describes the results of the designed and developed WPTECT for ECT inspection analytically and experimentally. It gives signal processing and features extraction insight and compares the resonance frequency points features with that of principal components analysis from the shape of transfer response. The chapter's outcomes characterise artificial slots' depths and widths parameters to prove the study concept for improving the capability of the ECT probe for NDT&E applications.

Chapter 5 describes the results of multiple features from integrating flexible coils and WPTECT. Its results characterise and reconstruct a 3D dented area due to natural corrosion and metal loss in a pipeline sample by integrating Flexible Printed Coils (FPC) array into a WPTECT and evaluating multiple features extraction, selection, comparison and fusion. It uses parallel-parallel topology of WPTECT to assess natural defects in a complex geometric ferrous metal structure using probe mapping and axial scanning. The merit of this chapter is

overcoming the challenges of inspecting complex curved structures such as pipelines where scanning is tedious, as mentioned in section 2.3.2 of the literature review.

Chapter 6 contains the results of five different topologies of WPTECT for optimal response, parameters, and features, including characterisation of inclined angular RCF crack parameters in a rail-line material using an optimised topology. It presents the results of designing and implementing the WPTECT topologies for multiple feature points capability, transfer-response and extracted feature optimisations based on lift-off assessment at a crack and no-crack position. Also, it includes the results of an optimised topology for quantitative investigation of the entire parameters of inclined angular RCF cracks in a railway material. One of the merits of this chapter is the characterisation of the whole parameters of inclined angular RCF cracks in a measurement result, unlike other methods that quantify one parameter while others are fixed [43-47].

Chapter 7 summarises the research work carried out and briefly outlines the key contributions. It also presents the research conclusions and outlines further work based on the current findings and the existing literature.

1.7 Chapter Summary

This chapter began by describing the general introduction of the study proposal and briefly reviewed its related background studies. The chapter gave insight into integrating magnetically-coupled resonant WPT and ECT to respond to quantitative NDT&E of different defects and operate at multiple resonance frequencies, leading to multiple feature points. The motivations of the general ideas of the entire study, from the integration of WPT and ECT advantages and requirement for signal conditioning to its application for dented (corroded) area reconstruction and topologies optimisation for evaluating rolling contact fatigue cracks and characterisation, are presented in this chapter. Similarly, the study objectives and achievements of the whole study narrowed down to specific applications in pipeline dent-area and rail line RCF cracks evaluation are also discussed in this chapter. Finally, the thesis structure is briefly described, including the methods and presentation of the thesis' remaining chapters.

Chapter 2. Literature Review

2.1 Introduction

The previous chapter gives the proposed introduction of WPT-based ECT research background and motivation, including the main aim and objectives and research methodology. This chapter presents a literature review of electromagnetic NDT&E techniques for assessing structural integrity. The most common techniques, including ECT, are reviewed and presented, including their application, merit, and demerit compared to others and highlighted the identified problems and challenges and proposed steps to address them. Furthermore, the chapter presents an outline review of magnetically-coupled resonant WPT and its integration and consideration for ECT application and their challenges and problems. Finally, the chapter concludes by summarising the problems and challenges of ECT and linking to WPT consideration.

2.2 Electromagnetic Non-destructive Testing and Evaluation Techniques

Non-Destructive Testing and Evaluation (NDT&E) techniques assess structural integrity by inspecting a whole or part of it while it's in operation without causing any damage or affecting serviceable function. Electromagnetic NDT&E is one of the leading NDT&E techniques primarily for localisation and characterisation of an object, material, or component and defect in a conductive structure without weakening its future usefulness non-invasively [27, 50]. In addition, it explores the advantage of an electric or magnetic field induction to a structure and integrity assessment, especially in engineering industries, including pipeline petrochemical industries [51-54] and railway transportation [40, 42, 55, 56]. A comprehensive literature review of current electromagnetic NDT&E applications, challenges, and problems are groupings under the following subheadings.

2.2.1 Magnetic Flux Leakage (MFL)

The Magnetic Flux Leakage (MFL) techniques detect magnetic flux irregularities from the induced normal flux patterns due to abnormalities in a ferromagnetic material saturated by a magnetic field [10]. The advantages of MFL techniques include resulting in a fast inspection without removing the insulation, which is an economical way to especially long runs of pipelines. It applies to the inspection of pipelines [52, 57], railways [9], water tank floors [58, 59], and other applications for quantitative NDT&E. Figure 2.1 shows the schematic of MFL principles for defect assessment, clearly indicating the effects of induced magnetic fields at the defect area. It first magnetises the material to be inspected using permanent magnets [60] or electromagnet [61], and the magnetic flux would leak-out if there is a defect due to a change in

magnetic permeability, as shown in figure 2.1 [51, 62]. The magnetic field sensor and processes can sense the leakage magnetic field around the defect to characterise the defect. The flux leakages depend on the defect's width, depth, and orientation parameters in addition to the speed of the magnetiser [9, 10]. The magnetiser choice for the induced magnetic field depends on the direction of the induced field and the type of excitation. On the type of excitation, there are different approaches to excitation of magnetiser unit, which include Direct Current MFL (DCMFL), Alternating Current MFL (DCMFL) or Pulse MFL (PMF) excitation. The ACMFL method is more sensitive to the surface and near-surface defects such as corrosions and cracks in pipeline structures due to skin effects compared to others [63]. However, the DCMFL lacks sufficient data for defect quantification, cannot detect omni-directional defects, and requires frequent demagnetisation to completely cancel out the residual magnetism developed by previous scans [63]. In comparison, the PMFL provides better defect depth estimation than DCMFL and ACMFL through time-to-frequency signal analysis. However, it cannot distinguish the influence of a neighbouring defect.

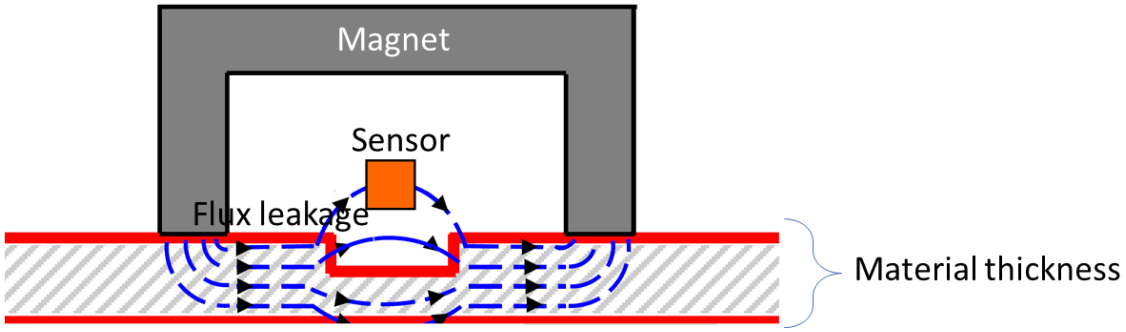

Figure 2.1 MFL principles-mechanism

The components of leakage flux exist along the three axes of the defect called radial, axial, and circumferential fields components. The intensity of the MFL components along the three axes has been investigated by [9, 64] to quantify the defect's width and length along the two surface axes and the depth parameter. The axial field is susceptible to a crack parameter perpendicular to the magnetisation axis while the circumferential field to the parameter along the axial direction. The axial component's highest response to the defect is exhibited for the length information and the circumferential component for the width. Furthermore, the radial field sensitively quantifies both the crack's width and depth [65]. Therefore, the sensitivity of the MFL signal is higher for a crack orientated perpendicular to the direction of the field components due to the sufficient leakage flux [66]. However, combining axial and circumferential excitation makes the MFL system have a large volume, especially in pipelines. Therefore, it causes low trafficability, which causes the blockage of the in-line inspection

resulting in major accidents. The disadvantage of the circumferential component is that its amplitude is generally lower than that of the other components and is more affected by noise and other disturbances [64]. Usually, radial components of the field provide better quantification of defects compared to other components.

Recently, the tri-axial MFL technique has been used by other researchers to investigate the spatial distributions of the three MFL components (axial, radial, and circumferential) for defect identification and sizing along the axial and tangential directions [67]. Tri-axial MFL testing provides detection of defects, including the complex defects in the three directions (3D), due to the influence of axial, radial, and circumferential flux leakage features more accurately than conventional MFL [64, 68]. However, it lacks substantial improvement for external and surface defects as it cannot distinguish between the defect from the internal and external sides of the material walls.

Another challenging issue to MFL is the motion-induced eddy current (MIEC) due to the velocity of the magnetiser, mainly when applied to pipeline and rail line inspection and other ferromagnetic structures. The MIEC generates a magnetic field that opposes the magnetisation field, corrupts and distorts the measured MFL signal's amplitude, and causes transient magnetisation and magnetic flux concentration effect closer to the magnetiser's rear pole [58, 61, 69, 70]. The magnetic field inside the sample does not instantly reach equilibrium because of the incomplete magnetisation. Therefore, the sensor reaches the defect tip before the magnetisation reaches the equilibrium state on the sample surface [61, 71, 72]. Studies have been conducted to obtain the minimum time required to fully magnetise the material [72], investigate the relationship between flux leakage and inspection velocity [61], and the prospects for high-speed MFL inspection upto 200 km/h [71]. Solutions have been proposed by [61, 72] to increase the axial length of the magnetizing coil (inter-pole distance) and the pole-piece thickness. However, this affects the smooth operation and reduction of magnetic energy consumption of the MFL system as the inter-polar distance must be as short as possible for optimising excitation energy [62].

Despite the progress and effort to improve the response and excitation signals and sensor optimisation of the MFL system, it is still limited to surface and subsurface defect inspection of ferromagnetic materials [9]. An electromagnet magnetiser needs strong power to magnetise a specimen into saturation level. It has been affected by the scanning speed [9], sensor lift-off and spatial resolution of the signals [73, 74], and inhomogeneous surface due to surface roughness [75]. Also, it cannot directly measure actual pipe wall thickness, and has limited detection of too small and complex SCC openings [76].

2.2.2 Alternating Current Field Measurement (ACFM)

ACFM technique was initiated at a University College London (UCL) to combine the advantage of the alternating current potential drop and eddy current in a material [77, 78]. It characterises surface or near-surface defects in ferromagnetic and non-ferromagnetic materials non-destructively to overcome directional detection limitations for both above and underwater structures [79, 80]. It has been applied to quantitatively evaluate axial cracks on the surface of a pipeline [81], RCF investigation in rail lines [82-84], and including assessment of the cluster of cracks colonies in other structures [85, 86]. The principles of the ACFM probe operation depend on alternating current flows in a thin skin near any conductor's surface by introducing a uniform current into a defect-free area of the conducting material. However, If the area contains a surface or near-surface defect, then the current is forced to flow around and underneath it, as seen in Figure 2.2(a), disturbing the resultant surface magnetic field [87]. The induced field (Bz) normal to the surface gives negative and positive responses at either end of the defect due to the generated current densities. It thus indicates length and depth, as seen in figures 2.2(b) and (c) [79]. Furthermore, along the direction of the current flow (y-axis), the field parallel to the crack indicates the crack width based on the two-peak values, as seen in figure 2.2 (d) [88].

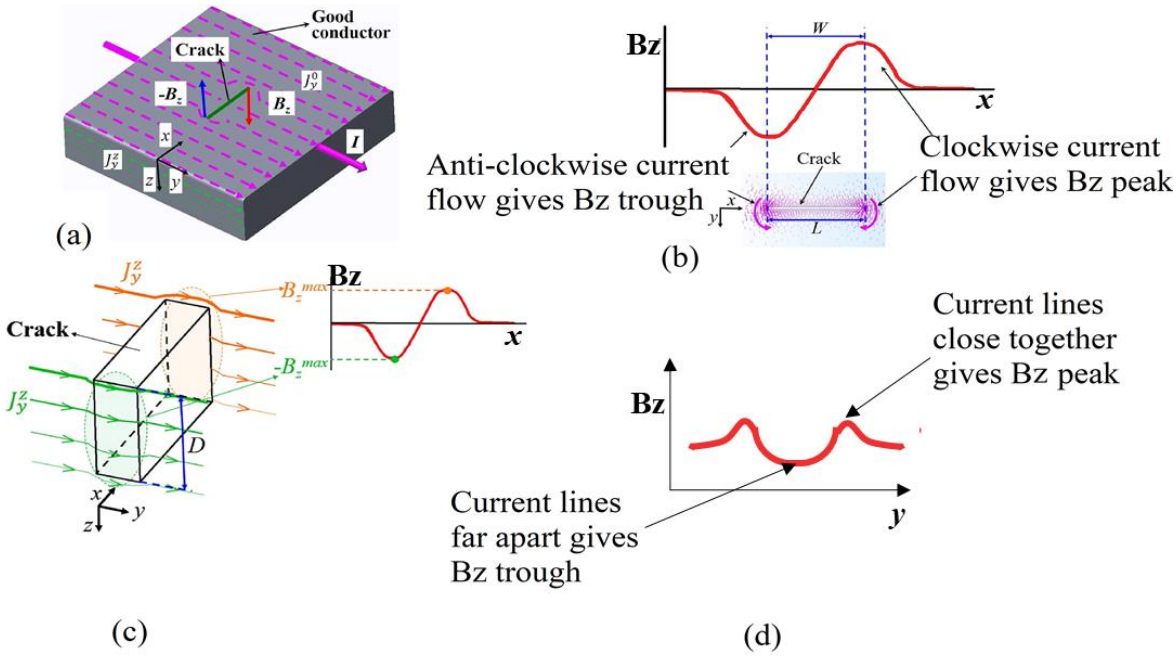

Figure 2.2 The principles of ACFM probe operation and its response signal for quantitative NDT&E (a) A picture of the current (I) applied to an inspecting material with a crack. (b) The detection principles of the crack length L by the field along the crack length (c) Detection principles of the crack depth D based on the field along the crack length [79] (d) Detection principles of the crack width by the field along the crack width.

The merits of the ACFM technique include characterising defects on the material above and underwater inspection for ferrous and non-ferrous metallic structures with little effect of probe lift-off distance and permeability. The good tolerance of lift-off distance effect on ACFM signal is due to the slighter decrease of the current induced by the magnetic flux [87, 89], making it attractive for rough surface inspection like weld area. Similarly, it allows the potential application of an array of sensors connected to the probe for mapping, especially railhead, to monitor the magnetic field disturbances due to cracks [90]. However, the ACFM technique is easier to detect defects, but the signal interpretation is harder to interpret for the non-trained operator.

One of the vital achievements from the ACFM potentials is the alternating current stress measurement (ACSM), a novel and operative electromagnetic NDT&E technique. The ACSM demonstrates that stress due to the bending and tension in a structure is proportional to the magnetisation of the inducing current frequencies before the yield point [91]. Compared to other NDT&E techniques, the ACSM has been described as having the benefit of portability, being quick to implement, cheap to undertake, and ideal for performing in-situ measurements during maintenance shutdown [92]. However, susceptibility to microstructural effect restricted spatial resolution and depth of penetration limit the application for surface stress assessment, especially on structures like rail lines, pipelines, and nuclear plants [92].

Despite the vast advantages of ACFM, it is still hard to characterise an inclined RCF and SCC cracks if the skin depth is small compared to crack depth like in ferrite steel. However, in non-ferrous metal, there is an asymmetry in the surface current density on either side of the inclined crack, which may give information of the inclined angle through-thickness depth, though it's hard to measure and interpret in practice. Also, since the ACFM uses an induction coil to induce a current in the material under test, the lower frequency could have less sensitivity to thinner surface defects at, say, 1kHz signal. However, higher frequencies and smaller coils can improve the sensitivity, but with the compromise of increased noise [93].

2.2.3 Remote Field Eddy Current (RFEC)

The RFEC technique uses a through-transmission effect [94] to transfer the energy from the exciter coil to penetrate through the sample wall and return to the receiving coil. It applies to investigate the likelihood of sensing and characterising internal and external defects mostly on pressurise tube samples [6, 95-102] and rarely on flat metallic structures [38, 103, 104]. In principle, the RFEC techniques were initially applied to pipeline tubes and operated based on a low frequency alternating current excitation for generating an EM field, as seen in Fig 2.3. The

gap between the exciter and detector coils is about 2 to 3 times the inner pipe diameter. It operates at a frequency at which the skin depth is approximately equal to the wall thickness for good field penetration depth [95]. It induces circumferential eddy currents which extend (axially and radially) in the wall of the pipe to the detector coil, though concentrated in the vicinity of the exciter coil. According to Lenz's law, the induced-eddy-current generated field modulates the primary magnetic field, proportional to the sample's conductivity, permeability, and geometrical nature, travelling through the tube's wall twice from near field to remote field area as seen in figure 2.3 [105]. An internal or external defect in the pipe sample can be detected by evaluating the change in induced voltage at the detector coil.

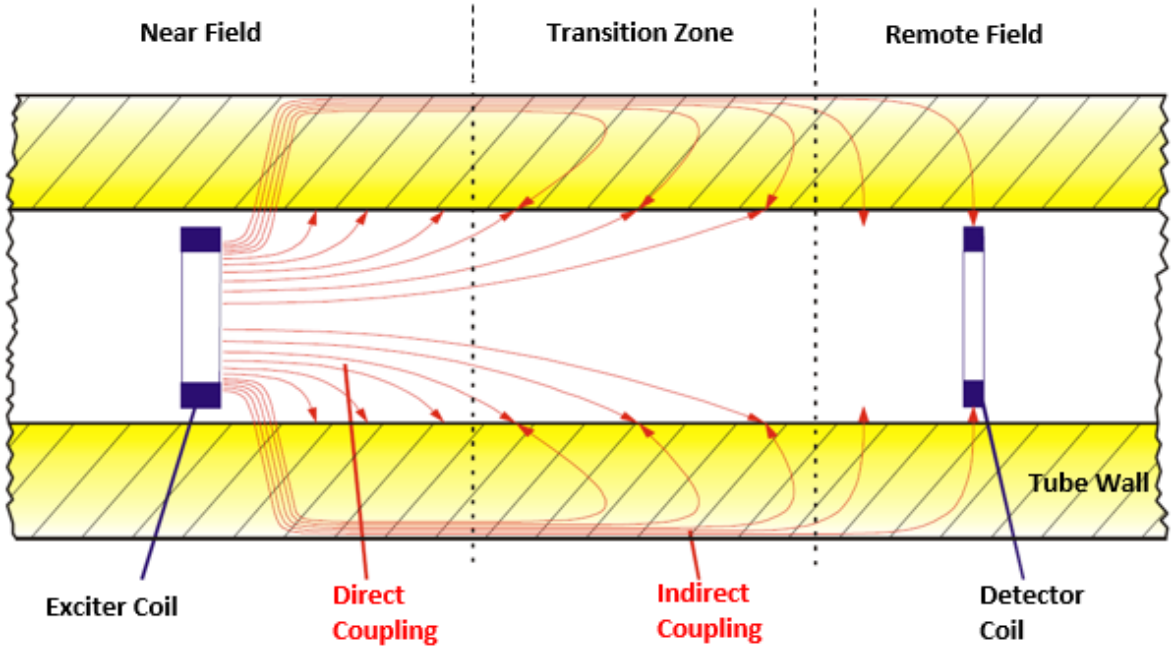

Figure 2.3 RFEC principles indicate the total magnetic field lines from the excitation current and eddy currents inside a pipeline sample.

The unique advantage of the RFEC technique is the assessment of internal and external surface defects [106] distinguishable using a zero-crossing time feature as has been presented in [95]. However, it suffers less sensitivity and poor signal-to-noise (SNR) ratio for axial defect characterisation due to a tiny perturbation in the pathway of the magnetic field. The insensitivity and poor SNR have been overcome by using an orthogonal magnetic field, demonstrating nearly equal sensitivity to frequent defects by adopting a self-differential mode pick-up coil [6]. Additionally, the challenge of responding with two peaks (primary peak and secondary peak) due to twice penetration to the wall of the pipe [94], which may lead to incorrect evaluations of defects [98], has been resolved by using dual receivers coaxially to the transmitter in differential mode [100].

Despite the improvement and modification of the RFEC technique, its sister technique, ECT, is more preferred to inspect non-ferromagnetic materials such as copper and brass due to the negligible permeability. The main distinguishing parameter between the ECT and RFEC is the spacing between exciter and detector coils and the distinguishing internal and external defects. Additionally, the RFEC technique has equal sensitivity to internal and external wall defects, less sensitivity to change in lift-off distance, and without limitation of skin effect [95, 97, 98]. However, weak testing signal and single spectrum are still challenging to RFEC techniques, though claimed to have been resolved by pulse excitation RFEC [38, 98, 103]. Still, the pulse excitation suffers distortion due to non-fundamental harmonic signals and the complex influence of permeability and conductivity in ferrous materials.

2.2.4 Magnetic Barkhausen Noise (MBN)

The MBN is one of the oldest micromagnetic NDT&E techniques discovered in 1919 by H. Barkhausen. He found that changing the magnetic field around the magnetic material could induce a rushing sound in the speaker due to small sudden changes in magnetic flux within the coil's confines [107]. However, its potential as an NDT&E was discovered long after that time. It is used for quality control in many industrial applications to determine the residual and applied stresses concentration [108-110], characterise the magnetic-easy axis [111], prediction of material hardness [112], and the influence of grain size [113] in a ferromagnetic material. In principle, it operates by magnetising a core using an alternating current, as seen in figure 2.4, which in response magnetises the test material under test, resulting in the domain wall movements within the material. The movement of the domain walls inside each grain due to the alteration in the size of adjacent domains induces an electric pulse in a conducting coil positioned near the test material. In the form of voltages, the total induced pulse by the complete domain wall movements represents a noise-like signal known as the Barkhausen Noise [114]. The induced (voltage) pulses depend on the material stress, hardness and microstructure [110, 115].

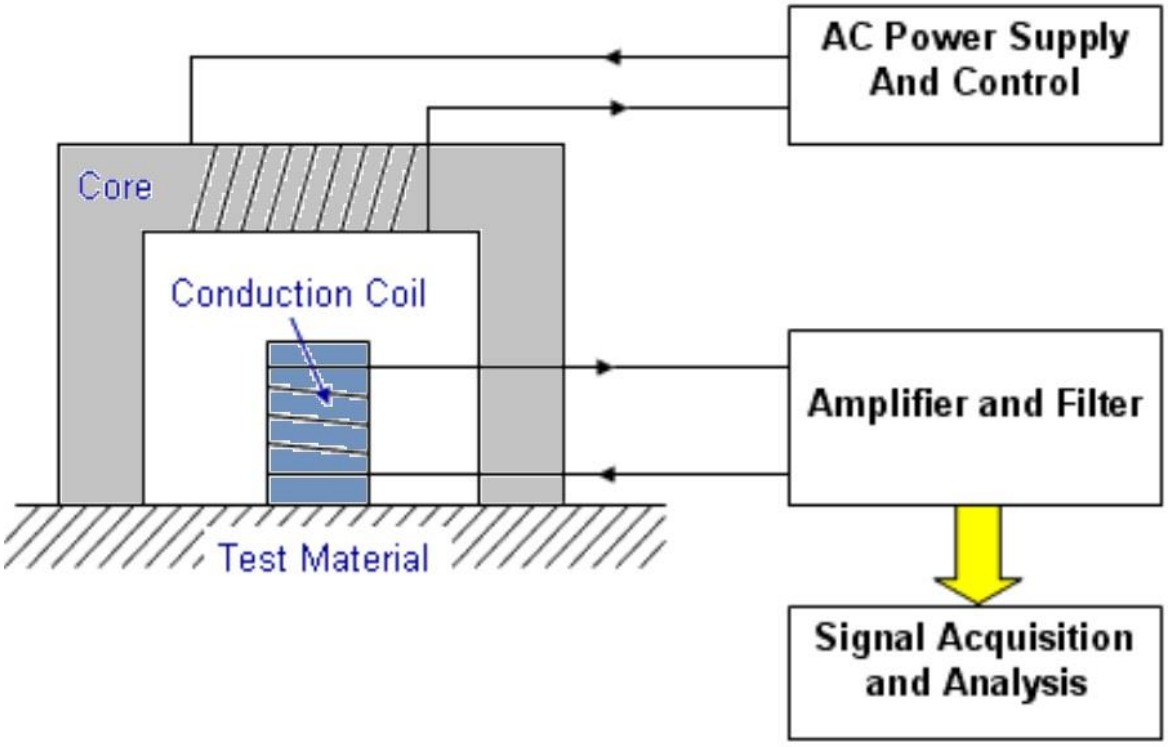

Figure 2.4 MBN system blocks adapted from [109]

The MBN technique has achieved significant improvements in assessing the sensitivity to residual stresses, variation of grain size, magnetic-easy axis, and prediction of material hardness. The achievement has been to different industrial scenarios on ferromagnetic materials to allow the stress evaluation of welded electrical steels [109], health monitoring conditions on materials for bridge structures [116], grinding process improvement [117], and inspecting surface hardness in deep drawn parts [110]. However, the MBN technique is under development and not yet consistent [118]. Furthermore, it has been applied in pipeline inspection to help interpret the MFL technique's results for evaluating stress concentrations around the pit corrosion [119]. However, it requires calibration on material specimens with different plastic deformations for quantitative analysis. Also, the tensile stress and Barkhausen noise relationship are affected by the thickness of the material coating.

2.2.5 Electromagnetic Acoustic Transducers (EMAT)

EMAT is an electromagnetic NDT&E technique capable of generating and receiving ultrasonic waves for ultrasonic inspection of ferromagnetic and paramagnetic metallic material structures [120]. It has been applied to the inspection of pipelines [120-122], rail lines [123, 124], and other metal manufacturing and processing [125] because of its advantages of fast detection speed, non-contact, and non-couplant requirement compared to the traditional piezoelectric (ultrasonic testing) method [126]. In principle, it operates by generating

ultrasound waves through either of the two mechanisms: magnetostriction for magnetic materials and Lorentz force for other metallic materials [127, 128]. Figure 2.5 shows the interaction between a relatively high frequency (RF) field generated by electrical coils and a static field generated by magnets to produce a Lorentz force. The interaction of the Lorentz force impact against metal lattice creates an ultrasonic wave that passes into the inspected material. In the receiving coil, the reverse of the excitation process occurs. The ultrasonic waves reflected from the material form an eddy current signal into the metallic structure based on electromagnetic induction and detect it through metals. When the frequency is over 20kHz, it is considered as an ultrasonic wave.

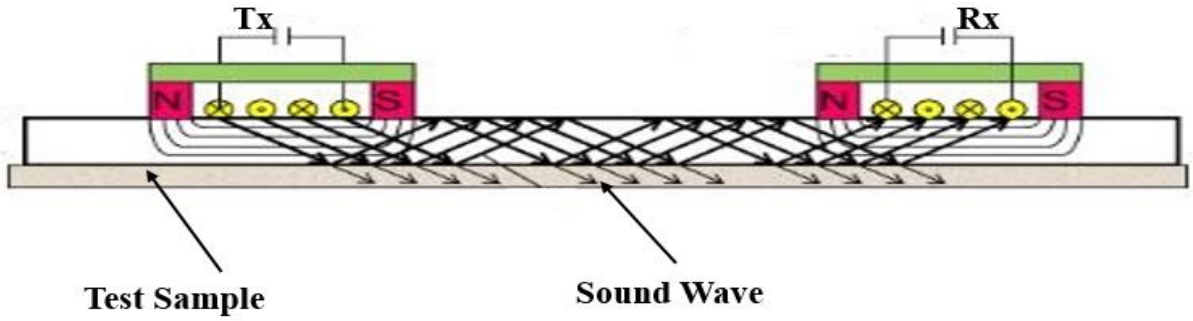

Figure 2.5 Principles of EMAT technique. Image copied from [120]

The advantage of EMAT is the production of wave modes used in ultrasonic testing [126], including some very unrealistic modes with conventional transducers. The wave modes applied to the operation of EMAT include shear wave [129], Shear horizontal wave [128], shear and longitudinal wave [130], helical shear horizontal wave-based [131], Lamb wave [132], Helical Lamb Wave [121], Rayleigh waves [133, 134], laser ultrasonic surface wave [11], and surface wavelengths [12]. However, the application of different wave modes to EMAT NDT&E possesses different characteristic behaviour.

As discussed in [135], the Shear Horizontal (SH) travels inside the pipe wall and uses to detect any crack and size the crack depth. The advantages of SH wave include simplified signal analysis and potential of its reflected wave not to cause waveform conversion when reflected at the boundary. The surface wave identifies the inner and outer surfaces defects because it travels to the inner surface of the pipe wall. The Lamb wave distinguishes cracks from no cracks and measures the wall thickness of the pipe because it travels circumferentially inside the pipe wall. The single-mode Lamb wave, generated at low frequency, improves the detection efficiency but does not increase the detection scope or reduce the number of permanent

magnets. Moreover, the application of axial and circumferential (bi-axial) guided waves has the potential of axial and circumferential crack detection [136].

Utilising the advantages of various wave modes obtainable with ultrasonic EMAT, further research on EMAT technology have applied for assessment of residual stress in railways [124, 129, 137] and weld defect [122, 138] and stress corrosion cracks [139, 140] in pipeline infrastructures because of its non-coupling agent requirement, higher accuracy, adaptable to high temperature as well as wide range detection [120]. However, one of the challenges to the EMAT technique is detecting near-surface defects due to the inherent limitation of the blind detection area, though a combination of ECT and bulk wave EMAT has been investigated for robustness to surface defect [138]. However, it is a challenge to separate defects in the weld region due to the unevenness and complexity of the weld area. But, the bulk wave EMAT travels inside the pipe wall rather than near-surface [138] and achieves a millimetre defect-recognition in a pipeline weld area [122].

However, EMAT has more challenges due to the requirements for power conditioning circuits and additional signal processing circuits. The challenges include lower conversion efficiency due to high energy consumption, inability to operate in a strong vibrating environment, lift-off issue, and weak response signal than other NDT&E techniques. Some researchers from the school of Engineering, Newcastle University and some Chinese Universities have been researching and proposing solutions to some challenging issues to the EMAT inspection. The research includes solutions to high energy consumption and low conversion efficiency [120], quantitative analysis of defect location due to the surface roughness [122], low efficiency due to large lift-off and susceptibility to noise [8], surface rolling contact fatigue crack in rail line [11], and fusion of EMAT and pulsed Eddy current testing (PECT) for the hybrid defects detection [138].

In another development, complete EMAT in-line inspection equipment was developed by industrial researchers from ROSEN group, PII Pipeline Solutions, and TransCanada Pipelines Ltd to advance the EMAT technology by bridging the gap between industries and academic research for pipeline crack inspection [139, 140]. However, the investigations are still in the infant stage as more challenges are required to be addressed and resolved.

2.2.6 Eddy Current Pulsed Thermography (ECPT)

Eddy current Pulsed thermography (ECPT) is an integrated NDT&E technique that captures the influence of pulsed eddy current distribution using infrared imaging over a relatively wide area in a metallic sample [141-144]. It has the advantages of non-contact inspection, fast coverage of large areas without scanning, volumetric heating concentration around the defect area, and large contrast between defective and non-defect regions [145]. Figure 2.6 [146] describes the principles of its operation, where the induction heater is excited by a short burst of electromagnetic excitation from the pulse generator to generate heat and induce eddy currents on the conductive material (sample) with crack. The induced heat diffuses into the sample in time until it reaches the equilibrium state and then cools down. The heat conducted by the sample's surface is captured through an IR camera, which displays the thermal imaging on the PC screen. The presence of defects on the sample disturbs the heat distribution, as seen in the image in figure 2.6 (a). The disturbance increases the induced EC density around the crack area and manifests in the heating and cooling stage behaviour depicted in figure 2.6 (b). The sum of the induced heat in the sample correlated to the square of the magnitude of electric current density in the sample, which is proportional to the electric field intensity vector [146]. The effect of diffused heat and the density of eddy current distribution has been applied for defect assessment in composite fibre reinforced polymer (CFRP) [147-149], rail track [40, 150-152], and some cases of spot welds area [153] and corrosion blister [154] in a surface and sub-surface of the structures.

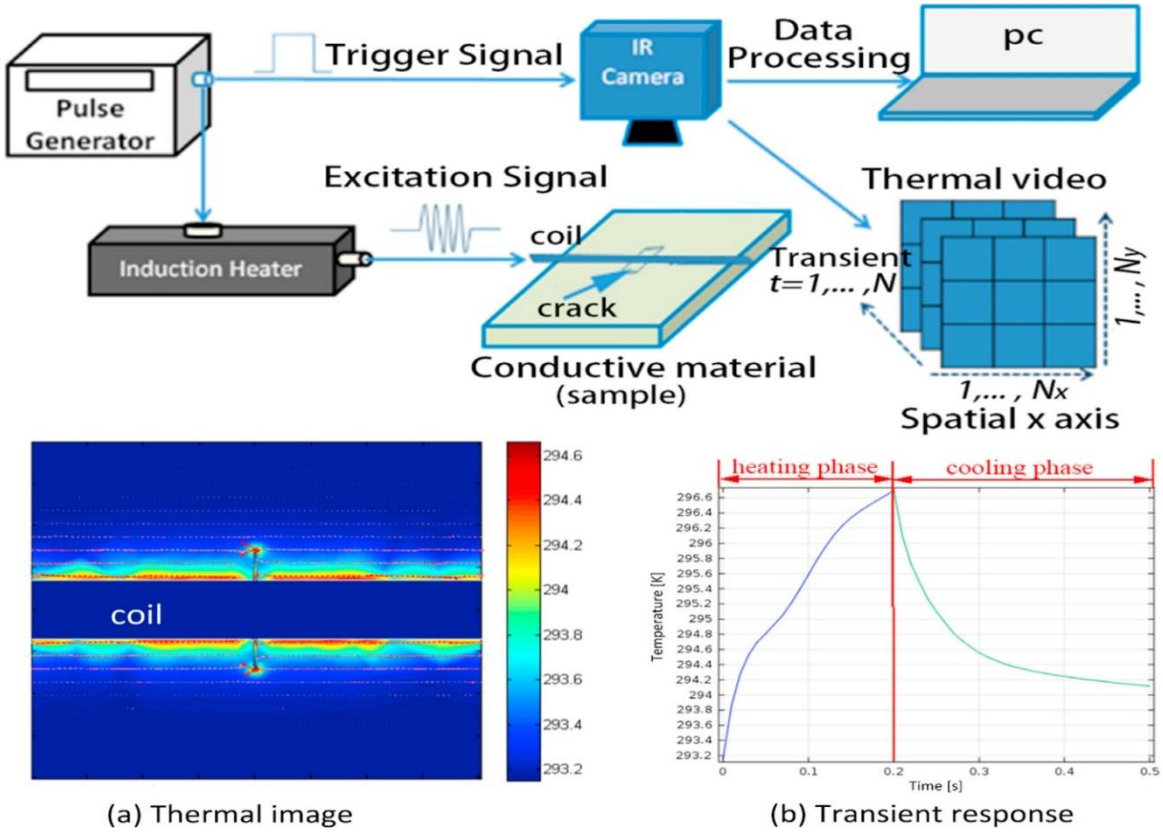

Figure 2.6 Basic outlines of an eddy current pulse thermography system. Image copied from [146].

In the CFRP application, the heating and cooling stage reasonably estimates electrical and thermal conductivities in the fibre direction of a different layer. However, it suffers an error increase as the depth of the layers increases due to the diffusive nature of the thermal waves [155]. In a rail track application, the ECPT technique requires pulse excitation with more extended time slots/ duration for a clear relationship between the defect parameters and the crack features like the thermal area-based and kurtosis-based feature [40, 156]. Similarly, the features from the principal components analysis (PCA) potentially have a linear relationship with the crack parameters, though with low reproducibility whereas, the maximum thermal response has the merit of high reproducibility, though with less monotonous relation with the crack parameter [40, 43, 44]. The PCA has the advantage of simple implementation and fast calculation speed of data reduction, can fully explain the linear correlation satisfactorily, but limited to lower order features correlation [148]. However, the investigation of corrosion blister by the ECPT in mild steel has been described based on the interaction of eddy current distribution and heat conduction in the sample [154]. Several extracted features can efficiently mitigate the non-uniform heating and improve the detectability of corrosion blister, though the thermal peak time outperforms other features.

Despite the numerous modifications of ECPT, it still has significant challenges. The equipment required for the PECT experiment is too expensive compared to that of other NDT&E techniques like pulse eddy current testing. Also, the equipment is so bulky and requires a high current to operate. The pulsed excitation signal has a broad frequency spectrum which produces circulation of fundamental and harmonic currents, affecting the response of the heating element and the diffused heating to the sample due to the harmonic frequency distortion [157]. The technique is limited to the application of inspecting conductive metals and conductive non-metals, as the heating depends on the Eddy current density and diffused heating [158]. Also, the system sensitivity decreases with defect depth due to the skin depth effect.

2.3 Eddy Current Testing Technique

Eddy Current Testing (ECT) is a prominent and widely used non-destructive testing and evaluation (NDT&E) technique for detection and characterisation of conductive metallic (materials) structures and their defect evaluation [16, 159, 160], in addition to the measurement of material thickness [3, 161-163], coating thickness [31, 164-166], conductivity [167-170], and permeability [171-173]. The uniqueness of ECT includes offering environmentally friendly and economical inspection non-destructively with high inspection speeds, detectability and offers good insight into conductive material and defects [4]. However, these attributes of ECT probe inspection are more highly realisable while inspecting non-ferrous than ferrous metallics structures.

2.3.1 Conventional Tx-Rx ECT probes

The simple and common probe for ECT used electromagnetic excitation (driver coil (solenoid)) and receiver (pick-up) units. The excitation unit, known as a transmitter (Tx), is always connected to a source of alternating current and induces an eddy current in the sample. The receiver (Rx) unit could be the same Tx coil as in the case of absolute probe [166, 174, 175], another separate coil(s) [176], or solid-state magnetic field sensors [177] for sensing the eddy current generated field from the surface of the material. Several investigators have described various probe configurations to detect and characterise a defect in conductive metallic structures at different modes. Among different ECT probes, inductive probes arrangements based on Tx and Rx coils arrangement with a magnetic axis perpendicular to the sample surface are considered promising architectures [4]. Despite their decreasing sensitivity at a lower frequency than the magnetic sensor [4], the Tx - Rx probe is simple to manufacture for different shapes and sizes suitable for different inspection tasks. However, it is sensitive to lift-off

variation, which is a general challenge to all probes of ECT [17]. This research reviews the principles of the Tx-Rx inductive ECT system probe according to how the coils wrap to the sample surface (configuration) and flexible probe and their interface with the test equipment (mode of operation).

2.3.1.1 Principles of operation of Tx-Rx ECT probe

The basic principles of an ECT require the measurement of a secondary magnetic field influenced by the eddy-currents in the inspection material. It works based on a time-varying current that passes through the transmitter (Tx) coil, creating a primary electromagnetic field (EMF), as seen in Figure 2.7. According to Faraday's law of electromagnetic induction, an eddy current is induced in the material whenever an electrically conducting material is near the Tx primary field, as shown in figure 2.7. Lenz's law explains that the induced eddy current flows in such a direction as to oppose the motion producing it by generating a secondary electromagnetic field opposite the primary magnetic field generated by the Tx, as seen in the two fields arrow depicted in Figure 2.7. As a result of these two opposing fields, primary and secondary, a back EMF is developed and causes an impedance change in each of the Tx and Rx coils. The coils impedance, a part of the separation between the two coils and the lift-off gap between material, varies according to the material's permeability, conductivity, surface, and subsurface geometry [178]. The conductivity and permeability, including the excitation signal frequency, determine the ECT signal standard penetration depth (δ), called skin effect [93].

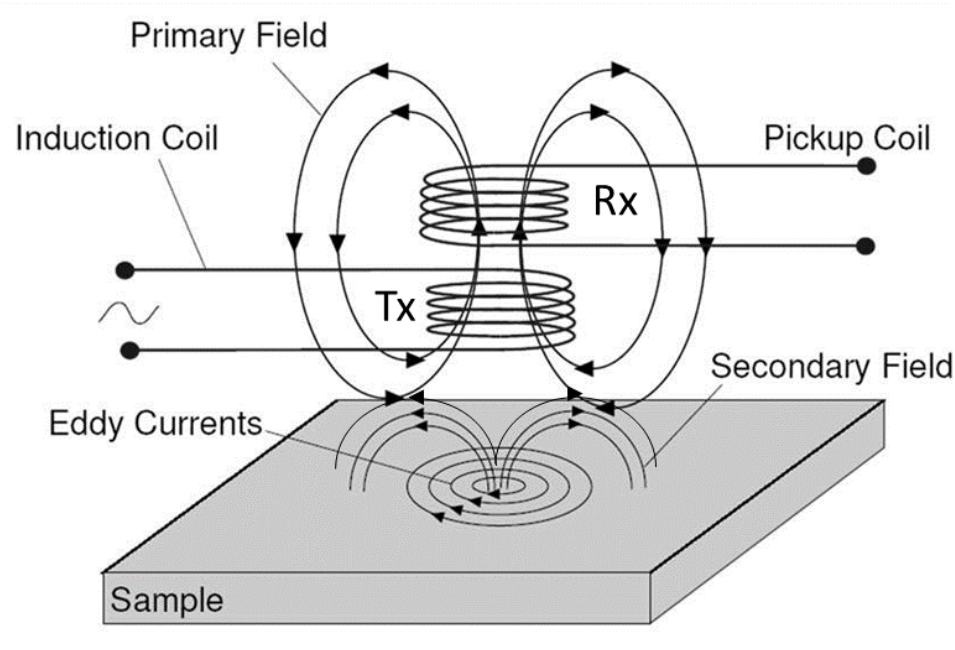

Figure 2.7 Principles of Tx-Rx ECT probe (helical coil) operation. Image Adapted from [179]

In contrast, the separation between the Tx and Rx (gap) and between the probe and the material (lift-off) determines the optimal probe response in a given excitation and coils probe configuration [15]. Thus, the Tx-Rx gap is a well-disciplined factor, while the lift-off and skin effect are the challenging factors affecting the inductive Tx-Rx ECT probe operation and performance. These factors are described in this section with regard to rigid and flexible inductive ECT coil probes.

2.3.1.2 Different Configuration of Tx-Rx ECT probe

The most widely used inductive coupling ECT probe configurations are absolute, differential, transmit-receive (Tx-Rx), and hybrid modes [4]. Moreover, the coil of ECT probes consists of flat spiral or helical winding coils. The flat and helical spiral winding coils arranged as an absolute probe for a single Tx coil [174, 180], axially side-by-side [181], or one coil above the other for two or more Tx-Rx coils arrangement [28, 172, 182, 183] at a specified lift-off distance from the sample surface. Figure 2.8 shows six conventional ECT coil probe configurations, inducing EC to the sample and eddy current generated field.

Figure 2.8 (a) and (b) are the absolute (single coil) probe showing the induced current to the sample based on multi-turn flat spiral planar and helical winding-like solenoid coils, respectively. The absolute probes are the easiest and simplest probes, made up of a single test coil (Tx), serving as Tx and Rx coils simultaneously, generating eddy currents and sensing changes in the eddy current field through impedance change [174]. However, measuring material thickness, permeability, and conductivity is inconvenient due to the lift-off noise and the variation of surrounding temperature and offset influences on the impedance changes.

The differential configuration of the absolute ECT probe (figure 2.8(c)) operates based on two active Txs coils in the differential form to eliminate the lift-off noise and other background noise caused by the primary magnetic field [184]. It does not require a reference signal to detect defects. The differential signal is zero when the two coils are placed over a non-defect area of the test material. However, a differential signal is produced when one coil is closer or placed over the defect area. The advantages of such differential arrangement include flexibility for zero-offset compensation, simplicity, low cost of fabrication, and common-mode noise reduction. This probe is very sensitive to defects and measures the permeability and conductivity of the material. However, it cannot detect defects bigger than the gap between the two coils, and it is insensitive to slow variation of properties such as gradual dimensional or temperature variations.

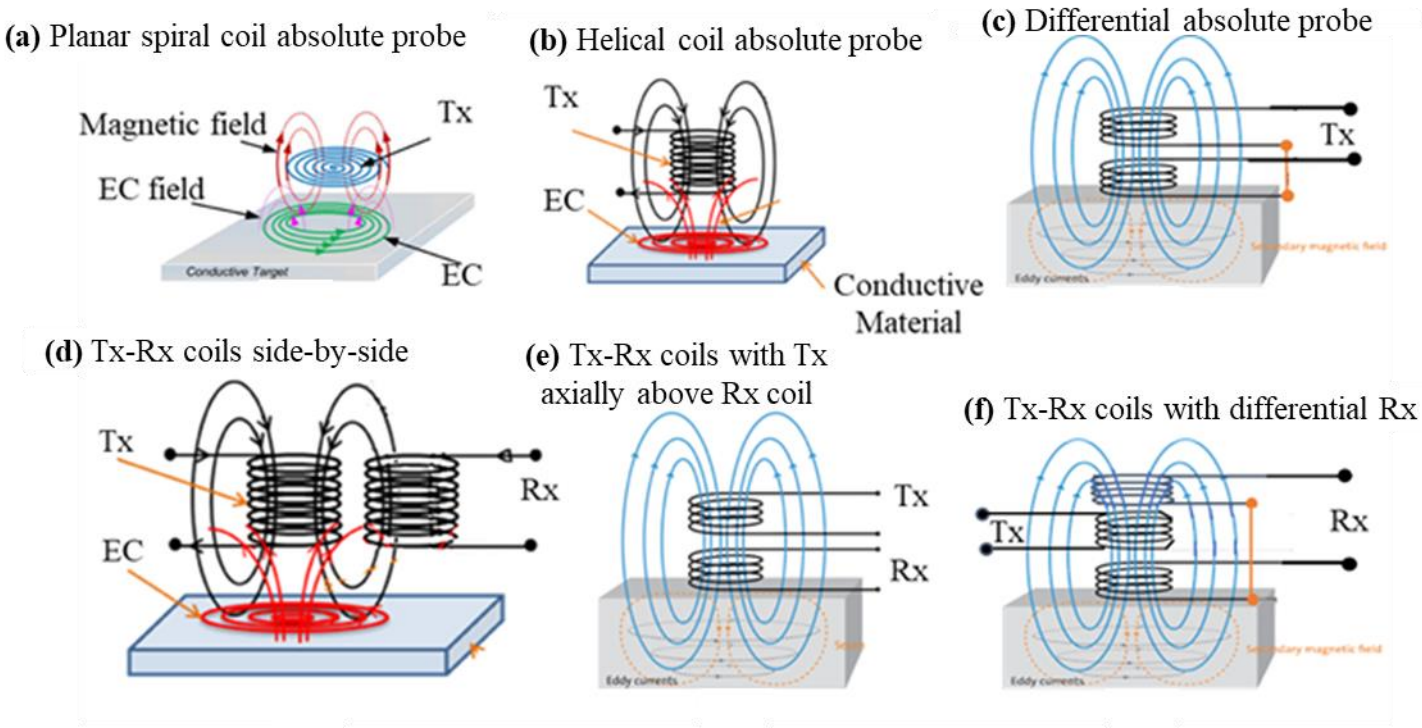

Figure 2.8 Inductively coupled Tx-Rx ECT probe arrangement on the sample surface

The arrangement of Tx-Rx coils side-by-side in contrast to absolute and differential coils arrangement, figure 2.8 (d) and (e) are the two axially helical (Tx-Rx) coils coupled side-by-side and Tx axially above Rx, respectively. The Tx-Rx side-by-side axially (figure 2.8(d)) has been applied to monitor the gap between two conducting concentric tubes, pressure tubes and calandria tubes in a nuclear reactor [185, 186] and parameters of two parallel plates separated by a gap [181]. In contrast, as shown in figure 2.8 (e), the Tx above Rx (Tx/Rx) configuration arrange as Rx coil sits axially between the sample and the Tx coil. This arrangement has been applied for the assessment of material microstructure and mechanical properties as well as thickness variations [187], measurement of permeability by reducing the lift-off effect [172], and measurement of coaxial hole size of finite-size metallic disk [188]. However, when the Tx coil is between the sample and the Rx coil, it characterises crack parameters as it has mostly applied to NDT&E of material and defects in the references [28, 189, 190]. These arrangements can also apply to the different geometry of spiral planar (Tx-Rx) coils such as circular, rectangular coils [63], etc. Therefore, the arrangement of Tx-Rx coils over the sample is application dependent. Most of the research on Rx closer to the sample characterise the material properties without considering the defect. In contrast, Tx closer to the sample is better for the application of defect parameters characterisation.

Comparing the planar and helical (Tx-Rx) spiral coils probe, the Tx-Rx helical coils coupled side-by-side (figure 2.8 (d)) possess higher Tx-Rx power transfer efficiency compared to a similar connection by the spiral planar (Tx-Rx) coils [191]. However, for the configuration of Tx over Rx (figure 2.8(e)), the spiral coils respond more efficiently than the helical coils due to the increasing mutual coupling between Tx and Rx and hence to the sample [191]. Therefore, the spiral planar coils configuration based on figure 2.8(d) is more preferred for remote eddy current inspection due to weak coupling between Tx and Rx. However, in the case of wireless power transfer for charging electric vehicles, figure 2.8(e) is more preferred due to strong Tx-Rx mutual coupling, especially for planar spiral coils.

Furthermore, the configuration of the Tx coil, axially over Rx, has been modified to three coils, including an additional coil serving as Tx or Rx. The three coils combine the advantages of a differential probe with that Tx-Rx probe. Figure 2.8(f) is the modified inductive coupling Rx-Tx-Rx probe, consisting of three coils with two differential Rx coils encircled Tx coil. They have been used for measuring permeability, conductivity, coating and material thickness and lift-off distance due to higher sensitivity and flexibility to sample parameters and geometry [3, 164, 171, 182, 192].

The response to defects based on the extracted features from such sensing probe (Tx, single-coil or double coils, Tx-Rx) appeared as either maximum amplitude, zero-crossing point, magnitudes of peak rising or descending points [4, 25]. However, they are prone to noise due to lift-off issues and direct linking-field in the case of two coils, among others. Therefore, more standard probe configurations based on modifying the probes mentioned above are being developed with more advantages, including bobbin (inside diameter) probes, outside diameter probes, uniform EC probes (one-directional and rotating direction) probes, array structure probe, among others [4]. The bobbing probe has structural simplicity and is low-cost [4], although it is only for axial defect detection inside a tube [4, 5]. As for complex geometrical defect detection, different solutions have been proposed using a rotating probe, array probe, and rotating field probes [4]. The uniform rotating eddy current probe has the advantage of being noise-free with high levels of data on the flaw compared to the conventional probe [193]. However, these probes are complex in structure and very expensive compared to others like bobbin probes. Generally, the Tx - Rx coils have a high response and sensitivity to alternating flux linkage [4]. However, they are physically inflexible and more sizeable than the defect, making them prone to lift-off variations in non-flat structures and possessing lower spatial resolution. Therefore, natural defects characterisation in a metallic structure, particularly with

complex geometry like the curved surface in a pipeline, remains a challenging task to conventional ECT. In such challenges, non-rigid Tx-Rx probes such as flexible Tx-Rx probes amenable to complex geometric shapes of different structures are required for NDT&E.

2.3.2 Flexible coils probe

In particular, complex curved structures such as oil and gas pipelines present a challenge during in-service inspection due to non-uniform lift-offs. The problem is worsened for underground pipes. Even after detecting its defects with the proper equipment and digging the defective segment for accessibility, the surface of the pipe can still be protected by compressed sand and coating. For inspecting such a structure without removing the coating, the probe has to be optimised for high lift-off inspection sensitivity at a certain coil gap [17]. However, this recent idea may only work effectively with flat and planar structures, where uniform lift-off can be easily achieved, which means it does not apply to curved surfaces. This issue can be resolved by using the flexible printed coil (FPC) array, where it has a fixed array of Tx and Rx coils on the same substrate. Its other benefit includes maintaining their mutual inductance if the same bending radius is applied on the Tx and Rx coils within its elastic limit [194]. Hence, it is less influenced by the pipeline curvature lift-off variations and offers the benefits of wide-area mapping capability with improved mutual inductance. Also, miniaturising the FPC array provides micro-spatial resolution and lightweight capabilities for NDT&E applications for detecting and quantifying micro defects in irregular metal structures [195-197]. For these reasons, flexible miniaturised coil arrays are used in one of these proposed WPTECT system studies.

ECT has recently adapted flexible arrays in the probe design [195, 197, 198] due to maintaining nearly constant resonance frequency, quality factor, and inductance value when bending Tx with Rx coils to any direction [194, 199]. The FPC array has been designed for inspection of curved surface structure because of its potential advantages, like good spatial resolution, high adaptability to different geometries, and high efficiency with much higher sensitivity than the traditional flexible printed circuit [196]. Different FPC array configurations, like single coils array, pair of Tx-Rx array, and single Tx with an array of Rx coils, were developed and investigated. The single Tx array has been used to measure tiny gaps between metallic and non-metallic surfaces [198]. Also, a pair of similar Tx and Rx flexible coils have been investigated for WPT efficiency on consumer electronics [194, 200] and integrated smart textile and flexible fabric [201, 202]. An array of Tx-Rx pairs of FPC, configured as a rosette eddy current array, were investigated for structural health monitoring and boosting the

sensitivity of fatigue crack detection [203, 204]. Instead of different pairs of Tx-Rx FPC coils, one excitation coil encircling an array of equally-spaced Rx coils has been evaluated with a higher response to defects due to improved mutual inductance and self-resistance [195-197]. The uniformly and equally structured fixed Tx array on differential and uniform Rx array for axial and tangential defects with a fraction of a millimetre depth has shown promising results based on a single-frequency ECT [205]. The axial and tangential defects are equally quantifiable by the FPC array. However, it suffers mutual interference between neighbouring coils and sensitivity reduction at the expense of spatial resolution [196].

2.3.3 Lift-off distance

Lift-off distance is an unavoidable challenge to ECT inspection. It occurs due to variation of sample thickness, vibration due to probe movement, or uneven sample surface. The noise generated by the lift-off effect modulates ECT response and influences the extracted features to cause erroneous quantitative NDT&E of defects. While assessing the suppression of lift-off in extracted features for application of ECT, different literature has been considered for sensor design approaches [15, 17], unique lift-off invariant (LOI) features [206, 207], and management of system response and extracted features processing [171, 192, 208-211]. Based on the sensor structural arrangement, there is an optimal lift-off to every coil gap, which leads to higher lift-off inspection at a given coil gap [17]. However, the idea is effective on loose, flat, and planar Tx and Rx coils tested on a flat non-ferrous metallic structure under axial alignment. Therefore, loose and separate Tx-Rx coils at a given coil gap could be used at an optimal lift-off to suppress these effects. Moreover, a unique feature, which is immune to lift-off variation like LOI [207, 212], phase spectrum of the PEC response [213], using a GMR-BC probe with an error compensation technique [214], and novel compensation peak frequency feature [208], have been used for thickness measurement. These features have been utilised to mitigate the lift-off influence amidst magnetic noise for crack depth information [215].

Furthermore, the extracted feature from the ECT signal response associated with the lift-off and sample influence has been controlled using conductivity and permeability invariant point measurement [15, 164]. The lift-off invariant measurement minimises error for the characterisation of defect parameters. However, the previous lift-off invariant point provided by different measurement systems appeared once in response, though there are multiple sample parameters, including permeability, conductivity, geometric shape, and defect. Similarly, lift-off has been reduced by response normalisation and reference signals manipulation [209] and differential response time and frequency domain analysis to classify defects [210]. However,

the lift-off immunity by such features is unique to a defect parameter and appeared once in the signal responses. Therefore, multiple lift-offs invariant points are vital for multiple parameter information to minimise characterisation error.

2.3.4 Standard penetration depth:

The capability of ECT to detect subsurface defects depends on the skin effect, as the induced eddy currents concentrate at the surface and decay exponentially with increasing depth, as explained by equations (2.1) and (2.2) [34, 173, 216]. Equation (2.1) describes the dependency of eddy current penetration depth on the signal frequency and electrical and magnetic properties of material whereas (2.2) describes the exponential decay of the eddy current density from the surface value to various depth values. f is the excitation frequency, σ is the electrical conductivity, μ_r is the relative permeability, μ_0 is the constant absolute permeability, *J(d)* is the current density at a given depth (d), and J_s is the surface current density. These factors should be suitably selected at the design level by the operator, based on the type of defect detection and sample. The lower frequencies are preferably for sample and defect bulk characterisation, whereas higher frequencies are for surface characterisation as the eddy current concentrate at the surface.

$$\delta = \sqrt{\frac{1}{\pi f \sigma \mu_r \mu_0}} \tag{2.1}$$

$$J(d) = J_s e^{-\frac{d}{\delta}} \tag{2.2}$$

The electrical conductivity (σ) and permeability (μ) play a vital role in the ECT of materials and defect characterisation. The σ is an intrinsic material property that measures the ability of a material to conduct electric current. In contrast, μ measures the magnetisation level that a material obtains in response to an applied magnetic field. The higher conductive material generates strong eddy currents, which is an advantage over the lower conductive material. In contrast, the higher permeability alters the indirect field linking Rx coil at a closer lift-off distance [217]. In a non-ferrous metal, the conductivity determines the ECT response, whereas, in ferrous metal, the conductivity and permeability make the interpretation of ECT response tedious as the permeability changes with remanence, excitation current amplitude, and frequency, which also has an impact on electrical conductivity detection [218]. Therefore, separation of permeability and conductivity influence while assessing materials and defect characterisation is a challenge to ECT, especially in ferrous metallic structures. Mingyang has measured the permeability of ferrite plates by exploring the conductivity Invariance

phenomenon under controlled lift-off [219] and later reconstructed conductivity and permeability using the lift-off invariant inductance and frequency features [220]. However, these invariance features are specific to such coils as the optimal lift-off to every sensor is unique depending on the distance between the transmitter and receiver (coil gap) [17] and also the little influence of the mitigated conductivity on permeability is for certain lift-off distance [219]. Furthermore, extraction of such invariance features requires the prior conductivity or permeability initial value to be known [220].

The frequency of operation is an essential factor in ECT, which depends on the defect and sample. For example, lower frequencies are aimed at surface and subsurface characterisation, whereas higher frequencies for surface characterisation due to the skin depth issue [221]. Owston demonstrated the feasibility of higher frequencies ECT (HFECT) up to 25MHz in the year 1969 when investigating surface defects in a thin metallic coating [222]. However, the HFECT has later extended up to 50MHz for assessing residual stress in surface-treated nickel-base superalloys [168]. Due to the advancement of spiral coils with a very low number of turns and the availability of higher frequency electronics devices, the HFECT nowadays operates up to 100MHz [93].

The HFECT appears to have strong sensitivity for precise measurements due to the high density of eddy current contributions at the material's surface. However, very low frequencies excitation induces too weak currents into the material, leading to noisy measurement by Tx-Rx coils as explained by Faraday’s law of induction [223]. Although, it has good penetration depths, which is suitable for deeper information and thickness assessment. Moreover, one of the major challenges to HFECT is that the capacitance between the probe and the measuring instrument cable becomes significant in the MHz range, thereby introducing noise into the system as the cable interacts with objects close to it. Therefore, efficient ECT operating frequency choice must consider the probe's structure, permeability, conductivity, and thickness of the target sample. For this reason, the HFECT is best applicable to only surface defects of all conductive materials. Still, the HFECT is relevant to the sub-surface defect inspection for materials with very low conductivity, such as Titanium alloys and carbon fibre composite samples [224].

The Tx-Rx coils are the best probe for HFECT due to their good sensitivity to conductivity measurement at higher frequencies [225]. However, the natural resonance of the coil limits the choice of operating frequency. Higher inductance (L) coils induce more current density but

have lower natural electrical resonant frequencies than low inductance coils [225]. This is because, before the natural electrical resonance, the coil response is dominated by inductive behaviour, while after, it's a capacitive behaviour. Therefore, to operate at higher frequencies, the inductance or capacitance of the coil must be decreased. However, reducing the inductance lowers the sensitivity, and reducing the capacitance is not always practical. The solution is to lower the resonance frequency point by connecting an external capacitor to improve the coil's inherent capacitor for maintaining sensitivity to ECT [226].

2.3.5 Excitation mode

The ECT excitation determines the actual behaviour of probes due to the interaction of induced eddy current and the presence of a defect or no defect in the material. It has metamorphosed through different stages including time domain, transient behaviour to frequency domain response, namely single-frequency [3, 27], multiple-frequency [4, 16, 162, 182, 220, 227-229] , swept-frequency ECT [28, 29, 31, 164, 165, 188, 189, 230, 231], pulsed or transient ECT [5, 27, 232], and resonance [28, 189, 226, 233, 234] eddy current testing. The four types of ECT excitation signals, single, multiple, pulse and sweep frequencies, are shown in figure 2.9 (a), (b), (c), and (d), respectively. Details of each excitation in ECT methods are briefly described in the following subheadings.

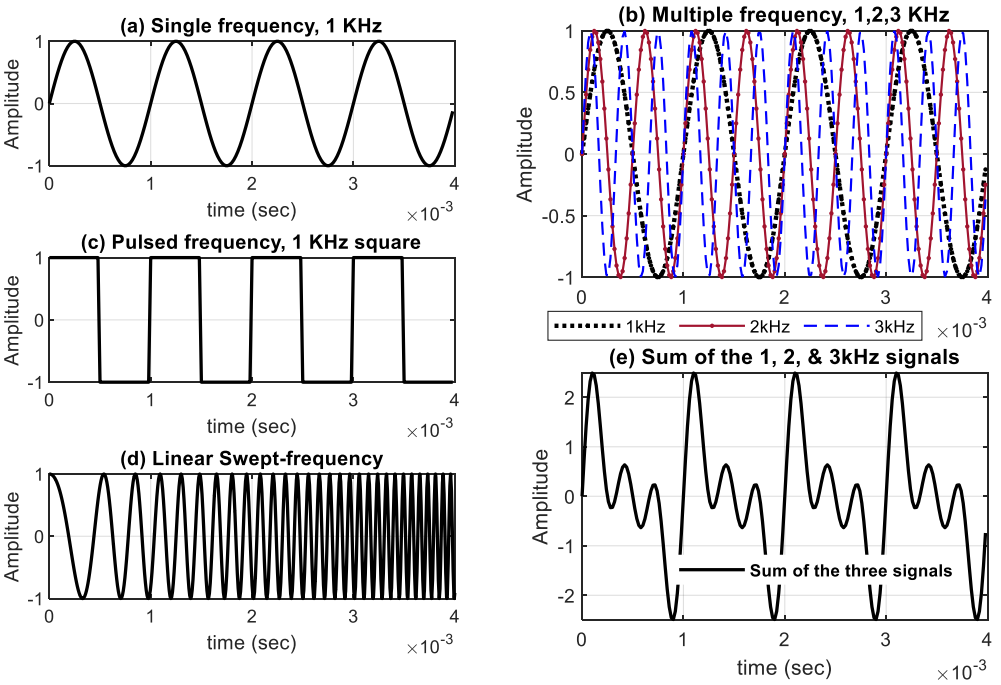

Figure 2.9 Different types of ECT excitation signal

(a) Single-frequency excitation (b) Multiple frequency signals at three different frequencies, 1, 2, and 3kHz (c) Pulsed signal (d) Swept frequency excitation varying linearly from 1kHz to 10kHz signal. (e) Multiple frequency excitation based on sum signals in (b).

2.3.5.1 Single Frequency ECT

The single-frequency ECT is the simplest and easiest ECT excitation mode for inducing eddy currents into the sample. The problem of single-frequency excitation is limited penetration depths to the surface and sub-surface of the sample due to the single-frequency nature, as seen in figure 2.9(a). The signal penetration depth depends on its frequency and material permeability, and conductivity [34]. Therefore, it is for surface and subsurface defect detection and characterisation [26]. Increasing the subsurface testing reduces the operational frequency to increase the standard skin depth [5]. However, as Faraday's law of induction stated, the induced voltage in coil sensors is proportional to the rate of change of magnetic field passing the coil, which is negatively affecting the signal-to-noise ratio at very low frequencies. Thus, the main drawback of single frequency ECT is the restriction to a single penetration depth, which can be resolved by multiple frequency excitation to the ECT probe.

2.3.5.2 Multiple Frequency ECT

This Multiple Frequency Eddy Current (MFEC) testing expands single frequency testing by allowing simultaneous and sequential excitation with multiple frequencies signals. Figure 2.9 (b) and (e) showed the three individual signal excitation and their corresponding sum, respectively. The simultaneous excitation is when the three signals are excited at a time as either a sum or product of individual signals, as seen in figure 2.9 (e). In contrast, sequential excitation is the serial excitation of one signal after the other in an orderly manner. The extracted features from the MFEC technique can simultaneously and sequentially check cracks' features in different material depths and significantly enhance the performance of the eddy current testing system.

The MFEC excitation technique has the advantages of resolving the acquired data affected by many variables like conductivity, permeability, material geometry, and probe lift-off by combining the extracted features at different frequencies [182]. Furthermore, it has an improved SNR over traditional double frequency techniques for complex-valued images up to 1100% due to noise reduction in the excitation through a fusion of features or raster scanning [4]. In another research, a dimensional spatial domain based on the pyramid data fusion method has been

applied to improve SNR in a multi-frequency excitation response by eliminating noise due to temperature variation, probe lift-off, and material geometry [235].

However, the simultaneous application of MFEC results in a shorter testing time with less power in each frequency component. Also, the sequential application of excitation requires sufficient time for the system to reach a steady-state before the subsequent excitation; thus, it is time-consuming [27]. Although MFEC testing attains data with further information, the response is limited to the depths of information equivalent to the exciting signal frequencies. The Pulsed excitation solves such problems because of its potential for a wide range of frequencies and a shorter time to inspect different depths [5].

2.3.5.3 Pulsed ECT

Pulsed eddy current (PEC) systems contain an excitation coil that induces a primary transient field while one or more sensing devices detect the secondary eddy current field from the sample [5]. It surpasses the single and multiple frequency testing because of transient response that contains as much information as an entire spectrum of excitations frequency-domain [5, 236, 237]. Besides having a broad spectrum of frequency components in its excitation, its signals possess standard features such as the time-to-peak amplitude, peak amplitude, and time-to-zero crossing [5]. In addition, it contains defect size, location, and depth in such features of its transient signal [27, 238, 239]. However, the components of different frequencies present different penetrate depths with not equal signal strengths. Hence, lower frequency components possess higher penetration depth and signal strength than high-frequency components, which makes the signal energy of different components not evenly distributed.

Despite the discriminating advancements, and better characterisation for surface and deep sub-surface flaws, it still has problems with lift-off issues, variation of coupling between Tx and Rx coil, and response distortion due to other harmonic frequencies and influence of materials' inhomogeneity. The lift-off variation changes the mutual inductance between the excitation coil and the test sample, especially when the inspection involves complex geometrical components like aircraft components [209]. The lift-off variations happened due to uncontrollable operator movement, coating thickness, irregular surface shape, or probe tilting during the scan [209]. Another challenge to PEC testing is the requirement for transforming signal response to the frequency domain, using Fourier transform and other advanced signal processing and interpolation, to link the features to different material layer information.

2.3.5.4 Swept Frequency ECT

Another EC testing uses **sweep frequency excitation** that enables inspection of complicated testing areas, especially where the probe scan is infeasible [29]. The swept-frequency domain response gives more complex information about the sample and defects [30, 32]. It has been applied for multilayer characterisation due to a wide range of frequencies band for different layers of interest [231], resulting from different depth information, which qualifies it for detecting thickness, permeability, and conductivity of materials coating [18, 29-31]. It Successfully measures material thickness without prior knowledge of electrical conductivity and magnetic permeability using the normalised impedance phase [240].

The swept-frequency ECT does not require frequency selection as it uses a broad range of frequencies for scrutinising sample parameters. It has a minor impact on the surrounding effects because of the fixed probe position, though it has problems with the precise location of the defect place for non-scanning mode. Nevertheless, the challenge of exact location and characterisation of the defect has been demonstrated by the traditional ECT using single and multiple frequencies at scanning or mapping mode. However, the single frequency suffers insensitivity and low SNR due to lift-off noise and other factors. The SNR and sensitivity to a defect have been improved by using the electrical resonance behaviour of the inductive probe [226].

2.3.6 Resonance ECT

Another existing ECT inspections examine defects at frequencies near the natural electrical resonance of the probe primarily to increase the sensitivity and SNR of the ECT probe [226]. For example, Robert [241] has investigated single-frequency near-natural electrical resonance performance by sweeping frequency response behaviour of an inductive probe to characterise cracks. However, the natural electrical resonance of the coil in an inductive probe depends on the coil's inherent capacitance, ohmic resistance, and the inductance of the probe. The natural electrical resonance of the probe occurs at the maximum power transfer of an unloaded coil, and the response dominates by inductive behaviour before the resonance and capacitive behaviour after the resonance [242]. The higher frequency nature of the natural resonance of an inductor is a critically challenging issue to ECT due to the skin effect issue. However, the lower conductive materials such as composite materials require higher frequencies outside the range of conventional ECT for sensitivity to shallow defect detection [224]. Therefore, near electrical resonance frequencies have been used by ECT to characterise defects in a low conductive

material like Titanium and Waspaloy for multiple frequency excitation [33, 241, 243, 244]. Although the near electrical resonance frequencies have a high sensitivity of detecting surface cracks, they still suffer from lift-off, probe tilting, sample inhomogeneity, and material geometric effects. These effects affect the resonance point by producing similar shifts to the resonant frequency from the defect signals. Subsequently, it could lead to potential false indications or the resonant frequency shifting that could render a single excitation frequency no longer at the most sensitive NERSE frequency [33]. Despite the challenges encompassing the natural resonance ECT, it is a valuable method for improving sensitivity and complements other ECT methods, primarily single and multiple frequency excitation.

The natural resonance occurs at higher frequencies than low- and high-frequency ECT inspection, depending on the value of inductance in addition to inherent parameters of the coil [226]. Therefore, considering the skin effect, the natural resonance frequency has been modified to a lower value by connecting an external capacitor to the probe to maintain sensitivity and advantages of lower frequency inspection [226, 233]. Compared to other ECTs, the resonance-based ECT operates at maximum energy transmission between Tx and Rx and optimal feature response [19, 21]. In addition, it uses swept-frequency excitation to provide the different depth information and defects parameters uncomparable to single-frequency ECT with inherent limiting sensitivity [27]. Moreover, it differs from pulsed ECT because its frequency domain response does not require further processing to the time domain for different layer information. In addition, it overcomes the problems of harmonic frequency distortion in the response signal due to the influence of harmonic eddy current currents in the response at every time [157].

2.3.7 Problems and Challenges of ECT

The literature review highlighted several challenges and problems for the most common electromagnetic NDT&E techniques for defect detection and characterisation. It appears that the critical challenge to different NDT&E methods depends on the nature of the sample and defect, probe configuration, and mode of operation, including environmental conditions and access to the material. However, NDT&E explores multi-sensing modalities to ascertain these critical issues using multiple techniques operating in a complementary mode for different challenges. Unfortunately, the multi-sensing modalities are sometimes complex in operation and expensive to purchase. It, therefore, opens challenges to a single method that can operate efficiently with the potential capability of multiple feature points for high sensitivity to multi-parameter sensing.

Considering the defect and sample's nature, ECT application to ferrous materials suffers response distortion due to sample permeability influence around the defect area, altering the remote field at a closer lift-off distance [217]. These consequences impacted extracted features' accuracy for quantifying defects and other materials' properties, including electrical conductivity and materials geometry. Therefore, mitigation of the permeability effect necessitates studying different features' sensitivity to probe lift-off distance at a defect and no defect positions for enhancing quantitative non-destructive evaluation (QNDE) of defects in structures such as rail lines, pipelines, turbine blades, etc.

For the configuration of ECT probe structure, the challenges to defect detection and characterisation of ECT include lowering the sensitivity due to lift-off noise influence from the limited number of features for mapping and scanning mode. Moreover, the current ECT techniques are sensitive to defects and have been applied for different NDT&E applications. However, the response depends on the indirect field that passes through the sample to the receiver, though direct fields link the Rx coil depending on the mutual coupling between Tx-Rx coils. The mutual coupling depends on the Tx-Rx coil gap, lift-off distance and nature of the surrounding material and decreases the SNR of the output ECT signal, especially at higher lift-off distances. Furthermore, the ECT system lacks efficient energy transfer to yield the most heightened sensitivity and provides fewer feature points that deprive the freedom of feature selection. These problems require ECT operation at resonance points and response modification through an electrical circuit configuration and mode of the probe operation.

Moreover, the resonance points and response shape features have different reactions to different defect parameters. However, the advantages of inductive probes coupled to the shifting and splitting of resonance response of WPT concept for charging an electric vehicle could help scrutinise multiple parameters information efficiently. In some cases, a special probe is required to inspect particularly a complex or curved surface like a pipeline with a natural defect, which remains a challenge to ECT. This problem could be solved using flexible coils as an inductive probe, especially an array of coils for non-scanning mode, as it allows area mapping of complex structures. The advantage of flexible coils array includes providing micro-spatial resolution, less influenced by lift-off variations, wide-area mapping capability, and improved mutual inductance insensitive to bending to curve surface [194]. Hence, integrating flexible coils probe operating as resonant WPT for charging electric vehicles could overcome ECT challenges related to the complex geometric sample for QND&E.

This study has focused on a novel approach based on the magnetically-coupled resonant WPT concept applied to the ECT probe to overcome some of the literature's identified problems and challenges to ECT inspection. Its contributions include designing, developing, and investigating Tx-Rx ECT for NDT&E systems operating at maximum power transfer and multiple feature points inspections. The target of ECT inspection at maximum energy transfer with multiple feature points is to replace conventional ECT probes due to its weak signal degradation resulting from the effect of lift-off distance and influence of sample parameters. Also, it can serve as an alternative to multi-modality sensing due to its complex and expensive nature. This contribution is achieved by integrating the concept of magnetically-coupled resonant wireless power transfer for charging electric vehicles into the ECT system, a novel idea in the history of ECT application.

2.4 Wireless Power Transfer (WPT) Consideration for ECT Application

The breakthrough of modern wireless power transfer (WPT) technologies for charging electric vehicles has emanated from the Massachusetts Institute of Technology (MIT) in 2007 [19]. It has progressed to various applications, including flexible electronics technology in wearable-flexible sensors [245], wireless charging systems in smartwatch strap [194], and other biomedical applications [246]. Furthermore, further evolution of these technologies led to simultaneous wireless communications of information and power transfer [246, 247], including sensing applications in this study for WPT-based ECT [23, 24]. In view of the current development of the WPT concept for charging electric vehicles [36, 248, 249] and the challenges and problems associated with different methods of ECT for defect quantification [4, 5, 17, 28, 45], this study has proposed their integration to improve the ECT probe for operation and responding at maximum energy transfer and potentials of multiple features points.

Compared to other ECTs' inductive probes, the novel magnetically-coupled resonant WPT-based ECT (WPTECT), as a new concept, uses magnetic resonance coupled behaviour for transmitter (Tx) and receiver (Rx) coils at a specific Tx-Rx coils gap and lift-off distance. It transfers maximum energy with a potential of multiple resonances points for exploring multiple parameters information [21, 250-252]. It also uses sweeping frequency excitation for different penetration depths and defect parameter variations at different layers, which is a challenge to single-frequency ECT [26]. The different layer information ease separation of permeability as ECT depends on conductivity. Although, in the conventional ECT inductive probe, the influence of permeability on Tx-Rx coil inductances has been mitigated at certain lift-off [49]. Moreover, due to multiple resonances from the response of magnetically-coupled resonant

WPTECT [21], the multiple feature points provide multiple parameter information such as depth, width and angle of crack. Similarly, the swept-frequency excitation in WPTECT overcomes the issue of less power in each frequency component due to shorter testing time as exhibited by simultaneous excitation of multiple-frequency ECT [27].

Getting closer to the sample by the magnetically-coupled resonant WPTECT Tx-Rx coils, the induced-eddy-current (EC) appeared as power loss in the sample at the expense of the extra generated power from the Tx coil, particularly when transmitting power is low [253]. The induced EC field modulates the field linking Rx coil through the sample by opposing the main field, causing an impedance change in the Tx-Rx coils due to the influence of conductivity, permeability, surface and subsurface geometry of the material in the vicinity of the Tx-Rx [178, 253]. Therefore, the Tx and Rx coils respond individually to the metallic sample and defect due to their distinct magnetic resonance couplings with the sample, which affect the overall power transfer efficiency. Operation at resonance frequency improves the response due to the coupling behaviour of each coil with the sample. The resonance occurs due to the elimination of the reactive power components by operating without leading or lagging between the current and voltage in a coil [35, 36]. The zero phase angle between current and voltage in a coil is achieved by connecting multiple reactive elements, like capacitors and inductors, together in series and/or parallel, named as topology configuration of WPT [36]. Different combinations of coil and capacitor form different topologies of WPT with a distinct response, quality factor expressions, and disadvantages due to individual unique impedance matching, leading to different measurement performance of WPT-based ECT systems [35, 36, 254, 255]. Therefore, it’s imperative to investigate each topology's response and feature performance for the eddy current NDT&E operation, which is one of this study's objectives.

On the issue of Health and Safety concerns on electromagnetic radiation, the magnetic resonant WPTECT belongs to non-ionisable radiation due to its magnetically-coupled (inductive) energy transfer. However, the produced time-varying magnetic fields, perpendicular to the metallic sample under investigation, exposes to the operator’s human body. The universal methods to protect against such non-ionising radiation are provided by the International Commission on Non-Ionising Radiation Protection (ICNIRP). It has been discussed in ref [256]. that Humans are non-magnetic objects and therefore can endure strong magnetic fields without undergoing any risk, as demonstrated by the magnetic resonance imaging (MRI) technique. The MRI technique generates around 1T of magnetic field compared to our proposed WPTECT with less than 10μT due to its milli-wattage transfer, which is much lower than the

set magnetic field density exposure limit (27μT) by the ICNIRP [257]. Therefore, it is realistic to expect our proposed WPTECT magnetic radiation to be safer for humans.

2.5 Chapter Summary

The chapter reviewed the summary of different electromagnetic NDT&E techniques for defect detection and characterisation of metallic structures such as pipelines and rail lines. It also linked the challenges and problems of other NDT&E techniques to the meritorious development of ECT as a popular NDT&E technique. In the same manner, the ECT technique as the common and most applicable NDT&E technique has been reviewed in-depth and presented its challenges and problems such as inefficient energy transfer, fewer feature points, sensitivity to lift-off, and susceptibility to permeability influences. Similarly, the chapter has discussed the challenges and problems, particularly in the ECT probe configuration and mode of operation for different excitation and resonance behaviour at different and sweeping frequencies. Furthermore, the chapter reviewed the consideration of WPT and its multiple resonances as an integral part of the probe excitation as proposed in the aim of this study.

The next chapter looks at the basics of induction current in inductive coupling Tx-Rx probe of ECT systems and magnetically-coupled resonant Tx-Rx probe, from the WPT, integration for the novel concepts of the WPTECT probe. Furthermore, it includes the methodologies of challenging defects on pipeline sample investigation, different topologies of magnetically-coupled resonant circuits of WPT for ECT optimisation and investigating the optimised topology on RCF crack in a rail line material.

Chapter 3. Design and Development of WPT-Based ECT System

3.1 Introduction

After reviewing the ECT and integration of the magnetically-coupled resonant WPT concept in chapter 2, this chapter revisited and investigated the Tx-Rx ECT induction probe magnetic theory leading to induced eddy current generated field. It also studies the different circuit topologies of the magnetically-coupled resonant WPTECT, the basic theory of the magnetically-coupled resonant Tx-Rx probe and its performance for multiple resonance capability linking to this research methodology. The research methodology is presented, resulting from the challenges and problems highlighted in chapter 2 based on three case studies. Firstly, the design, development and evaluation procedure of the WPTECT system for multiple resonances feature extraction, comparison and quantification of defect parameters in aluminium blocks. Secondly, the procedure for application of WPTECT to pipeline by integrating flexible coils array for the reconstruction of a dented area in the curvature of a pipeline is developed. Thirdly is the procedure of investigating WPTECT circuits and their topologies optimisation for eddy current non-destructive testing and applying an optimised topology to investigate RCF cracks in rail line material. Finally, it concludes by summarising the chapter achievement based on the developed procedure for conducting this study.

3.2 Inductively Coupled Tx-Rx ECT Probe Induction Current

The ECT system probe comprises an excitation source, $\boldsymbol{V_1}(v)$, primary magnetic field, $\vec{\boldsymbol{B}}_{\boldsymbol{p}}(T)$, induced-eddy-current in the sample ($\vec{\boldsymbol{J}}_{\boldsymbol{eddy}}$), secondary magnetic field ($\vec{\boldsymbol{B}}_{\boldsymbol{eddy}}$), and induced voltage ($\boldsymbol{V_2}$) to the Rx coil due to the influence of primary and secondary fields. The electrical variables, voltages, and currents, as seen in equation (3.1), are linked to electric and magnetic fields using the partial differential equation described as Maxwell's equations [258]. Equation (3.1) gives the linear link of time-domain insight into the relationship between electrical variables and magnetic variables starting from an input voltage (V_1) to Tx coil to the output voltage (V_2) in the Rx coil. From the relationship, flow of current through a coil produces field and conversely, an alternating field passing a coil induces a voltage. However, the Tx coil produces electromagnetic fields described by Maxwell's equations' differential and integral form. The differential form of Maxwell's equations, in time-domain, provides the basis for calculating the magnetic and electric field at a point in a space contrary to their integral forms for a field at an area. Maxwell's equations are derived from Gauss's law for electric fields and magnetic fields, Faraday's law of induction, and Ampere's law [258]. The four Maxwell's

equations are given by equations (3.2) to (3.5), where the symbols $E\ (V/m)$, $\rho\ (C/m^3)$, $\varepsilon_0\ (F/m)$, $\mu\ (H/m)$, and $J(A/m^2)$ denote electrical field, electric charge density, permittivity, permeability, and current density, respectively.

$$V_1(t) \rightarrow I_1(t) \rightarrow \overrightarrow{B_p}(r,t) \rightarrow \vec{J}_{eddy}(r,t) \rightarrow \vec{B}_{eddy}(r,t) \rightarrow\ I_2(t)\ \rightarrow V_2\ (t) \qquad (3.1)$$

Gauss's law for Electricity; $$\nabla \cdot \vec{E} = \frac{\rho}{\varepsilon_0} = 0 \qquad (3.2)$$

Gauss's law for Magnetism; $$\nabla \cdot \vec{B} = 0 \qquad (3.3)$$

Faraday's law of induction; $$\nabla \mathrm{x} \vec{E} = -\frac{\partial \vec{B}}{\partial t} \qquad (3.4)$$

Ampere-Maxwell equation; $$\nabla \mathrm{x} \vec{B} = \mu \vec{j} + \mu \varepsilon_0 \frac{\partial \vec{E}}{\partial t} \qquad (3.5)$$

The first law, (3.2), states that the net electric flux is proportional to the whole charge enclosed by the surface; hence, it is for static electric fields. The second equation, (3.3), describes the static magnetic field. The magnetic field lines expand to infinity & reverse; otherwise, neither start nor finish but create loops. It states that the magnetic field divergence is equal to zero because the magnetic flux cannot be enclosed within a closed surface of any shape. The third equation (3.4) states that the time changing magnetic field produces an electric field, whereas equation (3.5) tells that electric current or change in the electric field produces a magnetic field. The two equations describe the electromagnetic waves that can spread independently. They express that a magnetic field change can produce an electric field change, and vice-versa, and continues as well as an electromagnetic signal, ready and continuously spreads out to space.

The spreading field emanating from the Tx (primary field) induces voltage to the Rx coil according to Faraday's law of induction and, at the same time, eddy current to the material, as seen in figure 3.1. the eddy current generates a secondary field opposite to the main field according to Lenz's law. It carries information related to the material properties, distorts the main field, and influences the Tx and Rx impedances.

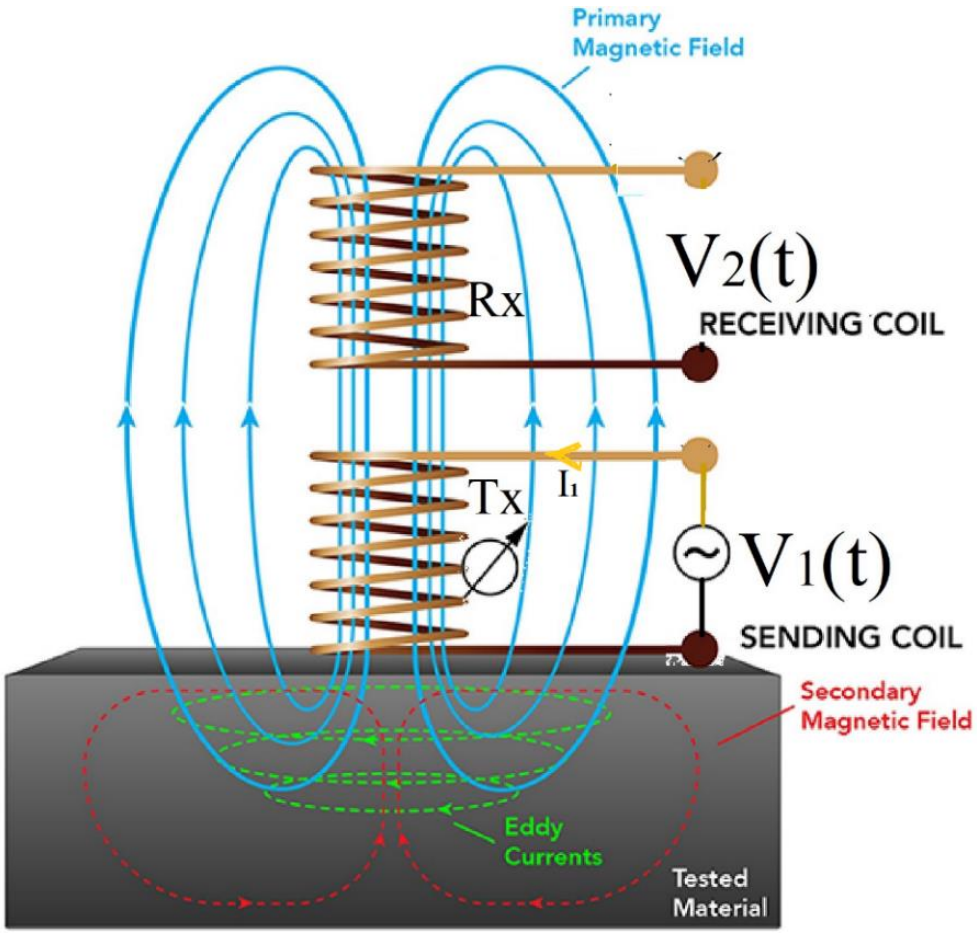

Figure 3.1 Tx-Rx probe and metallic materials, indicating excitation source (V1), eddy current, primary and secondary fields, and induced voltage (V2).

The Maxwell's equation (3.2) and the second term of equation (3.5) can become zero because, in a metallic conductor, the conduction current density, J, is much greater than the displacement current density due to the absence of build-up internal electric charge density (ρ) [259]. Also, field density, $\vec{B}$ is the superposition of the primary (external) field, $\vec{B}_p$ and the secondary field due to eddy current, $\vec{B}_{eddy}$. Therefore, the non-static Maxwell's equations (3.4) and (3.5) (Faraday's law of induction and Ampere's laws) are modified into equations (3.6) and (3.7) in the frequency domain, including the introduction of $\vec{J} = \sigma\vec{E}$ according to ohm's law.

$$\nabla x\vec{E} = -j\omega\left(\vec{B}_p + \vec{B}_{eddy}\right) \quad (3.6)$$

$$\nabla x\left(\vec{B}_p + \vec{B}_{eddy}\right) = \mu\sigma\vec{E} \quad (3.7)$$

In equation (3.7), the curl of $\vec{B}_p$ can be neglected because it is generated by the Tx and carries no information related to the material property. Therefore, equation (3.7) can be re-written as

$$\nabla x\left(\vec{B}_{eddy}\right) = \mu\sigma\vec{E} \quad (3.8)$$

Taking the curl of equation (3.8) again and substituting Faraday's law, equation (3.6) yields a new expression that contains primary and secondary fields given by equation (3.9). After rearranging the equation, the relationship between primary and secondary fields is finally achieved and written as equation 3.11.

$$\nabla \mathrm{x} \nabla \mathrm{x} \vec{B}_{eddy} = \mu\sigma \left(-\mathrm{j}\omega \left(\vec{B}_p + \vec{B}_{eddy} \right) \right) \tag{3.9}$$

$$-\nabla^2 \vec{B}_{eddy} + \nabla\left(\nabla \cdot \vec{B}_{eddy}\right) = -\mathrm{j}\omega\mu\sigma\left(\vec{B}_p + \vec{B}_{eddy}\right) \tag{3.10}$$

$$\nabla^2 \vec{B}_{eddy} + (-\mathrm{j}\omega\mu\sigma)\vec{B}_{eddy} \;\; = \;\; \mathrm{j}\omega\mu\sigma\vec{B}_p \tag{3.11}$$

Equation (3.11) is a second-order differential equation describing the behaviour of the secondary field of an ECT system for any primary field. It can be written to conform with the standard equation of non-homogeneous vector-Helmholtz, which has been solved for different excitations by specifying boundary conditions at infinity [259]. As described in [259], the standard vector-Helmholtz equation is given by equation (3.12). Compared to equation (3.11), the constant, $k^2 = -\mathrm{j}\omega\mu\sigma$ is a complex wave number, always assume the positive root in the solution, and related to the skin depth, δ^2 as $k^2 = \frac{2}{\delta^2} = \omega\mu\sigma$.

$$\nabla^2 \vec{B}_{eddy} + \mathrm{k}^2 \vec{B}_{eddy} \;\; = \;\; -k^2 \vec{B}_p \tag{3.12}$$

The eddy current generated field, B_{eddy} carries information of the material parameters such as permeability, conductivity and geometry, influence the received voltage by the Rx coil, change the impedance of the Tx and Rx coils amidst those multiple influences. The impedance changes appear as electrical variables, voltage and current at the Tx and Rx coils; hence classical circuit theories can further investigate the Tx-Rx network and additional signal conditioning circuits. The classical circuit theories give the essence of analytic properties for a linear circuit, linking different interelement behaviour for facilitating the design of predictable and non-predictable circuits. The circuit of Tx-Rx coils, communicating based on wireless power transfer principles, is considered and presented in the next section.

The inductive Tx-Rx probes are categorised into two classes based on the coils' mutual coupling, loosely coupled and tightly coupled systems. The tightly coupled system has a coupling factor closer to unity and mostly applies to the electrical power transformer. The loosely coupled systems have low coupling factors ranging from 0.01 to 0.5, depending on the application, which has primarily been used in wireless power transfer (WPT) Tx-Rx coils of charging electric vehicles and other electronics systems [260]. The low coupling coefficient results from a large distance between the two coupled coils (centre-to-centre) compared with the coil sizes and the absence of a high permeable magnetic path connecting them. The lower coupling causes lower power transfer efficiency. Therefore, the reduced power transfer

efficiency is counterbalanced by adding a resonance circuit to each Tx and Rx coil for upgrading. The resonance circuits, known as topologies, enhance the power transfer between Tx and Rx coils by matching the input and output impedance using a connection of compensating reactance elements [35, 254].

3.3 Magnetically-Coupled Resonant Tx-Rx Probe Circuits for WPT-based ECT

Wireless power transfer (WPT) is a means of interaction wirelessly through a time-varying electromagnetic field between two or more reactive components. The inductively-coupled Tx-Rx WPT system transfers energy magnetically, though at lower efficiency due to weak mutual interaction between Tx and Rx coils. The efficient energy transfer of the inductive-coupled Tx-Rx WPT is achieved through resonance techniques of WPT, known as resonance inductive power transfer (IPT), which is an advancement of inductive coupling of the Tx-Rx WPT system. It explores the advantages of a maximising magnetic field by generating an alternating current at the resonance point of operation by modifying circuit parameters and hence electrical variables, which control energy transfer. The circuit parameters are modified using compensating reactance to maximise the real power transfer. The maximise field linking Rx coil by the magnetically-coupled resonant WPT system offers the advantage of not exposing the human body to ionizing radiation because of its non-electric wave nature.

There are four basic compensating reactance topologies of magnetically-coupled resonant WPT [261], which are the core building circuits that led to this novel WPTECT topology research. Each Tx and Rx coil of the WPTECT probe is connected to a compensating reactance to control their resonance frequency by modifying their quality factors through lowering the Tx reactive power rating and cancelling out the Rx inductance effect [36]. They include Series (S) or Parallel (P) resonant capacitor connection to Tx and Rx coils in the form of primary – secondary; SS, SP, PS, or PP networks as seen in Figure 3.2 [36, 255]. RL and rs are the load and source impedances, respectively, while R1 and R2 are the Tx and Rx DC resistances, respectively. C1 and C2 are the compensating capacitances for the control of Tx and Rx resonance, respectively. As discussed in [36, 255, 262], different topologies have different impedance matching and quality factor equations, leading to different WPTECT systems' measurement performances.

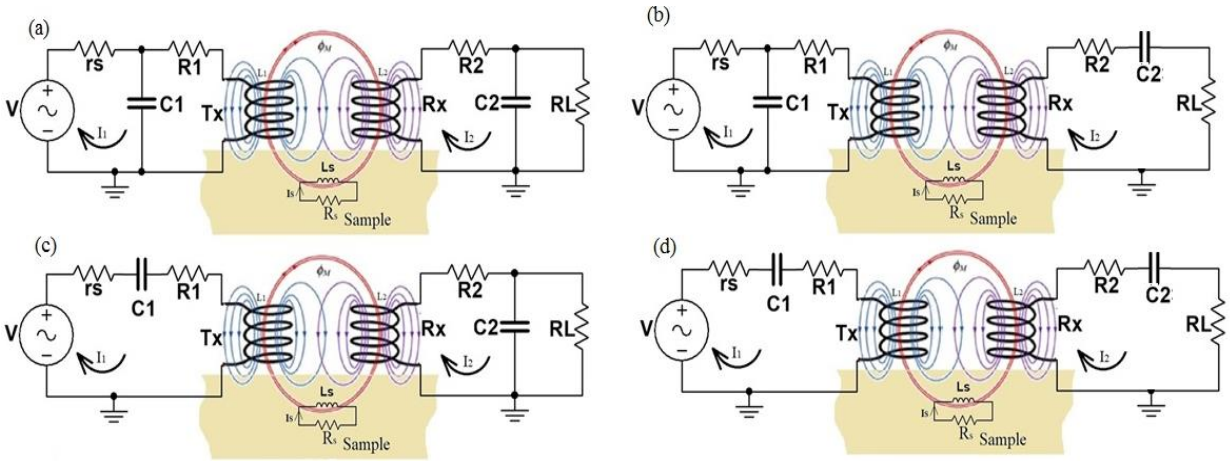

Figure 3.2 Basic WPTECT network topologies (a) PP (b) PS (c) SP (d) SS topologies

The application of WPT to ECT is based on the influence of the eddy current field on the power transfer between Tx and Rx according to electromagnetic induction law and Lenz's law. The magnetic field linking Rx passes through the metallic sample, modifies by the EC field, which carries information related to the permeability, conductivity, and geometrical nature of the metallic sample, and manifests on the features of the WPTECT response. As seen in figure 3.2, the inductance (Ls) of the metallic sample forms the eddy current (Is) loop with resistance Rs and couples inductively to the Tx and Rx inductors. The three current loops in the circuit: Tx excitation current (I_1), Rx induced-current (I_2), and the sample induced-eddy-current (I_s), are represented by equation (3.13) based on applying Kirchhoff's laws to the circuit in figure 3.2. Equation (3.13) is used to determine the dominant coil's parameters (self-inductance and -resistance) which vary according to the sample permeability, conductivity, and geometric nature due to eddy-current interruption. The sample acts as an inductor through which the eddy current circulates. In equation (3.13), M_{12}, M_{1s}, and M_{2s} are the mutual inductances for the Tx-Rx coils, Tx-sample, and Rx-sample, respectively, depending on their appropriate coupling coefficients and inductances. Also, Z_1, Z_2, and Z_s are the impedances of the transmitter and receiver topologies and metallic sample equivalent circuits, respectively. The primary (Tx) circuit self-impedances, Z_1 for each PP, PS, SP, and SS, are distinct and fully described in [263]. In contrast, the secondary (Rx) circuit self-impedances (Z_2) is computed by seeing the circuit from the induced voltage to the Rx.

$$\begin{pmatrix} V \\ 0 \\ 0 \end{pmatrix} = \begin{pmatrix} Z_1 & -j\omega M_{12} & -j\omega M_{1s} \\ -j\omega M_{12} & Z_2 & j\omega M_{s2} \\ -j\omega M_{1s} & j\omega M_{s2} & Z_s \end{pmatrix} \begin{pmatrix} I_1 \\ I_2 \\ I_s \end{pmatrix} \tag{3.13}$$

$$\begin{bmatrix} V(\omega) \\ 0 \end{bmatrix} = \begin{bmatrix} Z_1 + \dfrac{(\omega M_{1s})^2}{Z_s} & Z_{12} \\ Z_{21} & Z_2 + \dfrac{(\omega M_{s2})^2}{Z_s} \end{bmatrix} \begin{bmatrix} I_1 \\ I_2 \end{bmatrix} \tag{3.14}$$

Where, Z_{12} and Z_{21} are the forward and reverse transfer impedances, which depend on the type of WPTECT topology and are defined in subsection 3.4 for each topology used in this study. $Z_s = R_s + j\omega L_s$ is the metallic sample complex impedance which depends on the conductivity and permeability of the material.

Equation (3.14) is derived from equation (3.13) by eliminating the last row to modify the Tx and Rx models' behaviour by including the influence of sample parameters, Rs, Ls, and mutual couplings, M1s and M2s. However, the Rs and Ls of the sample depend on defect parameters and sample geometry in addition to material type. Their influence affects the Tx and Rx impedances, hence the resonance frequency, which manifests at the voltage and current frequency responses. Moreover, at the point of defect, the voltage and current change slightly due to the variation of sample parameters which causes a strong influence of eddy current density around the defect area due to the change in permeability, conductivity, and geometrical nature of the metallic sample.

The input voltage from the source, V(ω), is derived by evaluating equation (3.14) for the WPTECT as a two-port network and given by equation (3.15). The primary and secondary currents, I_1 and I_2 are related by the second row of equation (3.14), and each can be expressed as a function of the other. The values of I_1 and I_2 can as well be measured from the Tx and Rx coils, but the enclosed eddy current (I_s) in the material is defined by Ampere's circuital law as given by the expression in equation (3.16). The value of B in equation (3.16) is the superposition of the primary (B_p) and secondary (B_{eddy}) fields, determined by solving the differential equation (3.12). Similarly, the voltage induced to the Rx coil (V_{Rx}) is the superposition of the induced-voltages by the primary and secondary fields (B) [264]. It, therefore, depends on the mutual inductances ($M_{12}\ and\ M_{2s}$), induced eddy current (I_s) and current through the Tx coil (I_1) as described by equation (3.17). The induced voltage across the Rx coil determines the voltage drop across the load resistors, which is a characteristic impedance of the measuring instrument in this study. The source voltage ($V_1(\omega)$), Rx induced-volatage ($V_{Rx}(\omega)$), load resistance (RL), and source resistance (rs) determine the transfer response of WPTECT as described by transmission parameter (S21) in section 3.4 of this chapter.

$$V_1(\omega) = \left(Z_1 + \frac{(\omega M_{1s})^2}{Z_s}\right) I_1 + Z_{12} I_2 \tag{3.15}$$

$$\frac{1}{\mu_0}\oint B \cdot \partial s = I_s \tag{3.16}$$

$$V_{Rx}(\omega) = (-j\omega M_{12} I_1 - j\omega M_{s2} I_s) \tag{3.17}$$

The derived equations (3.15), including the source (r_s) and load (R_L) impedances and the voltage drop across the load defined the scattering parameter, S21 [265-267]. The S21 represents the forward voltage gain and is sometimes called the transmission coefficient [267]. It provides multiple resonances for freedom of features selection to facilitate multiple defect parameters comparisons using different WPTECT topologies. The multiple resonances depend on the Tx-Rx and sample coupling, r_s, R_L, and coil quality factor as described in the results of each case study.

The following section contains different case study methods describing specific WPTECT topology's applications to different challenges and problems of ECT. Furthermore, to assess how the derived WPTECT model from different topologies of WPTECT influences the S21 parameter, chapters 4, 5, and 6 for the different case studies evaluate the measured WPTECT response for different ECT challenges at different application scenarios.

3.4 Research Methodology

This research work contains the design, development and evaluation of WPTECT using analytical and experimental models to address the problems of low energy transfer and fewer feature points in the response of ECT probe. The attention is mainly geared toward the resonance behaviour of the transmit-receive (Tx-Rx) ECT coils probe. The procedure of conducting this research divides into different stages based on application-specific. The flow diagram of the study process given in figure 3.3 describes the flow of the study from the firstly investigated idea of WPTECT designed model to its features extraction, selection, fusion and comparison, system optimisation, and finally, application of the optimise system to a real-life scenario, rail line inspection. Each of the research solves challenging problems mentioned in chapter 2 and inside its corresponding chapter, as indicated in figure 3.3. The research methods of the experimental modelling are provided in the following subsections for the three different studies, whereas the details of analytical modelling are provided in section 3.3. The results of the studies are presented in chapters 4, 5, and 6 appropriately.

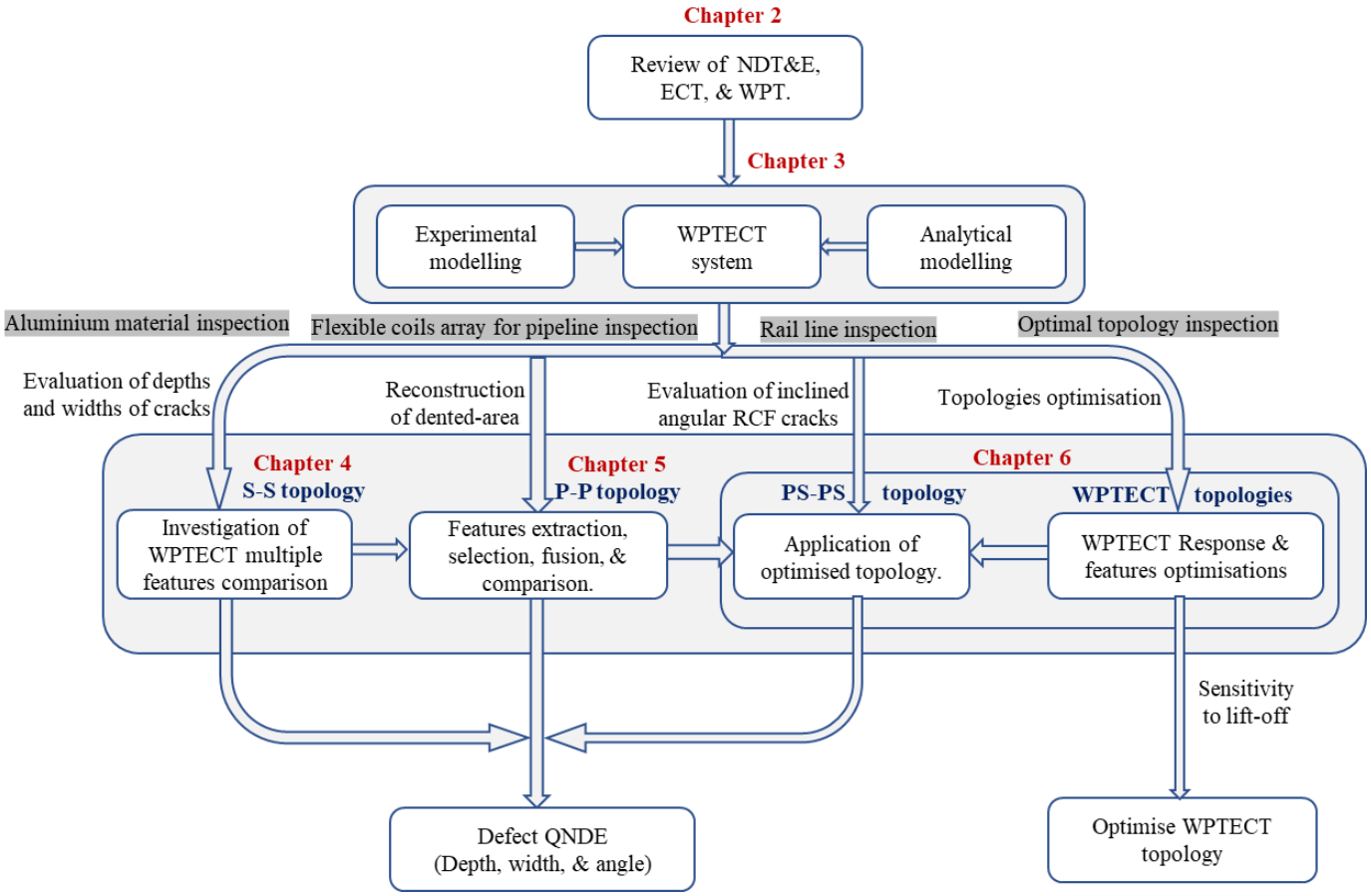

Figure 3.3 Research flow diagram for WPT-based ECT study

3.4.1 Study 1: WPTECT non-destructive evaluation of cracks in aluminium material

This section gives the design and development of the WPTECT system novel idea in ECT history as a sensing application. The WPTECT explores multiple resonances due to frequency shifting and splitting behaviour, which are sensitive to coupling variation between Tx-Rx probe and sample [37, 265, 267]. It also gives the design procedure of the experimental implementation and analysis of the WPTECT system, including measurements and instrumentation. The section contains the design and behavioural analysis of the inductive Tx-Rx probe based on a compensation topology of the WPT system in the presence of a metallic aluminium sample. The procedure of this investigation laid the foundation insight for splitting resonance points and response shape features from the probe response at different distinct behaviour to various defect parameters. Hence, this freedom for multiple features from WPT energy transfer could give the best information related to the sample for QND&E and explore methods' outcome results by this section in chapter 4. It started with the probe analysis and design procedure and then the experimental setting for the investigation.

3.4.1.1 Tx-Rx Probe analysis and design procedure

The concept of the WPT approach was initially applied for charging electric vehicles [19], but in this research, it has been extended to sensing application as a novel probe to eddy current testing. In this first WPTECT designed model, a series-series (SS) topology of WPTECT shown in figure 3.2(d) is considered because of its lower input and output impedance at a resonance frequency. The lower impedance allows maximum current flow through the Tx coil, leading to the maximum primary field for maximum induced eddy current to the metallic sample and voltage across the Rx coil.

Considering the SS topology of WPT in figure 3.2(d), evaluation of the sample's loop KVL expression in equation (3.13) provides the equation of eddy current (Is) as a function of the current through the Tx and Rx coils and their mutual coupling with the sample as given by equation (3.18). The derived value of Is in equation (3.18) is substituted into Tx and Rx loop KVL in equation (3.13) to generate Tx and Rx circuits models, which include the effect of sample parameters. The Tx and Rx units' models are analytically described by the derived expression given by equations (3.19) and (3.20). The models of the Tx and Rx unit described their self and transfer impedance. The self-impedance of each port includes the effect of a nearby metallic sample, as seen in figure 3.2(d), which is also applicable to other topologies.

$$I_s(\omega) = \frac{j\omega M_{1s}}{Z_s} I_1 - \frac{j\omega M_{2s}}{Z_s} I_2 \tag{3.18}$$

$$V_1(\omega) = \left(Z_1 + \frac{(\omega M_{1s})^2 (R_s - j\omega L_s)}{{R_s}^2 + (\omega L_s)^2}\right) I_1 - j\omega \left(M_{12} - M_{1s} \frac{j\omega M_{2s}}{R_s + j\omega L_s}\right) I_2 \tag{3.19}$$

$$0 = -j\omega \left(M_{12} - M_{2s} \frac{j\omega M_{1s}}{R_s + j\omega L_s}\right) I_1 + \left(Z_2 + \frac{(\omega M_{2s})^2 (R_s - j\omega L_s)}{{R_s}^2 + (\omega L_s)^2}\right) I_2 \tag{3.20}$$

The first part of the source voltage (V_1) given by equation (3.19) is the voltage drop due to the new self-input impedance, Z_{Tx_new} of the Tx unit, whereas the second part is due to the reflected transfer impedance contributed by the Rx unit in the presence of the metallic sample. The affected parameter of Z_{Tx_new} is the actual impedance of the Tx probe, $R_1 + j\omega L_1$ which is in series with the compensating capacitor, C_1. Similarly, the first part of the Rx model given by equation (3.20) is the reflected voltage drop from the Tx unit due to the transfer impedance, while the second term is the self-induced voltage across the Rx unit. The new Tx and Rx self-impedances, which includes the effect of metallic sample, finally derived the new resistance and inductance of the Tx and Rx coil as given by equations (3.21) and (3.22), respectively.

$$\therefore Z_{TX\_new} = R_{1\_new} + j\omega L_{1\_new} = R_1 + \frac{(\omega M_{1s})^2 R_s}{{R_s}^2 + (\omega L_s)^2} + j\omega\left(L_1 - \frac{(\omega M_{1s})^2 L_s}{{R_s}^2 + (\omega L_s)^2}\right) \quad (3.21)$$

$$Z_{\mathrm{Rx}\_new} = R_{2\_new} + j\omega L_{2\_new} = R_2 + \frac{(\omega M_{2s})^2 R_s}{{R_s}^2 + (\omega L_s)^2} + j\omega\left(L_2 - \frac{(\omega M_{2s})^2 L_s}{{R_s}^2 + (\omega L_s)^2}\right) \quad (3.22)$$

The variations of effective resistance (R_1) and inductance (L_1) of the Tx and that of Rx coils due to the effect of induced eddy current on the Tx-Rx coupling depends on the excitation frequency, mutual coupling between the coil and the sample, and sample parameters. The relationship is similar to the model used by some researchers for metallic object detection based on the WPT system [253, 268, 269]. The presence of the metal sample near the Tx or Rx increases losses due to the reduction in magnetic field passing through the coil section due to the eddy current's effect in the sample. It then reduces Tx and Rx inductances, as seen in equations (3.21) and (3.22) and hence the resonance frequency point increases. In contrast, it increases the equivalent self-inductor resistance, which affects the voltage and current responses at the resonance point. However, at the defect region, the voltage and current change slightly due to the variation of sample parameters resulting from a strong influence of eddy current density.

The values of new inductance (L_{1_new}) and resistance (R_{1_new}) of Tx and that of Rx coil change the resonance point and the magnitudes of voltages across Rx and Tx coils leading to new values of input and output voltages. The magnitude and frequency of the response signal at the resonance point contain information about the sample's electrical conductivity, magnetic permeability, and defect parameters. The response of a Tx-Rx WPT system has been evaluated and measured using voltage gain in the form of a transmission coefficient of the scattering parameters, S21, as defined by equation (3.23) [20, 265, 266]. The Tx-Rx voltage ratio in the expression of S21 given by equation (3.23) depends on the type of WPTECT topology, which can be obtained by evaluating equation (3.13) in the absence of a metallic sample. The derived ratio of output voltage (V_L) across RL and input voltage (V_1) as a function of frequency is given by equation (3.24) for the series-series topology (figure 3.2(d)) in this study. Similarly, the frequency at which the Tx and Rx circuits resonate is equal for achieving a maximum power transfer efficiency and response symmetry. The resonance frequency (f0) is theoretically derived by setting the imaginary part of the equivalent impedance of each Tx and Rx network to zero as a condition for the resonance point to occur in a network. The derived resonant frequency is given by equation (3.25).

$$S_{21} = 2\frac{V_L(\omega)}{V_1(\omega)}\sqrt{\frac{r_s}{R_L}} \tag{3.23}$$

$$\frac{V_L(\omega)}{V_1(\omega)} = \frac{j\omega M_{12}(R_L)}{\left(r_s + \left(\frac{1}{j\omega C1}\right) + (R_1 + j\omega L_1)\right)\left((R_2 + j\omega L_2) + \left(\frac{1}{j\omega C2}\right) + R_L\right) + (\omega M_{12})^2} \tag{3.24}$$

$$f_0 = \frac{1}{2\pi}\sqrt{\frac{1}{L_1C_1}} = \frac{1}{2\pi}\sqrt{\frac{1}{L_2C_2}} \tag{3.25}$$

However, according to the circuit theories, analysis and experimental study, the Tx-Rx WPT response given by equation (3.24) has two split frequencies in an over-coupled operation region [265, 270]. The over-coupled region occurred at the higher mutual coupling ($M_{12} = K_{12}\sqrt{L_1L_2}$) between Tx and Rx coils, depending on the distance between the two coils and their parameters. The coupling coefficient (K_{12}) of the Tx-Rx above which the resonance frequency of the S_{21} split into two is called critical coupling point (K_{12C}). The numerical value of K_{12C} is obtained by differentiating (3.24) with respect to M_{12} and equating to zero, as derived in ref. [271, 272]. It depends on the Tx and Rx coils' quality factor (Q) resulting from the load and source resistance, parameters of the coil and operating frequency, as given in equation (3.26) for a series compensated reactance. The two splitting frequencies at over-coupled-region of operation are derived in the refs. [272-277].

$$K_{12C} = \sqrt{\frac{(r_s + R_1)(R_2 + R_L)}{\omega^2 L_1 L_2}} = \sqrt{\frac{1}{Q_1 Q_2}} \tag{3.26}$$

The interaction of the Tx-Rx probe with the sample affects the mutual coupling between Tx and Rx, proportional to the sample parameters. The model, given by equation (3.23), described the numerical response of the Tx-Rx probe system for the circuit given in figure 3.2(d), SS topology. The designed values of the Tx-Rx parameters are given in Table I and used to compute the numerical model of S21 given by equation (3.23). The numerical response of the analytical model described by equation (3.23) is presented in the results section as a guide to the experimental model's response. The same Table I parameters used to evaluate model equation (3.23) are considered to develop the experimental model in the next section to prove the model's viability for sensing application.

Table I Experimental parameters and variables

Item	Note	Value
Sample and defect study	Scanning 8 slots on two different aluminium samples (sample1 and sample2).	
Transmitter and Receiver (Tx & Rx)	Inductance, L1=L2, N=15 turns of 26 AWG, 0.43mm	1.2μH
	Equivalent resistance, R1=R2	0.8Ω
	Resonant capacitor, C_1=C_2	4pf
f_0	Design resonance frequency (air)	70MHz
Measuring instrument	E5071B, Vector network analyser (VNA) with port1 and port2 having equal 50Ω characteristics ($r_s = R_L = 50\Omega$).	
VNA Operating frequency	Swept frequency excitation (1601 points per sweep frequency)	65MHz-80MHz

3.4.1.2 Experimental settings

Figure 3.4 shows the experimental system diagram and feature extraction approach. It shows the scanning mode block-arrangements for different units and the methods for features extraction-flow from data to projection via sample. Simple and low-cost rectangular spiral coils were used in the proposed Tx-Rx WPTECT experimental model as a novel probe. The two identical rectangular (Tx-Rx) coils have been configured as series-series WPT compensation topology and connected to a vector network analyser (VNA -E5071B) through port1 and port 2 in figure 3.4. The E5071B (300kHz to 8.5GHz) model operates on a sweep signal, measures the transmission coefficients, S21 and other scattering parameters, and displays the results on the screen. The Tx and Rx signals at the VNA ports are converted internally into a mixer's intermediate frequency (IF) signal, then into a digital signal by an inbuilt analog to digital converter (ADC) and finally sent to the processor for screen display and storage. One ADC is available for each port signal, and the conversions take place simultaneously. Each of the inbuilt ADCs has a 16-bit resolution and a sampling rate of 570k samples per second. Then, a microprocessor analyses the digital data and displays the results on the screen at a sweep speed of 9.6 μs/point.

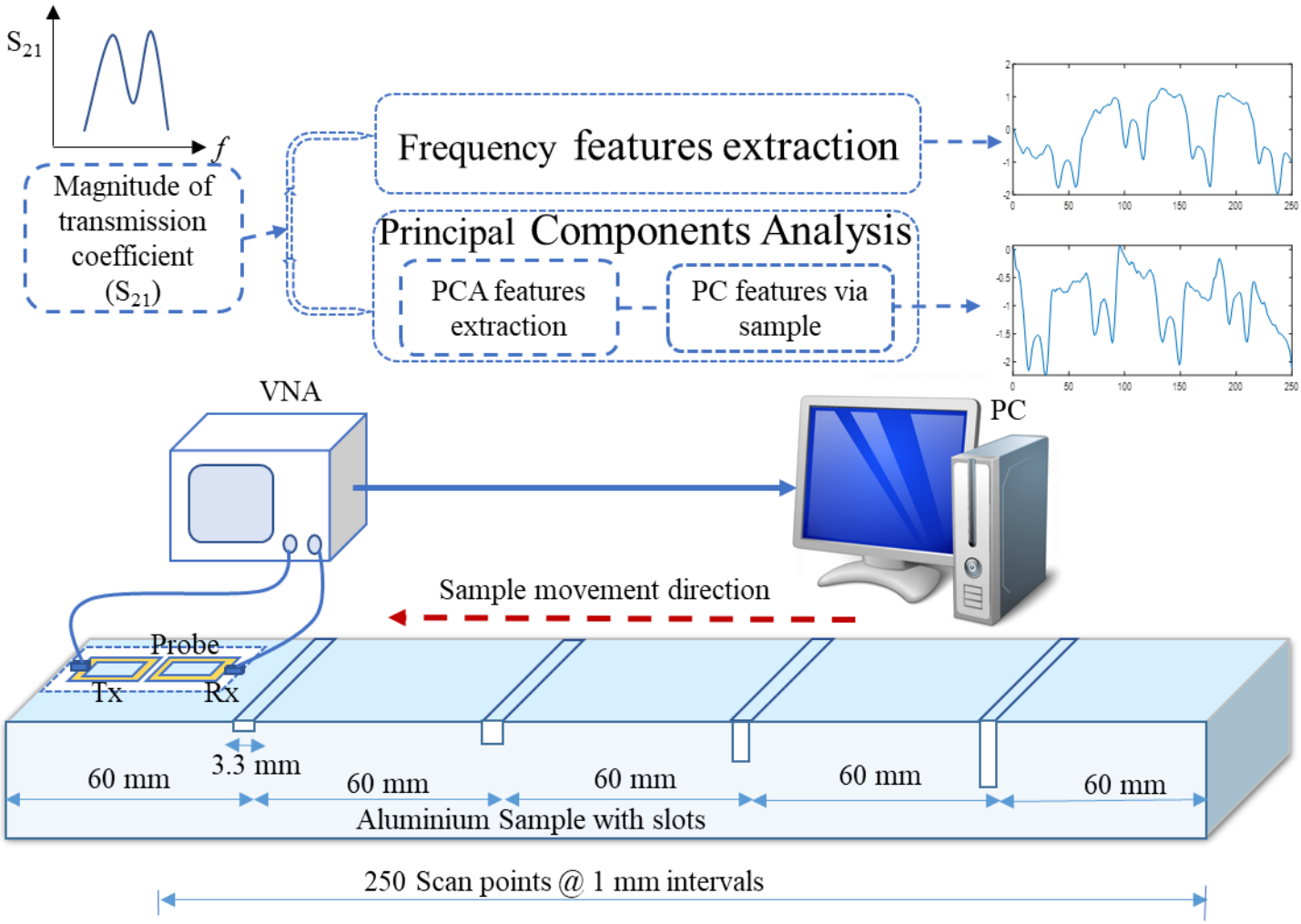

Figure 3.4 WPTEC based system diagram

For achieving the purposes of the novel WPTECT idea, two Aluminium samples were prepared to contain different slots. The first sample has a 50mm width by 300mm length by 10mm depth containing four different artificial surface slots. The surface slots are 2mm, 4mm, 6mm, and 8mm deep, and each has a 3.3mm width along the scan axis. The second sample has a 76.2mm width by 300mm length by 12.7mm thickness. It has four different surface slots with 1mm, 2mm, 3mm, and 4mm widths and each one with 4mm depth. The configured probe was arranged side-by-side and placed on the sample1 surface, as seen in figure 3.4, to investigate the slots parameters by scanning the sample. The Tx-Rx side-by-side coils are coaxially separated by a 4mm gap and lift-off by 2mm distance above the sample by considering the size of each coil (2.3cm x 3.3cm). The Tx unit was connected to port1 of the VNA, while the Rx unit was connected to port2. The excitation to the Tx unit and response from the Rx unit was based on their respected connection to port 1 and 2 operations of VNA. The excitation field penetration to the sample depends on operating frequency due to the skin depth exhibited by the sample; however, the slots are on the surface of the sample. The primary and secondary

fields linked Rx coils, but only the primary field carried the sample geometrical shape information due to EC generated field influence. Although, both the generated fields induced voltage to the Rx coil.

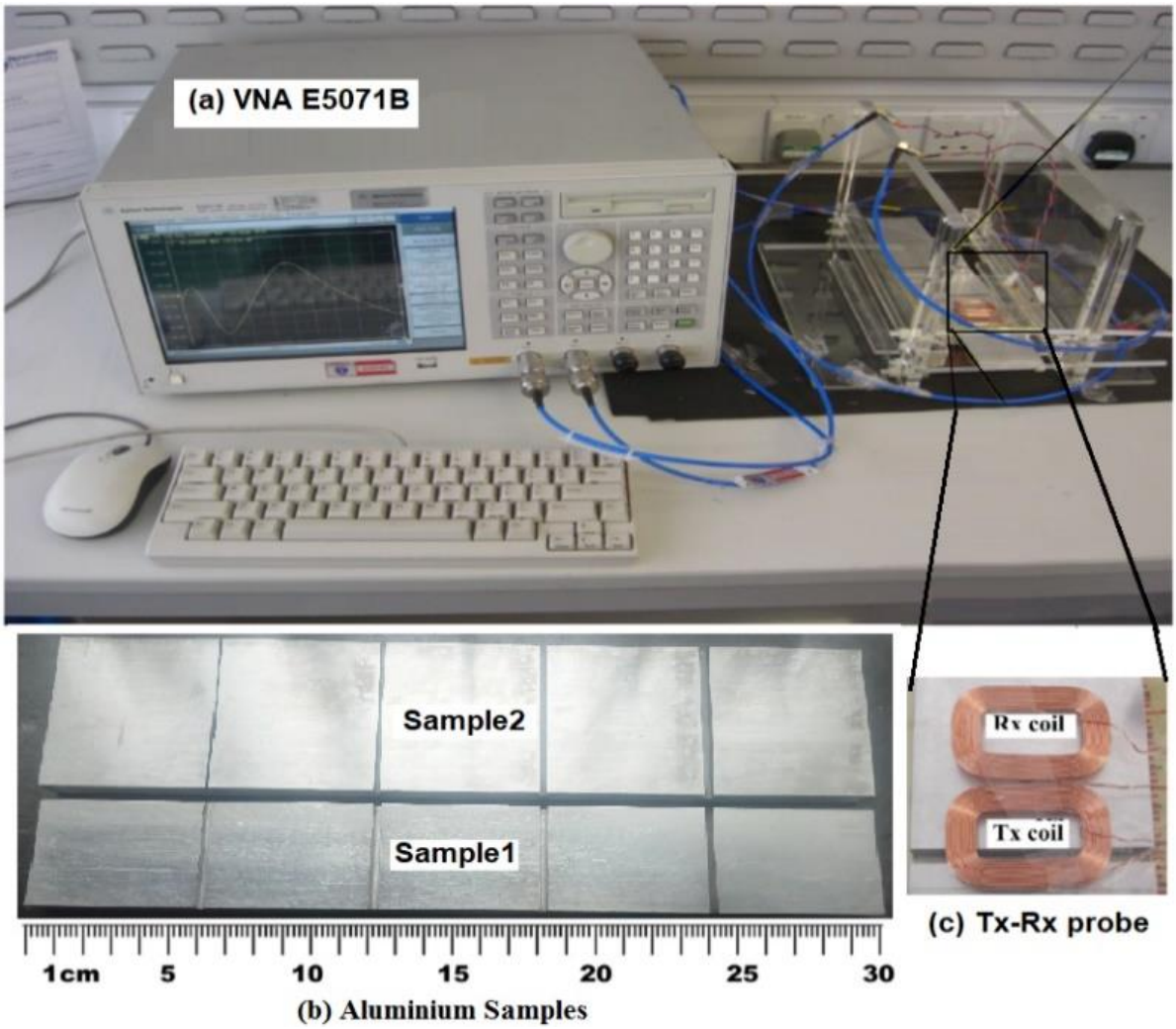

Figure 3.5 WPTECT testing system (a) Experimental set-up (b) Tested sample (c) Rx-Tx coil configuration

Figure 3.5 shows the experimental set-up, which includes a Tx-Rx probe, Two Aluminium (Al) samples, vector network analyser (VNA) and resonance capacitors for Tx and Rx configuration. The sample was freely moved for 249mm distance at each step of a 1mm interval along the scan axis. Each scan point measurement contained the magnitude of the transmission coefficient, S21 values for 1601 frequency points from 65 to 80MHz at a step of 9.375kHz. The transmission coefficient values, S21 in dB, were recorded and processed for feature extraction on a personal computer. Similarly, sample2 was scanned using the same experimental setting parameters of sample1. A numerical simulation software, MATLAB, was used for signal processing, feature extraction and mapping to sample surfaces with slots. Also, features extraction using principal components analysis (PCA) were evaluated statistically based on the

'M' shape of S21 responses. The PCA and resonance point features are mapped to spatial positions and compared with dedicated defect parameters to show the potential of WPTECT for NDT&E. the results and other hints for WPT consideration are described in chapter 4.

3.4.2 Study 2: WPT-Based ECT Using Flexible Printed Coils Array for pipeline inspection

In this section, a methodology of WPTECT system design and development is presented. It includes the basis and configuration of a probe based on integrating flexible multiple receiving coils array, pipeline sample with a dented area due to metal loss and natural corrosion, measuring instrument, data mining, feature imaging, and defect characterisation. The details of the pipeline sample used for the investigation are described in Table II values. The basis and configuration of the probe and the whole experimental set-up are described in the following subsections. Furthermore, multiple features extraction and comparison, including fusion for 3D reconstruction of the examined defect, are evaluated in the results section of chapter 5.

3.4.2.1 Flexible Probe groundwork and configuration

The probe consists of Flexible Printed Coils (FPC), allowing wide-area mapping capability of complex structures at higher spatial resolution and flexibility to different geometric shapes [197]. It maintains self and mutual inductance for bending it to follow the curve of the pipeline surface [194], which makes it less affected by lift-off variations. In this study probe, the FPC array is fabricated on polyimide film with a thinner trace thickness and line spacing, which are advantageous for spatial resolution and sensitivity enhancement [197]. It contains four layers with Tx covering the top and bottom layers, while 64 equal-spaced similar Rx coils are distributed in the two middle layers. The two different layers for each Tx and Rx array are connected in series through vias to maximise the mutual inductance between Tx and Rx coils array, improving the Rx response and increasing the signal-to-noise ratio.

Figure 3.6 shows the Tx-Rx coils array used in this study, offering an excitation Tx coil surrounding a uniformly spaced and multiple detection Rx coils array. The Rx coils have identical inductance values that are 1.9µH while the Tx has an inductance of 1.26µH, measured using HAMEG® programmable LCR bridge HM8118 operating at 200kHz. The structure of the Tx coil allows a considerable magnetic field to be evenly distributed across the Rx array. When the Tx coil is excited, it generates a spatially periodic magnetic field that induces a voltage in each Rx and eddy currents in the sample surface. The eddy current flow concentrates around the edge of the defect according to the current continuity theorem. Hence, the generated eddy current field disturbs the primary field, which manifests on the induced voltage across the Rx coil, carrying information on the sample and the defect.

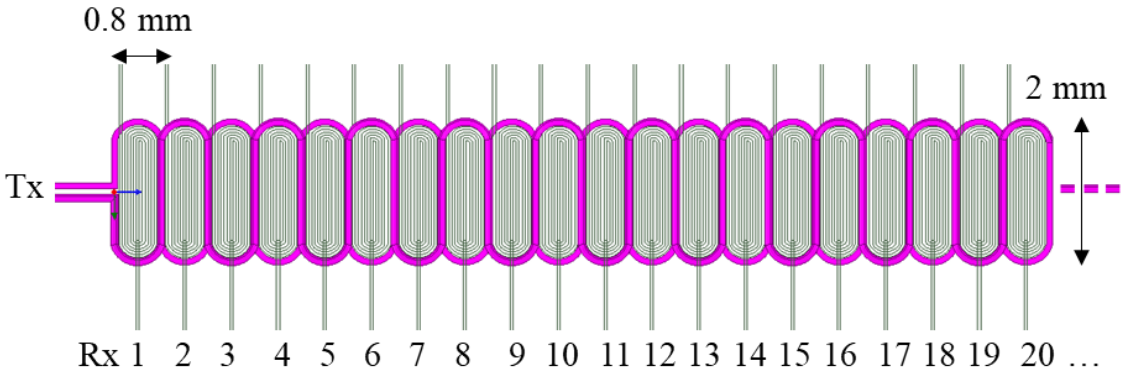

Figure 3.6 FPC array structure

A flexible sensor made up of an array of receivers was used because of its advantages for area mapping at higher spatial resolution and flexibility to different geometric shapes [197]. The first 16 channels of the FPC array were used for dent-area inspection using a vector network analyser (VNA) to capture Tx-Rx's 'M' shape response. The Tx and Rx channels were configured as parallel resonance network topology by connecting a capacitor in parallel, as presented in figure 3.2(a). The values of L1, L2, R1 and R2 of the FPC array were inherent, while C1 and C2 were determined based on the resonance frequency, specific coil inductance, and quality factors. The parameters and values of the FPC array and their compensating capacitors are given in Table II below. The resonance, f0, is chosen to meet the condition for splitting resonance frequency by considering high-frequency sensitivity to surface dent, input and output characteristic impedance and the limitation of measuring instrument, VNA. The swept-frequency range is 300kHz - 19MHz for this study, WPTECT system.

Table II Study II Experimental parameters and variables

Item	Note	Value
Defect study	Mapping and scanning a dent-area due to natural corrosion and metal loss in a class-A, AWWA, pit cast, cast-iron pipeline sample.	
Transmitter, Tx	Inductance, L1	1.26µH
	Equivalent resistance, R1	16.2Ω
	Resonant capacitor, C1	500pf
	Quality factor at f0	3.2
Receiver, Rx array	Each Rx has 0.8mm spatial resolution, and all the channels covered around 54mm in length.	
	Each Rx Inductance, L2	1.9µH
	Each Rx equivalent resistance, R2	400Ω

	Resonant capacitor, C2 for each Rx	300pf
	Quality factor at f0	0.2
f0	Design resonance frequency (air)	6.5MHz
Measuring instrument	E5071B, Vector network analyser (VNA) with port1 and port2 having equal 50Ω characteristics ($r_s = R_L = 50\Omega$).	
Operating frequency	Swept frequency excitation (1601 frequency points)	300KHz-19MHz

3.4.2.2 Experimental settings

The system diagram is presented in figure 3.7, which includes WPT based ECT instrumentation using VNA and FPC array, signal collection, multiple feature extraction, selection and fusion for quantitative Non-Destructive evaluation (QNDE). Figure 3.7 area is illustrated in figure 3.8 as an experimental set-up in the photo. The experimental set-up and the FPC coil array over a cast-iron pipeline (cut) sample with a natural dent from the industry are illustrated in figure 3.8. The FPC array was configured as the parallel-parallel topology of WPTECT and connected to a vector network analyser (VNA-E5071B) with Tx to port1 and Rx to port2. The Rx channels were connected sequentially, one at a time, because of the VNA connection constraint and to reduce mutual coupling between neighbouring Rx channels.

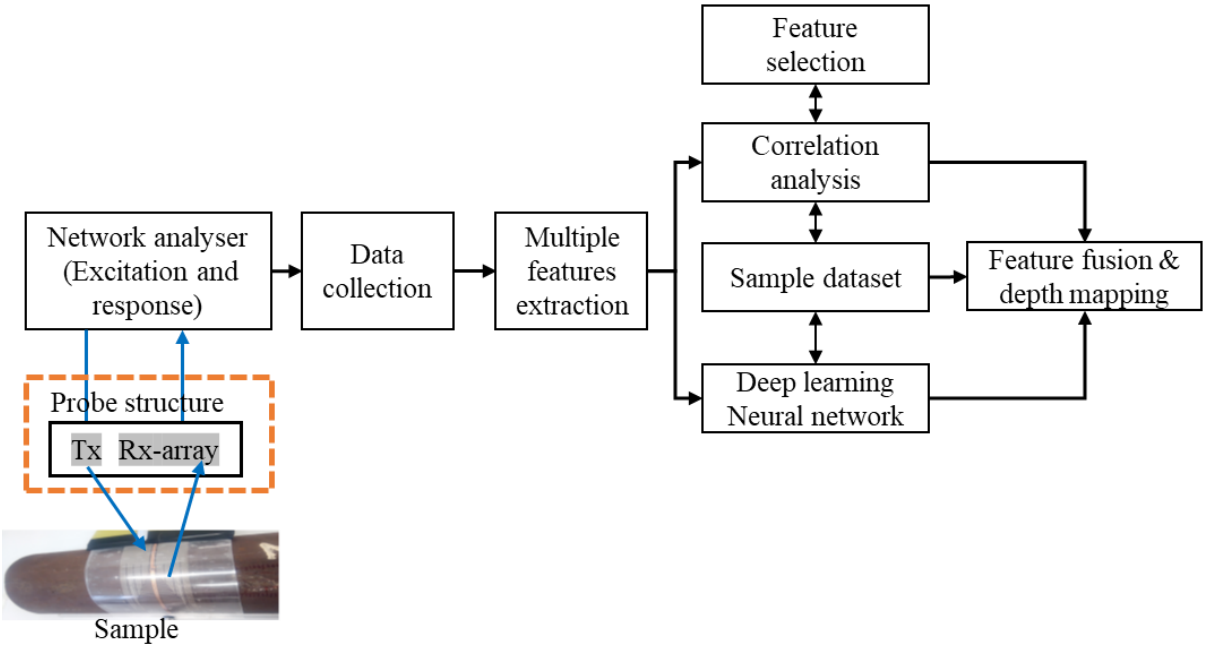

Figure 3.7 system block diagram of WPT based flexible coil array ECT

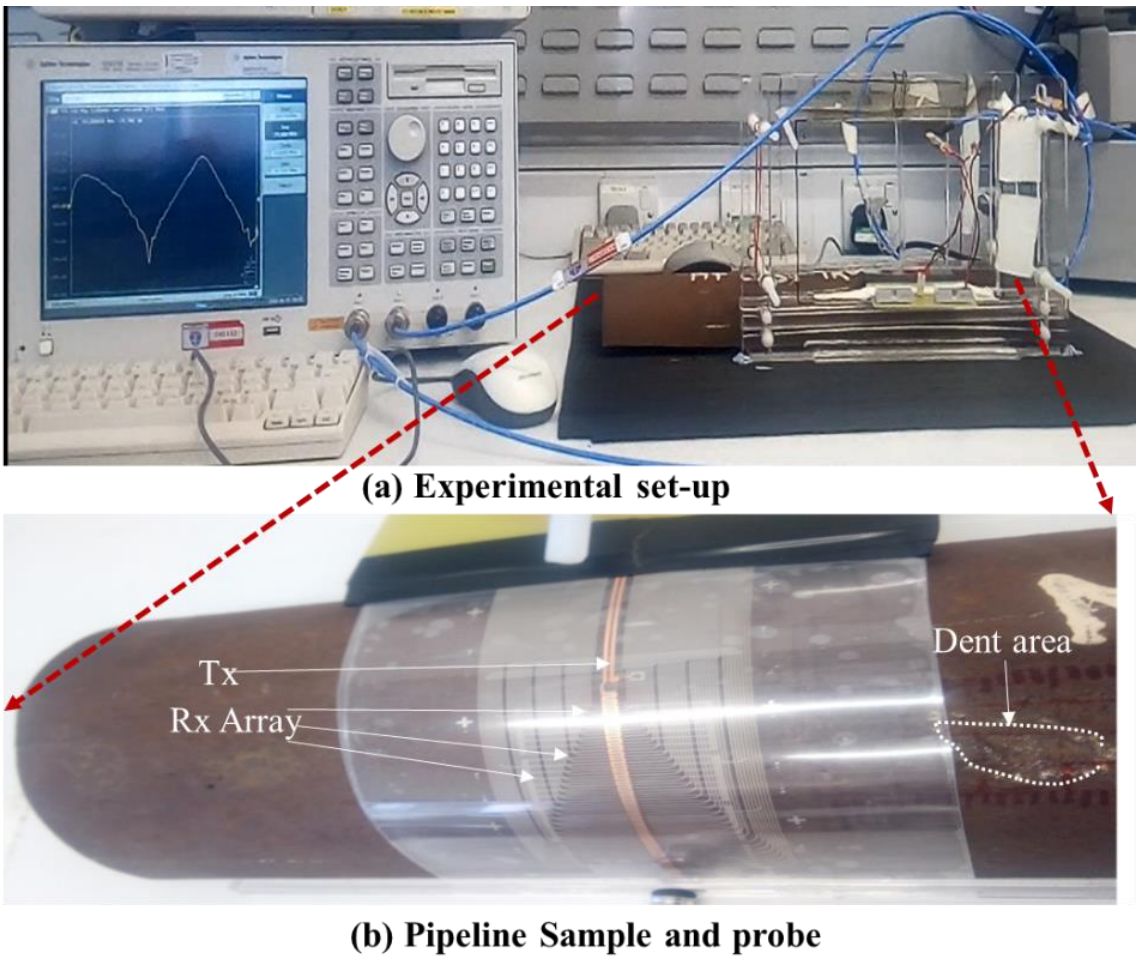

Figure 3.8 Experimental set-up and the FPC coil array over the pipeline sample

The data measured using the VNA instrument, S21, has 1601 swept-frequency points among 300kHz -19MHz for every channel at a measurement point on the sample, as illustrated in figure 3.8, the experimental set-up. For each of the measurement positions of each C-scan, each of the 16 Rx-channels covered 0.8mm Y-spatial position and 2mm X-spatial position with lift-off for the Z-spatial position. For measurement of the dented area, the probe C-scan measurement was conducted by moving the sample axially at an equal interval of 2mm for 40mm distance for the defect to cross the probe. To investigate the capability of the proposed WPTECT system for surface dent mapping and reconstruction, multiple features, including resonant magnitudes and principal component analysis, were extracted from the dual resonant response and demonstrated in chapter 5. The methods for optimal selection of the WPT topology and optimal operational frequency for multiple resonances, as discussed in section 3.3, are presented in the following subsection.

3.4.3 Study 3: Optimisation of WPT-Based ECT and RCF Cracks investigation

This section proposes methods of an experimental investigation for optimising WPTECT topology to characterise models of inclined angular RCF cracks by minimising the influence of lift-off and sample permeability in the response signal. The study procedure starts with the preparation of the required metallic sample mirroring rail materials and RCF cracks. Secondly, five Tx-Rx probes were configured; the first four are the basic topologies described in figure 3.2, and the fifth is a combination of PP (figure 3.2 (a))) and SS topologies (figure 3.2 (d)) topologies. Thirdly, design of an experimental setup, including instrumentation and supporting structures for the probe and sample, data capturing for each probe configuration. Finally, evaluation of the system response for comparing different topologies' features extraction and mapping to inclined angular cracks parameters from an optimised topology. The section explains the details of each stage in the following paragraph and subsections.

Table III Sample and crack parameters

Material		AISI 1045 Carbon steel (300mm ×30mm ×63mm)			
Conductivity, σ		6.17×106 S/M			
Permeability, μ		B-H curve			
Cracks		θ^0	L (mm)	d (mm)	w0 (mm)
	S1	10	0.38	0.07	1.13
	S2	15	0.45	0.12	0.85
	S3	20	0.81	0.28	0.66
	S4	25	0.90	0.38	0.51
	S5	30	0.88	0.44	0.46
	S6	35	1.03	0.59	0.48
	S7	40	0.91	0.58	0.44
	S8	45	1.06	0.75	0.43
	S9	90	1.32	1.32	0.37

Researchers have been using samples with micro-slots at an inclined geometry to simulate distinctly inclined angular cracks mirroring the factual industrial structures [40, 45]. Therefore, a carbon steel sample was chosen in this study because it's commonly used for rail production. By considering the natural size of most RCF cracks found in a rail, nine distinct milli-cracks were fabricated using wire electric discharge machining with a wire diameter of 0.2mm. Their

parameters and sample size are given in Table III. Figure 3.10(b) shows the 3D picture of the fabricated sample, indicating nine cracks, S1-S9 equally spaced 30mm interval. 90^0 inclined crack imitates the vertical RCF crack while the rest of the inclined angular (10^0 to 45^0) cracks cover the range of typical angle of RCF crack.

3.4.3.1 WPTECT probes design and configuration

Figures 3.2 (a) - (d) show WPTECT circuit diagrams of basic topologies for comparison study and investigating RCF cracks amidst lift-off and sample influence. Each of the four WPTECT topologies has C1 and C2 connected in series or parallel to L1 and L2, respectively, to control the resonance point. The resonance frequency is theoretically obtained by setting the imaginary part of the equivalent impedance of the Tx and Rx topologies to zero and given by equations (3.25) and (3.27) corresponding to series and parallel LC resonance, respectively. The values of C1 and C2 of the four topologies given in figure 3.2 were derived from equations (3.25) and (3.27) by appropriately chosen 1MHz resonance frequency due to consideration of the Tx/Rx natural resonance, nature of the surface defect, and the limitation of the experimental measuring instrument, a network analyser (E5071B). The probe capability to detect and quantify such cracks depends on the incident and reflected voltages measured by the frequency characteristics of the power transmission coefficient (S21) parameter response. However, the size of Tx and Rx coils are larger than the models of the fabricated RCF cracks' sizes. Furthermore, as given in Table IV, the Tx and Rx coils of the probe are identical in this study; hence the Tx- and Rx- topologies in each probe are symmetrical.

$$f_{0\_parallel} = \frac{1}{2\pi}\sqrt{\frac{1}{L_iC_i} - \frac{{R_i}^2}{{L_i}^2}} \cong \frac{1}{2\pi}\sqrt{\frac{1}{L_iC_i}};\ \text{because}\ \frac{1}{L_iC_i} \gg \frac{{R_i}^2}{{L_i}^2} \qquad (3.27)$$

The fifth probe in this study combines SS and PP topologies' advantages and simultaneously acts as a resonance compensation and is called advanced impedance matching (IM) circuit. In conventional magnetically-coupled resonant WPT applications, the advanced IM circuit takes the form of an L-type matching network [278], which is adjustable to T-network or π-network. These networks are typically inserted between the excitation sources (or load) and the Tx (or Rx) resonance networks to reduce the reflection by matching the excitation source (or load) and Tx (or Rx) coil impedances. In comparison, L-type matching networks are simple and easier to implement, and the π-networks have a greater degree of design freedom, such as the flexibility of selecting the Q-value of the system. Therefore, this study considers an L-type matching

network as it can sufficiently maintain the high efficiency, though the π-matching network allows more design flexibility to Q-value of the system. Additionally, the L-type matching network has fewer component requirements, less circuit space, and minimal stray reactance and capably transforms lower to higher or vice-versa impedances between two different networks such as excitation source and resonance Tx coil in a primary electric circuit of WPT for satisfying maximum power transfer conditions [279]. There are four such L-impedance matching networks, and grouped into lowpass or highpass L-matching networks. They are not resonance networks but operate at a desired (cut-off) frequency corresponding to resonance frequency for optimal primary or secondary resonance WPTECT topology performance. The design procedure, including examples, is described on pages 73 to 80 of ref. [279].

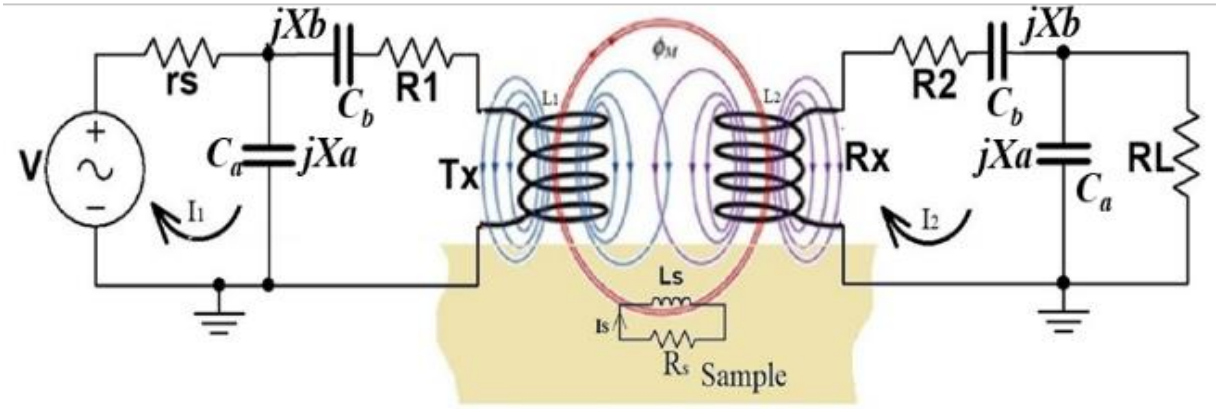

Figure 3.9 Modified topology (L-matching) from the combination of S-S and P-P (PS-PS) topologies

However, the L-type matching network in this investigation is the inverted L-type matching network, which combines the benefits of PP and SS topologies' capacitive reactances. The benefits include reducing the effective reactance of Tx coil by the series reactance, Xb and reducing the stress on parallel reactance, Xa for only supplying a section of total reactive power to maintain the system oscillation [280]. Figure 3.9 shows the hybrid topology, a combination of SS and PP topologies. It has a unique attribute when $jXb < jXa$; more current passes through the Tx coil, and more voltage induces to the Rx coil, Which is the case with this designed model. Otherwise, less voltage is induced to the Rx coil. In this design, an input (rs) and output (RL) characteristic impedance of the VNA are considered in addition to the Tx - Rx DC resistances (R1 and R2) for finding the compensating reactance, Xa and Xb at maximum power transfer condition. Let the characteristic impedance of VNA be $Zc=Rc+jXc=50+j0$ Ω at port1 and port2. The two compensating reactances, *jXa* and *jXb* of the PS-PS topology, at the resonance frequency, determine the two capacitors, *Ca* and *Cb*, respectively, based on expressions (3.28)

and (3.29) using the principles of the L-matching network [279]. The parameters of the topologies and instruments of this study's experimental set-up are given in Table IV.

$$X_a = -\frac{{R_C}^2 + {X_c}^2}{X_c + QR_c} \tag{3.28}$$

$$X_b = Qr_1 - X_1 \tag{3.29}$$

$$Q = \pm\sqrt{\frac{R_c}{r_1}\left(1 + \left(\frac{X_c}{R_c}\right)^2\right) - 1} \tag{3.30}$$

Table IV Tx-Rx probe configured parameters and experimental variables

Item	Description	Value
Defect study	Inclined angular RCF cracks model on Carbon steel sample	
Tx & Rx coils (Manufacturer Part No.: IWAS3010AZEB130KF1)	Inductance, L1 = L2	12.900µH
	Equivalent resistance, R1 = R2	0.700Ω
	Resonant capacitor, C1 = C2	1.900nf
PS-PS topology Matching capacitors	Ca	1.9615nf
	Cb	26.713nf
f_0	Design resonance frequency (air)	1MHz
Measuring instrument	E5071B, VNA with port1 and port2 having equal characteristics (Xc = 0, Rc = 50 Ω)	
Sweeping frequency	Swept-frequency excitation (1601 frequency points)	1MHz–7MHz

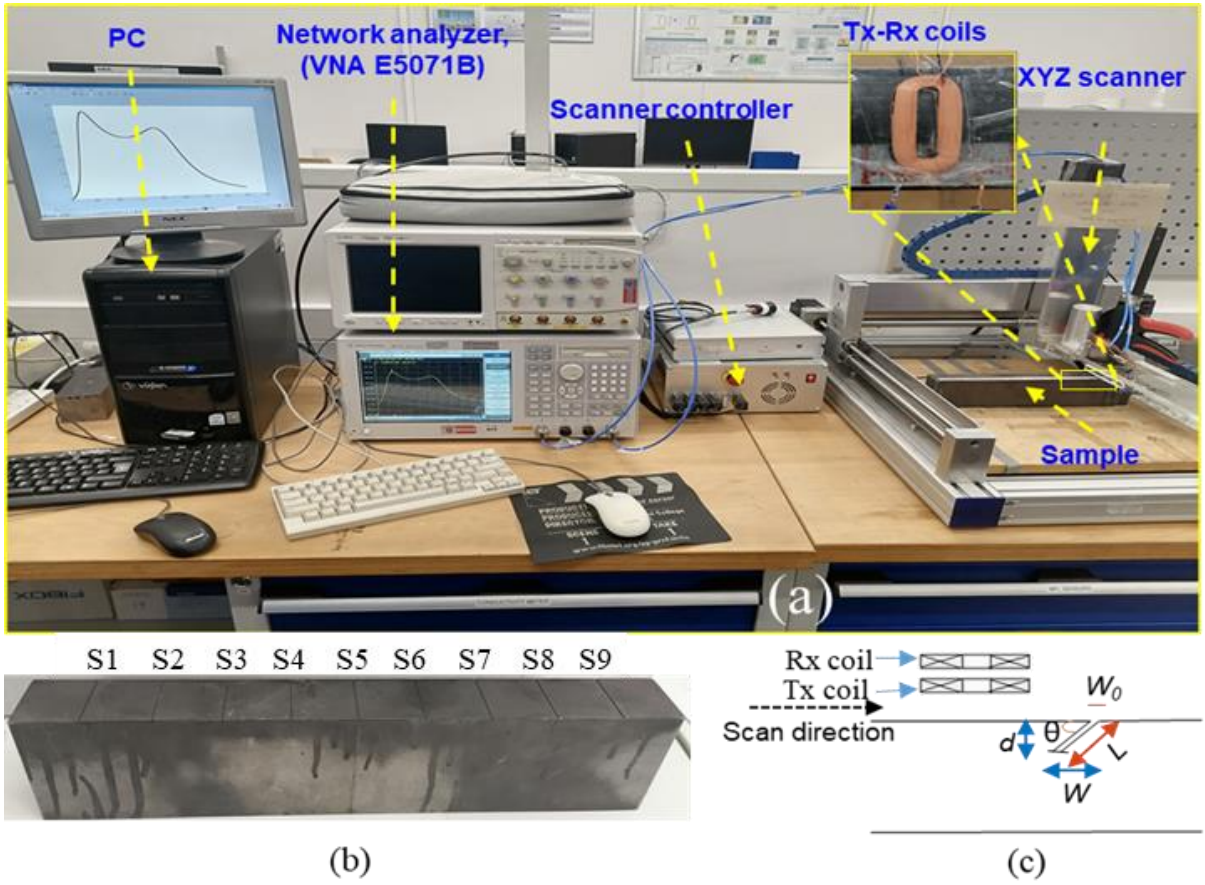

Figure 3.10 Experimental setup diagrams (a) Photograph of the instruments and peripheral components (b) Carbon steel sample with nine angular slots, S1 – S9 (c) Arrangement of Tx-Rx, scan direction and sample with crack parameters, L=slanting length, W=width, W0= crack mouth/opening, d= depth, and θ=inclination angle.

3.4.3.2 Experimental setup

The experimental setup presented in figure 3.10(a) includes WPT-based ECT instrumentation using the VNA (E5071B), configured Tx-Rx coils of the five WPTECT topologies, XYZ scanner and its controller, fabricated sample for the investigation, and a personal computer (PC) for synchronizing CNC scanner and data capturing and processing. Whereas figures 3.10(b) and (c) show the photo of the fabricated sample and the Tx-Rx probe arrangement throughout the investigation in this study. The Rx coil is placed coaxially above the Tx coils at a constant axial separation (gap) of 0.2mm, as seen in figure 3.10(c). The designed experimental setup includes configured probes connected one after the other to the VNA, always Tx to port1 and Rx to port2 for each specific investigation. Three different experimental investigations were carried out as depicted in figure 3.11, the experimental investigation flow chart. The first investigation compared different WPTECT topologies to find an optimised topology capable of providing multiple resonances and also to optimise the

topology for the minimum influence of lift-off sensitivity for inspecting inclined angular RCF cracks in a rail-line material, carbon steel sample. The comparison assessed the sensitivity to various lift-offs of each topology's extracted features response for a crack and no-crack position. Secondly, it was the multiple features optimization, from the response of an optimised topology, by scanning over a crack at different lift-off to optimise the performance of the feature for an inclined angular RCF crack characterisation. The investigation suppressed the influence of lift-off and sample permeability from the extracted features by finding an optimal lift-off level. Thirdly, it investigated features extraction, selection, and mapping to the crack parameters for QNDE of the inclined angular RCF cracks. In this investigation, the optimal lift-off level was used to scan the nine inclined angular RCF cracks models, S1 to S9, for relevant features extraction and processing for QNDE.

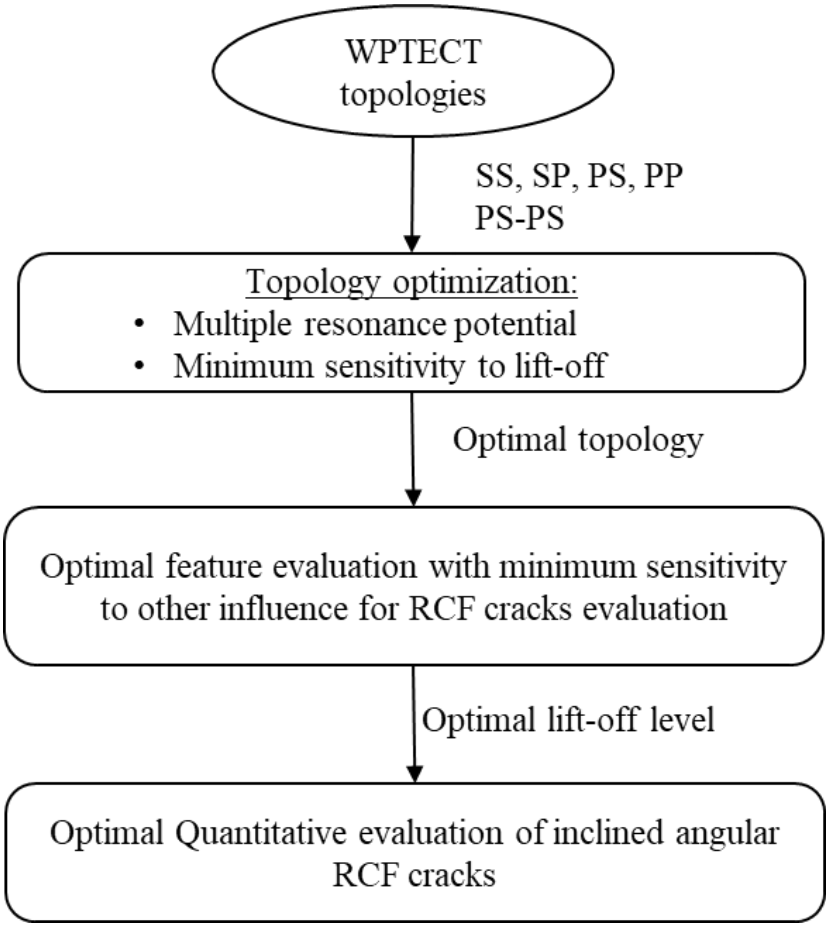

Figure 3.11 Experimental investigation flow chart

An Agilent RF Network Analyser (VNA, E5071B) was used to measure the topologies' response (S21) in each of three procedural investigation flow charts. Section 3.4.1 described the operation of the VNA-E5071B model used in this study. It has constant and equal characteristic impedances at each port: the source and load impedance to the configured probe

of WPTECT topologies. Operation at constant load and source impedances allowed the lift-off distance and sample influence to be the only factor affecting the coupling between Tx and Rx. It also avoids the conflicting optimization of the two impedances simultaneously, as they cannot be optimised at a time [250]. S21 responses were measured as the data for further feature extraction and processing. Each of the S21 response point measurements has 1601 frequencies swept points from 1MHz–7MHz. The measured S21 carries information related to the sample parameters due to the coupling effect between Tx-Rx and the sample. The analysis and comparison of the data of different topologies optimisation and the topology for application to inclined angular RCF cracks quantification are presented in chapter 6.

3.5 Chapter summary

This chapter contributes to the design and development of magnetically-coupled resonant WPTECT Tx-Rx probes using different topologies operating at maximum energy transfer and offering multiple resonance points for multiple feature points. It also analysed the inductive coupling Tx-Rx probe and linked it to the magnetically-coupled resonant Tx-Rx WPTECT probe for the experimental study design for NDT&E inspection. It then linked the theoretical and practical studies of the magnetically-coupled resonant Tx-Rx probe to facilitate designing different case studies of WPTECT systems for multiple feature investigation and their sensing applications.

The first designed Tx-Rx probe was applied to evaluate crack parameters in aluminium samples and investigate multiple features extraction and comparison for different crack parameters. The second designed probe was a flexible printed coils array applied for 3D reconstruction of the natural surface dented area in the curvature of the pipeline sample to investigate feature extraction, selection, and fusion, including individual and fused features comparison. The third case study designed investigations of five different probes for transfer response and features optimisation based on different circuit topologies of WPTECT. An optimised topology was then applied to characterise inclined angular RCF cracks in a rail line material. The analysis and discussion of the results for each case study are provided in the following three chapters 4, 5, and 6.

Chapter 4. WPT-Based ECT Non-Destructive Evaluation of Cracks

4.1 Introduction

Chapter 3 has presented the research methodology for NDT&E of defects in metallic structures based on the magnetically-coupled resonant wireless power transfer (WPT)-based ECT (WPTECT). Crack is one of the defects. It is vital to detect and quantify it in metallic structures for guaranteeing safer structural operation. However, cracks in metallic structures initiate from the surface due to different causes and propagate through the structure, leading to sudden breakdowns. Failure to detect cracks in the structures such as rail tracks, pipelines, and aeroplanes early can result in fatal accidents. Eddy current techniques (ECT) are generally used to inspect conducting metallic structures to detect such cracks. Moreover, for the two coils (Tx-Rx) inductive coupling probe, the coil's impedance, which is affected by the sample influence, lift-off distance and separation between the two coils, varies according to permeability, conductivity, surface, and subsurface geometry of the material [178]. Therefore, more ECT response features for mapping different crack parameters could improve the performance of the ECT probe.

The previous chapter reviewed ECT and other electromagnetic NDT&E for materials defect detection and characterisation and integration, including the integration of the WPT concept. This chapter presents the first study model of WPTECT and its evaluation technique in the history of the ECT technique. It describes principles consideration of magnetically-coupled resonant WPTECT, results of the designed and developed WPTECT, signal processing and features extraction from resonance frequency points and principal components analysis. The results are discussed, and finally, the conclusion and future work for improving this concept idea to the real applications of NDT&E are highlighted.

4.2 WPT-based ECT Tx-Rx Coils probe

From the review of ECT, sensor design and signal conditioning are essential research areas for quantitative testing and evaluation. However, crack quantification relies on the variations of sensing mechanism and signal amplitude, which is susceptible to noise under various interferences, thus providing a limited number of features for evaluation at weak energy transfer from transmitter to receiver. This study proposes the magnetically-coupled resonant WPT application to NDT&E as a novel ECT to the best of our knowledge. The novelty of this technique is the maximum energy transfer and capability of multiple resonance frequencies as features for crack detection and characterisation. Multiple resonances allow the selection of

specific features for the best sample and crack characteristics as the response results from the generated field and the field linking Rx coil.

The principles of magnetically-coupled resonant Tx-Rx probes operations is described in section 3.3 of chapter 3. The magnetic field linking the Rx coil depends on the direct and indirect field linkage. The direct field from Tx coil to Rx coil carries no sample information, and the indirect field from Tx coil through a sample to Rx coil carries sample information. However, conductive-material-sample (CMS) near the field generated by the primary coil, as seen in figure 4.1, affects the magnetic field linking Rx. Apart from the induced-eddy-current influence on indirect field linking Rx, power transfer from Tx to Rx is also affected by electrical conductivity, magnetic permeability, the sample volume and inhomogeneity of the material in the vicinity of the probe. These factors manifest their influence on the defect signal features. Therefore, the WPTECT approach has potential application to material defect detection and characterisation. The results of WPTECT for crack quantification are described in stages in the next section based on the method described in section 3.4.1 of chapter 3.

The basic principles of conventional two coils (Tx-Rx) magnetically-coupled resonant WPT operation and its operation for ECT sensing application allow efficient energy transmission with splitting frequency at a higher coupling point [281-283]. The number of splitting frequencies depends on the number of Tx and Rx coils in addition to optional relay coils [282]. The additional relay coils improve the efficiency of power transfer range like up to 5 m lengths in [284], which is advantageous for enhancing response at higher lift-off distance inspection. This study evaluated a series-series (SS) topology of WPTECT because of its low input and output impedance at the resonance point, which provides maximum Tx coil current operation. The higher maximum current amplitude operation induces higher flux strength, which causes a higher response signal. Figure 4.1 shows the series-series (SS) WPT topology circuit diagram using compensating capacitors, C1 and C2 and Tx and Rx series resistors, R1 and R2, respectively. The two inductors, L1 and L2, are the Tx and Rx inductances, respectively and m_{12} as the mutual coupling for the two coils. The response based on S21 depends on the voltage ratio for the load resistor, RL and Vs, as a response measurement of the WPT systems [20]. The response of the SS topology is described in chapter 3, section 3.4.1 by S21 parameter (equation (3.23)).

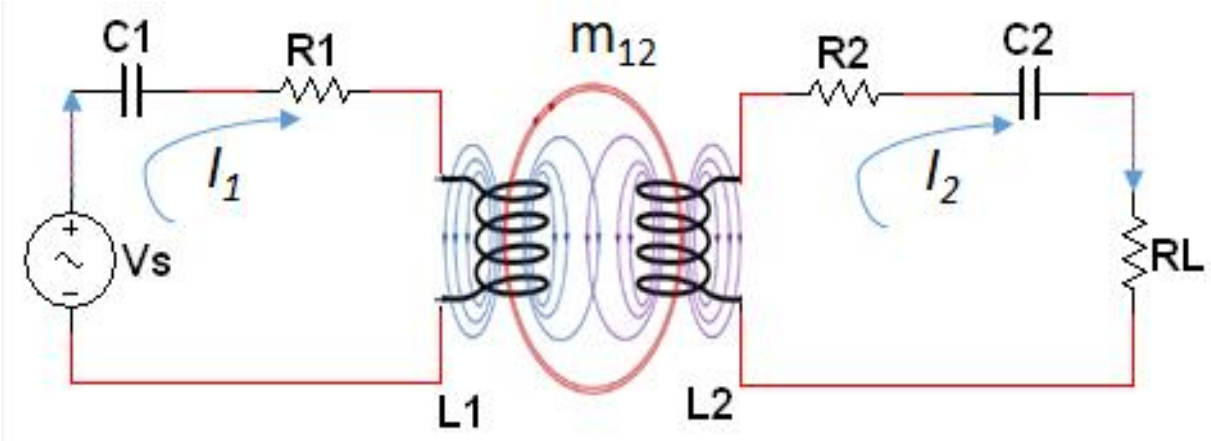

Figure 4.1 Two-coil Tx-Rx of magnetically-coupled resonant WPT circuit diagram

Figure 4.2 shows the numerical S21 values for different coupling coefficients of Tx-Rx to indicate the response to the mutual coupling between the Tx-Rx and the sample. The coupling factor ($K_{12} = \frac{M_{12}}{\sqrt{L_1 L_2}}$) ranges from 0.1 to 0.2, which indicates how weakly the two coils (Tx-Rx) are mutually coupled, though the splitting frequency occurs when the coupling exceeds 0.1 due to the high frequency that influences the coil's quality factor. The coupling factor linearly depends on the Tx-Rx mutual inductance, depending on the sample influences determined by equations (3.21) and (3.22). The first peak frequency of the S21 increases, whereas the second peak decreases for increasing the Tx-Rx coupling factor. Furthermore, higher coupling causes a wider frequency gap between the two splitting frequencies. However, the presence of a metallic sample reduces the Tx-Rx inductance to a new value due to the mutual coupling effect of the Tx-Rx coils and the sample. It extracts more power from the transmitter proportionate to the eddy current losses, which significantly impacts the system's parameters, especially for low-power applications [253, 285]. The influence of the induced eddy current on the impedance characteristics of the Tx and Rx coils, given by equations (3.21) and (3.22), contains information related to the parameters and variables of the sample with defects. The expected response of the designed WPTECT in this study should follow the power transfer capability of the Tx-Rx WPT as defined by equation (3.24) and described by figure 4.2. Figure 4.2 shows the analytical results of the WPTECT model described by equation (3.23) using the experimental parameters and variables given in Table 1. The resonance, f0, is chosen to meet the condition for splitting resonance frequency by considering high-frequency sensitivity to surface crack, input and output characteristic impedance, and the measuring instrument's frequency range limitation. The lower coupling coefficient provided by the side-by-side arrangement of the Tx-Rx coils (figure 3.5(c)) cannot provide splitting frequency behaviour at

lower frequencies because of lower quality factors far below the WPT critical coupling factor [37, 270, 272, 277, 286].

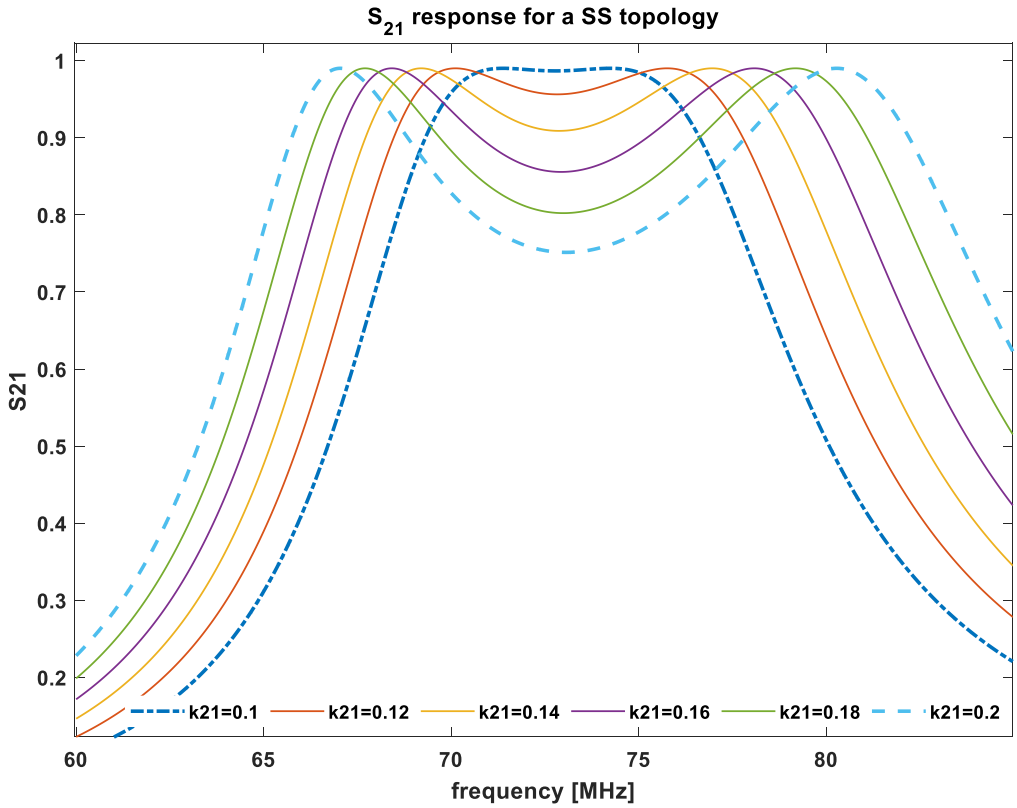

Figure 4.2 Response of SS WPTECT topology using the derived model (3.23) without metallic sample for various mutual coupling

4.3 Results and Discussion

The transfer response, S12, contained 1601 frequency points by 250 scan points each at an interval of 1mm distance. Figure 4.3 shows five plots of the selected scan-axis position for the transmission coefficient magnitude S12 (in dB) for scanning sample1 and sample2. The S12 shape depends on the type of material and its geometric parameters. The 'M' shape or double resonances have information of the Tx-Rx probe-samples system relationship (lift-off and geometry), defect shape and depths due to a wide range of frequencies, and material inhomogeneity [37, 265, 267, 286-288]. The S12 data recorded using the measuring instrument, VNA, is similar to S21 because the Tx and Rx magnetic resonance networks depicted in figure 3.2(d) are symmetrical and reciprocal; hence they are used interchangeably. The feature points, such as splitting frequencies around the resonance points and response shapes via multiple features through principal component analysis, are extracted, compared, discussed, and evaluated below.

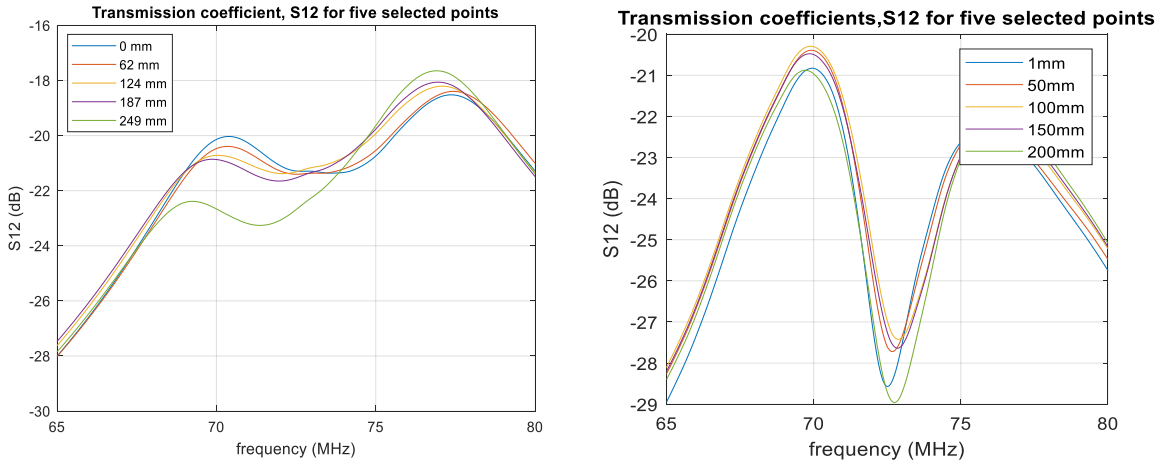

(a) S12 values for Sample 1 (b) S12 values for sample 2

Figure 4.3 S12 values for five selected scan distances

4.3.1 PCA feature extraction

Application of principal component analysis (PCA) to extract relevant features from WPTECT responses was investigated as an alternative to resonance frequency features extraction in the next section. PCA is one of the statistical tools that help extract principal components (dominant features) from a set of multivariable data. It gives the maximum amount of possible variance by projecting the data into a normalised subspace. The PCA application on the data reduces it to another set of features based on frequency points called principal components (PC). As seen from the flow chart of PCA computation in figure 4.4, data is reconstructed by subtracting column elements from their corresponding column mean values. The new data set are then used to compute the covariance matrix and eigenvalues. After computing the Eigen-signals from the eigenvalues, three of the most significant signals, PC1, PC2 and PC3, are chosen according to the highest variance eigenvalues.

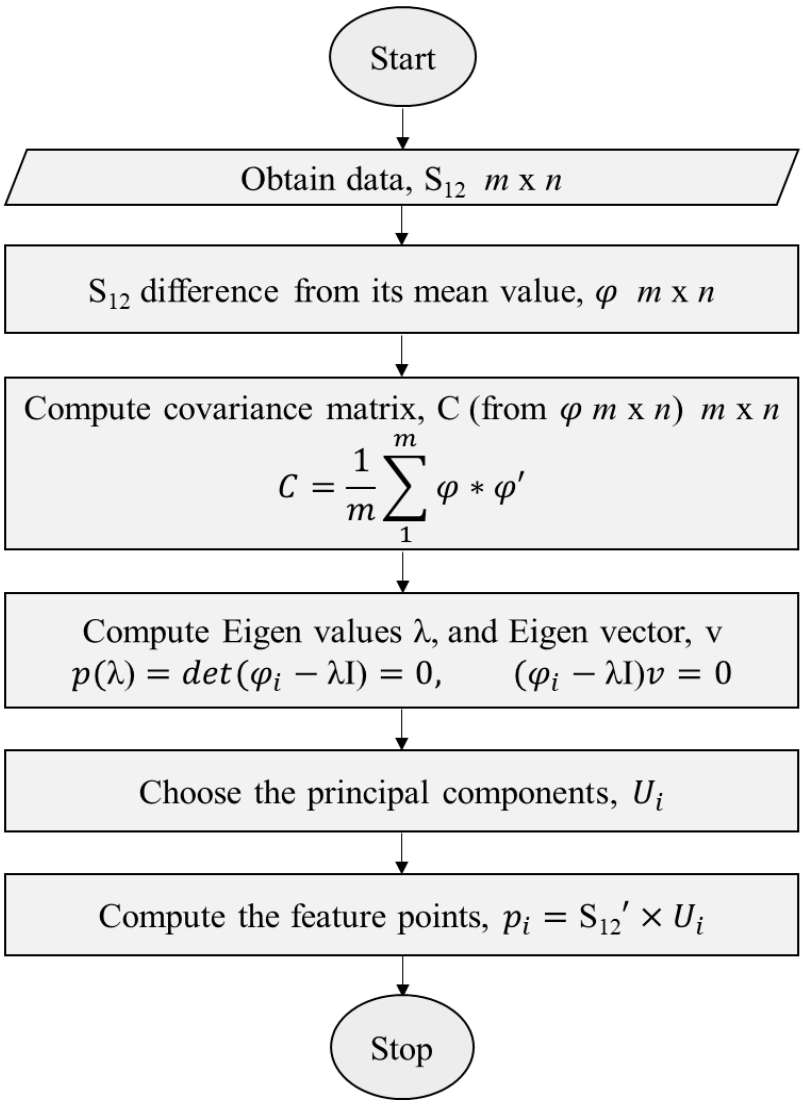

Figure 4.4 Flow chart of PCA computation

To evaluate the study of these coils configurations (Tx-Rx coils axially side-by-side) in scan mode, resultant data recorded in VNA were the various transmission coefficients (S12) for the whole sweeping frequency at every scan point. S12 values were the input training data to PCA for features extraction. PCA features are the principal components (PC) obtained as the Eigen signals from the highest variant Eigenvalues of the covariance matrix. The original data, S12, was then multiplied by each of the three selected PC to obtain the data projection via sample surface. The features projected by PCA based on the first three PC (PC1, PC2, and PC3) via sample surface are plotted in figures 4.5 and 4.6 for sample1 and sample2 evaluation. Where S1, S2, S3, and S4 areas show the slot area signals for each corresponding slot position.

The PC features projected via sample show a significant relationship with each slot parameter and their positions. Among the three selected PC with the highest variance, the second and third PCs from sample1 and sample2 inspection detected the slots as seen in figures

4.5 and 4.6, respectively. The PC2 and PC3 features detect the slot position relative to the Rx position and Tx position respectively along the scan-axis in each sample as seen in figure 3.5(c) Rx-Tx coil arrangement. Its magnitudes change significantly around each slot area towards three unique points; two maxima and one minimum. This phenomenon occurs in all the four slots for PC2 and PC3, as seen in figure 4.5 for sample1. The two edges of the extracted PCA features on slots signal response, PC2 and PC3, are not symmetric because of the varying depth for all the slots areas.

Similarly, figure 4.6 shows the variation of extracted PC values with visibility to only three slots by PC2 and PC3 due to the size of the Tx-Rx probe compared to slot widths. The first extracted PC, PC1 feature for sample1 and sample2, shows variations along the scan-axis, which are not correlated to slots position on the sample. Therefore, it reflects the first magnitude feature, which indicates neither slot width nor depth parameters information. This behaviour could be due to either unavoidable lift-off noise dominating the first resonance area in the response signal or instrumental error due to port1 of the VNA connection to the Tx unit.

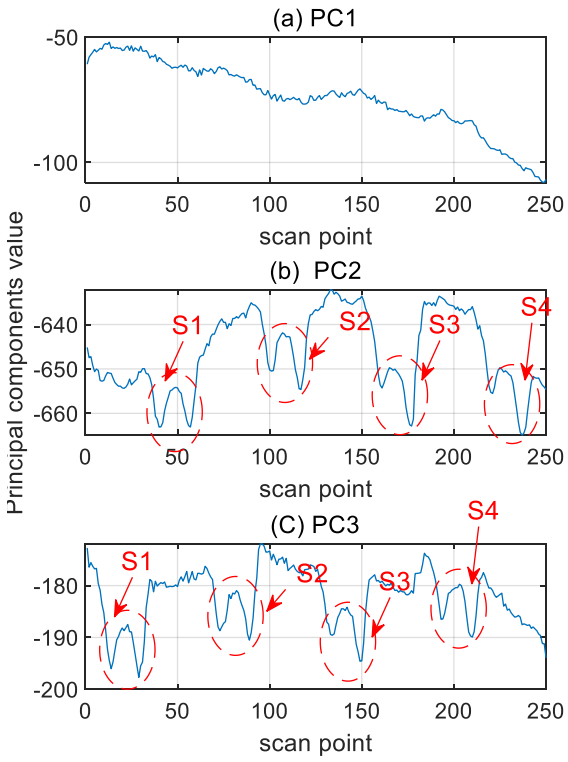

Figure 4.5 PCA features for depth parameter evaluation of sample1 slots

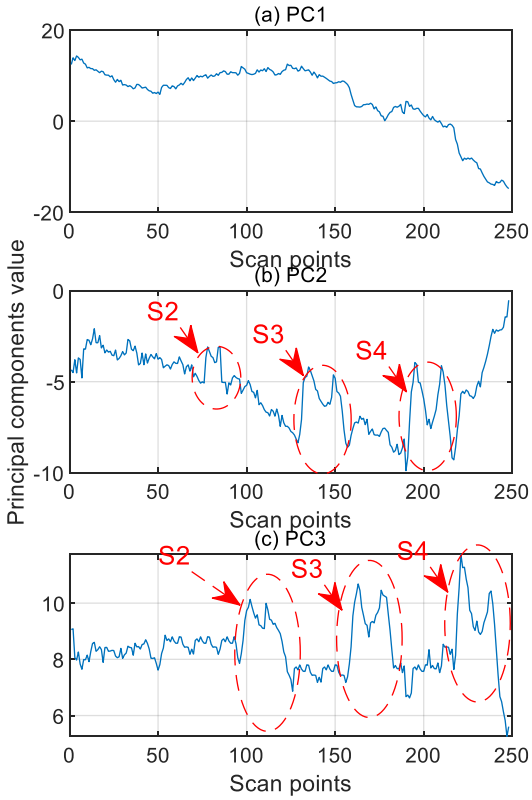

Figure 4.6 PCA features for width parameter evaluation of sample2 slots

4.3.2 Resonance Point Features Extraction

There are two resonance frequencies and their S12 magnitudes as four features used for defect analysis. All these features varied as the probe scanned the samples for slot and non-slot positions. MATLAB numerical simulation software is used to extract these features from the data at every scan point signal on the samples. The shifting position of feature points at different scanning points (249mm long) gave different frequency features and their S12 (dB) magnitude values.

Figure 4.7 shows the variation of frequency features along the scan-axis for slot and non-slot areas on the sample1 with different slot depths. Similarly, figure 4.8 shows that of sample2 with varying widths of the slot. The spatial position of first and second frequency features (f_1 and f_2) around the slot positions are due to the relative position between Rx and Tx on the sample, respectively. The two frequency features vary from the start scan point to the last scan point due to increased slot depth and width for sample1 and 2, respectively proportional to the eddy current density and perhaps lift-off influence. There is a significant feature variation for the slot parameters and their positions in every slot area. The frequency features increased to a peak value in figures 4.7 and 4.8 slot areas as the Rx and Tx coils approached the slot position. It also dropped to a minimum value at the slot centre and then raised to another peak value immediately as it passed the slot position. The frequencies of the two peak values depend on the slot depth, while their width depends on the slot width along the scan axis. These features variations are used in this study for slot quantification. The extracted features variation is due to mutual coupling between the Tx-Rx coils and each coil to the sample.

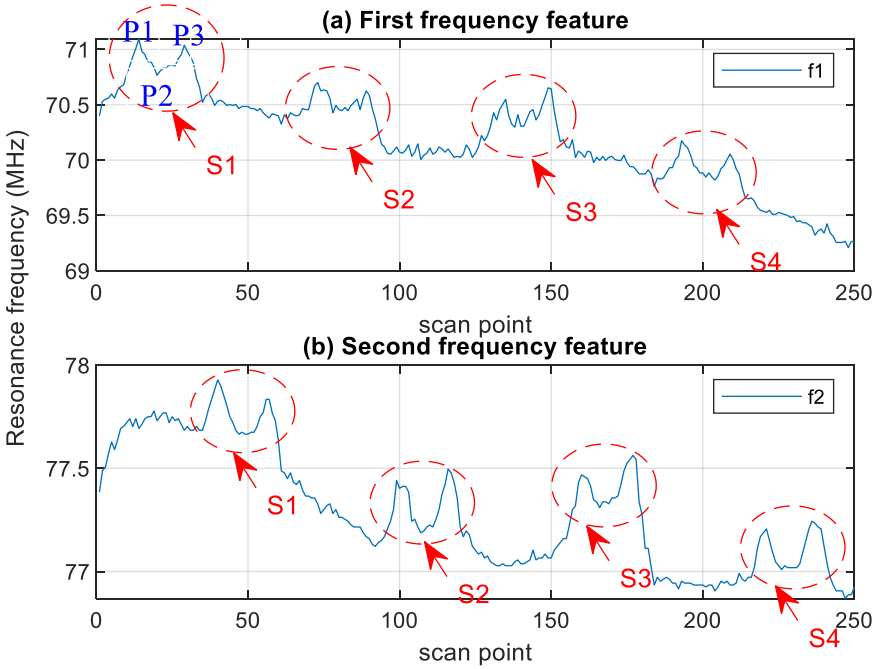

Figure 4.7 Sample1 frequency features

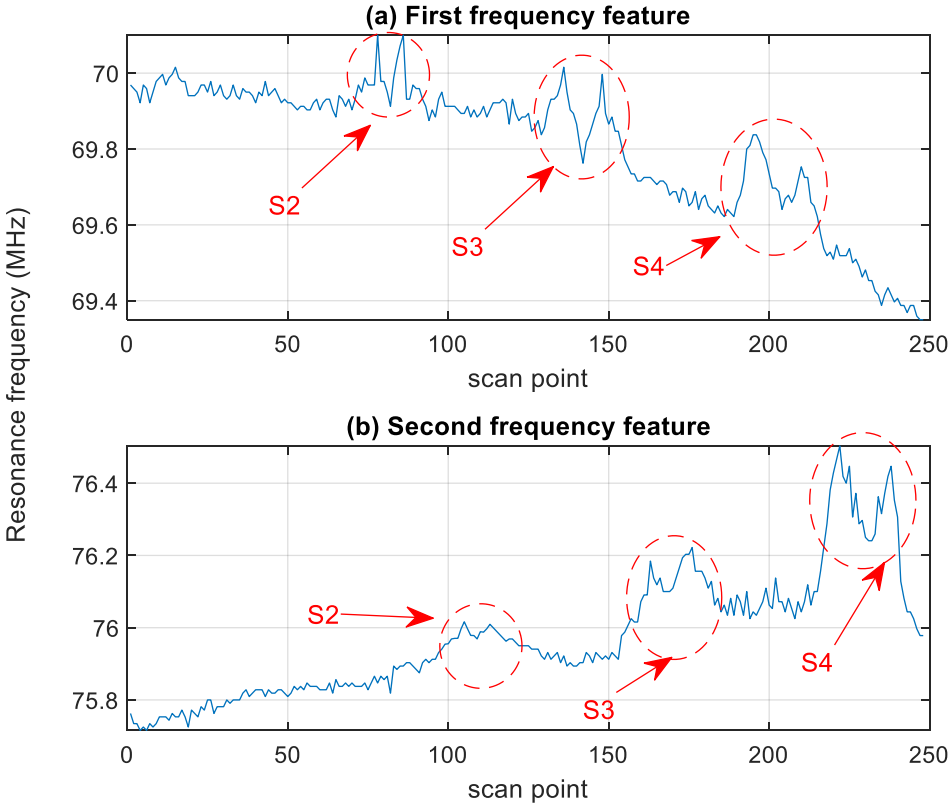

Figure 4.8 Sample2 frequency features

The magnitude features are the two-peak magnitudes of the transmission coefficients, S21 of extracted frequency features (f_1 and f_2). They were extracted from the S21 response of

scanning sample1 with different slot depths and sample2 with varying slot widths. Figures 4.9 and 4.10 show the two-peak magnitudes, first (m_1) and second (m_2) magnitude features variations along the scan-axis of sample1 and sample2, respectively. The feature shows a decreasing and increasing trend for the first and second magnitude features, respectively, from the beginning to the end of scanning. The sample1 first magnitude feature decreases from the start scan point to the last point by -2.4dB with negligible sensitivity to slot parameters, as seen in figure 4.9(a). Likewise, the second magnitude feature increases to the end of scan point by 1.01dB with considerable sensitivity to slot parameters as in figure 4.9(b). The second magnitude feature variation around the slot area is similar to that of the first frequency feature in figures 4.7(a) and 4.8(a). Figure 4.10 shows similar trends to that of figure 4.9, but with the first magnitude feature starting at -20.83dB and ending at -21.76dB. Similarly, the second magnitude feature starts from -22.2dB and ends at -21.73dB with negligible sensitivity to the first slot. The second magnitude feature from the S21 responses of scanning sample1 and sample2 detect the slots due to the change in conductivity around the slot, which alters the eddy current density in the slot vicinity.

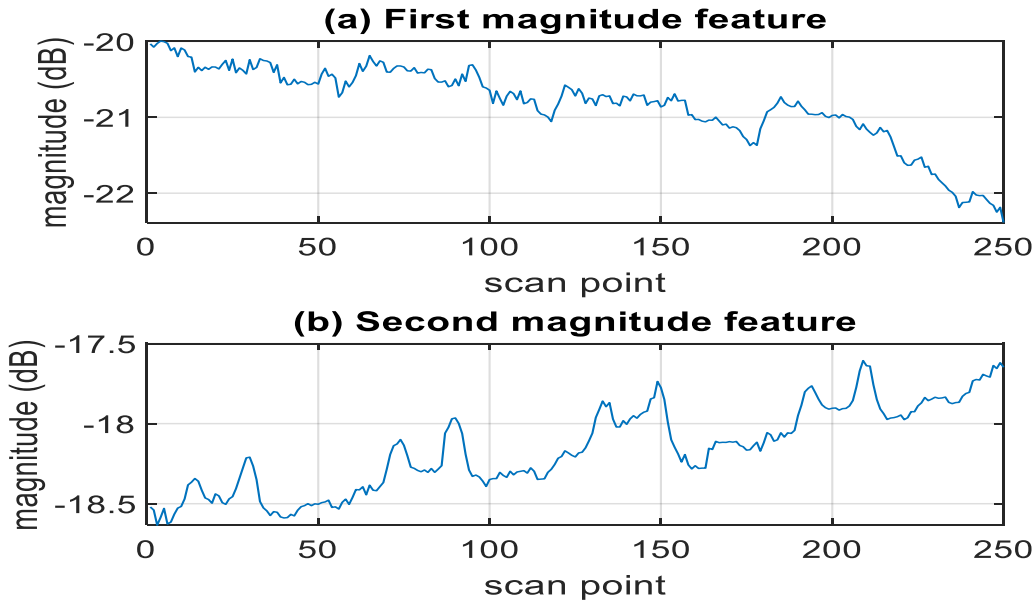

Figure 4.9 Sample1 magnitude features

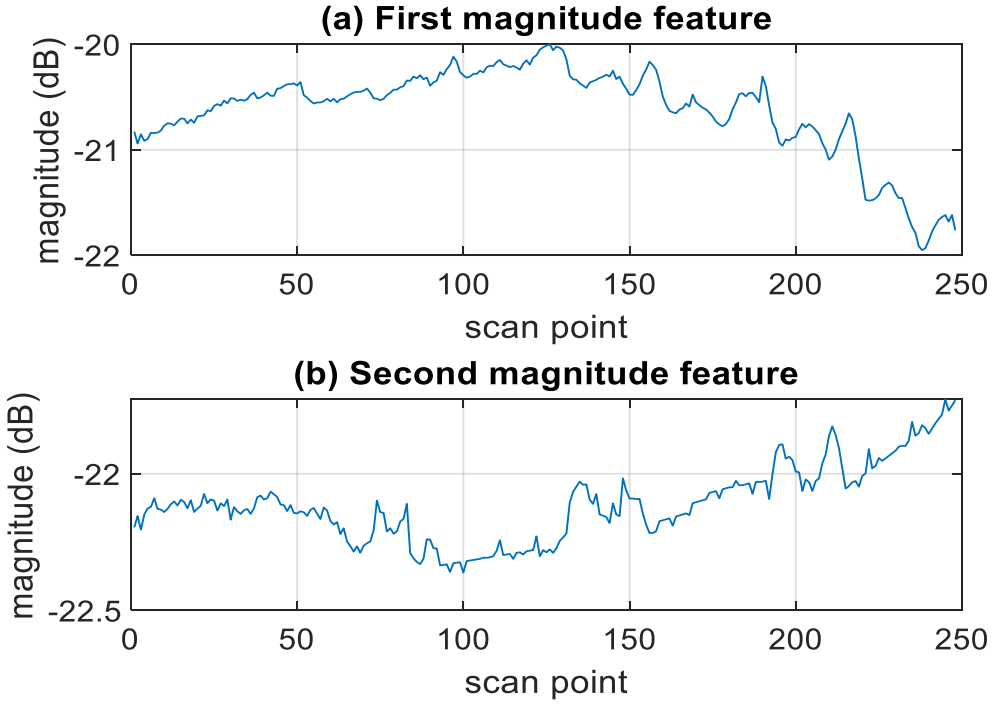

Figure 4.10 Sample2 magnitude features

The extracted features at the resonance points show meaningful information about slots and non-slot areas in the sample. Their behaviours for the slot area are used to map the slot parameters for quantitative non-destructive evaluation (QNDE) in the next section, discussing results.

4.3.3 Discussion of results

Eight different surface slots from the two samples were detected and characterised in this study. Sample1 has four surface slots along the scan-axis with 3.3mm equal widths and 2mm, 4mm, 6mm and 8mm as depths, respectively. The slots positions were at the 60, 120, 180 and 240mm distance on the sample. The second sample, sample2, also has four slots of 3mm equal depth but varying widths of 1mm, 2mm, 3mm, and 4mm serially. The four slots are equally spanned 60mm apart as in sample1. The point features are the two split frequencies and their S12 magnitude in decibel, whereas, for the PCA features, three PCs with the highest variants are selected and presented. The peak values for both the resonance points and PCA features around each slot correlate with the actual slot parameters for detection and quantification insight.

Figure 4.7 (a) presents three important feature points represented by P1, P2, and P3 as first, second, and third turning points, respectively. These points have similarly appeared in the

remaining slot areas, S2, S3, and S4, of all the remaining features with sensitivity to slot area. The extracted features on the scan-axis corresponding to the positions of Rx and Tx coils characterise the slots on sample1 and sample2. The middle point of the extracted features, P2 in each of the plotted slot signal features, corresponds to the actual position of the slot in the sample. The Rx coil position detected the slot centre by the P2 points in figures 4.5(c), 4.6(b), 4.7(a), 4.8(a), 4.9(b) and 4.10(b), which are at 22nd, 82nd, 142nd and 202nd scan points for S1, S2, S3, and S4 areas, respectively. Similarly, the Tx coil detected the slot position by p2 point, as seen in figures 4.5(b), 4.6(c), 4.7(b) and 4.8(b) at 49th, 109th, 169th, and 229th scan points for S1, S2, S3, and S4, respectively for both sample1 and sample2 investigation. P2 determines the actual slot location and distance between every two adjacent slots in the sample. The distance between P2 of each adjacent slot's feature signal is the same and equals 60mm for sample1 and sample2, which indicates the centre-to-centre distance between every two adjacent slots in the samples.

Table V Estimated slot widths using features from sample1 response

slot	Actual slot width (mm)	Features width estimation (P1 to P3)				
		Resonance point features width (mm)			PCA feature width (mm)	
		f1	f2	m2	PC2	PC3
S1	3.30	3.75	4.00	4.00	4.25	3.75
S2	3.30	4.00	4.25	4.00	4.00	4.00
S3	3.30	3.50	4.00	4.00	4.00	3.75
S4	3.30	4.00	3.75	3.75	4.00	4.25

The frequency at points P1 and P3 reach peak value compared to other scan axes around the slot area. The two peak points (P1 and P3) span before and after the slot along the scan axis. Their behaviour is due to the higher field generated by the eddy current at their position proportional to the slot width and depending on the feature response shape and Tx-Rx coil geometry. The slot width equals a quarter axial length from P1 to P3 in the slot signal of the extracted features. Table V gives the values of the slot width from the resonance point and PCA

features for sample1. The first frequency feature has a comparatively better width estimation based on the relative deviation of the estimated width from the actual one.

The same as previous widths estimation in sample1 applies to the slot widths estimation in sample2 investigation. Sample2 has four slots with various widths, each at equal 3mm depth. Previously, P1 to P3's width determines the slot width, as demonstrated and given in Table V. To quantify the slots in sample2, width estimation, Table VI compares actual slot width and various features widths estimation. From assessing various features width in sample2, three slots are presented in Table VI because the first slot with 1mm width has a negligible response due to the size of Tx-Rx coils and scan steps. Also, based on the width estimation, frequency features are surface parameters and have comparatively better width estimation capability.

Table VI Estimated slot widths using extracted features from sample2 response

Slot	Actual slot width (mm)	Features width estimation (P1 to P3)				
		Resonance point features width (mm)			PCA feature width (mm)	
		f1	f2	m2	PC2	PC3
S2	2.00	2.00	2.00	2.25	1.75	2.25
S3	3.00	3.25	3.25	3.25	3.50	3.25
S4	4.00	3.75	4.00	3.75	3.75	4.25

For the slot depth estimation, features extracted from scanning sample1 are evaluated and presented. Similar to the width information, the first magnitude and PC1 show no information related to the slot depths. Figure 4.11 shows the variation of the extracted features, P2 at the slot signal area, S1, S2, S3, and S4 from the extracted first and second frequencies, second magnitude, and PC2 and PC3 features. The results show that the higher the slot depth, the lower the frequencies features, and the higher the second magnitude and PCA features (PC3). The second PCA feature (PC2) in figure 4.11(d) has no correlation to depth information in this study, which could be due to the nature of the sample material and defect parameters. It can be seen that different features have a different correlation to slot depths. The slot depth relates to the dominant point around the slot, where eddy current density has a higher deviation. Also, the

first and second frequency features reflect slot depths, as expected from frequency penetration depth behaviour.

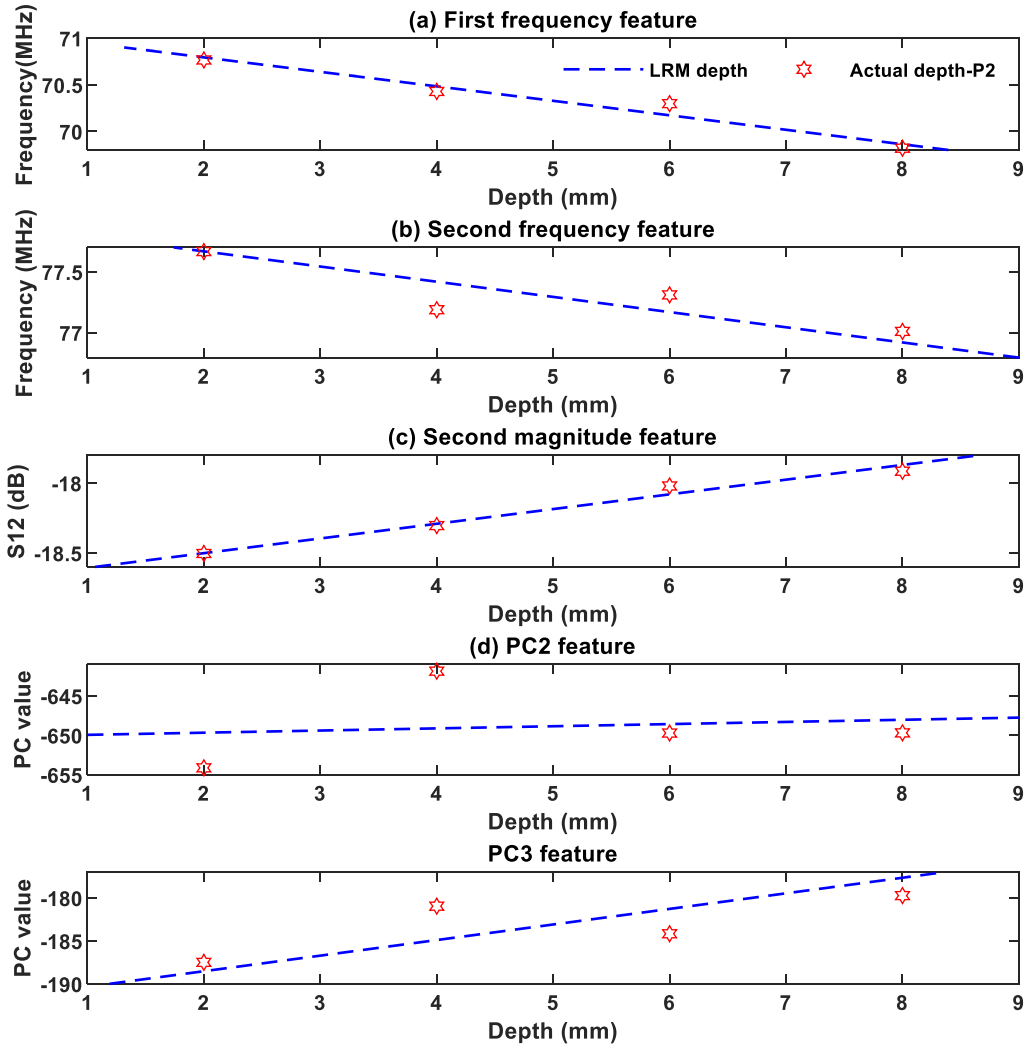

Figure 4.11 Feature comparison with slots depths

4.4 Chapter Summary

This chapter has achieved the first-time design, development and evaluation of WPTECT, in the history of ECT, as a prototype idea for sensing application. It investigated multiple features for slots detection and quantification experimentally using the WPT concept based on high-frequency ECT. Eight slots from two Aluminium samples were characterised and compared using the statistical principal component analysis (PCA) from the response shape feature and frequencies and magnitude from the multiple resonances' features. From the demonstrated features of the resonance frequency points and statistical approach, the results

have shown that each slot width along the scan-axis is proportional to the width of the two sides around the slot, where eddy-current density is highest. Also, the smaller the slot depth, the higher the frequency features and the lower the magnitude feature. From now, it has been demonstrated in this chapter that the WPT approach is a valuable platform for improving a Tx-Rx probe of ECT on comprehensive QNDE through multiple feature extraction and mapping to the slots parameters for scanning, including non-scanning NDT&E of metallic structures.

The evaluated results in this first WPTECT model are limited to artificial slots for QNDE sizing and location as a first studied concept idea tested in aluminium material. The coils of the investigated Tx-Rx probe in this study work on flat structures as it is rigid. Therefore, chapter 5 considers a flexible printed coils array as a magnetically-coupled resonant probe to reconstruct dent area due to natural corrosion and metal loss in the pipeline. It emphasises different feature extraction, selection and fusion for the complex metallic structure and tiny natural dent defects investigation at lower frequency because of the skin depth issue.

Chapter 5. WPT-Based ECT Using Flexible Printed Coils Array for Pipeline Inspections

5.1 Introduction

The previous chapter 4 study characterised artificial slots on aluminium material using the magnitude and frequency of the resonance characteristics and principal components analysis (PCA) features. However, the results were tested on flat aluminium material containing artificial cracks. Due to non-complex geometry problems and the absence of permeability issues in the flat aluminium bar, a new magnetically-coupled resonant WPT technology integrating flexible printed coils (FPC) array probe based on sweep frequency excitation is presented in section 3.4.2 of chapter 3 for inspecting curvature surface with a defect. Therefore, this chapter presents the results of section 3.4.2 methodology for overcoming the challenges of inspecting complex curved structures such as oil and gas pipelines mentioned in section 2.3.2 of the literature review. It extends the study to reconstruct a dented area due to natural corrosion and metal loss in a pipeline sample due to the advantages of the FPC array probe and evaluate features extraction, selection, comparison and fusion. Different from chapter 4, it uses parallel-parallel topology of magnetically-coupled resonant (WPTECT) using area mapping and axial scanning to assess natural defects (dent area) in a complex ferrous metal structure (pipeline). It includes the results and discussion of WPTECT system response, features extraction, comparison, selection, fusion and 3D defect reconstruction.

5.2 WPT-Based ECT Flexible Printed Tx-Rx Coils Array Probe

Recent progression of magnetically-coupled resonant wireless power transfer (WPT) and flexible printed devices exposed opportunities to address defect detection and reconstruction challenges under complex geometric situations. The WPT technology has maximum energy transfer and a constant efficiency over a certain distance range [256, 289], while the FPC array probe is adaptable to complex geometry for scanning and area mapping. The advantages of WPT-based ECT, including swept-frequency excitation for obtaining different depth information and defect parameter, are combined with those of the FPC array to test curved structures in this study. The configured magnetic resonance Tx-Rx FPC array probe consists of a single Tx coil encircling array of identical Rx coils for achieving curve area mapping at a single scan with constant lift-off distance for each Rx in the array.

The parallel-parallel (PP) topology of WPTECT depicted in figure 3.2(a) for a Tx coil and each Rx coil, provides higher sensitivity to metallic objects and less sensitivity to noise influence due to its larger input and output impedance at resonance [253]. Figure 5.1 shows the

equivalent circuit diagram of the PP, Tx-Rx, WPT system, including a metallic sample and an excitation voltage source (V), two coils as a receiver (Rx) and transmitter (Tx) and load resistance (R_L). I1, I2 and Is are the excitation current through Tx, Rx induced current due to field linkage and sample's induced-eddy-current, respectively. Similarly, R1, R2, and Rs are the Tx coil, Rx coil, and metallic sample resistances. L1, L2, and Ls are the Tx, Rx, and sample self-inductance, respectively. Also, C1 and C2 are the required compensated capacitors for Tx and Rx resonance to occur, respectively.

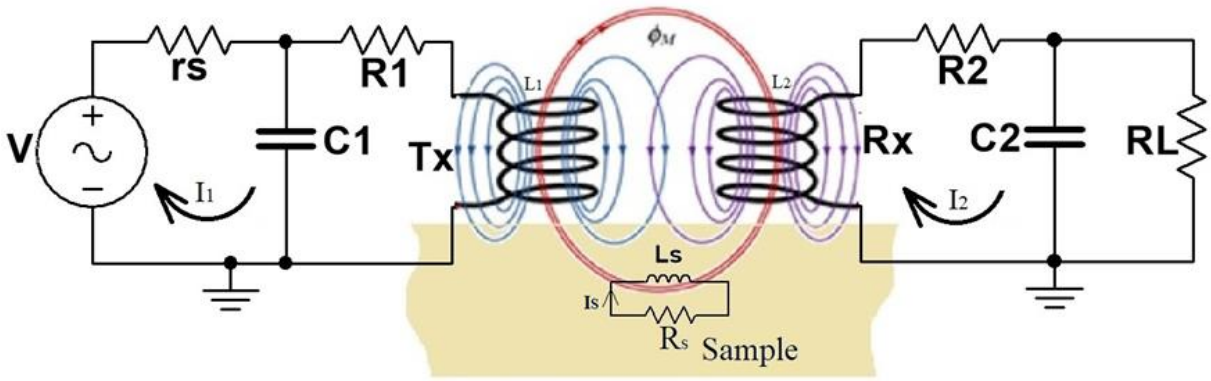

Figure 5.1 Equivalent circuit of Tx-Rx WPTECT and metallic sample

The resonance frequency (f_0) for the Tx and Rx circuits shown in figure 5.1 is considered to be equal for achieving a maximum power transfer efficiency and for the dual peak of S21 response to be symmetric about a resonance point. f_0 is theoretically derived by setting the imaginary part of the equivalent admittance of each Tx and Rx network to zero as a condition for the resonance to occur. The expression of the derived resonant frequencies is given in section 3.4.3 by equations (3.27), which applies to Tx and Rx resonance frequencies in this study.

From the WPTECT circuit loop KVL expression given by equation (3.13), the voltage ratio of the P-P topology is derived by substituting the transmitter and receiver circuit units' equivalent impedances, Z1 and Z2, as given by equations (5.1) and (5.2), respectively. The model of derived voltage ratio is given by equation (5.3) and substituted into equation (3.23), describing the S21 response of WPTECT. In equation (5.3), the mutual coupling between Tx and Rx, M_{12} is mathematically defined by an expression $K_{21}\sqrt{L_1L_2}$, also, r_s and R_L are the characteristic impedances of port1 and port2 of the VNA, respectively. The designed values of the Tx-Rx parameters, experimental parameters and variables given in Table II are considered for computing the numerical model of S21 provided by equation (5.4) as a function of the mutual coupling (K_{21}) between Tx-Rx.

$$Z_1 = r_s + \left(\frac{1}{j\omega C1}\right)//(R_1 + j\omega L_1) \tag{5.1}$$

$$Z_2 = (R_2 + j\omega L_2) + \left(\frac{1}{j\omega C2}\right)//R_L \tag{5.2}$$

$$\frac{V_{RL}(\omega)}{V(\omega)} = \frac{j\omega M_{12}\left(\left(\frac{1}{j\omega C2}\right)//R_L\right)}{\left(r_s + \left(\frac{1}{j\omega C1}\right)//(R_1 + j\omega L_1)\right)\left((R_2 + j\omega L_2) + \left(\frac{1}{j\omega C2}\right)//R_L\right) + (\omega M_{12})^2} \tag{5.3}$$

$$\therefore S_{21} = 2\frac{V_L(\omega)}{V(\omega)}\sqrt{\frac{r_s}{R_L}} = \frac{j4\pi f K_{21}\sqrt{L_1 L_2}\left(\left(\frac{1}{j\omega C2}\right)//R_L\right)}{Z_1 Z_2 + \left(2\pi f K_{21}\sqrt{L_1 L_2}\right)^2}\sqrt{\frac{r_s}{R_L}} \tag{5.4}$$

The S21 response depends on the frequency, Tx-Rx inductances for constant load and source impedance and coupling between Tx-Rx in the absence of a metallic sample as described by equation (5.4). Furthermore, the absolute values of the transmission coefficient, S21, over a specific range of frequency gives the frequency response behaviour of a Tx-Rx P-P topology of the WPT system to predict the experimental model's response to this study. However, the S21 response provides two (splitting) resonance frequencies, analytically and experimentally, at an over-coupled region of operation, similar to the S-S topology in chapter 4, which has been described by the behaviour of the WPT system [265, 270]. The over-coupled region occurred at the higher mutual coupling (K_{21}) between Tx and Rx coils, which depends on the distance between them and their parameters and the metallic sample influence. The influence of the metallic sample and its interaction with the Tx-Rx coils affects the mutual coupling between Tx and Rx, proportional to the sample geometry and parameters.

Figure 5.2(a) shows the S21 response of the analytical model for different coupling coefficients (K21) of the Tx-Rx P-P WPTECT topology to indicate the response to the mutual coupling between the Tx-Rx and the sample. The two peak points of the response, S21, increase due to an increase in the mutual coupling between Tx-Rx coils. The Tx and Rx mutual coupling indicate the Tx-Rx interaction with the metallic sample and defect similar to the response of the laboratory model (figure 5.2(b)) using the FPC coil array in this study. The frequency and magnitudes of the two peak points depend on the selected capacitors (C1 and C2) and Tx and Rx coils parameters, in addition to the mutual coupling. As discussed in [255], different topologies of magnetically-coupled resonant Tx-Rx systems can be designed and developed by selecting Tx-Rx suitable capacitors, C1 and C2, to control the frequency behaviour of the WPTECT system. The presence of metallic sample and defect (pipeline and dent area in this study) extracts more power from the transmitter proportionate to the eddy current losses in the

sample, which significantly impacts the system's parameters, especially for low-power applications [253, 285].

Figure 5.2(b) describes the normalised values for measured S21 of the 16 Rx channels at the first measurement point on the pipeline surface. The two resonances in the 'M' shape response are not symmetrical because the FPC array is configured (non-symmetric) as one excitation coil with multiple received coils illustrated in figure 3.6 and the probe parameters shown in Table II. In comparison with the analytical model response and considering a single Rx channel, the experimental transfer response (figure 5.2(b)) resembles the analytical model (figure 5.2(a)) for different Tx-Rx coupling factors. The Tx and Rx array's mutual couplings are only affected by the influence of the metallic sample within their coverage area. This chapter will demonstrate the results of the WPT-based ECT systems using FPC array, including area mapping and scanning on a curved sample and multiple feature extraction, selection, and fusion for dent area characterisation based on the implementation of described system design methods in Section 3.4.2.

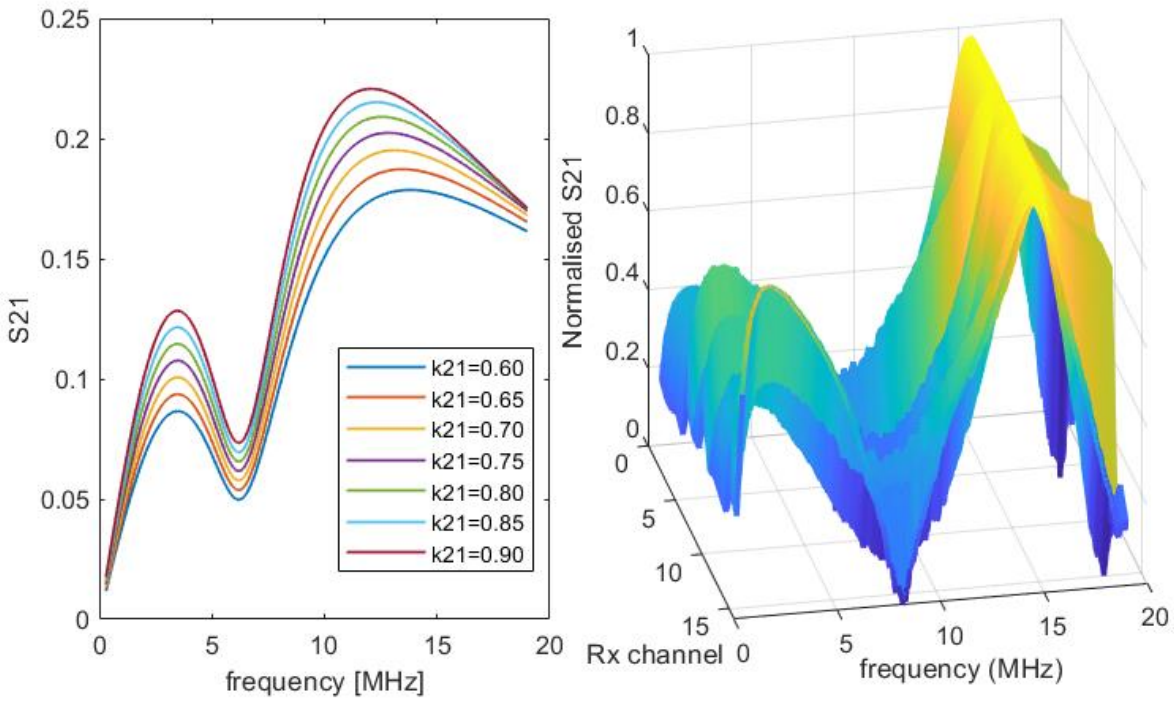

(a) (b)

Figure 5.2 WPT system transmission coefficient, S21 responses

(a) Tx-Rx WPT system response for different coupling factors (b) WPT based ECT System responses for 16 Rx channels at a specific sample point

5.3 Multiple Features Processing

The data for features extraction, selection and fusion for mapping defect parameters are obtained and investigated using various measurement point system responses, including the first point measurement shown in figure 5.2(b) for inspecting the dedicated cut pipeline sample with a natural dent. As mentioned in chapter 3, the actual depths of the inspected dent area in the pipeline sample is measured using a stylus profilometer for comparison with the extracted and fused features. The feature analysis and selection using cross-correlation analysis between the actual depths and extracted features are presented here. The section also evaluates and compare feature fusion using a deep learning approach and correlation method, including the single feature for best mapping to the actual depth of the dented area.

5.3.1 Multiple feature extraction

The first C-scan measurement point of the 16 Rxs channel (figure 5.2(b)) shows that the frequency responses (S21) with 'M' shape provides multiple variables and feature points, including lift-off information for mapping to defect parameters. Extended from multiple feature extraction of transient responses presented [25], four features are extracted and investigated from the frequency responses, S21, including the peak values of the two resonance peak points (M1 and M2) and principal component analysis (PCA). The PCA is applied to each Rx dataset by subtracting each observation element from its corresponding average value and forming a covariance matrix. Then, the Eigen-signals are computed from the eigenvalues, and the most significant signals are chosen according to the highest eigenvalues. The projection to spatial points of the chosen Eigen-signals are the extracted PCA features. The first PCA feature is applied for the two resonances. The two PCA features are PC_{11} and PC_{21}, characterising the 'shape' of the two resonance responses. The extracted features from the peak response point at a surface point on the sample were first normalised to a range of [0,1] and then subtracted from its corresponding extracted features of a non-defect presented in figure 5.2(b) to remove the influence of signal noise and other inherent disturbances. The four features profile can be visualised and compared with the dent profile measured by a stylus profilometer.

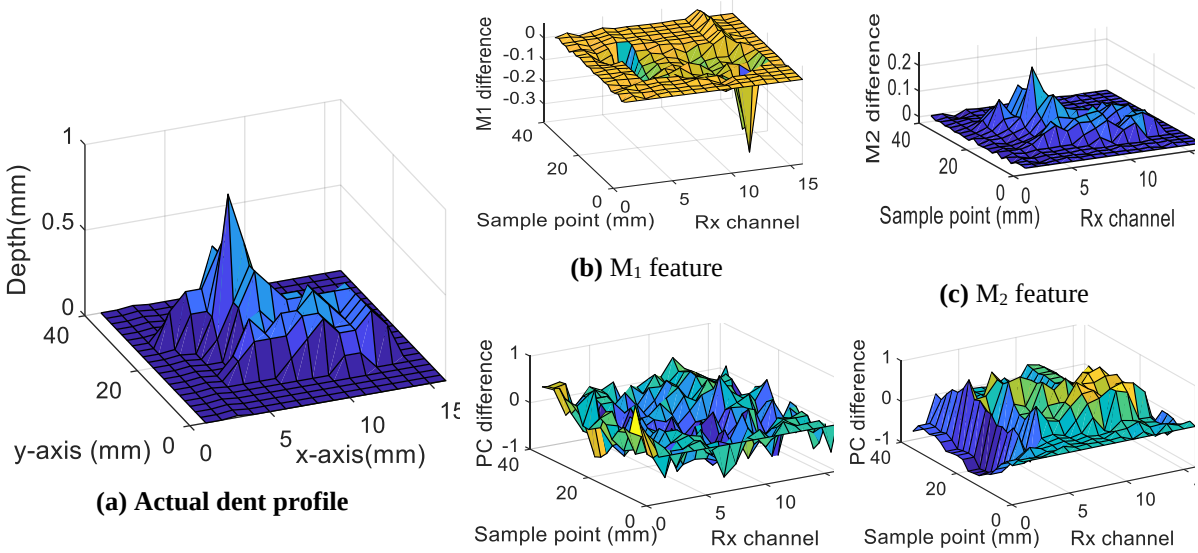

(a) Actual dent profile

(b) M_1 feature

(c) M_2 feature

(d) PC_{11} PCA feature

(e) PC_{21} PCA feature

Figure 5.3 Actual dent profile and extracted features

(a) Dent measured profile (b) M_1 feature of the (first) peak value of Tx resonance (c) M_2 feature of the (second) peak value of Rx resonance (d) PC_{11} PCA feature of (first) Tx resonance, principal component & (e) PC_{21} PCA feature of (first) Rx (second) resonance

Figure 5.3(a) illustrates the dent depth profile against the curvature surface. The 3D plots in figure 5.3 use measurement positions of array spaces and C-scan as Rx channel and sample position in line with the x and y-axis of the measured dent profile. In contrast, the extracted features in figure 5.3(b)-(e) illustrates the M_1 feature of the peak values of Tx resonance (first resonance), M_2 feature of the peak values of Rx resonance (second resonance), PC_{11} PCA feature of Tx resonance principal component (first), and PC_{21} PCA feature of Rx (second) resonance, respectively. Different features show different contours and correlations with the actual depths of the dented area. The M_1 is negatively correlated to the actual depth of the dented area as it shows decreasing behaviour toward the dented area points. The M_2 feature is positively correlated to the depth of the dented area as detected by Rx coils. The increasing behaviour of M_2 towards the depth of the dented area is similar to the finding by single resonance ECT for crack depth evaluation [28, 189]. Different features behaviours relate to individual Tx and Rx responses towards the dented area as depicted by the dual peak of the "M" shape response. Therefore, different features have different characteristics with depth, and different feature extraction has a different reflection of defect characters. None of the extracted features reflects the defect contour with good correlation.

The whole responses of the features to the dented area are attributed to the very-low inductances and high self-resistances of the Tx and every Rx coil under different frequency

operations as described in Table II. A comparison of different feature correlations with defect depths for feature analysis, feature selection and feature fusion using correlation and deep learning methods for defect mapping are investigated in the following subsections.

5.3.2 Feature analysis and selection for defect depth

The extracted multiple features have different characters of the defect depths, as illustrated in figure 5.3. The relevant features for defect depth information need to be selected and fused for 3D defect mapping and reconstruction. The correlation method is used for the multiple feature analysis and selection. The correlation coefficients for a set of features at every measurement point measure its relevancy to the actual depth parameter. The cross-correlation between real depths of the dented area, along the x-axis (Rx array direction) and the extracted features at every measurement point (y-axis), was evaluated. Figure 5.4 shows the correlation coefficients between an array of the extracted feature, each with its dedicated depths at each measurement point. A correlation coefficient of ± 1 indicates a perfect degree of features correlation with the defect parameter, as seen from figure 5.4. The positive correlation by M_2 and PC_{21} and negative one by M_1 features were due to the behaviour of the WPT system's dual response toward the two peak resonance values and overall response shape, as shown in figure 5.2(b). The first resonance peak M_1 decreases while the second peak M_2 increases as the distance to the dent decrease, which is caused by decreasing mutual coupling between Tx-Rx coils, as seen in figures 5.3(b) and (c). However, PC_{11} has the lowest correlation, whereas the second magnitude M_2 has the highest correlation coefficient with the defect depth due to the Rx response with the sample and defect. The correlation analysis can be applied to a single feature analysis, but it lacks the freedom of feature selection for the optimal application of quantitative non-destructive evaluation (QNDE) of the defect. Furthermore, it is understandable, one single Tx excitation and multiple Rx illustrates location information during NDT&E without scanning. For the use of multiple features, correlation-based and deep learning-based feature fusions are applied and compared in this study, in addition to the application of the single feature.

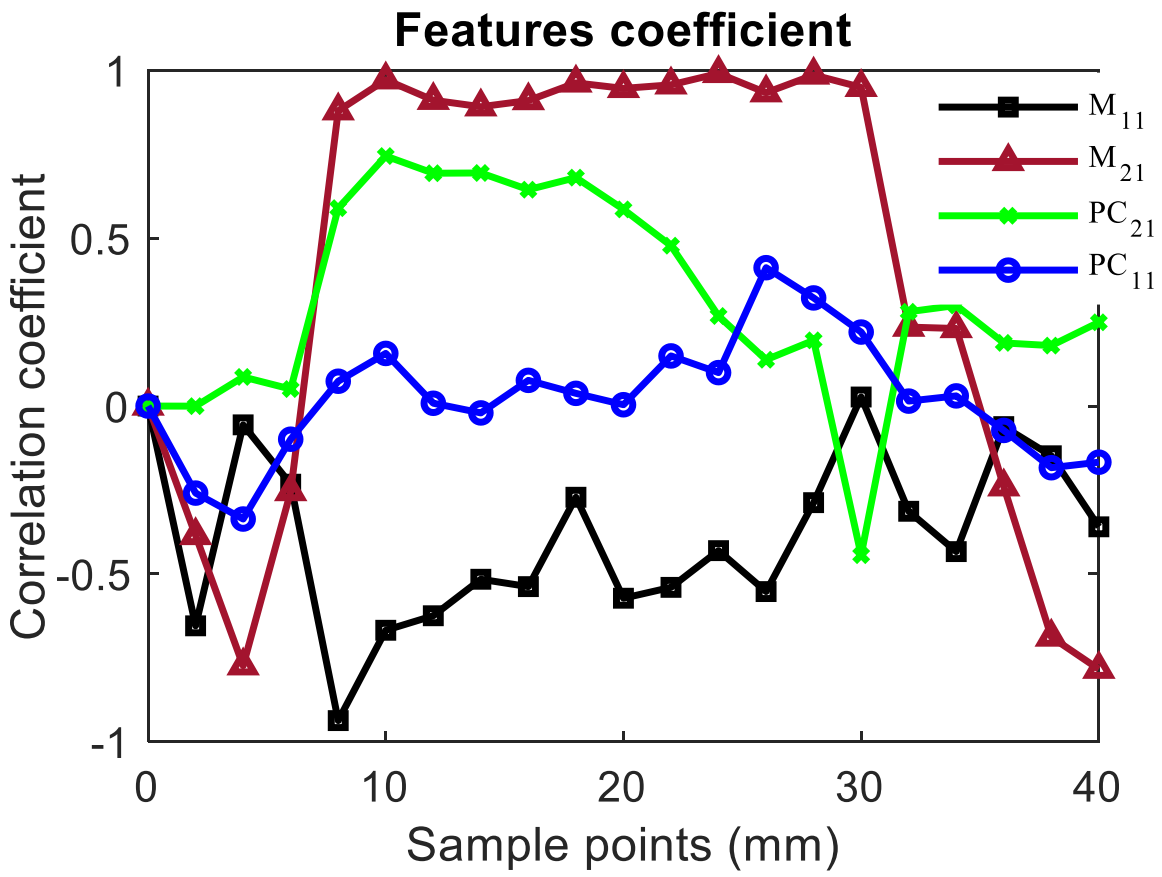

Figure 5.4 Features correlation with the sample dent depths for all measurement points

5.3.3 Feature fusion for defect depth and 3D mapping

In this section, two feature fusion approaches, deep learning-based fusion and Canonical correlation analysis (CCA) based fusion, are utilised to strengthen the WPT-based ECT's capability for mapping the defect area. The quantitative analysis of different feature extractions and fusion strategies are conducted in terms of R-Squared (R^2) value and mean square error (MSE) values between defect parameters and features. R-Squared is a statistical measure of data fit that indicates the proportion of the variation of dependent variables described by the independent variables in a regression model, whereas the MSE represents how close a regression line is to a set of points.

This study applied the two-layer feed-forward deep learning network to build the learning model between features and defect depths to implement the deep learning-based feature fusion of the four extracted features for defect 3D mapping. The first 50% of the features and actual depths data served as training; the rest 50% is used for validation using the trained neural network model. Four features, each with the same dimension $F_{16\times21}$ were reshaped to 1D signal $F_{1\times336}$. Thus, the whole feature set is $F_{4\times336}$ serves as input for the network. The target to train the model is real defect depth parameters with the same dimension of 1×336. The model used

a Levenberg-Marquardt technique for optimising network structure at different iterations. The MSE of the training set is lower than 0.001, and that of the testing and validation set is lower than 0.01, which indicates that the model can well describe the relationship between four features and the defect depths. After validation of the deep learning model, the whole four features set, M_1, M_2, PC_{11}, and PC_{21}, are fused by the model, mapping the 3D profile of the defect shown in figure 5.5(b).

The features fusion was also realised using multiway Canonical Correlation Analysis (CCA) to validate the deep learning techniques' capability for feature fusion. The multiway CCA [290] is an extension of CCA [291] that solves the features fusion problem by permitting multiple subjects' data to be fused in such a way as to extract components common to all. It forms a linear combination from both datasets for maximising an individual variable's weight and effectiveness of the parameter set as a whole. The detailed implementation of the multiway CCA was explained in [290-293] for evaluating the multiway correlation between a linear combination of different extracted features. In this study, the CCA weighted factors were calculated between defect depths and individual feature sets according to [290]. Then, each feature set is multiplied by the weighted factors and summed together to obtain the CCA fusion feature.

It is observed that the actual defect profile illustrated in figure 5.5(a) has a good agreement with fused features by the deep-learning technique and multiway CCA in figure 5.5(b) and (c), respectively. There are minor differences shown in non-defect areas. However, the goodness-of-fit for the defect and non-defect areas can be quantitatively determined. To quantitively evaluate the fused features' capability for mapping the defect areas, the R^2 value, which is the square of the correlation between the defect parameters and the fused features, and mean-squared-error (MSE), which states the closeness of a regression line to the actual defect depth, are used for different feature sets. The computed R^2 value and MSE are given in Table VII.

It is shown in Table VII, the fused features by deep learning network have the highest R^2 value and lowest MSE value, proving it is the best feature for mapping the defect using a WPT-based ECPT system. The CCA fusion feature shows reasonable R^2 and MSE value compared to single features. Thus, it is well understood that fusion features, including deep learning and CCA, can merge the behaviour of sub-features and show their capability for defect mapping and reconstruction. Besides the fused features, M_2 (second resonant magnitude) also has a 0.9104 R^2 value and 0.0016 MSE value, indicating that the system's frequency band 14.5MHz-16.0MHz are more sensitive to surface dent. PC_{11}, PC_{21}, from the two resonance, can also illustrate Rx resonance has better depth responses than Tx resonance as resonance peak values.

The fusion of multiple features with different weightings by using deep learning and correlation methods have better performance of depth estimation than a single feature in terms of R^2 value and MSE. The deep learning method for the multiple feature fusion has the best performance of depth prediction.

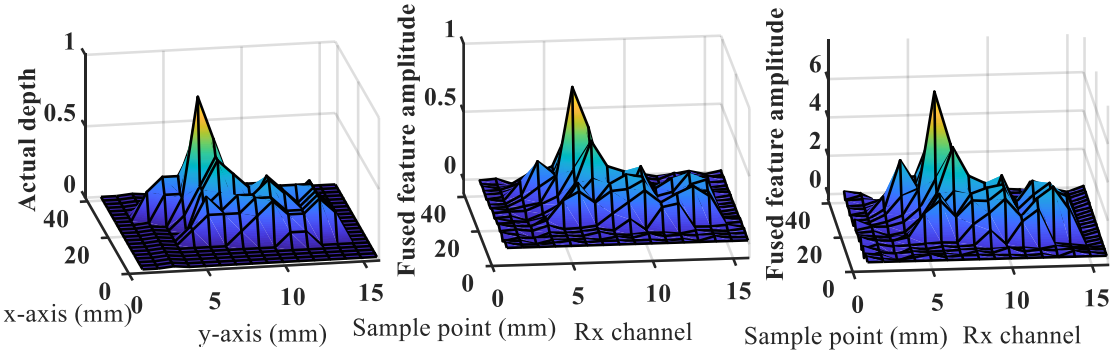

(a) (b) (c)

Figure 5.5 Fused features mapping to depths at different measurement points

(a) Dent measurement profile, (b) fused feature by deep learning, (c) fused feature by CCA

Table VII R-squared and MSE values for comparison of extracted and fused features

Features for characterisation of defect depths	R^2	Mean square error (MSE)
Deep learning-based feature fusion	0.9253	0.0013
CCA-based feature fusion	0.9171	0.0015
M_1	0.2755	0.0143
M_2	0.9104	0.0016
PC_{11}	0.2690	0.0135
PC_{21}	0.4318	0.0147

5.4 Chapter Summary

This chapter contributed to an experimental system of wireless power transfer-based eddy current testing using a flexible printed coils array made up of a single Tx coil encircles an array of Rx coils. It has demonstrated its feasibility for NDT&E of curvature surfaces such as oil and gas pipelines. The proposed flexible probe contributes to ECT on complex structures, where scanning is impossible for area mapping. The study's aim in this chapter has achieved by integrating magnetically-coupled resonant wireless power transfer (WPT) and flexible coils array for eddy current testing of a pipeline sample containing a surface dented area due to metal loss and natural corrosion. The dual resonance response S21 of the integrated system has been investigated in this chapter for multiple feature extraction, selection, fusion, and mapping for a

3D defect reconstruction and characterisation. The extracted features correlation analysis shows that the second resonance peak values feature has the highest correlation with the dented area's depth profile and has the highest R-squared value and lowest mean square error for the single features. It explained that the FPC array has one excitation coil (Tx) and multiple received coils (Rxs) with the second resonances, from Rxs, having better local information. It also demonstrates the Rx resonance unit's capability for responding to eddy current losses in the sample and defect compared to the Tx resonance unit. Also, the deep-learning-based feature fusion has surpassed the multiway canonical correlation analysis in the feature fusion for the 3D reconstruction of the dent, as the former has the highest R-squared value and lowest mean square error.

The results in this study are only specified to the depths of surface dent-area characterisation of complex metallic structures inspection, pipeline sample. Based on the multiple feature extraction and fusion for defect mapping, further optimisation of comparison of topologies of WPTECT system including a selection of WPT topologies, coils and capacitance parameters, their equivalent quality factors [255, 262] and their performance for sensitivity and functionality of quantitative NDT&E are given in the next chapter. In the next chapter, different resonance networks or components of WPTECT topologies are optimised in terms of multiple resonance capability, feature selection and comparison to achieve optimal NDT&E. The next chapter also extends to different types of defects and their parametric estimation like rolling contact fatigue (RCF).

Chapter 6. Optimisation of WPT-Based ECT Apply to RCF Cracks

6.1 Introduction

The results of the previous Magnetically-Coupled Resonant Wireless Power Transfer (WPT)-based ECT (WPTECT) studies provided the design concept, quantified slots' depths and widths and reconstructed dented area due to natural corrosion through multiple feature extraction, selection, and fusion [23, 24]. In the previous studies, chapters 4 and 5, each implemented study is based on a single WPTECT topology, though different topologies have different frequency responses depending on reactive compensation arrangement. Furthermore, magnetic permeability affects the ECT frequency response in ferrous material, especially at a closer lift-off distance, leading to extracted features' distortion proportionate to lift-off distance [217]. Previously, the influence of lift-off and material permeability around the crack area has not been considered by the WPTECT studies. Thus, to avoid the effect, a probe lift-off assessment needs to be conducted for quantitative non-destructive evaluation of rail lines, pipeline structures, turbine blades, and so on. Therefore, the results in this chapter extend the study, aims to optimise WPTECT topologies and characterise inclined angular RCF crack parameters in a rail-line material using an optimised topology.

This chapter presents the results and discussion of the five different WPTECT topologies designed and developed in section 3.4.3 of chapter 3, research methodology. Also, it includes the results of an optimised topology for quantitative investigation of the entire parameters of inclined angular RCF cracks in a railway material. The chapter ends with further discussions of results contribution, achievements and conclusion.

6.2 MCR-WPTECT Topologies Insight

Notably, multiple feature points are one of the unique attributes of each WPTECT topologies compared to other ECT in addition to efficient energy transfer. However, the splitting frequency behaviour, which provides multiple feature points, occurs in the voltage ratio and output power at a higher coupling coefficient [267], depending on the source and load resistances and coil quality factor. The response of such WPTECT topologies' capabilities is presented in this subsection based on different basic topologies and the advanced topology of WPTECT.

6.2.1 Basic topologies of MCR-WPTECT

Section 3.3 of chapter 3 has described the circuits of the four basic topologies of WPTECT considered in this results presentation, including the results of investigated topologies presented

in chapters 4 and 5. The results in chapter 4 investigated the designed and developed series topology for multiple resonances response to characterised cracks parameters on Aluminium samples as a first designed model for WPTECT in the history of ECT methods [24]. Furthermore, the results of parallel topology have been presented in chapter 5 for multiple feature extraction, selection, and fusion to characterise and map the 3D natural dent-area due to metal loss and corrosion on a pipeline sample [23]. The WPT series compensation topology provides low input and output impedance for a maximum current at resonance, which leads to maximum field generation. In contrast, the parallel topology compensation provides a higher efficiency transfer response to metal and defects with less sensitivity to noise influence due to its current source nature and higher input and out impedance at the resonance point [253]. However, the four basic WPTECT topologies (figure 3.2) have distinct performance and quality factors, constraining an individual topology's frequency response [261]. Therefore, the results in this chapter give an insight into the four basic topologies of WPTECT and help in assessing an optimal topology for enhancing the response and sensitivity to other defect parameters.

However, to offer multiple resonances at reduced Tx-Rx and sample coupling, the Tx coil consumes a high reactive power for the configured basic topologies (figure 3.2) due to reduced Tx-Rx and sample coupling. Consequently, the Tx parallel capacitor suffers from a higher voltage, while the series suffers from a higher current, delivering the required reactive power [280]. Subsequently, the Rx parallel capacitor requires a small Tx current to generate a high current in the resonant coil, leading to high-performance switches' requirements due to higher resonant voltage than Tx. In contrast, the Rx series capacitor requires a larger Tx current, which leads to low efficiency due to high Tx coil loss. Hence, the load and source impedances contribute to controlling the current consumption in the Tx and Rx coils, respectively, and their resonance behaviour, including the splitting frequency attribute. Therefore, it is not practically wise to consistently implement series or parallel topologies for the Tx coil, as they depend on the behaviour of specific application requirements [35]. The application requirement may include instrumentation input (source) and output (load) impedance matching, range of frequency of operation, coil quality factor, coupling between Tx-Rx and sample, and so on, as they determine the nature of WPTECT frequency and time responses.

6.2.2 Advanced WPTECT topology

However, a combination of series and parallel compensation (figure 3.9), called hybrid topology, might harness the advantage of both topologies for sensing application. The advantage of hybrid topology over basic topologies is reducing the effective reactance of Tx

coil by the series reactance (Xb) and reducing the stress on parallel reactance (Xa) as its only supplies a section of total reactive power to maintain the oscillation [280]. The hybrid topology acts as a resonance compensation and impedance matching at the same time. Therefore, this study applies a combination of series and parallel capacitors compensation to each Tx and Rx network, as presented in figure 3.9 of section 3.4.3 and represented in figure 6.1(a) Parallel/Series-Parallel/Series (PS-PS) WPTECT hybrid circuit diagram.

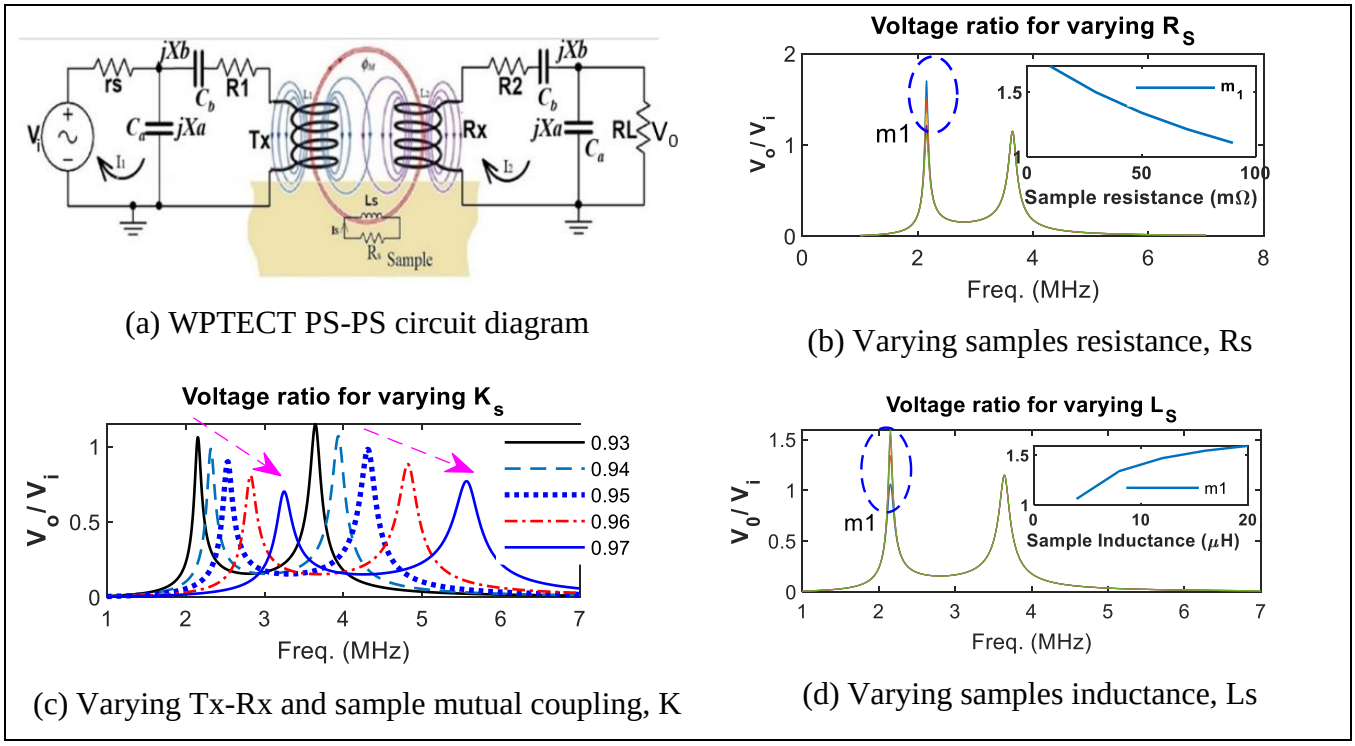

(a) WPTECT PS-PS circuit diagram

(b) Varying samples resistance, Rs

(c) Varying Tx-Rx and sample mutual coupling, K

(d) Varying samples inductance, Ls

Figure 6.1 PS-PS topology of WPTECT and LTSpice analysis of ac sweep voltage transfer ratio. The circuit is like SS topology if Ca =0 & Cb>0; else, PP topology if Ca >0 and Cb=∞.

Figure 6.1(a) shows the hybrid topology, a combination of SS and PP topologies. The two coils, Tx and Rx inductors, coupled inductively with the inductance Ls of the metallic sample equivalent circuit, including its resistance Rs and the eddy current Is. It has a unique attribute when $jXb < jXa$; more current passes through the Tx coil, and more voltage induces to the Rx coil. Otherwise, less voltage induces to the Rx coil. The circuit model is described numerically by the same model in chapter 3. The three loops in the circuit: Tx excitation current, Rx induced-current, and the sample induced-eddy-current are described in chapter 3 and represented by equations (3.13) and (3.14), where M_{12}, M_{1s}, and M_{2s} are the mutual inductances for Tx-Rx, Tx-sample, and Rx-sample, respectively. The impedances of the transmitter (Z_1) and receiver (Z_2) are, respectively, given by equations (6.1) and (6.2). By evaluating equation (3.14) in the absence of the metal sample, that is $M_{1s} = M_{2s} = 0$, the ratio of voltage across the load

resistance, RL (V_{RL}) to that of the source voltage (V) can be derived as the expression given by equation (6.3).

$$Z_1 = r_s + \left(\frac{1}{j\omega Ca}\right) // \left(\left(\frac{1}{j\omega Cb}\right) + R_1 + j\omega L_1\right) \tag{6.1}$$

$$Z_2 = \left(R_2 + j\omega L_2 + \left(\frac{1}{j\omega Cb}\right)\right) + \left(\frac{1}{j\omega Ca}\right) // R_L \tag{6.2}$$

$$\frac{V_{RL}}{V} = \frac{-j\omega M_{12} \cdot \left(\left(\frac{1}{j\omega Ca}\right) // R_L\right)}{(Z_1 Z_2 + (\omega M_{12})^2)} \tag{6.3}$$

To evaluate the frequency response of the circuit model in figure 1(a), LTSpice simulates the behaviour of the circuit model using ac sweep analysis by varying Rs, Ls, and coupling between Tx-Rx probe and sample (K_S). This variation depends on the defect parameters and sample geometry in addition to the type of material. Figure 6.1(b) - (d) show the voltage ratio of the WPTECT circuit, providing multiple feature points that respond to the variation of sample parameters. The response has shown that the first peek (m1) of the dual response is more affected by the variation of Rs and Ls, as seen in figure 6.1(b) and (d), which is due to the extra power supply by the Tx coil to compensate for the eddy current losses [253]. The inset figure 6.1(b) and (d) indicate conductivity and permeability variation due to variation of crack parameter, described by decreasing and increasing behaviour of the m1 feature resulting from increasing Rs and Ls, respectively. In addition, the variation of K_S affects both the magnitudes and frequencies of the dual-peak response, as seen in figure 6.1(c). Therefore, the impact of the defect on the response depends on a specific parameter, as conductivity and permeability effect are the consequences of all defect parameters variation. However, the lift-off effect contributes to the K_S, which shifts the magnitudes and frequencies of the dual peak response (figure 6.1(c)). The response of the circuit simulation described in figure 6.1(b) to (d) show that the voltage ratio of the WPTECT circuit can provide multiple features that respond to the variation of sample parameters. In addition to the source and load resistances, the voltage ratio described the scattering parameter, S21, given by equation (3.23) in chapter 3.

Because of the skin depth problem, the scattering parameter (S21) better perceives measuring signal integrity at high frequency. This study's S21 response depends on the measurement instrument's frequency, sample, and defect parameters at constant source and load resistance. The S21 multiple peak response of WPTECT for a given range of frequency depends

on the topology's input and output matching requirement in addition to the Tx-Rx coils parameters and their coupling condition to the sample. To assess the extent to which these pieces of evidence influence S21 response, this study designed and developed the five (basic and PS-PS) WPTECT topologies. And the chapter presents the results of their topologies response and feature optimisation and quantitatively investigate the RCF cracks in a railway material amidst different other parameters by an optimised topology.

6.3 Optimisation of WPTECT Topologies

The potential of WPTECT topologies responding with multiple resonances for multiple feature points from different topologies of magnetically-coupled resonant WPTECT probes depends on a certain critical coupling point. The critical coupling point is a function of inductive mutual coupling, load and source resistance and frequency of operation, which determine the topology's quality factor [276]. These factors are considered from the experimental set-up parameters such as the measuring instrument's characteristic impedance and frequency range. The parameters and variables of the configured Tx-Rx probe influence the splitting frequency of the WPTECT transfer response. However, the characteristic impedances of port1 and port2 of the measuring instrument, Vector network analyser (VNA) are the load and source impedance of the Tx-Rx WPTECT probe and cannot be optimised since they are constant. The mutual coupling of the Tx-Rx coils must be maintained as constant to avoid variation of coils gap and lift-off issues as they affect optimal operation.

This study evaluated the nature of different topologies of WPTECT responses behaviour under experimental conditions to assess their multiple feature capabilities using sweeping frequency excitation covering the designed resonance frequency. In addition, the section discussed the results of WPTECT responses to crack and no-crack at various lift-off distances for sensitivity to lift-off assessment. The responses of the five topologies of WPTECT considered in this investigation are compared to find the optimal topology for multiple feature capability and less sensitivity to lift-off variation and sample influence. The investigation results are based on the methodology and the designed magnetically-coupled resonant WPTECT Tx-Rx probe and experimental variables and parameters described in Table IV, section 3.4.3 of chapter 3.

6.3.1 Optimise WPTECT topology for multiple features potentials

The WPTECT transfer response, S21 of different network topologies, forms frequency splitting at different conditions. The task here is to find the topologies of WPTECT that can

provide frequency splitting response within the frame of experimental set-up parameters and variables. The five different topologies of magnetically-coupled resonant WPTECT are investigated. Figure 6.2 shows the S21 response (dB) and indicates the extrema points positions for crack and no-crack at zero lift-off distance for the five WPTECT topologies. Zero-lift-off, 0mm value represents the thickness of insulation of Tx coil wire's lamination. The magnitudes of the peak point features (m_1 and m_2) at a crack point are higher than that of the no-crack position for all the topologies due to the higher eddy current density around the crack area.

As seen in figure 6.2(a), the PP and PS-PS topologies responded with a dual-peak response providing three extrema point features, m_1, m_0, and m_2 and their corresponding frequencies. The nature and capability of forming the dual peak response are due to the satisfaction of the frequency splitting condition of Tx-Rx WPTECT discussed in [37, 270, 272, 277, 286]. Therefore, the critical coupling points for frequency splitting condition of PP and PS-PS topologies are much lower than that of SS, SP, and PS topologies for the given range of frequency operation at 50Ω source and load impedances, and other given parameters of the Tx-Rx probe.

However, figure 6.2(b) described the SS, SP and PS WPTECT topologies providing a single-peak transfer response. The higher critical coupling point by Rx-series, PS and SS topologies is caused by their zero reflected reactance and increasing reflected resistance for increasing frequency [35]. In addition, the SS topology requires very smaller load resistance than the VNA characteristic impedance to achieve frequency splitting behaviour at lower frequencies [254]. Whereas, the SP topology's single peak response is due to decreasing secondary quality factor with increasing frequency which leads to a higher load resistance requirement for achieving frequency splitting [35], as confirmed in [254] and [294] for R greater than 190Ω and 250Ω, respectively. The S21 responses of PS and SP topologies are similar for crack and no-crack positions, as seen in figure 6.2(b), due to the reciprocal nature (S12 of PS = S21 of SP and vice versa) of the two topologies' circuits. The transfer response of SS topology differs from other topologies by having a wide response margin between the crack and no-crack position because of its lower impedance at resonance, leading to maximum circulating current and lower mutual coupling than the critical coupling for frequency splitting condition [36]. The drastic drop of peak frequency from crack to no-crack points is attributed to the drastic increase of the SS topology reflected resistance due to increased mutual inductance between Tx-Rx and sample [36]. The behaviour of these five WPTECT topologies responses is further analysed in terms of sensitivity to crack and no crack position at various lift-off distances.

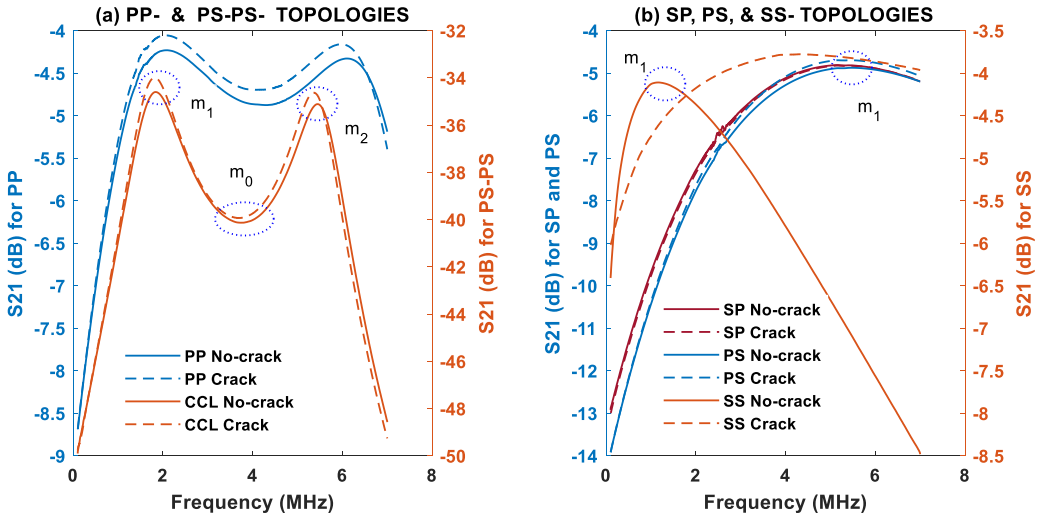

Figure 6.2 WPTECT topologies S21 response to crack and no-crack position

6.3.2 Optimise Topology for Response sensitivity to lift-off distance

Fortunately, apart from the multiple resonance potentials of magnetically coupled resonant WPTECT probe, the frequency and magnitude at extrema points of the S21 transfer response are also affected by lift-off distance and sample parameters. Thus, the task here is to numerically evaluate the response of the five WPTECT topologies for achieving the optimal topology, which provides the lowest sensitivity to lift-off variation under the same experimental set-up parameters and variables. The study extracted extrema point features at different lift-off distances to numerically ascertain each probe's sensitivity to sample influence. The probe's sensitivity to crack at a lift-off point was computed as a percentage change of extrema points, m_1, m_0, and m_2 points feature for each topology using the expression given by equation (6.4) [38, 295]. Where *x* is the magnitude (m) or frequency (f) of the extrema point feature while *nc* and *c* represent no-crack and crack point at i's lift-off point.

$$Feature\ sensitivity, Sx(i) = \frac{S_{nc}(i) - S_c(i)}{S_{nc}(i)} \times 100\% \qquad (6.4)$$

Figure 6.3 shows the extrema points sensitivity index to a crack, Sx, for increasing lift-off distance from 0mm to 11.6mm at an interval of 0.2mm. The 0mm value represents the thickness of insulation of the Tx coil wire's lamination. The sensitivity index (Sm) magnitude increases from zero-lift-off value to a peak value and then sharply decreases to zero (0%) at higher lift-off, including the frequency sensitivity index, Sf for m_1 of PS-PS, PP, SP, and PS topologies. Additionally, the frequency features sensitivity index (Sf) of m_0 and m_2 decrease to a zero sensitivity for increasing the lift-off distance, as seen in figure 6.3 (b), (c), (e), and (f). The sensitivity behaviours of the extracted features could be due to the attenuation of permeability influence around the crack area at a particular lift-off value exceeding a distance determined by

the geometric size of the Tx-Rx coil [217]. For the extracted features from the responses of the PS-PS and PP topologies, both Sm and Sf of m_1 have a higher rate of increase than that of m_0 and m_2 features due to the probe arrangement; Rx coil above Tx coil shown in figure 3.10(c).

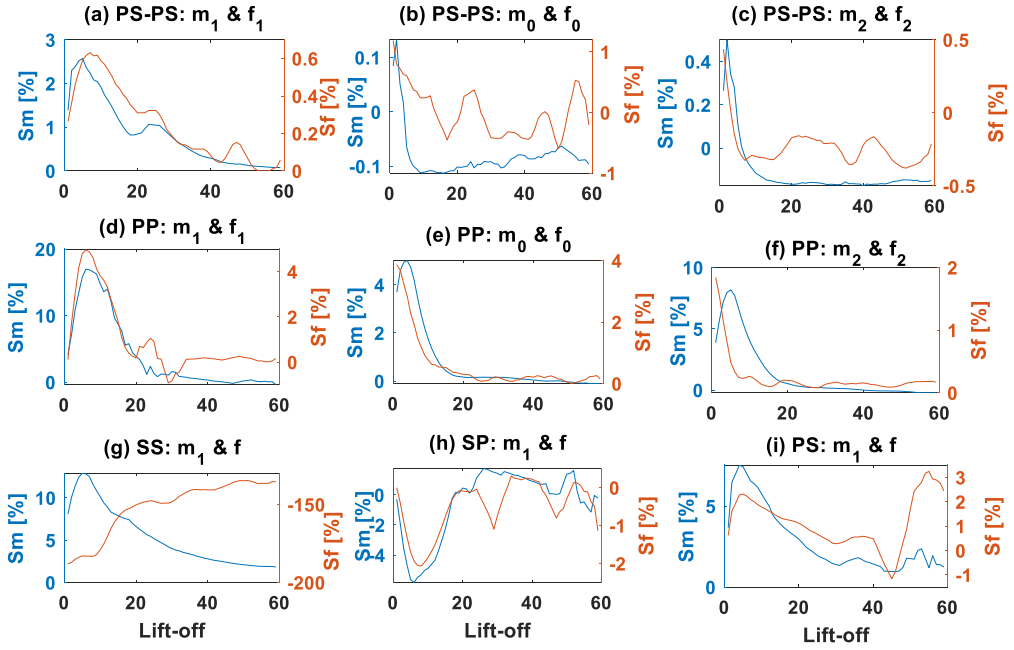

Figure 6.3 WPTECT topologies' crack and no-crack sensitivity to lift-off distances

Generally, the features of PS-PS topology in figure 6.3(a), (b), & (c) provide minimum sensitivity to lift-off distance (Sm and Sf) compared to other topologies, which indicates less influence of lift-off effect on the response for crack and no-crack points on the sample. The behaviour could be due to the advantage of series and parallel resonance in the topology by sharing the total stress of reactive power by the series compensating reactance (Xb) and the parallel (Xa) to maintain the oscillation [280]. The minimum sensitivity to lift-off by the PS-PS topology is based on the stated experimental set-up variables and parameters in Table IV. In view of this performance, the PS-PS topology has been selected to further investigate features performance because of its less sensitivity influence on lift-off and sample permeability in addition to the capability of multiple features based on this study's experimental parameters and variables.

6.4 Multiple Features for Optimal Assessment of RCF Cracks

The response of the PS-PS topology provides multiple resonances within the range of operating frequency at a minimum influence of lift-off and sample permeability around the crack, as explained in section 6.3 above. Therefore, this section investigates the response and extracted features of the probe configured as PS-PS circuit topology by scanning a crack on the

sample at lift-off distances below and after the lift-off value of the peak sensitivity index, Sm in figure 6.3(a). The value of 0.4mm and 1.2mm lift-offs have been chosen because they fell below and after the peak of Sm and Sf of m_1 extrema point feature of the PS-PS topology response. The scanning arrangement of Tx-Rx coils above the sample and inclined angular crack for this experimental investigation has shown in figure 3.10(c), whilst the results are presented in this section.

To ascertain the optimal lift-off level, a 45^0 angular crack was inspected by placing the Tx-Rx coils at a 7.5mm distance before the crack and scanned for a 15mm distance at a 0.1mm scan step using a 0.4mm lift-off value. The procedure was repeated for 1.2mm lift-off values. Figure 6.4 shows the S21 linear response at the two lift-off values at the beginning of the scan. The response indicates that the higher the lift-off, the higher the S21 value with a higher rate of increase by the first peak feature point, m_1. The higher increase rate of Sm of m_1 feature is due to the closeness of the Tx coil to the sample than the Rx coil (figure 3.10(c)). Thus, the S21 increase at the peak feature point by the lower lift-off is more pronounced than that of the higher lift-off coil, Rx. This finding confirms why the sensitivity index, Sm of m_1, is higher than m_2 in the previous results presented in figure 6.3.

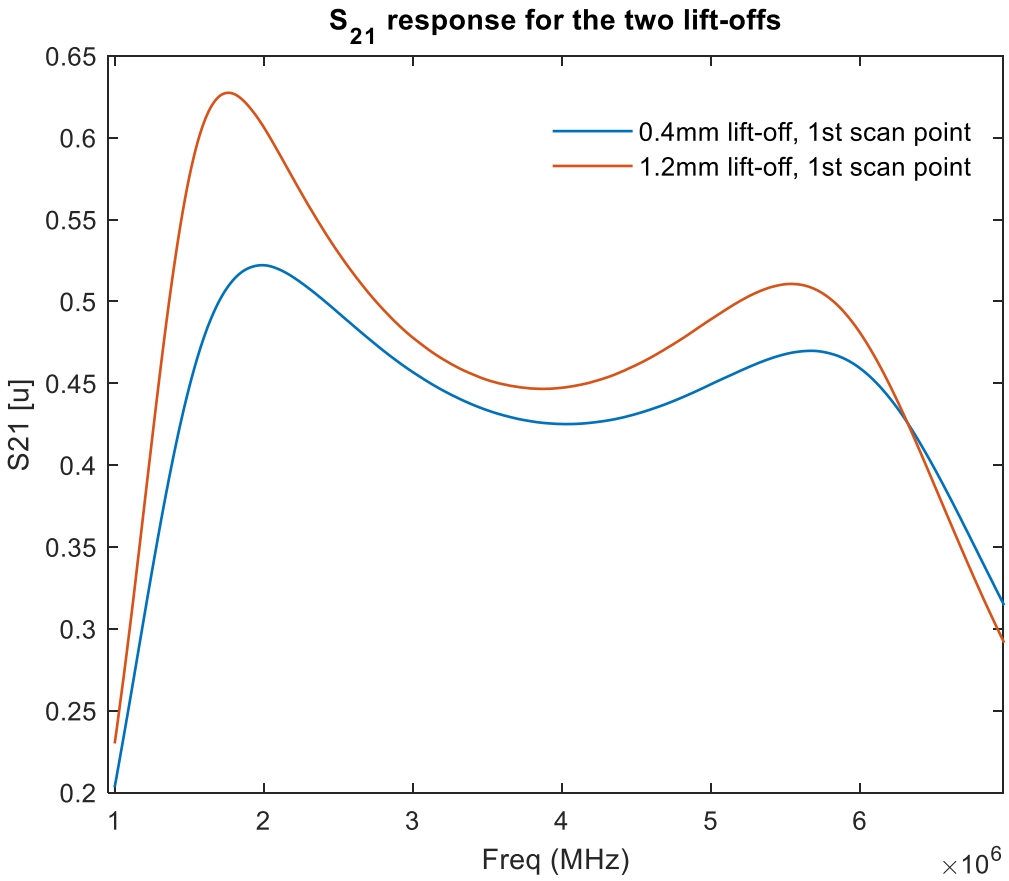

Figure 6.4 Linear response of PS-PS WPTECT topology at a non-crack point for two considered lift-off values

Upon scanning a 45^0 crack at the two lift-offs, extrema point features were considered to optimise the PS-PS topology response. Figure 6.5 shows the extracted extrema points features, m_1, m_0, and m_2, from the linear response, S21 at 0.4mm and 1.2mm lift-off values for ascertaining the effect of lift-off and sample permeability on the extracted features. The m0 and m2 extracted features at 0.4mm lift-off (figure 6.5 (h) and (l)) are visibly corrupted by noise and distorted compared to the m0 and m2 extracted features at 1.2mm lift-off (figure 6.5 (b) and (f)). The extracted feature m_1 is less affected at lower and higher lift-off values than other extrema point features because its frequency has a higher penetration depth than that of other extrema points features. However, the higher the frequency (shorter wavelength), the higher the feature sensitivity to surface influence. Also, the closer the probe to the sample, below the optimal lift-off value of the fixed Tx-Rx gap [17], the more the lift-off effect and influence of the sample's permeability on the extracted features. Therefore, scanning at a lift-off above the threshold value reduces the influences of lift-off and sample on the extracted features; however, the optimal arrangement of the Tx-Rx gap has to be maintained as described previously by [15, 17]. Hence, a 1.2mm lift-off can be used to scan the nine (9) models of inclined angular RCF cracks, C1 to C9 (figure 3.10(b)) for quantitative non-destructive evaluation (QNDE) in the next section.

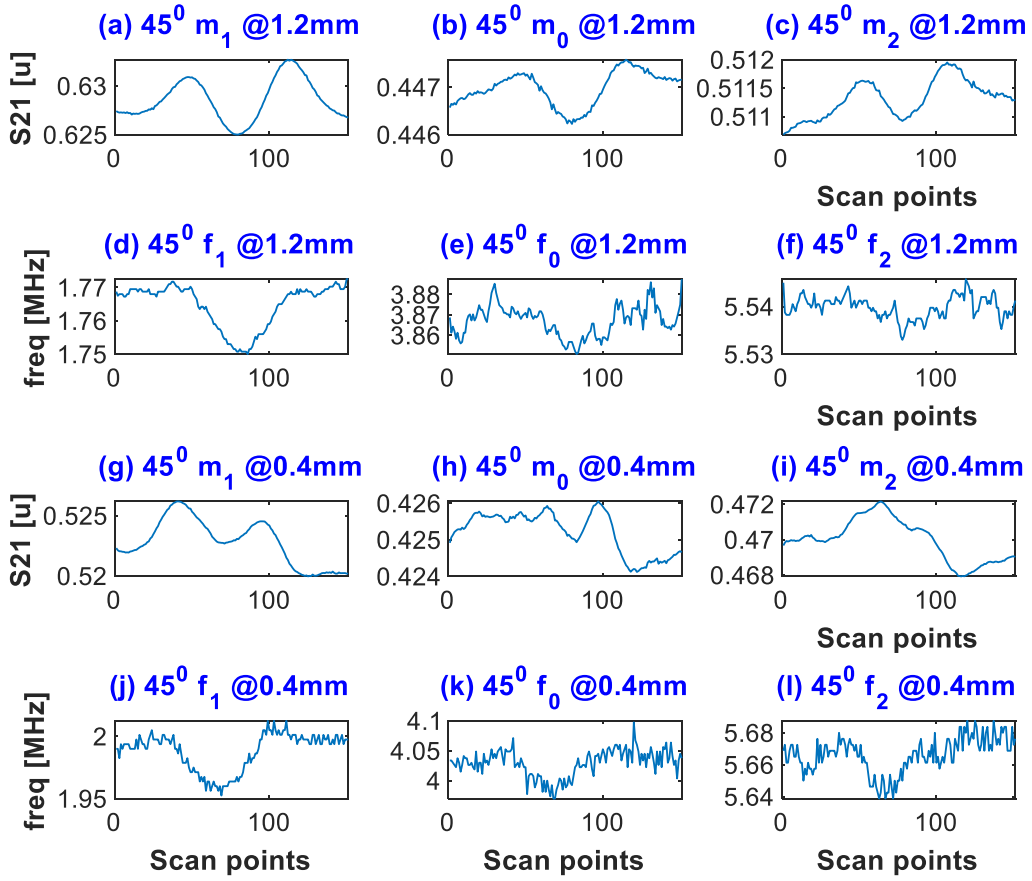

Figure 6.5 Extrema point Features for scanning a 45^0 inclined crack at (a) – (f) 1.2mm lift-off distance (g) – (l) 0.4mm lift-off distance

6.5 Optimised Features for Inclined Angular RCF Cracks Evaluation

Unavoidably, rolling contact fatigue (RCF) causes natural crack formation in the railhead, leading to rupture. Eddy current testing (ECT) is commonly used to quantify such RCF cracks because of its higher sensitivity to a surface flaw, though with limited feature points. The optimised topology combined advantages of other topologies in addition to its magnetically coupled resonant for excitation and sensing circuits and utilisation of multiple resonance responses compared to other ECT methods.

This section aims to characterise inclined angular RCF crack parameters in a rail-line material via an optimised topology of WPTECT. This section introduces reviews of why WPTECT considered for the inclined angular RCF cracks evaluation compared to other NDT&E techniques are introduced. It also presents extracted multiple resonance points and principal components analysis features from WPTECT response for detection and quantification insight into inclined angular RCF cracks parameters, including depth, width, and

angle, from the experimentally designed WPTECT in section 3.4.3. The discussions of the cracks characterisation include fitting parameters for showing the goodness of fitting the extracted features to cracks parameters, as described in section 3.4.3 by Table III, sample and crack parameters. For this study measurement of the modelled nine inclined angular cracks, two different scans were conducted; (1) to detect the nine cracks and (2) to quantify the cracks parameters. The first scanning is for the localisation of the crack, while the second quantifies the entire RCF crack parameters.

6.5.1 WPTECT for angular RCF cracks characterisation and traditional NDT&E

Previously, rail structural degradation due to RCF has been assessed by combining automated optical cameras and eddy current testing (ECT) during the manufacturing process, although magnetic induction sensors and ultrasonic transducers have been used for the in-service rails [41]. The optical camera, ECT, and magnetic induction sensors have been used to evaluate the surface crack, whereas the ultrasonic transducer for internal crack assessment. These methods operate so that each technique counterparts the deficiencies of the other technique while inspecting RCF crack, which is time-consuming. To reduce the scanning time of large area coverage, laser ultrasonic technology and a hybrid intelligent method have been combined and applied for high-speed and precision online rail RCF crack detection [46]. The processed feature from laser ultrasonic achieved fast classification and evaluation of the RCF depth parameter. However, the ultrasonic technique is limited to low-speed inspection and is unsuitable for surface defect inspection with a crack depth of less than 4mm [41]. Magnetic flux leakage (MFL) techniques have been applied for rail inspection of surface and subsurface-breaking cracks at higher speeds. However, MFL signals for subsurface cracks are distorted by the influence of permeability around the crack and depends on the direction of the magnetic axis for cracks characterisation [217]. To detect surface and subsurface angular RCF crack, an eddy current pulsed thermography (ECPT) technique has been used to quantify angular parameter because of its combined quality of electromagnetic excitation and thermal diffusion [40]. It facilitates mapping the features from pulse heating and cooling behaviour of the gathered cracks to reconstruct inclined angular RCF crack parameters with a higher percentage of fitting parameters [40, 43, 44]. However, the broad frequency spectrum of pulse excitation produces circulation of fundamental and harmonic currents, affecting the response of the heating element and the induced heating to the sample due to the harmonic frequency distortion. Therefore, as further discussed in [41], none of the above mentioned NDT&E techniques can significantly enhance the assessment of RCF cracks in rails if not modified or applied in

combination with other methods. The previous NDT&E studies quantified one crack parameter at a measurement result, while other parameters were assumed to be unchanged, as demonstrated in [40, 43-47]. Therefore, the RCF crack geometric parameters characterisation at a measurement result is a challenging factor.

In this study, magnetically-coupled resonant WPTECT is considered for RCF cracks characterisation due to its efficient energy transfer with the potential of frequency splitting behaviour for multiple parameter sensing. Compared to other ECTs, the novel WPTECT uses a magnetically coupled multiple resonance Tx-Rx probe operating at sweep frequency excitation for different layer information at a certain lift-off point. Different layer information ease separation of permeability as ECT depends on conductivity. Also, the effect of permeability on coil inductance can be mitigated at a certain lift-off distance as described by permeability invariant point [49], which is also applicable in this study.

Each previously implemented WPTECT was based on a single topology [23, 24], though each topology has different frequency responses depending on reactive compensation arrangement. In view of the challenges associated with different techniques of assessing RCF cracks, this section presents the results of WPTECT for crack quantification as described in section 3.4.3 of the research methodology. It uses a modified parallel/series-parallel/series (PS-PS) WPT topology, due to its lowest response sensitivity to lift-off variation as described in section 6.3.2, to investigate multiple features for mapping the entire profile of RCF cracks in a railway material.

6.5.2 Inclined angular RCF Cracks localisation

The nine cracks were axially scanned from a 10mm distance before the first crack (C1) for a 270mm distance to cover the nine cracks at a 0.3mm scan step by placing the Tx-Rx coils at a 1.1mm lift-off. The results of detecting the cracks, including the S21 response indicating the feature points and the extracted features, are given in figure 6.6. The three extrema points, m_1, m_0, and m_2, for 1601 linearly spaced frequency points from 1MHz to 7MHz range of S21 response are the extracted features as indicated in figure 6.6(a). As shown in the figure, the double resonances demonstrate the relationship between the Tx–Rx probe and sample geometry, permeability, and conductivity, including lift-off for a wide range of frequencies. The multiple resonances have multiple variables and features for mapping to the cracks' parameters. The two peak points, m_1 and m_2, depend on the Tx and Rx topologies, respectively, though the S21 response is not symmetrical despite the identical coils. The magnitude of the m1 is higher than that of m_2 because the Tx coil has dominant behaviour in the first peak, m_1,

and is more responsive at 1.1mm lift-off for being nearer to the sample than the Rx coil as seen in figure 3.10(c).

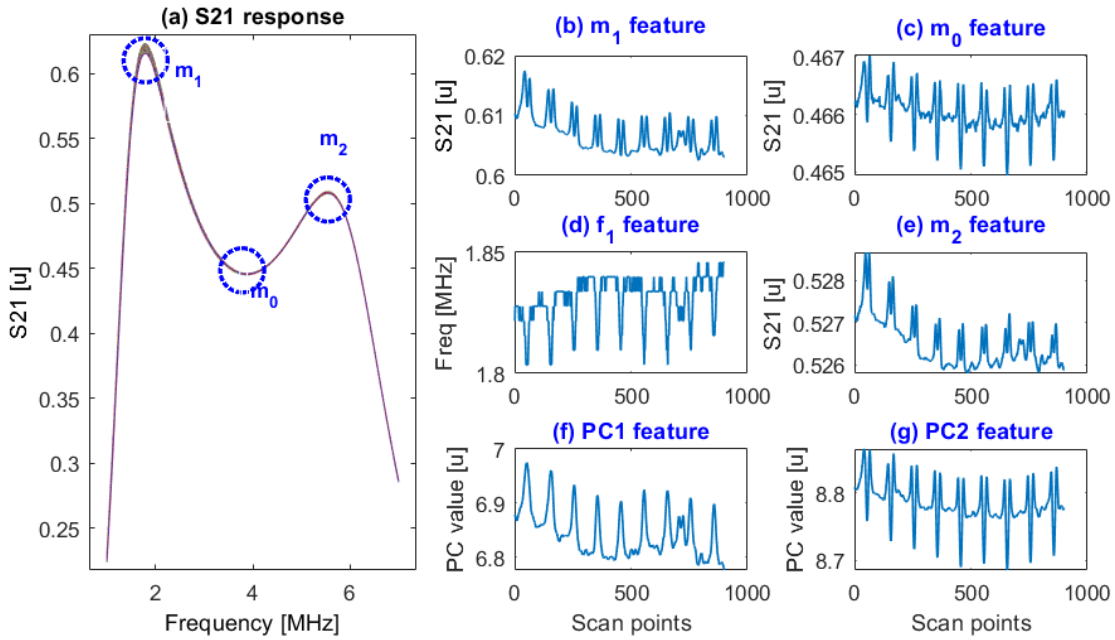

Figure 6.6 WPTECT System response for scanning cracks and extracted feature morphology at 1.1mm lift-off (a) Linear response, S21 of WPTECT PS-PS topology indicating m_1, m_0, and m_2 feature points and extracted S21 (b) magnitude, m_1 (c) magnitude, m_0, (d) frequency, f_1 from m_1 point, (c) magnitude, m_2, (f) Computed PC1 and (f) Computed PC2 features along the scan-axis

For investigating the detectability of the models of inclined angular RCF cracks, multiple resonance features from m_1, m_0 and m_2 were extracted and presented in figures 6.6 (b), (c), and (e) as magnitude features and (d) as the frequency feature of m_1 point. This study has not reported the frequency features for m_0 and m_2 because they show no information about the cracks. Furthermore, the response shape in figure 6.6 (a) has information related to the sample geometry, conductivity, and permeability. Therefore, the shape of the S21 response was statistically evaluated using principal components analysis (PCA) for demonstrating further statistical feature extraction. The capability, flowchart, and algorithm of PCA features extraction have been demonstrated in the previous study [23, 24]. Therefore, in this context, the first and second principal components (PC1 and PC2) are the features used to detect and characterise the inclined angular RCF cracks model because of their higher percentage variant around the crack. The PC1 and PC2 are given in figure 6.6 (f) and (g), respectively.

The six extracted features detected nine cracks are m_1, m_0, m_2, f_1, PC1, and PC2 portrayed by “n” or “m” shape spatially covers before and after each crack along the scan-axis. The significant decreasing trend of m1 and m2 features could result from sample permeability or

lift-off distances due to varying sample thickness, probe movement, or uneven sample surface. It is very noticeable at m2 features because the Rx coil has a higher lift-off distance than the Tx coil due to the Tx-Rx probe and sample layout (figure 3.10(c)). m_0 feature is less affected by the lift-off distance because it's a frequency point at which the absolute values of real and imaginary parts of the S21 are minimum but opposite in magnitude.

This section aims to detect the cracks, but the influence of permeability could as well be mitigated as it has been done by permeability-invariant-point at certain lift-off [49]. Furthermore, the lift-off noise has been mitigated by response normalisation and reference signals management [209], time- and frequency-domain differential response analysis [210], using a GMR-BC probe with an error compensation technique [214] and combining PCA and support vector machine [296]. In this research, the demonstrated PCA features in figure 6.6 (f) and (g) are less affected by lift-off noise because they depend on the response shape. However, PC2 is more robust to lift-off variation compared to PC1, as seen in figures 6.6 (f) and (g), respectively. Similar features will be investigated and reprocessed for quantification insight from the WPTECT system response of individual crack scanning results in the next section.

6.5.3 Cracks quantification

For each crack parameter quantification, the nine cracks were then individually scanned by positioning the Tx-Rx coils at a 7.5mm distance before the crack and scanned for a 15.0mm distance at a 0.1mm scan step and a 1.2mm lift-off distance. The extracted features from this scanning results comparable to the extracted features in figure 6.6(a) are presented in figure 6.7. Figure 6.7 (a) to (f) show the extracted features, m_1, m_0, m_2, f_1, PC1, and PC2, described by an "n" or "m" shape along the scan axis. The crack's width depends on the extracted feature's width along the scan-axis, while the depth depends on the peak amplitude of the feature as presented in ECT quantification of crack [24, 28, 45, 297]. Additionally, the width and depth of an inclined crack angle have been used to determine the crack angle [45] and would be used in this section for inclined crack features derivation. Therefore, this study started extracting the feature points for depths and widths information along the scan-axis of each of the nine cracks. Then, the features for angle quantification were derived as a function of the depth features and the crack's slanting length, trigonometrically.

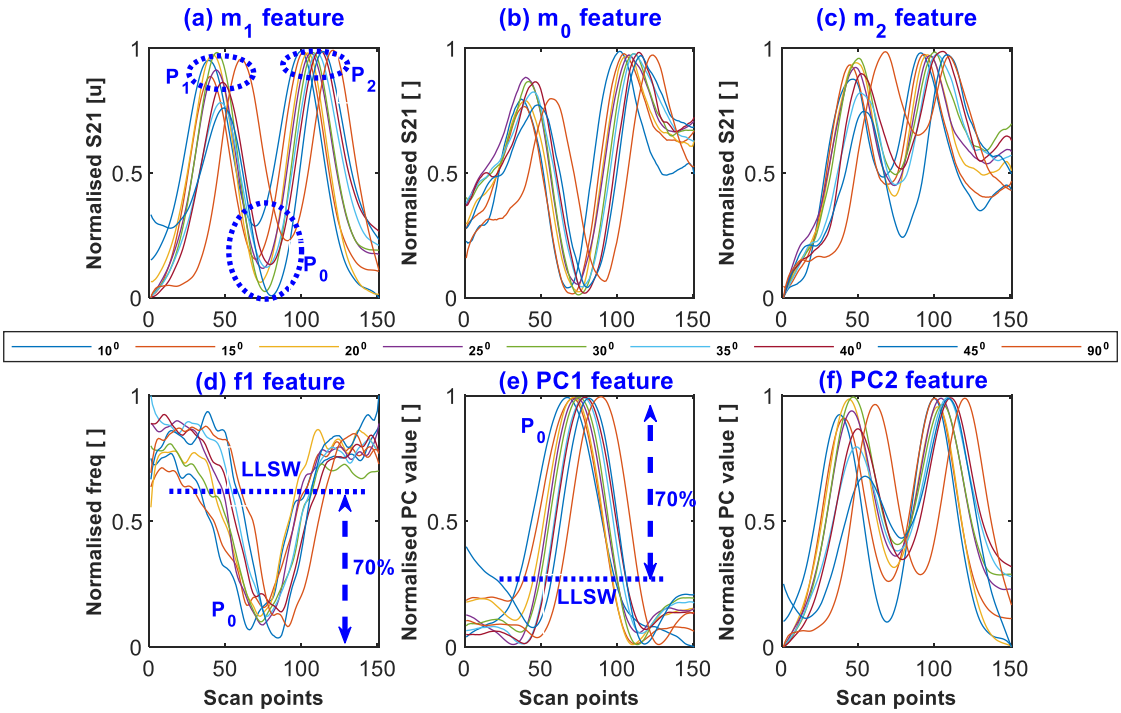

Figure 6.7 Normalised extracted features of the nine cracks, indicating LLSP (P_1, P_0, P_2) of (a) m_1, (b) m_0, (c) m_2, (d) f_1, including LLSW (e) PC1, including LLSW and (f) PC2

The magnitude of each feature profile at points P_1, P_0, and P_2 of the nine cracks' extracted features (figure 6.7) were evaluated and defined as the length of the line scan peak (LLSP). P_1 and P_2 are the points around the crack where the eddy current density has the highest deviation, whereas P_0 is the middle of the crack. The crack depth depends on the LLSP feature, P_1, P_0, and P_2, while the width depends on the length of the line scan width (LLSW) feature. The extracted features of depth and the slanting length determine the inclined angle features of the cracks using the trigonometric identity. The actual inclined crack depth (d) depends on the slanting length (L) at a given angle (θ) as determined using the trigonometric identity expressed by equation (6.5). Being the depth makes a right angle with the slanting length; therefore, the inclined angle of the crack depends on the ratio of depth feature and slanting length as expressed by equation (6.6) according to the trigonometric identity of Euclidean geometry. The computed depths values are presented in Table III and are the parameters for comparison with the LLSP features.

$$d = L \times \sin(\theta) \tag{6.5}$$

$$\theta = \sin^{-1}\left(\frac{depth, d}{L}\right) \; ; \; \therefore \; \theta\_feature \; \alpha \; \frac{LLSP}{L} \tag{6.6}$$

The LLSPs (P_1, P_0, and P_2) of the extracted features (m_1, m_0, m_2, f_1, PC1, and PC2) were evaluated to quantify the cracks' depths. Figure 6.8 (a) to (e) show the extracted LLSP of the eight inclined cracks and the vertical crack against actual crack depth. The depth of the inclined cracks increases from 0.07 to 0.75mm for C1 to C8 cracks, respectively, as indicated in Table III, while the vertical crack, C9, has 1.32mm. The results, shown in figures 6.8 (a), (b), and (c), indicate the linear (increasing) relationship of the three LLSPs (P_1, P_0, and P_2) from m1, m0, and m2 with the actual crack depth serially from the first inclined crack, C1 to the last inclined crack, C8. Likewise, the LLSP, P_0 from f_1, and PC1 features depicted in (d) and (e) of the figure decrease for increasing depth of the crack. The vertical crack, C9 (1.3mm depth) LLSP features are indicated by the right-axis of figures 6.8 (a), (b), and (c), each has approximate values (P_1= P_0= P_2) of 0.6, 0.4, and 0.5 unit for m_1, m_0, and m_2 respectively. The LLSPs of PC2 shows no monotonic relationship with actual crack depths.

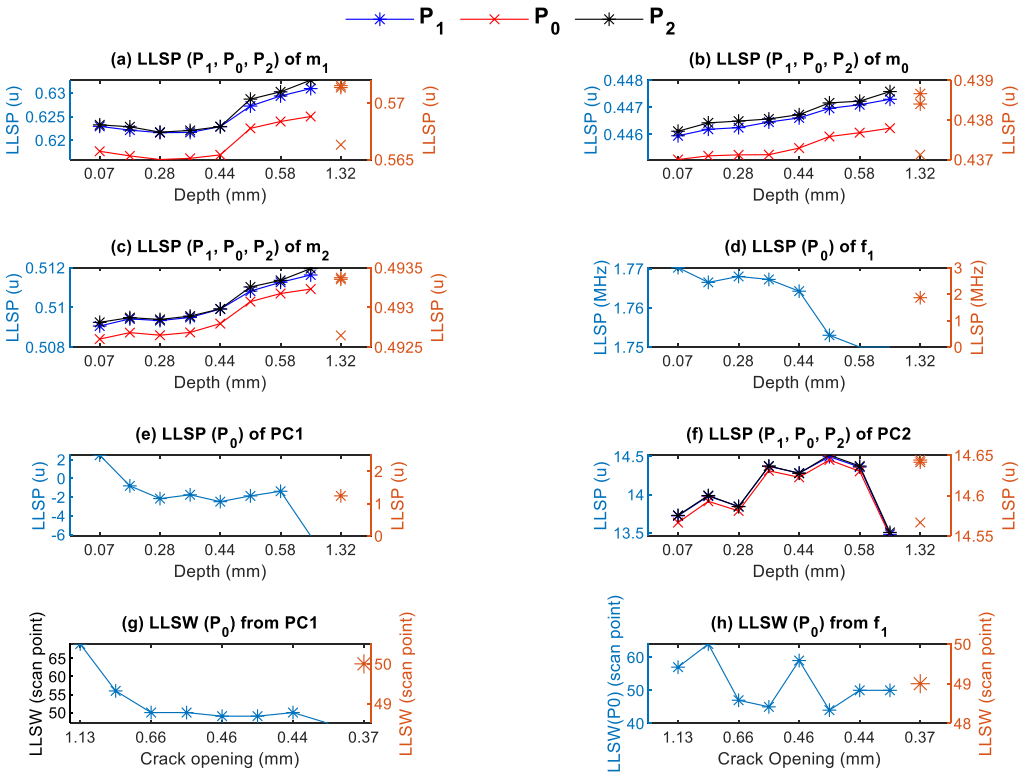

Figure 6.8 Extracted LLSP and LLSW features against the crack depth and opening parameters, respectively. (a) – (f) crack depth and (g) – (h) crack opening information.

The LLSPs of the extracted features in figure 6.8(a) – (e) form a linear relationship with the actual depths of the crack. Therefore, a linear regression model is formed for feature depth prediction to determine how best each feature reconstructs the actual depth. The predicted depths of the inclined cracks, C1 to C8, linearly depend on the LLSP (P_1, P_0, and P_2), each from m_1, m_0, m_2, f_1, and PC1. They are the features with a linear relationship to the actual depth of

the crack. The linear regression model from the curve fitting tool apps in the MATLAB® software was used to compute the model's fitting parameters, R^2 value, and RMSE for the cracks reconstruction. The computed LLSP versus actual depth and its statistical errors analysis are studied to show the regression model's goodness and compare with other literature on ECT depth quantification results in the next section. The computed R^2 and RMSE are presented in Table VIII. The LLSP from m_0 feature has the highest goodness of fitting, R^2, and minimum RMSE because it is a point at which the Tx and Rx topologies have an equal response if they operate as an absolute probe and single resonance. Moreover, among the two resonance points, m_1 and m_2, the second resonance has a better-predicted depth as indicated by the R^2 value and RMSE. Furthermore, the first resonance frequency feature (f_1) has better depth model fitting than its corresponding S21 magnitude feature (m_1).

The width information is related to the spatial position of the extracted features. Therefore, the extracted features from scanning nine cracks were normalised using min-max normalisation, [0 1] scale for same scale comparison. Figure 6.7 shows the normalised features of the nine cracks extracted from the magnitude (a) m_1, (b) m_0, (c) m_2, and frequency of m_1 (d) f_1, and statistically computed PCA features (e) PC1, and (f) PC2. Among the extracted features, f_1 and PC1 have only P_0 as LSSP features, as seen in figures 6.8 (d) and (e). The width quantification is accomplished using the LLSW of f1 and PC1 features as they are the features with a single peak value.

The LLSW feature has been measured as the spatial distance along the scan-axis on the extracted feature between two points where the point P_0 of LLSP features ascend or descend to 70% of its value as indicated in figure 6.7 (d) and (e). Figure 6.8 (g) to (h) show the plot of LLSW against the crack opening, w0. The LLSW features derived from the PC1 feature show decreasing behaviour as the inclined crack opening decreases from crack C1 to C8, as seen in figure 6.8(g). The LLSW from PC1 is more linearly related to the actual width of the cracks than that of the f_1 display. The reason for decreasing behaviour by the LLSW for decreasing width is because the two points at which the eddy current density is highest depend on the crack opening.

Similarly, a linear regression model was used to compute the regression model parameters, R^2 value, and RMSE for mapping LLSW and crack opening parameters. From Table VIII, the PC1 features reconstruct the crack opening by 93%, whereas the frequency feature is not good for width information. The worst fitting parameter of LLSW from the f_1 feature emphasises the weakness of f_1 for width behaviour as it is more influenced by noise right from the extracted features in figure 6.7(d).

Table VIII Goodness of fit: Crack opening and depth reconstruction (linear model of a 2nd-degree polynomial) fitting parameters

	Crack depth LLSP						Crack Opening LLSW	
	R^2 -Value			RMSE (mm)			R^2 - Value	RMSE (mm)
LLSP:	P_1	P_0	P_2	P_1	P_0	P_2	LLSW	LLSW
m_1	0.69	0.71	0.69	0.16	0.15	0.16	-	-
m_0	0.96	0.90	0.95	0.05	0.09	0.07	-	-
m_2	0.89	0.86	0.87	0.10	0.10	0.10	-	-
f_1	-	0.83	-	-	0.11	-	0.27	0.25
PC1	-	0.63	-	-	0.17	-	0.93	0.08

The angle feature depends on the depth feature LLSP (P_1, P_0, and P_2) from m_1, m_0, m_2, f_1, PC1, and PC2 extracted features together with the slanting length (L) based on the trigonometric identity. Being the depth makes a right angle with the slanting length; therefore, the inclined angle of the crack depends on the ratio of depth feature and slanting length as expressed by (5) according to the trigonometric identity of Euclidean geometry. The ratio of LLSP and their corresponding slanting length, L of a crack, was computed using equations (6.5) and (6.6). The ratio is proportional to the angle feature, and it's used to characterise the inclined angle of the cracks in this study. Figure 6.9 shows the plot of angle features, θ_features, derived from the depth features, LLSP against the actual angle of the cracks. The left axis is the angle features for inclined cracks, C1 to C8, while the right axis is for the vertical crack, C9. The θ_features decrease sharply from 10^0 to 20^0 and then steadily to 45^0 respectively for the inclined cracks, C1 to C8 cracks. The vertical crack, C9, observes the lowest value. The decrease of θ_features for increasing the inclination angle of the crack is due to the increasing eddy current, as demonstrated by other researchers using inclined angular crack [45, 297] that the higher the inclined angle of the crack, the lower the eddy current density along the direction of crack elongation. Furthermore, the derived θ_features at P_1, P_0, and P_2 are considerably nearer in each of the extracted features, m_1, m_0, m_2, and PC2, as illustrated in figure 6.8 (a), (b), (c), and (f) respectively. Similarly, the θ_features of the vertical crack, C9 indicated by the right-axis in figure 6.9(a), (b), (c), and (f), have equal θ_features at LLSP (P_1, P_0, and P_2) extracted from m_1, m_0, m_2 and PC2 as 0.43, 0.33, 0.37 and 10.6 respectively.

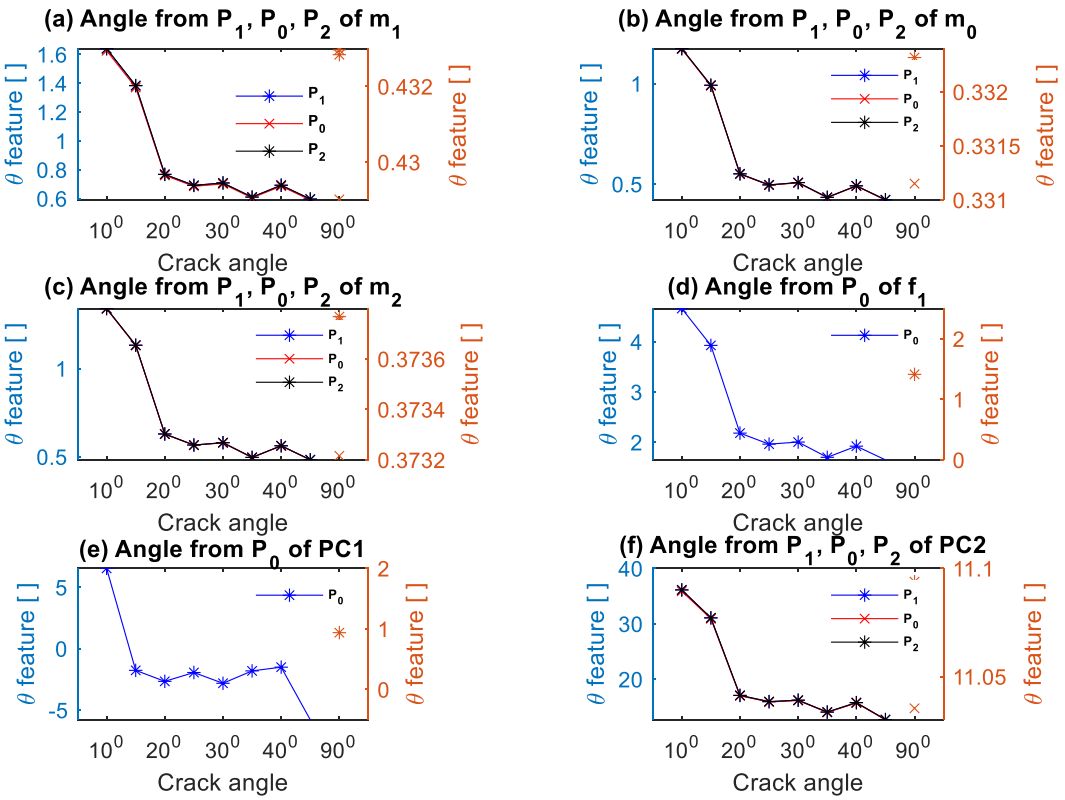

Figure 6.9. Angle features derived from LLSP against cracks angles

The θ_features shown in figure 6.9(a) – (f) were compared for a linear relationship with the inclined angle of the cracks. To find the fitting parameters for predicting the actual angle of the inclined cracks, C1 to C8, a linear regression model is also computed using the "curve fitting tool apps" of MATLAB® software. The computed curve fitting parameters, R^2 value, and RMSE are presented in Table IX. The θ_features from LLSP of PC2 have the best fitting parameters compared to other extracted features. Furthermore, the θ_feature from LLSP of m_0 has better R^2 and RMSE than that of the other two resonance features, m_1 and m_2, reflecting its capability for depth estimation. However, the second resonance has better angle prediction than the first resonance, as indicated by the R^2 value and RMSE in Table IX.

Table IX Crack inclined angle reconstruction (linear model of a 2nd-degree polynomial) fitting parameters

	R^2 -Value			RMSE (^{0})		
θ_feature from LLSP:	P_1	P_0	P_2	P_1	P_0	P_2
m_1	0.760	0.760	0.758	7.099	7.098	7.124
m_0	0.773	0.773	0. 773	6.902	6.906	6.903
m_2	0.771	0.771	0.771	6.936	6.940	6.941

f_1	-	0.784	-	-	6.731	-
PC1	-	0.514	-	-	10.100	-
PC2	0.791	0.791	0.790	6.625	6.630	6.643

6.6 Further Results Discussion

This study investigated five WPTECT topologies for multiple resonances to find an optimal topology, optimise its response, and extract features for inclined angular RCF cracks quantification. The optimised WPTECT topology has been realised by comparing the sensitivity of each topology's response to lift-off at a crack and no-crack position. The optimised topology response has been further investigated by scanning a crack at different lift-offs to find a threshold lift-off for optimal features response to scanning a crack. The lift-off level for optimal feature response has been used to scan the nine cracks individually for optimal crack parameters QNDE. The quantifying cracks in this study are compared with other related literature and discussed in this section.

Among the topologies' responses described in figure 6.2, the PS-PS and PP topologies provide dual peak response due to their higher input and output impedance at resonance, leading to lower critical Tx-Rx coupling than other topologies. However, the PP topology has shown higher power transfer efficiency than the PS-PS topology, making it capably preferred over the PS-PS topology for inspection at an application that requires higher eddy current power. Nevertheless, the lower power transfer response by the PS-PS combined topology is due to the power drop across the series capacitors, Cb connected to each Tx and Rx coils as seen in its circuit diagram presented in figure 6.1(a). Conversely, PS-PS topology has minimal sensitivity indices (Sm and Sf) to lift-off distance at the crack and no-crack points. Compared to other topologies, the lower value Sm and Sf's indicated by PS-PS topology confirm the advantages of combining SS and PP topologies. The advantages are due to the sharing of the stress of total reactive power among the two compensating capacitors, Ca and Cb, for maintaining steady oscillation [280]. Therefore, the multiple features of PS-PS topology are applied to ECT to facilitate efficient quantification of RCF crack parameters as it suppresses the lift-off and sample influences like variation of permeability around the crack area at a certain lift-off distance. Although the lift-off distance for optimal operation is limited to the gap between Tx and Rx coils and their geometry, as shown by the previous research [17].

The lift-off level for optimal characterisation of inclined angular RCF cracks depends on the lift-off value for a peak value of sensitivity index (Sm), which is a point above which the

influence of sample permeability around the crack partakes minimum effect on the extracted feature compared to that of conductivity. The lift-off sensitivity indices of Sm and Sf, described in figures 6.3 (a), (b), and (c) from the extracted features m_1, m_0, and m_2 of PS-PS topology, indicated the threshold lift-off point by the peak sensitivity index. The Sm from m_1 showed the highest threshold lift-off at 1mm (5th lift-off point) due to the Tx coil being closer to the sample than the Rx coil in the structural arrangement of the Tx-Rx probe. Therefore, the conductivity influence weakens the permeability influence on the m_1 feature after 1mm lift-off because the rate of permeability decreases in a crack region due to the increasing lift-off distance being higher than that of conductivity influence. The results of scanning a crack at lift-off 1.2mm located the crack by the magnitudes of the extrema points, m_1, m_0, and m_2 features as seen in figure 6.5(a) – (c) and frequency of m1 in figure 6.5 (d) without features distortion. However, at 0.4mm lift-off distance, only m_1 and f_1 features have vividly detected the crack location, as seen in figure 6.5(g) and (j), respectively, due to higher penetration of f_1 compared to f_0 and f_2. Furthermore, scanning the crack at a lift-off above the threshold lift-off of m_1 extrema point feature has less influence on the sample's surface noise; however, the optimal arrangement of the Tx-Rx gap has to be maintained as described previously by [15, 17].

The WPTECT response generates multiple resonances from the sweeping frequency excitation for multiple parameters evaluation. The multiple feature points overcome the complexity of crack parameters characterisation. For scanning the models of inclined angular cracks at 1.2mm lift-off, the derived features from m_1, m_0, m_2, and f_1, including PC1 and PC2, respond to crack parameters as described in figures 6.6 and 6.7. Different features have different characteristics, such as robustness to lift-off, as in m0 and PC2 features. The frequency features, f_0 and f_2, are more susceptible to the other parameters that are influenced by the coupling between Tx-Rx and sample than depth and width parameters. In contrast, the magnitude features depend on the variation of the sample's conductivity and permeability and the coupling effect. Those mentioned above could be why having the worst fitting parameter of LLSW derived from the f_1 feature. Furthermore, the LLSP derived from m_0 has the best depth information based on the R^2 -value. It localised the crack centre due to the wide variation of conductivity between the two opening tips of the RCF crack, as discussed in [217]. The suitability of these features on RCF crack parameters is further compared with other kinds of literature.

As presented in Table X, most of the published NDT&E for crack quantification articles were varying the crack parameter to be quantified, while other parameters were considered as

constant as described in [43-47]. In real applications, the peak value of system response is affected by the depth, width, inclined angle and orientation parameters. Therefore, considering one parameter as constant in a measurement setting while quantifying the other is only applicable to known cracks. This proposed study quantified the width, depth, and inclined angle in each of the nine distinct cracks from a measurement setting while the cracks are different. The lower R^2 values in this study compared to other NDT&E studies could be due to the mutual influence of varying other crack parameters while quantifying each parameter.

The proposed WPTECT used scanning mode on the same rail sample with Ref [40] to quantify crack opening width, depth and inclined angle using frequency transfer response with multiple feature points at maximum energy transfer. However, the ref. [40] recognised and quantified the variation of inclined angles parameter by neglecting the influence of crack opening width and depth variations using eight temporal and spatial features from the thermal and first-order differential imaging responses, including their skewness and kurtosis-based features. The eight features require longer pulse excitation time slots, which provide a lower fundamental frequency of the pulse excitation for deeper heat diffusion for visibly characterizing the inclined angle. Although, it sacrifices the influence of other crack parameters. Our proposed WPTECT quantified all the crack parameters using 14 subfeatures from the LLSP, θ_feature and LLSW reprocessed features, linearly related to crack depth, inclined angle and opening width, respectively. The approach by [40] is a multi-sensing modality ECPT using infrared imaging, covering a relatively wide area affected by pulse eddy current heating. The ECPT has significant advantages on large-area scans with high lift-off and measuring depth defects but requires a high current to operate and has high cost and is bulky.

The better performance of quantitative results from ref. [46] could be due to their larger cracks sizes than those of the cracks considered in this study, which are proportionate to the size of the natural RCF cracks. Similarly, the better performance results from the thermography techniques in refs [43, 44, 47] could be due to their samples having cracks with one variable parameter, unlike other evaluated nine dissimilar cracks in a sample used in this study. However, the proposed WPTECT shows uniquely good application attributes to RCF cracks quantitative NDT&E in a railway and other rolling contact materials degradation. The attributes include simplicity in operation, availability of cheap WPT IC chip for signal processing to replace VNA in real-life application, cheaper probe and capability of quantitative NDT&E at scanning and non-scanning modes of operation. To compare this work with other research on

such cracks quantification using electromagnetic NDT&E methods, Table X gives some facts of cracks parameter reconstruction.

Table X Comparison for crack parameters reconstruction

Year, Sample	**Reference**	**Note**	**Maximum R^2 (min RMSE)**	**Methods**	**Quantified parameter**
2019, +rail (material) sample	J. Yi [46]	Quantified cracks depths at a constant angle (45^0), length (7mm), and width (0.3mm). Extracted features: kernel principal component, KPCA, Wavelet packet transform (WPT), and SVM	97.85% (0.0019mm)	Laser ultrasonic technology and a hybrid intelligent method	Depth
2021, AISI 1045 carbon steel +rail sample	J. Zhu [40]	Quantified angle at distinct cracks' pocket (slanting) lengths and opening. Features: Area-based, kurtosis, skewness, and sum value from thermal distributions and response.	98.6% (-)	ECPT	Angle
2019 carbon steel +rail sample	J. Zhu [43], [44]	Quantified Pocket length at a constant angle (45^0), length (63mm), and width (0.3mm). Features: max temperature, PCA-based thermal, PCA-based 1^{st} order differential.	99.9% (-)	ECPT	Slanting (Pocket) length

2019 Aluminium block	N. Faris [45]	Quantified depths at constant width (0.3mm) and angles. Quantified angle at constant width (0.3mm) and depths. Features: skewness, length of line scan (LLS), and the maximum length of line scan (LSmax).	Depth, Angle: 99.2%, 99.7% (0.198mm, 2.903°) respectively.	Pulse ECT	Depth and Angle
2021 AISI 1045 carbon steel	H. Xia [47]	Quantified vertical depths at a constant width. Features: temperature increase Ti, thermal contrast Tc, and thermal difference, TAB	99.72% (-)	Induction thermography	Depth
2021 AISI 1045 carbon steel	Our Proposed work	Quantified depths, angles, and widths each at distinct parameters. Features: Resonance (peak/extrema) points and PCA from the response shape.	Depth, width & angle: 96.4%, 93.1% & 79.1% (0.05mm, 0.1mm & 6.6^0) respectively.	Magnetically-coupled resonant WPT-based ECT (WPTECT)	Depth, Width & angle

6.7 Chapter Summary

This chapter contributes to the design, development and evaluation of five different topologies of WPTECT and their response optimisation for the characterisation of inclined angular RCF cracks. The study achievement compares the response of different WPTECT topologies for potentials of achieving multiple resonances and less sensitivity to lift-off distances, including preferred feature extraction for inclined angular RCF cracks characterisation. The results show that parallel-parallel (P-P) topology and combined parallel/series-parallel/serial (PS-PS) topology provide multiple resonances for multiple feature points within the operating frequency range and other experimental conditions. It also includes the results of multiple peak magnitudes and frequencies of the WPTECT response, which are more affected by the coupling between Tx-Rx and sample due to variation of the lift-off distance in addition to the defect depth parameters. In contrast, the sample effect of conductivity and permeability on the multiple peak magnitude is more pronounced at the first peak magnitude.

The optimisation results show that the PP and PS-PS topologies exhibited the lowest critical coupling point by providing multiple resonances within the considered experimental parameters and variables. Compared to other WPTECT basic topologies, the combined parallel-series (PS-PS) topology better suppresses lift-off and sample influence due to its lowest sensitivity to lift-off distances. The optimised PS-PS topology combined the advantages of series (Ca) and shunt (Cb) capacitors in each Tx and Rx network by reducing the coil's effective reactance and sharing the total reactive power to maintain oscillation and serves as impedance matching [298]. It also benefits multiple resonances at different frequencies with the higher frequency resonance for better surface information and lower frequency resonance for better subsurface information. Thus, it is applied to characterise the inclined angular RCF cracks furtherly.

The multiple resonances for multiple feature points and principal components analysis features from the response of optimised PS-PS topology mapped the parameters of the inclined angular RCF crack. Responding to crack parameters, the extracted features from the magnitude of the second resonance point are always better than those from the first magnitude. The study compared the quantification results of RCF parameters with the other related literature to show the capability of the multiple-resonance response of WPTECT on responding to eddy current losses in the sample and defect. These advantages lead to characterising the entire parameters of inclined angular RCF cracks in a measurement result, unlike other techniques that quantified one parameter by assuming other parameters as constant, despite their influence on the response

signal [43-47]. The reconstructed depth, opening width, and angle of the RCF crack have maximum goodness of fit of a model correlation, R^2-value of 96.4%, 93.1%, and 79.1%, respectively. Similarly, it has a minimum RMSE of 0.05mm, 0.08mm, and 6.6^0 for the depth, opening width, and angle of the RCF crack parameters, respectively. The demonstrated crack characterisation results are only given for the surface characterisation of the RCF crack parameter in a ferromagnetic material which can be extended to natural RCF cracks in railway sites as future work.

Chapter 7. Conclusion and Further Work

The studies in this thesis have investigated defect detection and characterisation using magnetically-coupled resonant wireless power transfer (WPT)-based eddy current testing (WPTECT) of metallic structures such as pipelines and rail lines. It has designed and developed WPTECT systems for slots quantification in aluminium blocks, integrated flexible printed coils array to the designed WPTECT and applied to pipeline inspection, and then optimised the different circuit topologies for WPTECT quantitative NDT&E and applied to rail line material. Therefore, this final chapter summarises the thesis deductions, significant contributions in the different conducted studies and suggests the probable enhancement of the WPTECT for the NDT&E system in terms of future research projections.

7.1 Research Conclusion

The extensive application of the ECT for NDT&E in the rail lines and oil and gas pipeline industries for assessment of their structural integrity is due to its responsive qualities to inspection at different environments, including harsh environments with low operating cost, broad operating conditions, ease of integration into other NDT&E techniques among other things. These merits could not be harnessed without their associated problems and challenges. For the configuration of ECT probe structure, the challenges to defect detection and characterisation of ECT include low efficient energy transfer to yield the most heightened sensitivity to defects, the limited number of features for mapping to defect parameters, the influence of sample parameters, and lift-off noise. This study modified ECT inspection to operate at maximum energy transfer with multiple feature points and optimised their response capability for multiple resonances at optimal feature points using Tx-Rx probes from the concept of magnetically-coupled resonant WPT for electric vehicle charging. The advantages of magnetically-coupled resonant probes coupled to the shifting and splitting resonance frequency response of WPTECT include efficient multiple parameters information for defects characterise. Particularly defect characterisation in a complex or curved surface like a pipeline and rolling contact defect in a rail line which remains a challenge to ECT.

The purpose of this study was to design, develop, and investigate magnetically-coupled resonant WPTECT for assessing metallic structures and defects non-destructively. These novels' WPTECT probes operate at the resonance frequency, allowing maximum energy transfer and potentially producing multiple feature points for freedom of feature selection and optimal defect evaluation to overcome the fewer feature points and degradation of weak ECT

signals. The advanced new sets of features used in this study investigation were the multiple resonance points magnitudes and their frequencies, including their minima point, and another statistical analysis of the response shape from the principal component analysis. The extracted features were evaluated and compared, including their fusion, for defect characterisation in the application of pipeline defect and fatigue cracks in railway material investigations.

The investigation started with developing the WPTECT model using a traditional rigid Tx-Rx coils probe to investigate multiple features for different crack parameters quantification in aluminium blocks as a novel ECT. Then, it integrated WPT and flexible coils array to compare the multiple features, including their fusion for 3D reconstruction of the dented area in a pipeline due to corrosion and metal loss. Thirdly, it investigated the responses of different WPTECT topologies optimisation and evaluated inclined RCF cracks in railway material using optimised WPTECT topology. The three investigated models of WPTECT is centred around three independent pieces of research achievement mentioned in the below three paragraphs.

1. The first designed WPTECT model developed and investigated the response of series-series (SS) WPTECT topology on scanning two Aluminium samples containing eight slots based on high-frequency ECT. The SS topology provides a higher current at the resonance point, leading to higher flux passing through the sample linking to the receiver coil. The resonance frequency points and statistical approach, based on principal components analysis, from the shape of the response, have been achieved and compared. The relationships, features to parameters, were appropriately evaluated to quantify the slots parameters on the two samples. It has been found that the slot width along the scan-axis is related to the width of the two sides, before and after the slot, where eddy-current density is highest and the smaller the slot depth, the higher the frequency features and the lower the magnitude feature. The multiple features to multiple parameters relationship make the WPTECT approach a valuable platform for improving ECT probe on comprehensive quantitative non-destructive evaluation (QNDE) through multiple feature extraction and mapping to the slots parameters for scanning metallic structures non-destructively.
2. The recent progression of inductive wireless power transfer (WPT) and flexible printed devices opens opportunities to address defect detection and reconstruction challenges under complex geometric situations. Chapter 5 of this study addressed this challenge. It integrated parallel topology of WPTECT, sweep frequency excitation, and flexible printed coils array to reconstruct dented areas in a pipeline due to natural corrosion and metal loss. The explored flexible probe contributes to ECT on complex structures, where scanning is not feasible for area mapping, in addition to multiple feature points capability. The results of chapter 5

evaluated the two magnitudes features of the dual resonant response and the principal components analysis from the shape of the two resonant areas for correlation analysis, feature selection, and fusion. The second resonance peak values feature (m2) has the highest correlation with the dented area's depth profile based on R-squared value and mean square error compared to other single features. Also, the deep learning-based multiple feature fusion outperforms canonical correlation analysis feature fusion and non-fused features for the 3D reconstruction of the dent, based on its lowest mean square error and highest R-squared value**.** The merit of the chapter is overcoming the challenges of inspecting complex curved structures, pipelines, where scanning is not feasible using multiple features comparison, as mentioned in section 2.3.2 of the literature review.

3. The response of the Eddy current testing (ECT) system is affected by variations in magnetic permeability around the defect in addition to the lift-off issue for inspection of a ferrous metal structure. Also, the transfer responses of different WPTECT topologies are distinct due to their different quality factor expressions and unique impedance matching, leading to different measurement performances. This study presented the results of comparing five different topologies of WPTECT for multiple feature points capabilities and their extracted extrema-resonance points and shape of the response as features in chapter 6. The results also included features extraction for the characterisation of inclined angular RCF cracks from an optimised topology. From the topology's comparison, the parallel-parallel (P-P) topology and combined parallel/series-parallel/serial (PS-PS) topology provided multiple resonances within the range of operating frequency and other experimental parameters. The magnitude and frequency of the multiple peak responses were more affected by the coupling variation due to changes in lift-off distance. In contrast, the sample conductivity and permeability changes were more noticeable in the response magnitude. The features from the response of PS-PS topology characterised the inclined angular RCF crack capably in a measurement result contrary to other techniques that quantify one parameter keeping the others fixed. The second resonance magnitude feature was always better than the first magnitude due to the higher frequencies' sensitivity to surface defects. The merits of presented results in chapter 6 were the optimal topology assessment and characterisation of the whole parameters of inclined angular RCF cracks at a measurement, unlike other methods that quantify one parameter while others are fixed.

The transfer response of WPTECT quantified different defect parameters by providing energy-efficient multiple point-based and principal component analysis features from the

response shape. The magnitude and frequency of the resonance point-based features, including that of the minimum point in-between the two resonance (maxima) points (m1, m0, m2, f1, f0, f2), are the novel feature points (known as the extrema point) unique to WPTECT response that other ECT methods have never utilised prior to this study. In comparison, the principal component analysis features are the statistical features computed based on the principal components. The first three highest principal components were used in this study for QNDE of the investigated defects due to their highest deviation with respect to the presence of a defect. These were the multiple features in addition to the fused features utilised in this study.

This WPTECT study is the first comprehensive investigation of integrating magnetically-coupled resonant WPT and ECT in NDT&E for maximum energy transfer and multiple feature points. Prior to this study, the Tx-Rx ECT probe response operated at low efficiency and with fewer feature points capability for quantitative NDT&E of materials and defects. However, the source of weakness in this study that could limit WPTECT from responding with multiple resonances was the absence of sweeping frequency excitation and very low coupling between primary and secondary coils. Furthermore, some critical areas in this study have not been given much attention due to time limitations or measuring instruments' capability. Some of these areas are presented in the next section as this research future work.

7.2 Research Further Work

A magnetically-coupled resonant WPTECT is expected to further research based on the conclusion drawn from this study to develop an excellent system of materials' defect detection and characterisation of metallic structures, such as pipelines, rail lines, and so on

1) The study used different metallic samples, such as nonferrous metallic samples in chapter 4 and ferrous metallic samples in chapters 5 and 6 with different topologies of the WPTECT. This thesis has not studied the comparison of differences like properties of metallic samples as it’s from different case examples, though the ferrous and nonferrous metallic samples have different properties (permeability, conductivity, geometry, among others) that can lead to optimising topology for specific material inspection. The sample parameters, including the lift-off noise, affect the WPTECT system’s response, leading to different samples inspection with different responses to the distinct topology of WPTECT due to their different material properties in addition to their geometrical nature. Future work will further investigate the optimisation of the ‘M’ shape response from the magnetically-coupled resonant WPTECT transfer function. The multiple features of the WPTECT response are

responding differently to different sample parameters. Therefore, future work can focus on the WPTECT topologies optimisation for material characterisation to investigate each of the multiple feature's appropriateness to each individual sample parameter and possibly the surrounding properties like in multiple layer behaviour. A similar future study can lead to comprehensive multiple layer characterisation, as in the case of two concentric conductive tubes in nuclear reactor fuel channels, consisting of a pressure tube (PT) contained within a calandria tube (CT) mentioned in the literature review, subsection 2.3.1.2.

2) Future work will extend the study of WPTECT systems using miniaturised WPT IC chips as portable systems or a permanently installed sensor system for in-situ structural health monitoring especially using an optimised topology of WPTECT. It can be programmed to automatically extract, select, correlate, and fuse the multiple features proportionate to each defect parameter and make their characterisation easier to integrate into artificial intelligence and the internet of things (AIoT). It can also include the flexible printed coils array probe for a permanent monitoring system, due to its unique characteristics mentioned in subsection 2.3.2. to pipeline and other complex geometric shapes samples.
3) There have been some attractive advances recognised in this thesis arising from the splitting resonance frequency of WPTECT transfer response (S21) that needs additional study. In this thesis, majorly analysis of the S21 frequency and magnitude at the resonance points in addition to the principal component analysis was carried out for sweep frequency excitation, including its topology analysis for multiple resonance capability. However, the transfer response, S21 is a complex parameter with real, imaginary, and phase angle. Each component can give different performance measures to certain sample and defect parameters. The same experimental set-ups used in chapters 4, 5, and 6 results can be used for the multiple phase features analysis. It could be possible for the phase feature to outperform the frequency and magnitude features for QNDE as demonstrated in ref [213, 299] for the evaluation of sample parameters.
4) The excitation frequency in this study extended to the high-frequency band, which is more sensitive to surface defect information but not suitable for subsurface and deeper surface information due to the skin depth factor. Future work can focus on the range of excitation frequencies within the lower frequency band to inspect subsurface and external defects in addition to the surface defects evaluation conducted in this study.

References

[1] K. Lu, "The Future of Metals," *Science*, vol. 328, no. 5976, pp. 319-320, 2010, doi: 10.1126/science.1185866.

[2] S. J. Findlay and N. D. Harrison, "Why aircraft fail," *Materials Today*, vol. 5, no. 11, pp. 18-25, 2002/11/01/ 2002, doi: https://doi.org/10.1016/S1369-7021(02)01138-0.

[3] M. Lu *et al.*, "Thickness measurement of circular metallic film using single-frequency eddy current sensor," *NDT & E International*, vol. 119, p. 102420, 2021/04/01/ 2021, doi: https://doi.org/10.1016/j.ndteint.2021.102420.

[4] A. N. AbdAlla, M. A. Faraj, F. Samsuri, D. Rifai, K. Ali, and Y. Al-Douri, "Challenges in improving the performance of eddy current testing: Review," *Measurement and Control*, vol. 52, no. 1-2, pp. 46-64, 2019, doi: 10.1177/0020294018801382.

[5] A. Sophian, G. Y. Tian, and M. Fan, "Pulsed Eddy Current Non-destructive Testing and Evaluation: A Review," *Chinese Journal of Mechanical Engineering*, vol. 30, no. 3, pp. 500-514, 2017/05/01 2017, doi: 10.1007/s10033-017-0122-4.

[6] X. Xu, M. Liu, Z. Zhang, and Y. Jia, "A Novel High Sensitivity Sensor for Remote Field Eddy Current Non-Destructive Testing Based on Orthogonal Magnetic Field," *Sensors*, vol. 14, no. 12, 2014, doi: 10.3390/s141224098.

[7] W. Shi, W. Chen, C. Lu, J. Zhang, Y. Chen, and W. Xu, "Optimal Design of Spiral Coil EMATs for Improving Their Pulse Compression Effect," *Journal of Nondestructive Evaluation*, vol. 40, no. 2, p. 38, 2021/04/23 2021, doi: 10.1007/s10921-021-00771-z.

[8] D. Si, B. Gao, W. Guo, Y. Yan, G. Y. Tian, and Y. Yin, "Variational mode decomposition linked wavelet method for EMAT denoise with large lift-off effect," *NDT & E International*, vol. 107, p. 102149, 2019/10/01/ 2019, doi: https://doi.org/10.1016/j.ndteint.2019.102149.

[9] G. Piao, J. Li, L. Udpa, S. Udpa, and Y. Deng, "The Effect of Motion-Induced Eddy Currents on Three-Axis MFL Signals for High-Speed Rail Inspection," *IEEE Transactions on Magnetics*, vol. 57, no. 4, pp. 1-11, 2021, doi: 10.1109/TMAG.2021.3060390.

[10] Y. Long, S. Huang, L. Peng, S. Wang, and W. Zhao, "A Characteristic Approximation Approach to Defect Opening Profile Recognition in Magnetic Flux Leakage Detection," *IEEE Transactions on Instrumentation and Measurement*, vol. 70, pp. 1-12, 2021, doi: 10.1109/TIM.2021.3050185.

[11] Y. Jiang, H. Wang, S. Chen, and G. Tian, "Visual quantitative detection of rail surface crack based on laser ultrasonic technology," *Optik*, vol. 237, p. 166732, 2021/07/01/ 2021, doi: https://doi.org/10.1016/j.ijleo.2021.166732.

[12] R. E. Malkin, A. C. Franklin, R. L. T. Bevan, H. Kikura, and B. W. Drinkwater, "Surface reconstruction accuracy using ultrasonic arrays: Application to non-destructive testing," *NDT & E International*, vol. 96, pp. 26-34, 2018/06/01/ 2018, doi: https://doi.org/10.1016/j.ndteint.2018.03.004.

[13] R. Sutthaweekul, G. Tian, Z. Wang, and F. Ciampa, "Microwave open-ended waveguide for detection and characterisation of FBHs in coated GFRP pipes," *Composite Structures*, vol. 225, p. 111080, 2019/10/01/ 2019, doi: https://doi.org/10.1016/j.compstruct.2019.111080.

[14] M. D. Buhari, G. Y. Tian, and R. Tiwari, "Microwave-Based SAR Technique for Pipeline Inspection Using Autofocus Range-Doppler Algorithm," *IEEE Sensors Journal*, vol. 19, no. 5, pp. 1777-1787, 2019, doi: 10.1109/JSEN.2018.2879348.

[15] Z. Jin *et al.*, "Methods of Controlling Lift-Off in Conductivity Invariance Phenomenon for Eddy Current Testing," *IEEE Access*, vol. 8, pp. 122413-122421, 2020, doi: 10.1109/ACCESS.2020.3007216.

[16] D. J. Pasadas, P. Baskaran, H. G. Ramos, and A. L. Ribeiro, "Detection and Classification of Defects Using ECT and Multi-Level SVM Model," *IEEE Sensors Journal*, vol. 20, no. 5, pp. 2329-2338, 2020, doi: 10.1109/JSEN.2019.2951302.

[17] D. I. Ona, G. Y. Tian, R. Sutthaweekul, and S. M. Naqvi, "Design and optimisation of mutual inductance based pulsed eddy current probe," *Measurement*, vol. 144, pp. 402-409, 2019/10/01/ 2019, doi: https://doi.org/10.1016/j.measurement.2019.04.091.

[18] W. Cheng and H. Hashizume, "Determination of Layers' Thicknesses by Spectral Analysis of Swept-Frequency Measurement Signals," *IEEE Sensors Journal*, vol. 20, no. 15, pp. 8643-8655, 2020, doi: 10.1109/JSEN.2020.2982944.

[19] A. Kurs, A. Karalis, R. Moffatt, J. D. Joannopoulos, P. Fisher, and M. Soljačić, "Wireless Power Transfer via Strongly Coupled Magnetic Resonances," *Science*, vol. 317, no. 5834, p. 83, 2007, doi: 10.1126/science.1143254.

[20] Y. Zhuang, A. Chen, C. Xu, Y. Huang, H. Zhao, and J. Zhou, "Range-Adaptive Wireless Power Transfer Based on Differential Coupling using Multiple Bi-directional Coils," *IEEE Transactions on Industrial Electronics*, pp. 7519-7528, 2019, doi: 10.1109/TIE.2019.2945304.

[21] Z. Liao, Y. Sun, Z. Ye, C. Tang, and P. Wang, "Resonant Analysis of Magnetic Coupling Wireless Power Transfer Systems," *IEEE Transactions on Power Electronics*, vol. 34, no. 6, pp. 5513-5523, 2019, doi: 10.1109/TPEL.2018.2868727.

[22] C. Wu, Z. Zhang, X. Cheng, and G. Xie, "An integrated multimode battery charger in a Qi compliant wireless power receiver," *Analog Integrated Circuits and Signal Processing*, 2020/01/14 2020, doi: 10.1007/s10470-019-01582-z.

[23] L. U. Daura, G. Y. Tian, Q. Yi, and A. Sophian, "Wireless power transfer-based eddy current non-destructive testing using a flexible printed coil array," *Philosophical Transactions of the Royal Society A: Mathematical, Physical and Engineering Sciences*, vol. 378, no. 2182, p. 20190579, 2020, doi: doi:10.1098/rsta.2019.0579.

[24] L. U. Daura and G. Y. Tian, "Wireless Power Transfer Based Non-Destructive Evaluation of Cracks in Aluminum Material," *IEEE Sensors Journal*, vol. 19, no. 22, pp. 10529-10536, 2019, doi: 10.1109/JSEN.2019.2930738.

[25] T. Chen, G. Y. Tian, A. Sophian, and P. W. Que, "Feature extraction and selection for defect classification of pulsed eddy current NDT," *NDT & E International*, vol. 41, no. 6, pp. 467-476, 2008/09/01/ 2008, doi: https://doi.org/10.1016/j.ndteint.2008.02.002.

[26] H. Tesfalem, A. D. Fletcher, M. Brown, B. Chapman, and A. J. Peyton, "Study of asymmetric gradiometer sensor configurations for eddy current based non-destructive testing in an industrial environment," *NDT & E International*, vol. 100, pp. 1-10, 2018/12/01/ 2018, doi: https://doi.org/10.1016/j.ndteint.2018.07.007.

[27] A. Sophian, G. Y. Tian, D. Taylor, and J. Rudlin, "Electromagnetic and eddy current NDT: a review," *Insight Non Destr Test Cond Monit*, vol. 43, no. 5, pp. 302-306, 2001.

[28] L. Janousek, A. Stubendekova, and M. Smetana, "Novel insight into swept frequency eddy-current non-destructive evaluation of material defects," *Measurement*, vol. 116, pp. 246-250, 2018/02/01/ 2018, doi: https://doi.org/10.1016/j.measurement.2017.11.039.

[29] A. Stubendekova and L. Janousek, "Influence of selected defect parameter on response signals in swept frequency electromagnetic nondestructive testing," *2016 ELEKTRO*, pp. 593-596, 16-18 May 2016 2016, doi: 10.1109/ELEKTRO.2016.7512146.

[30] X. Mao and Y. Lei, "Thickness measurement of metal pipe using swept-frequency eddy current testing," *NDT & E International*, vol. 78, pp. 10-19, 2016/03/01/ 2016, doi: https://doi.org/10.1016/j.ndteint.2015.11.001.

[31] C.-C. Tai, "Characterization of coatings on magnetic metal using the swept-frequency eddy current method," *Review of Scientific Instruments*, vol. 71, no. 8, pp. 3161-3167, 2000, doi: 10.1063/1.1304862.

[32] J. Svatos and J. Vedral, "The Usage of Frequency Swept Signals for Metal Detection," *IEEE Transactions on Magnetics*, vol. 48, no. 4, pp. 1501-1504, 2012, doi: 10.1109/TMAG.2011.2173174.

[33] R. R. Hughes and S. Dixon, "Performance analysis of single-frequency near electrical resonance signal enhancement (SF-NERSE) defect detection," *NDT & E International*, vol. 102, pp. 96-103, 2019/03/01/ 2019, doi: https://doi.org/10.1016/j.ndteint.2018.11.008.

[34] J. S. Kim, S. H. Im, and G. S. Park, "A study on the skin effect and eddy current distributions in conductive media," in *2017 20th International Conference on Electrical Machines and Systems (ICEMS)*, 11-14 Aug. 2017 2017, pp. 1-4, doi: 10.1109/ICEMS.2017.8056094.

[35] Z. Zhang, H. Pang, A. Georgiadis, and C. Cecati, "Wireless Power Transfer—An Overview," *IEEE Transactions on Industrial Electronics*, vol. 66, no. 2, pp. 1044-1058, 2019, doi: 10.1109/TIE.2018.2835378.

[36] P. Machura and Q. Li, "A critical review on wireless charging for electric vehicles," *Renewable and Sustainable Energy Reviews*, vol. 104, pp. 209-234, 2019/04/01/ 2019, doi: https://doi.org/10.1016/j.rser.2019.01.027.

[37] W. Niu, J. Chu, W. Gu, and A. Shen, "Exact Analysis of Frequency Splitting Phenomena of Contactless Power Transfer Systems," *IEEE Transactions on Circuits and Systems I: Regular Papers*, vol. 60, no. 6, pp. 1670-1677, 2013, doi: 10.1109/TCSI.2012.2221172.

[38] C. Yang, B. Gao, Q. Ma, L. Xie, G. Y. Tian, and Y. Yin, "Multi-Layer Magnetic Focusing Sensor Structure for Pulsed Remote Field Eddy Current," *IEEE Sensors Journal*, vol. 19, no. 7, pp. 2490-2499, 2019, doi: 10.1109/JSEN.2018.2886816.

[39] Z. Petrovic, "Catastrophes caused by corrosion," *Vojnotehnicki glasnik*, vol. 64, pp. 1048-1064, 01/01 2016, doi: 10.5937/vojtehg64-10388.

[40] J. Zhu *et al.*, "Characterization of Rolling Contact Fatigue Cracks in Rails by Eddy Current Pulsed Thermography," *IEEE Transactions on Industrial Informatics*, vol. 17, no. 4, pp. 2307-2315, 2021, doi: 10.1109/TII.2020.3003335.

[41] M. Ph Papaelias, C. Roberts, and C. L. Davis, "A review on non-destructive evaluation of rails: State-of-the-art and future development," *Proceedings of the Institution of Mechanical Engineers, Part F: Journal of Rail and Rapid Transit*, vol. 222, no. 4, pp. 367-384, 2008, doi: 10.1243/09544097jrrt209.

[42] S. L. Grassie, "Rolling contact fatigue on the British railway system: treatment," *Wear*, vol. 258, no. 7, pp. 1310-1318, 2005/03/01/ 2005, doi: https://doi.org/10.1016/j.wear.2004.03.065.

[43] J. Zhu, G. Y. Tian, Q. Min, and J. Wu, "Comparison Study of Different Features for Pocket Length Quantification of Angular Defects Using Eddy Current Pulsed Thermography," *IEEE Transactions on Instrumentation and Measurement*, vol. 68, no. 5, pp. 1373-1381, 2019, doi: 10.1109/TIM.2018.2890053.

[44] J. Zhu, Q. Min, J. Wu, and G. Y. Tian, "Probability of Detection for Eddy Current Pulsed Thermography of Angular Defect Quantification," *IEEE Transactions on Industrial Informatics*, vol. 14, no. 12, pp. 5658-5666, 2018, doi: 10.1109/TII.2018.2866443.

[45] F. Nafiah, A. Sophian, M. R. Khan, and I. M. Zainal Abidin, "Quantitative evaluation of crack depths and angles for pulsed eddy current non-destructive testing," *NDT & E International*, vol. 102, pp. 180-188, 2019/03/01/ 2019, doi: https://doi.org/10.1016/j.ndteint.2018.11.019.

[46] Y. Jiang, H. Wang, G. Y. Tian, Q. Yi, J. Zhao, and K. Zhen, "Fast classification for rail defect depths using a hybrid intelligent method," *Optik*, vol. 180, pp. 455-468, 2019/02/01/ 2019, doi: https://doi.org/10.1016/j.ijleo.2018.11.053.

[47] H. Xia, J. Wu, Z. Xu, J. Wang, and C. Wang, "Defect Visualization and Depth Quantification in Scanning Induction Thermography," *IEEE Sensors Journal*, vol. 21, no. 9, pp. 10437-10444, 2021, doi: 10.1109/JSEN.2021.3060916.

[48] A. Cosham and P. Hopkins, "The effect of dents in pipelines—guidance in the pipeline defect assessment manual," *International Journal of Pressure Vessels and Piping*, vol. 81, no. 2, pp. 127-139, 2004/02/01/ 2004, doi: https://doi.org/10.1016/j.ijpvp.2003.11.004.

[49] W. Yin *et al.*, "Permeability invariance phenomenon and measurement of electrical conductivity for ferrite metallic plates," *Insight - Non-Destructive Testing and Condition Monitoring*, vol. 61, pp. 472-479, 08/01 2019, doi: 10.1784/insi.2019.61.8.472.

[50] S. K. Dwivedi, M. Vishwakarma, and P. A. Soni, "Advances and Researches on Non Destructive Testing: A Review," *Materials Today: Proceedings*, vol. 5, no. 2, Part 1, pp. 3690-3698, 2018/01/01/ 2018, doi: https://doi.org/10.1016/j.matpr.2017.11.620.

[51] F. Li, J. Feng, H. Zhang, J. Liu, S. Lu, and D. Ma, "Quick Reconstruction of Arbitrary Pipeline Defect Profiles From MFL Measurements Employing Modified Harmony Search Algorithm," *IEEE Transactions on Instrumentation and Measurement*, vol. 67, no. 9, pp. 2200-2213, 2018, doi: 10.1109/TIM.2018.2813839.

[52] H. M. Kim, C. G. Heo, S. H. Cho, and G. S. Park, "Determination Scheme for Accurate Defect Depth in Underground Pipeline Inspection by Using Magnetic Flux Leakage Sensors," *IEEE Transactions on Magnetics*, vol. 54, no. 11, pp. 1-5, 2018, doi: 10.1109/TMAG.2018.2853618.

[53] R. L. Qingshan Feng, Baohua Nie, Shucong Liu, Lianyu Zhao and Hong Zhang, "Literature Review: Theory and Application of In-Line Inspection Technologies for Oil and Gas Pipeline Girth Weld Defection," *Sensors*, vol. 17, no. 50, 2017, doi: 10.3390/s17010050.

[54] Y. Shi, C. Zhang, R. Li, M. Cai, and G. Jia, "Theory and Application of Magnetic Flux Leakage Pipeline Detection," *Sensors*, vol. 15, no. 12, 2015, doi: 10.3390/s151229845.

[55] A. G. Antipov and A. A. Markov, "Evaluation of transverse cracks detection depth in MFL rail NDT," *Russian Journal of Nondestructive Testing*, vol. 50, no. 8, pp. 481-490, 2014/08/01 2014, doi: 10.1134/S1061830914080026.

[56] J. E. Garnham, F. J. Franklin, D. I. Fletcher, A. Kapoor, and C. L. Davis, "Predicting the life of steel rails," *Proceedings of the Institution of Mechanical Engineers, Part F: Journal of Rail and Rapid Transit*, vol. 221, no. 1, pp. 45-58, 2007, doi: 10.1243/09544097jrrt66.

[57] Y. Ege and M. Coramik, "A new measurement system using magnetic flux leakage method in pipeline inspection," *Measurement*, vol. 123, pp. 163-174, 2018/07/01/ 2018, doi: https://doi.org/10.1016/j.measurement.2018.03.064.

[58] A. L. Pullen, P. C. Charlton, N. R. Pearson, and N. J. Whitehead, "Magnetic Flux Leakage Scanning Velocities for Tank Floor Inspection," *IEEE Transactions on Magnetics*, pp. 1-8, 2018, doi: 10.1109/TMAG.2018.2853117.

[59] X.-c. Song, S.-l. Huang, and W. Zhao, "Optimization of the magnetic circuit in the MFL inspection system for storage-tank floors," *Russian Journal of Nondestructive Testing*, vol. 43, no. 5, pp. 326-331, 2007/05/01 2007, doi: 10.1134/S1061830907050063.

[60] H. M. Kim, H. R. Yoo, and G. S. Park, "A New Design of MFL Sensors for Self-Driving NDT Robot to Avoid Getting Stuck in Curved Underground Pipelines," *IEEE Transactions on Magnetics*, 2018, doi: 10.1109/TMAG.2018.2846283.

[61] A. G. Antipov and A. A. Markov, "3D simulation and experiment on high speed rail MFL inspection," *NDT & E International*, vol. 98, pp. 177-185, 2018/09/01/ 2018, doi: https://doi.org/10.1016/j.ndteint.2018.04.011.

[62] H. Q. Pham, Q. T. Trinh, D. T. Doan, and Q. H. Tran, "Importance of Magnetizing Field on Magnetic Flux Leakage Signal of Defects," *IEEE Transactions on Magnetics*, vol. 54, no. 6, pp. 1-6, 2018, doi: 10.1109/TMAG.2018.2809671.

[63] a. T. M. Chukwunonso K. Okolo, "Pulsed magnetic flux leakage method for hairline crack detection and characterization," *American Institute of Physics*, vol. 8, pp. 047207/1 - 047207/12, 2018, doi: 10.1063/1.4994187.

[64] G. Kopp and H. Willems, "Sizing limits of metal loss anomalies using tri-axial MFL measurements: A model study," *NDT & E International*, vol. 55, pp. 75-81, 2013/04/01 2013, doi: https://doi.org/10.1016/j.ndteint.2013.01.011.

[65] J. Wu, Y. Sun, Y. Kang, and Y. Yang, "Theoretical Analyses of MFL Signal Affected by Discontinuity Orientation and Sensor-Scanning Direction," *IEEE Transactions on Magnetics*, vol. 51, no. 1, pp. 1-7, 2015, doi: 10.1109/TMAG.2014.2350460.

[66] B. Liu, L.-y. He, H. Zhang, Y. Cao, and H. Fernandes, "The axial crack testing model for long distance oil-gas pipeline based on magnetic flux leakage internal inspection method," *Measurement*, vol. 103, pp. 275-282, 2017/06/01/ 2017, doi: https://doi.org/10.1016/j.measurement.2017.02.051.

[67] T. Azizzadeh and M. Safizadeh, "Identification and Sizing of Neighboring Pits Using Three-Axis Magnetic Flux Leakage Technique," *Journal of Testing and Evaluation*, vol. 49, no. 3, pp. 1837-1852, 05/01 2021, doi: 10.1520/JTE20180287.

[68] S. Liu *et al.*, "A novel method of omnidirectional defects detection by MFL testingunder single axial magnetization at the production stage of lathyferromagnetic materials," *Sensors and Actuators A*, vol. 262, pp. 35–45, 2017. [Online]. Available: http://dx.doi.org/10.1016/j.sna.2017.04.038.

[69] D. Zhiye *et al.*, "3-D FEM Simulation of Velocity Effects on Magnetic Flux Leakage Testing Signals," *IEEE Transactions on Magnetics*, vol. 44, no. 6, pp. 1642-1645, 2008, doi: 10.1109/TMAG.2007.915955.

[70] Z. Chen, J. Xuan, P. Wang, H. Wang, and G. Tian, "Simulation on high speed rail magnetic flux leakage inspection," in *2011 IEEE International Instrumentation and Measurement Technology Conference*, 10-12 May 2011 2011, pp. 1-5, doi: 10.1109/IMTC.2011.5944294.

[71] P. Wang, Y. Gao, G. Tian, and H. Wang, "Velocity effect analysis of dynamic magnetization in high speed magnetic flux leakage inspection," *NDT & E International*, vol. 64, pp. 7-12, 2014/06/01/ 2014, doi: https://doi.org/10.1016/j.ndteint.2014.02.001.

[72] B. Feng, Y. Kang, Y. Sun, and Z. Deng, "Magnetization Time Lag Caused by Eddy Currents and Its Influence on High-Speed Magnetic Flux Leakage Testing," *Research in Nondestructive Evaluation*, pp. 1-16, 2018, doi: 10.1080/09349847.2018.1459988.

[73] C. K. W. Okolo, "Modelling and Experimental Investigation of Magnetic Flux Leakage Distribution for Hairline Crack Detection and Characterization," PhD, Wolfson Centre for Magnetics, School of Engineering, Cardiff University, unpublish PhD Thesis, C1049450, 2018.
[74] A. Simm, "Quantitative Interpretation of Magnetic Field Measurements in Eddy Current Defect Detection," PhD, School of Electrical and Electronic Engineering Newcastle University, Newcastle University, Unpublish PhD thesis, 2012.
[75] A. P. Juna, "On the characterisation and detection of Rolling Contact Fatigue (RCF) type cracks in railway vehicle wheels using an Alternating Current Field Measurement (ACFM) technique," PhD, School of Metallurgy and Materials, University of Birmingham, unpublish PhD Thesis, 2017.
[76] H. R. Vanaei, A. Eslami, and A. Egbewande, "A review on pipeline corrosion, in-line inspection (ILI), and corrosion growth rate models," *International Journal of Pressure Vessels and Piping*, vol. 149, pp. 43-54, 2017/01/01/ 2017, doi: https://doi.org/10.1016/j.ijpvp.2016.11.007.
[77] A. M. Lewis, D. H. Michael, M. C. Lugg, and R. Collins, "Thin-skin electromagnetic fields around surface-breaking cracks in metals," *Journal of Applied Physics*, vol. 64, no. 8, pp. 3777-3784, 1988, doi: 10.1063/1.341384.
[78] W. Dover, R. Collins, and D. H. Michael, "Review of developments in ACPD and ACFM," *British Journal of Non-Destructive Testing*, vol. 33, pp. 121-127, 03/01 1991.
[79] S. Zhao, L. Sun, J. Gao, J. Wang, and Y. Shen, "Uniaxial ACFM detection system for metal crack size estimation using magnetic signature waveform analysis," *Measurement*, vol. 164, p. 108090, 2020/11/01/ 2020, doi: https://doi.org/10.1016/j.measurement.2020.108090.
[80] W. Li, X. a. Yuan, G. Chen, J. Ge, X. Yin, and K. Li, "High sensitivity rotating alternating current field measurement for arbitrary-angle underwater cracks," *NDT & E International*, vol. 79, pp. 123-131, 2016/04/01/ 2016, doi: https://doi.org/10.1016/j.ndteint.2016.01.003.
[81] Y. Feng, L. Zhang, and W. Zheng, "Simulation analysis and experimental study of an alternating current field measurement probe for pipeline inner inspection," *NDT & E International*, vol. 98, pp. 123-129, 2018/09/01/ 2018, doi: https://doi.org/10.1016/j.ndteint.2018.04.015.
[82] G. L. Nicholson, A. G. Kostryzhev, X. J. Hao, and C. L. Davis, "Modelling and experimental measurements of idealised and light-moderate RCF cracks in rails using an ACFM sensor," *NDT & E International*, vol. 44, no. 5, pp. 427-437, 2011/09/01/ 2011, doi: https://doi.org/10.1016/j.ndteint.2011.04.003.
[83] M. Papaelias, C. Roberts, C. Davis, B. Blakeley, and M. Lugg, "Further developments in high-speed detection of rail rolling contact fatigue using ACFM techniques," *Insight - Non-Destructive Testing and Condition Monitoring*, vol. 52, pp. 358-360, 07/01 2010, doi: 10.1784/insi.2010.52.7.358.
[84] M. P. Papaelias, M. C. Lugg, C. Roberts, and C. L. Davis, "High-speed inspection of rails using ACFM techniques," *NDT & E International*, vol. 42, no. 4, pp. 328-335, 2009/06/01/ 2009, doi: https://doi.org/10.1016/j.ndteint.2008.12.008.
[85] J. Ge, B. Hu, and C. Yang, "Investigation of the approximate decomposition of alternating current field measurement signals from crack colonies," *Mechanical Systems and Signal Processing*, vol. 160, p. 107878, 2021/11/01/ 2021, doi: https://doi.org/10.1016/j.ymssp.2021.107878.
[86] H. Rowshandel, G. L. Nicholson, J. L. Shen, and C. L. Davis, "Characterisation of clustered cracks using an ACFM sensor and application of an artificial neural network," *NDT & E International*, vol. 98, pp. 80-88, 2018/09/01/ 2018, doi: https://doi.org/10.1016/j.ndteint.2018.04.007.
[87] A. Raine and M. Lugg, "A review of the alternating current field measurement inspection technique," *Sensor Review*, vol. 19, no. 3, pp. 207-213, 1999, doi: 10.1108/02602289910279166.
[88] W. Li, X. a. Yuan, G. Chen, X. Yin, and J. Ge, "A feed-through ACFM probe with sensor array for pipe string cracks inspection," *NDT & E International*, vol. 67, pp. 17-23, 2014/10/01/ 2014, doi: https://doi.org/10.1016/j.ndteint.2014.06.006.
[89] C. Guo-ming, L. Wei, and W. Ze-xin, "Structural optimization of 2-D array probe for alternating current field measurement," *NDT & E International*, vol. 40, no. 6, pp. 455-461, 2007/09/01/ 2007, doi: https://doi.org/10.1016/j.ndteint.2007.03.002.

[90] E. E. Magel, "Rolling contact fatigue: a comprehensive review," U.S. Department of Transportation. Federal Railroad Administration, 2011/11 2011.
[91] K. Chen and F. P. Brennan, "A theoretical and experimental study of alternating current stress measurement under different loading modes," *The Journal of Strain Analysis for Engineering Design*, vol. 33, no. 4, pp. 291-303, 1998, doi: 10.1243/0309324981513002.
[92] P. J. Withers, M. Turski, L. Edwards, P. J. Bouchard, and D. J. Buttle, "Recent advances in residual stress measurement," *International Journal of Pressure Vessels and Piping*, vol. 85, no. 3, pp. 118-127, 2008/03/01/ 2008, doi: https://doi.org/10.1016/j.ijpvp.2007.10.007.
[93] S. Hillmann, M. H. Schulze, and H. Heuer, "High-Frequency Eddy Current Techniques," in *Handbook of Advanced Non-Destructive Evaluation*, N. Ida and N. Meyendorf Eds. Cham: Springer International Publishing, 2018, pp. 1-28.
[94] H. Fukutomi, T. Takagi, and M. Nishikawa, "Remote field eddy current technique applied to non-magnetic steam generator tubes," *NDT & E International*, vol. 34, no. 1, pp. 17-23, 2001/01/01/ 2001, doi: https://doi.org/10.1016/S0963-8695(00)00026-8.
[95] Q. Xiao, J. Feng, Z. Xu, and H. Zhang, "Receiver Signal Analysis on Geometry and Excitation Parameters of Remote Field Eddy Current Probe," *IEEE Transactions on Industrial Electronics*, pp. 1-1, 2021, doi: 10.1109/TIE.2021.3063958.
[96] S. She, Y. Chen, Y. He, Z. zhou, and X. Zou, "Optimal design of remote field eddy current testing probe for ferromagnetic pipeline inspection," *Measurement*, vol. 168, p. 108306, 2021/01/15/ 2021, doi: https://doi.org/10.1016/j.measurement.2020.108306.
[97] W. Zhang, Y. Shi, Y. Li, and Q. Luo, "A Study of Quantifying Thickness of Ferromagnetic Pipes Based on Remote Field Eddy Current Testing," *Sensors*, vol. 18, no. 9, p. 2769, 2018. [Online]. Available: https://www.mdpi.com/1424-8220/18/9/2769.
[98] Q. Luo, Y. Shi, Z. Wang, W. Zhang, and Y. Li, "A Study of Applying Pulsed Remote Field Eddy Current in Ferromagnetic Pipes Testing," *Sensors*, vol. 17, no. 5, p. 1038, 2017. [Online]. Available: https://www.mdpi.com/1424-8220/17/5/1038.
[99] R. Falque, T. Vidal-Calleja, and J. V. Miro, "Defect Detection and Segmentation Framework for Remote Field Eddy Current Sensor Data," *Sensors*, vol. 17, no. 10, p. 2276, 2017. [Online]. Available: https://www.mdpi.com/1424-8220/17/10/2276.
[100] Q. Luo, Y. Shi, Z. Wang, W. Zhang, and D. Ma, "Method for Removing Secondary Peaks in Remote Field Eddy Current Testing of Pipes," *Journal of Nondestructive Evaluation*, vol. 36, no. 1, p. 1, 2016/11/22 2016, doi: 10.1007/s10921-016-0379-z.
[101] N. Kobayashi, S. Ueno, S. Nagai, M. Ochiai, and N. Jimbo, "Remote field eddy current testing for steam generator inspection of fast reactor," *Nuclear Engineering and Design*, vol. 241, no. 12, pp. 4643-4648, 2011/12/01/ 2011, doi: https://doi.org/10.1016/j.nucengdes.2011.03.054.
[102] D. Robinson, "Identification and sizing of defects in metallic pipes by remote field eddy current inspection," *Tunnelling and Underground Space Technology*, vol. 13, pp. 17-27, 1998/01/01/ 1998, doi: https://doi.org/10.1016/S0886-7798(98)00090-X.
[103] B. Yang, J. Xu, H. Wu, and Y. He, "Magnetic field shielding technique for pulsed remote field eddy current inspection of planar conductors," *NDT & E International*, vol. 90, pp. 48-54, 2017/09/01/ 2017, doi: https://doi.org/10.1016/j.ndteint.2017.05.001.
[104] H. Wang *et al.*, "Simulation and experimental study of remote field eddy current testing on flat conductive plate," *International Journal of Applied Electromagnetics and Mechanics*, vol. 33, pp. 1261-1266, 2010, doi: 10.3233/JAE-2010-1247.
[105] H. Hoshikawa, H. Saitou, J. Koido, and Y. Ishibashi, "Energy flow in remote field eddy current nondestructive testing," *IEEE Transactions on Magnetics*, vol. 26, no. 2, pp. 885-888, 1990, doi: 10.1109/20.106459.
[106] N. Burais and A. Nicolas, "Electromagnetic field analysis in remote field eddy current testing systems," *IEEE Transactions on Magnetics*, vol. 25, no. 4, pp. 3010-3012, 1989, doi: 10.1109/20.34353.
[107] H. Barkhausen, "Two phenomena revealed with the help of new amplifiers," *Phys. Z*, vol. 29, no. 6, pp. 401-403, 1919.
[108] K. Mandal *et al.*, "Detection of stress concentrations around a defect by magnetic Barkhausen noise measurements," *Journal of Applied Physics*, vol. 80, no. 11, pp. 6391-6395, 1996, doi: 10.1063/1.363657.

[109] P. Vourna, A. Ktena, P. E. Tsakiridis, and E. Hristoforou, "An accurate evaluation of the residual stress of welded electrical steels with magnetic Barkhausen noise," *Measurement*, vol. 71, pp. 31-45, 2015/07/01/ 2015, doi: https://doi.org/10.1016/j.measurement.2015.04.007.

[110] H. Dong, X. Liu, Y. Song, B. Wang, S. Chen, and C. He, "Quantitative evaluation of residual stress and surface hardness in deep drawn parts based on magnetic Barkhausen noise technology," *Measurement*, vol. 168, p. 108473, 2021/01/15/ 2021, doi: https://doi.org/10.1016/j.measurement.2020.108473.

[111] T. W. Krause, L. Clapham, and D. L. Atherton, "Characterization of the magnetic easy axis in pipeline steel using magnetic Barkhausen noise," *Journal of Applied Physics*, vol. 75, no. 12, pp. 7983-7988, 1994, doi: 10.1063/1.356561.

[112] S. Ding, G. Tian, and R. Sutthaweekul, "Non-destructive hardness prediction for 18CrNiMo7-6 steel based on feature selection and fusion of Magnetic Barkhausen Noise," *NDT & E International*, vol. 107, p. 102138, 2019/10/01/ 2019, doi: https://doi.org/10.1016/j.ndteint.2019.102138.

[113] J. Liu, G. Tian, B. Gao, K. Zeng, Y. Xu, and Q. Liu, "Time-Response-Histogram-Based Feature of Magnetic Barkhausen Noise for Material Characterization Considering Influences of Grain and Grain Boundary under In Situ Tensile Test," *Sensors*, vol. 21, no. 7, p. 2350, 2021. [Online]. Available: https://www.mdpi.com/1424-8220/21/7/2350.

[114] F. Qiu, M. Jovičević-Klug, G. Tian, G. Wu, and J. McCord, "Correlation of magnetic field and stress-induced magnetic domain reorientation with Barkhausen Noise," *Journal of Magnetism and Magnetic Materials*, vol. 523, p. 167588, 2021/04/01/ 2021, doi: https://doi.org/10.1016/j.jmmm.2020.167588.

[115] Z. D. Wang, Y. Gu, and Y. S. Wang, "A review of three magnetic NDT technologies," *Journal of Magnetism and Magnetic Materials*, vol. 324, no. 4, pp. 382-388, 2012/02/01/ 2012, doi: https://doi.org/10.1016/j.jmmm.2011.08.048.

[116] K. Zgútová and M. Pitoňák, "Attenuation of Barkhausen Noise Emission due to Variable Coating Thickness," *Coatings*, vol. 11, no. 3, p. 263, 2021. [Online]. Available: https://www.mdpi.com/2079-6412/11/3/263.

[117] J. Heinzel, R. Jedamski, J. Epp, and B. Karpuschewski, "In-process measurement of Barkhausen noise and resulting productivity increase potential in grinding of case hardened steel," *CIRP Journal of Manufacturing Science and Technology*, vol. 32, pp. 37-45, 2021/01/01/ 2021, doi: https://doi.org/10.1016/j.cirpj.2020.11.011.

[118] S. Santa-aho, A. Laitinen, A. Sorsa, and M. Vippola, "Barkhausen Noise Probes and Modelling: A Review," *Journal of Nondestructive Evaluation*, vol. 38, no. 4, p. 94, 2019/09/21 2019, doi: 10.1007/s10921-019-0636-z.

[119] K. Mandal, D. Dufour, and D. L. Atherton, "Use of magnetic Barkhausen noise and magnetic flux leakage signals for analysis of defects in pipeline steel," *IEEE Transactions on Magnetics*, vol. 35, no. 3, pp. 2007-2017, 1999, doi: 10.1109/20.764901.

[120] G. Zhong, G. Y. Tian, J. S. Meng, and B. Gao, "Excitation power design base on series resonant electromagnetic ultrasonic sensor for pipeline NDT," in *2016 IEEE Far East NDT New Technology & Application Forum (FENDT)*, 22-24 June 2016 2016, pp. 131-135, doi: 10.1109/FENDT.2016.7992011.

[121] Z. Wang, S. Wang, Q. Wang, W. Zhao, and S. Huang, "Development of a Helical Lamb Wave Electromagnetic Acoustic Transducer for Pipeline Inspection," *IEEE Sensors Journal*, vol. 20, no. 17, pp. 9715-9723, 2020, doi: 10.1109/JSEN.2020.2990795.

[122] D. Si *et al.*, "EMD of EMAT NDT in X70 Pipeline Weld Defects," in *2017 Far East NDT New Technology & Application Forum (FENDT)*, 22-24 June 2017 2017, pp. 254-258, doi: 10.1109/FENDT.2017.8584608.

[123] P. A. Petcher, M. D. G. Potter, and S. Dixon, "A new electromagnetic acoustic transducer (EMAT) design for operation on rail," *NDT & E International*, vol. 65, pp. 1-7, 2014/07/01/ 2014, doi: https://doi.org/10.1016/j.ndteint.2014.03.007.

[124] M. Hirao, H. Ogi, and H. Fukuoka, "Advanced ultrasonic method for measuring rail axial stresses with electromagnetic acoustic transducer," *Research in Nondestructive Evaluation*, vol. 5, no. 3, pp. 211-223, 1994/09/01 1994, doi: 10.1007/BF01606409.

[125] Y. Zhang *et al.*, "Design of a new type of omnidirectional shear-horizontal EMAT by the use of half-ring magnets and PCB technology," *Ultrasonics*, vol. 115, p. 106465, 2021/08/01/ 2021, doi: https://doi.org/10.1016/j.ultras.2021.106465.
[126] F. Honarvar and A. Varvani-Farahani, "A review of ultrasonic testing applications in additive manufacturing: Defect evaluation, material characterization, and process control," *Ultrasonics*, vol. 108, p. 106227, 2020/12/01/ 2020, doi: https://doi.org/10.1016/j.ultras.2020.106227.
[127] A. A. Mozhayko and S. A. Manninen, "Features of Signal Processing in the Study of Defects in Metallic Mediums Using an Electromagnetic Acoustic Wave," Cham, 2021: Springer International Publishing, in International Youth Conference on Electronics, Telecommunications and Information Technologies, pp. 557-563.
[128] H. Miao and F. Li, "Shear horizontal wave transducers for structural health monitoring and nondestructive testing: A review," *Ultrasonics*, vol. 114, p. 106355, 2021/07/01/ 2021, doi: https://doi.org/10.1016/j.ultras.2021.106355.
[129] V. V. Murav'ev, L. V. Volkova, A. V. Platunov, and V. A. Kulikov, "An electromagnetic-acoustic method for studying stress-strain states of rails," *Russian Journal of Nondestructive Testing*, vol. 52, no. 7, pp. 370-376, 2016/07/01 2016, doi: 10.1134/S1061830916070044.
[130] H. Liu *et al.*, "Uniaxial stress in-situ measurement using EMAT shear and longitudinal waves: Transducer design and experiments," *Applied Acoustics*, vol. 175, p. 107781, 2021/04/01/ 2021, doi: https://doi.org/10.1016/j.apacoust.2020.107781.
[131] S. Huang, Z. Wang, S. Wang, Q. Wang, and W. Zhao, "Characteristic analysis of electromagnetic acoustic transducers for helical shear horizontal wave based on magnetostrictive effect," *Review of Scientific Instruments*, vol. 92, no. 2, p. 025006, 2021, doi: 10.1063/5.0023382.
[132] A. R. Clough and R. S. Edwards, "Characterisation of hidden defects using the near-field ultrasonic enhancement of Lamb waves," *Ultrasonics*, vol. 59, pp. 64-71, 2015/05/01/ 2015, doi: https://doi.org/10.1016/j.ultras.2015.01.012.
[133] B. Dutton, A. R. Clough, M. H. Rosli, and R. S. Edwards, "Non-contact ultrasonic detection of angled surface defects," *NDT & E International*, vol. 44, no. 4, pp. 353-360, 2011/07/01/ 2011, doi: https://doi.org/10.1016/j.ndteint.2011.02.001.
[134] L. Xiang, D. Greenshields, S. Dixon, and R. S. Edwards, "Phased Electromagnetic Acoustic Transducer Array for Rayleigh Wave Surface Defect Detection," *IEEE Transactions on Ultrasonics, Ferroelectrics, and Frequency Control*, vol. 67, no. 7, pp. 1403-1411, 2020, doi: 10.1109/TUFFC.2020.2968151.
[135] Q. Feng, R. Li, B. Nie, S. Liu, L. Zhao, and H. Zhang, "Literature Review: Theory and Application of In-Line Inspection Technologies for Oil and Gas Pipeline Girth Weld Defection," *Sensors*, vol. 17, no. 1, p. 50, 2017. [Online]. Available: https://www.mdpi.com/1424-8220/17/1/50.
[136] L.-J. Yang, J. Zhang, Y.-H. Xing, S.-W. Gao, Z. Xie, and H.-W. Fu, "Development of a biaxial grid-coil-type electromagnetic acoustic transducer," *Measurement Science and Technology*, vol. 32, no. 2, p. 025102, 2020/11/26 2020, doi: 10.1088/1361-6501/abbc88.
[137] V. V. Murav'ev, L. V. Volkova, V. E. Gromov, and A. M. Glezer, "Estimation of the residual stresses in rails using electromagnetic–acoustic introduction–reception of waves," *Russian Metallurgy (Metally)*, vol. 2016, no. 10, pp. 992-995, 2016/10/01 2016, doi: 10.1134/S003602951610013X.
[138] W. Guo, B. Gao, G. Yun Tian, and D. Si, "Physic perspective fusion of electromagnetic acoustic transducer and pulsed eddy current testing in non-destructive testing system," *Philosophical Transactions of the Royal Society A: Mathematical, Physical and Engineering Sciences*, vol. 378, no. 2182, p. 20190608, 2020, doi: doi:10.1098/rsta.2019.0608.
[139] J. Sutherland *et al.*, "The Role of Effective Collaboration in the Advancement of EMAT Inline Inspection Technology for Pipeline Integrity Management: A Case Study," in *2012 9th International Pipeline Conference*, 2012, vol. Volume 2: Pipeline Integrity Management, pp. 1-7, doi: 10.1115/ipc2012-90021. [Online]. Available: https://doi.org/10.1115/IPC2012-90021
[140] R. Kania *et al.*, "Validation of EMAT Technology for Gas Pipeline Crack Inspection," in *2012 9th International Pipeline Conference*, 2012, vol. Volume 2: Pipeline Integrity Management, pp. 73-77, doi: 10.1115/ipc2012-90240. [Online]. Available: https://doi.org/10.1115/IPC2012-90240

[141] Y. Gao *et al.*, "Electromagnetic pulsed thermography for natural cracks inspection," *Scientific Reports*, vol. 7, no. 1, p. 42073, 2017/02/07 2017, doi: 10.1038/srep42073.
[142] A. Yin, B. Gao, G. Y. Tian, W. L. Woo, and K. Li, "Physical interpretation and separation of eddy current pulsed thermography," *Journal of Applied Physics*, vol. 113, no. 6, p. 064101, 2013, doi: 10.1063/1.4790866.
[143] G. Y. Tian, J. Wilson, L. Cheng, D. P. Almond, E. Kostson, and B. Weekes, "Pulsed Eddy Current Thermography and Applications," in *New Developments in Sensing Technology for Structural Health Monitoring*, S. C. Mukhopadhyay Ed. Berlin, Heidelberg: Springer Berlin Heidelberg, 2011, pp. 205-231.
[144] J. Wilson, G. Y. Tian, I. Z. Abidin, S. Yang, and D. Almond, "Pulsed eddy current thermography: system development and evaluation," *Insight - Non-Destructive Testing and Condition Monitoring*, vol. 52, no. 2, pp. 87-90, // 2010, doi: 10.1784/insi.2010.52.2.87.
[145] L. Cheng, "Eddy Current Pulsed Thermography for NonDestructive Evaluation of Carbon Fibre Reinforced Plastic for Wind Turbine Blades," PhD, School of Electrical and Electronic Engineering, Newcastle University, Unpublish PhD thesis, 2013.
[146] B. Gao, X. Li, W. L. Woo, and G. Yun Tian, "Quantitative validation of Eddy current stimulated thermal features on surface crack," *NDT & E International*, vol. 85, pp. 1-12, 2017/01/01/ 2017, doi: https://doi.org/10.1016/j.ndteint.2016.09.002.
[147] M. Pan, Y. He, G. Tian, D. Chen, and F. Luo, "Defect characterisation using pulsed eddy current thermography under transmission mode and NDT applications," *NDT & E International*, vol. 52, pp. 28-36, 2012/11/01/ 2012, doi: https://doi.org/10.1016/j.ndteint.2012.08.007.
[148] X. Lu, Q. Yi, and G. Y. Tian, "A Comparison of Feature Extraction Techniques for Delamination of CFRP Using Eddy Current Pulse-Compression Thermography," *IEEE Sensors Journal*, vol. 20, no. 20, pp. 12415-12422, 2020, doi: 10.1109/JSEN.2020.2993154.
[149] Q. Yi, G. Y. Tian, H. Malekmohammadi, J. Zhu, S. Laureti, and M. Ricci, "New features for delamination depth evaluation in carbon fiber reinforced plastic materials using eddy current pulse-compression thermography," *NDT & E International*, vol. 102, pp. 264-273, 2019/03/01/ 2019, doi: https://doi.org/10.1016/j.ndteint.2018.12.010.
[150] X. Chen, G. Y. Tian, S. Ding, J. Ahmed, and W. L. Woo, "Tomographic Reconstruction of Rolling Contact Fatigues in Rails using 3D Eddy Current Pulsed Thermography," *IEEE Sensors Journal*, pp. 1-1, 2021, doi: 10.1109/JSEN.2021.3086307.
[151] R. Yang, Y. He, B. Gao, G. Y. Tian, and J. Peng, "Lateral heat conduction based eddy current thermography for detection of parallel cracks and rail tread oblique cracks," *Measurement*, vol. 66, pp. 54-61, 2015/04/01/ 2015, doi: https://doi.org/10.1016/j.measurement.2015.01.024.
[152] J. Peng, G. Tian, L. Wang, X. Gao, Y. Zhang, and Z. Wang, "Rolling contact fatigue detection using eddy current pulsed thermography," in *2014 IEEE Far East Forum on Nondestructive Evaluation/Testing*, 20-23 June 2014 2014, pp. 176-180, doi: 10.1109/FENDT.2014.6928257.
[153] A. Taram *et al.*, "Nondestructive testing of resistance spot welds using eddy current thermography," *Appl. Opt.*, vol. 57, no. 18, pp. D63-D68, 2018/06/20 2018, doi: 10.1364/AO.57.000D63.
[154] Y. He, G. Y. Tian, M. Pan, D. Chen, and H. Zhang, "An investigation into eddy current pulsed thermography for detection of corrosion blister," *Corrosion Science*, vol. 78, pp. 1-6, 2014/01/01/ 2014, doi: https://doi.org/10.1016/j.corsci.2013.09.001.
[155] Q. Yi, G. Y. Tian, H. Malekmohammadi, S. Laureti, M. Ricci, and S. Gao, "Inverse reconstruction of fibre orientation in multilayer CFRP using forward FEM and eddy current pulsed thermography," *NDT & E International*, vol. 122, p. 102474, 2021/09/01/ 2021, doi: https://doi.org/10.1016/j.ndteint.2021.102474.
[156] F. Liu, J. Zhu, G. Y. Tian, C. Ulianov, and Z. Wang, "Investigations for inclination angle characterization of angular defects using eddy current pulsed thermography," *Infrared Physics & Technology*, vol. 100, pp. 73-81, 2019/08/01/ 2019, doi: https://doi.org/10.1016/j.infrared.2019.05.016.
[157] L. Miao, B. Gao, H. Li, and G. Tian, "Resonant frequency tracking mode on eddy current pulsed thermography non-destructive testing," *Philosophical Transactions of the Royal Society A: Mathematical, Physical and Engineering Sciences*, vol. 378, no. 2182, p. 20190607, 2020, doi: doi:10.1098/rsta.2019.0607.

[158] R. Ghoni, M. Dollah, A. Sulaiman, and F. M. Ibrahim, "Defect Characterization Based on Eddy Current Technique: Technical Review," *Advances in Mechanical Engineering*, vol. 6, p. 182496, 2014, doi: 10.1155/2014/182496.

[159] M. M. Saari, N. A. Nadzri, M. A. H. P. Zaini, N. H. Ramlan, and K. Tsukada, "A Low-frequency Eddy Current Probe Based on Miniature Fluxgate Array for Defect Evaluation in Steel Components," *IEEE Transactions on Magnetics*, pp. 1-1, 2021, doi: 10.1109/TMAG.2021.3076441.

[160] M. B. Kishore, J. W. Park, S. J. Song, H. J. Kim, and S. G. Kwon, "Characterization of defects on rail surface using eddy current technique," *Journal of Mechanical Science and Technology*, journal article vol. 33, no. 9, pp. 4209-4215, September 01 2019, doi: 10.1007/s12206-019-0816-x.

[161] N. Ulapane, K. Thiyagarajan, J. V. Miro, and S. Kodagoda, "Surface Representation of Pulsed Eddy Current Sensor Signals for Improved Ferromagnetic Material Thickness Quantification," *IEEE Sensors Journal*, vol. 21, no. 4, pp. 5413-5422, 2021, doi: 10.1109/JSEN.2020.3034571.

[162] J. Ge, N. Yusa, and M. Fan, "Frequency component mixing of pulsed or multi-frequency eddy current testing for nonferromagnetic plate thickness measurement using a multi-gene genetic programming algorithm," *NDT & E International*, vol. 120, p. 102423, 2021/06/01/ 2021, doi: https://doi.org/10.1016/j.ndteint.2021.102423.

[163] J. Bao, B. Ye, S. Luo, X. Wang, and J. Wu, "Thickness Measurement of Titanium Alloy Sheet Based on Eddy Current Method With a Novel Simplified Model," *IEEE Transactions on Instrumentation and Measurement*, vol. 70, pp. 1-9, 2021, doi: 10.1109/TIM.2020.3011272.

[164] X. Meng, M. Lu, W. Yin, A. Bennecer, and K. J. Kirk, "Evaluation of Coating Thickness Using Lift-Off Insensitivity of Eddy Current Sensor," *Sensors*, vol. 21, no. 2, p. 419, 2021. [Online]. Available: https://www.mdpi.com/1424-8220/21/2/419.

[165] W. Cheng, "Swept-frequency eddy current testing to characterize a nonmagnetic metallic plate and a nonconductive coating over it," *International Journal of Applied Electromagnetics and Mechanics*, vol. 59, pp. 1-9, 11/27 2018, doi: 10.3233/JAE-171129.

[166] Y. Wang, M. Fan, B. Cao, B. Ye, and D. Wen, "Measurement of coating thickness using lift-off point of intersection features from pulsed eddy current signals," *NDT & E International*, vol. 116, p. 102333, 2020/12/01/ 2020, doi: https://doi.org/10.1016/j.ndteint.2020.102333.

[167] W. Cai, C. Jomdecha, Y. Zhao, L. Wang, S. Xie, and Z. Chen, "Quantitative evaluation of electrical conductivity inside stress corrosion crack with electromagnetic NDE methods," *Philosophical Transactions of the Royal Society A: Mathematical, Physical and Engineering Sciences*, vol. 378, no. 2182, p. 20190589, 2020, doi: doi:10.1098/rsta.2019.0589.

[168] B. A. Abu-Nabah and P. B. Nagy, "High-frequency eddy current conductivity spectroscopy for residual stress profiling in surface-treated nickel-base superalloys," *NDT & E International*, vol. 40, no. 5, pp. 405-418, 2007/07/01/ 2007, doi: https://doi.org/10.1016/j.ndteint.2007.01.003.

[169] B. A. Abu-Nabah and P. B. Nagy, "Lift-off effect in high-frequency eddy current conductivity spectroscopy," *NDT & E International*, vol. 40, no. 8, pp. 555-565, 2007/12/01/ 2007, doi: https://doi.org/10.1016/j.ndteint.2007.06.001.

[170] X. Ma, A. J. Peyton, and Y. Y. Zhao, "Measurement of the electrical conductivity of open-celled aluminium foam using non-contact eddy current techniques," *NDT & E International*, vol. 38, no. 5, pp. 359-367, 2005/07/01/ 2005, doi: https://doi.org/10.1016/j.ndteint.2004.10.003.

[171] M. Lu, R. Huang, W. Yin, Q. Zhao, and A. Peyton, "Measurement of Permeability for Ferrous Metallic Plates Using a Novel Lift-Off Compensation Technique on Phase Signature," *IEEE Sensors Journal*, vol. 19, no. 17, pp. 7440-7446, 2019, doi: 10.1109/JSEN.2019.2916431.

[172] M. Lu, W. Zhu, L. Yin, A. J. Peyton, W. Yin, and Z. Qu, "Reducing the Lift-Off Effect on Permeability Measurement for Magnetic Plates From Multifrequency Induction Data," *IEEE Transactions on Instrumentation and Measurement*, vol. 67, no. 1, pp. 167-174, 2018, doi: 10.1109/TIM.2017.2728338.

[173] Z. Deng, Y. Sun, Y. Kang, K. Song, and R. Wang, "A Permeability-Measuring Magnetic Flux Leakage Method for Inner Surface Crack in Thick-Walled Steel Pipe," *Journal of Nondestructive Evaluation*, vol. 36, no. 4, p. 68, 2017/09/20 2017, doi: 10.1007/s10921-017-0447-z.

[174] M. Ganesh, M. Ravan, and R. K. Amineh, "Electromagnetic Induction Imaging at Multiple Depths With a Single Coil," *IEEE Transactions on Instrumentation and Measurement*, vol. 70, pp. 1-9, 2021, doi: 10.1109/TIM.2021.3050659.
[175] N. Ida, K. Betzold, and W. Lord, "Finite element modeling of absolute eddy current probe signals," *Journal of Nondestructive Evaluation*, vol. 3, no. 3, pp. 147-154, 1982/09/01 1982, doi: 10.1007/BF00566556.
[176] B. Cao, C. Li, M. Fan, B. Ye, and S. Gao, "Analytical modelling of eddy current response from driver pick-up coils on multi-layered conducting plates," *Insight - Non-Destructive Testing and Condition Monitoring*, vol. 60, pp. 77-83, 02/01 2018, doi: 10.1784/insi.2018.60.2.77.
[177] K. Mohammed Asadullah, S. Jian, L. Bodong, P. Alexander, and K. Jurgen, "Magnetic sensors – A review and recent technologies," *Engineering Research Express*, pp. 1-18, 2021, doi: https://doi.org/10.1088/2631-8695/ac0838.
[178] A. Sophian, G. Y. Tian, D. Taylor, and J. Rudlin, "A feature extraction technique based on principal component analysis for pulsed Eddy current NDT," *NDT & E International*, vol. 36, no. 1, pp. 37-41, 2003/01/01/ 2003, doi: https://doi.org/10.1016/S0963-8695(02)00069-5.
[179] H. Heuer, *Eddy Current Imaging for Electrical Characterization of Silicon Solar Cells and TCO layers*. 2015.
[180] R. R. Robaina, H. T. Alvarado, and J. A. Plaza, "Planar coil-based differential electromagnetic sensor with null-offset," *Sensors and Actuators A: Physical*, vol. 164, no. 1, pp. 15-21, 2010/11/01/ 2010, doi: https://doi.org/10.1016/j.sna.2010.09.008.
[181] M. S. Luloff, D. Desjardins, J. Morelli, and T. W. Krause, "Solution for a transmit-receive eddy current probe above a layered planar conductive structure," *NDT & E International*, vol. 96, pp. 1-8, 2018/06/01/ 2018, doi: https://doi.org/10.1016/j.ndteint.2018.02.003.
[182] M. Lu, Y. Xie, W. Zhu, A. Peyton, and W. Yin, "Determination of the Magnetic Permeability, Electrical Conductivity, and Thickness of Ferrite Metallic Plates Using a Multifrequency Electromagnetic Sensing System," *IEEE Transactions on Industrial Informatics*, vol. 15, no. 7, pp. 4111-4119, 2019, doi: 10.1109/TII.2018.2885406.
[183] M. Lu *et al.*, "Determination of Surface Crack Orientation Based on Thin-Skin Regime Using Triple-Coil Drive–Pickup Eddy-Current Sensor," *IEEE Transactions on Instrumentation and Measurement*, vol. 70, pp. 1-9, 2021, doi: 10.1109/TIM.2020.3044729.
[184] Z. Gang, X. Rui, C. Yu, L. Haowen, and Y. Kexin, "Research on Double Coil Pulse Eddy Current Thickness Measurement," in *2017 10th International Conference on Intelligent Computation Technology and Automation (ICICTA)*, 9-10 Oct. 2017 2017, pp. 406-409, doi: 10.1109/ICICTA.2017.97.
[185] G. Klein, M. S. Luloff, J. E. Morelli, and T. W. Krause, "Evaluation of Concentric Tube Model for Pressure Tube to Calandria Tube Gap Measurement," *IEEE Sensors Journal*, vol. 19, no. 15, pp. 6233-6239, 2019, doi: 10.1109/JSEN.2019.2909493.
[186] G. Klein, J. Morelli, and T. W. Krause, "Analytical model of the eddy current response of a drive-receive coil system inside two concentric tubes," *NDT & E International*, vol. 96, pp. 18-25, 2018/06/01/ 2018, doi: https://doi.org/10.1016/j.ndteint.2018.03.003.
[187] S. Kahrobaee, M. S. Haghighi, and I. A. Akhlaghi, "Improving nondestructive characterization of dual phase steels using data fusion," *Journal of Magnetism and Magnetic Materials*, vol. 458, pp. 317-326, 2018/07/15/ 2018, doi: https://doi.org/10.1016/j.jmmm.2018.03.049.
[188] R. Huang, M. Lu, X. He, A. Peyton, and W. Yin, "Measuring Coaxial Hole Size of Finite-Size Metallic Disk Based on a Dual-Constraint Integration Feature Using Multifrequency Eddy Current Testing," *IEEE Transactions on Instrumentation and Measurement*, vol. 70, pp. 1-7, 2021, doi: 10.1109/TIM.2020.3026762.
[189] A. Stubendekova and L. Janousek, "Impact of defect extent on swept frequency eddy current responses in non-destructive evaluation," *Electrical Engineering*, vol. 99, no. 4, pp. 1275-1281, 2017/12/01 2017, doi: 10.1007/s00202-017-0650-z.
[190] A. Štubendeková and L. Janoušek, "Non–Destructive Testing of Conductive Material by Eddy Current Air Probe Based on Swept Frequency," *Journal of Electrical Engineering*, vol. 66, pp. 174-177, 05/01 2015, doi: 10.2478/jee-2015-0028.
[191] S. Chen, Y. Yang, and Y. Luo, "Comparison of spiral and helix coils in magnetic resonant coupling wireless power transfer," in *2017 IEEE 2nd Information Technology, Networking,*

Electronic and Automation Control Conference (ITNEC), 15-17 Dec. 2017 2017, pp. 721-724, doi: 10.1109/ITNEC.2017.8284826.

[192] M. Lu, X. Meng, R. Huang, L. Chen, A. Peyton, and W. Yin, "Measuring Lift-Off Distance and Electromagnetic Property of Metal Using Dual-Frequency Linearity Feature," *IEEE Transactions on Instrumentation and Measurement*, vol. 70, pp. 1-9, 2021, doi: 10.1109/TIM.2020.3029348.

[193] H. Hoshikawa and K. Koyama, "A New ECT Probe with Rotating Direction Eddy Current," 1996, pp. 1091-1098.

[194] S. Jeong *et al.*, "Smartwatch Strap Wireless Power Transfer System With Flexible PCB Coil and Shielding Material," *IEEE Transactions on Industrial Electronics*, vol. 66, no. 5, pp. 4054-4064, 2019, doi: 10.1109/TIE.2018.2860534.

[195] L. Liu, D. Chen, M. Pan, W. Tian, W. Wang, and Y. Yu, "Planar Eddy Current Sensor Array With Null-Offset," *IEEE Sensors Journal*, vol. 19, no. 12, pp. 4647-4651, 2019, doi: 10.1109/JSEN.2019.2901351.

[196] D. Chen, Y. Li, M. Pan, and W. Tian, "Flexible planar electromagnetic sensor array fabricated with printing electronic technology," *Measurement*, vol. 129, pp. 499-503, 2018/12/01/ 2018, doi: https://doi.org/10.1016/j.measurement.2018.07.048.

[197] R. Xie *et al.*, "Fatigue Crack Length Sizing Using a Novel Flexible Eddy Current Sensor Array," (in eng), *Sensors (Basel)*, vol. 15, no. 12, pp. 32138-51, Dec 21 2015, doi: 10.3390/s151229911.

[198] T. Ding, X. Chen, and Y. Huang, "Ultra-Thin flexible eddy current sensor array for gap measurements," *Tsinghua Science and Technology*, vol. 9, no. 6, pp. 667-671, 2004.

[199] K. Sondhi *et al.*, "Flexible screen-printed coils for wireless power transfer using low-frequency magnetic fields," *Journal of Micromechanics and Microengineering*, vol. 29, no. 8, p. 084006, 2019/06/21 2019, doi: 10.1088/1361-6439/ab26ff.

[200] M. Bissannagari, T.-H. Kim, J.-G. Yook, and J. Kim, "All inkjet-printed flexible wireless power transfer module: PI/Ag hybrid spiral coil built into 3D NiZn-ferrite trench structure with a resonance capacitor," *Nano Energy*, vol. 62, pp. 645-652, 2019/08/01/ 2019, doi: https://doi.org/10.1016/j.nanoen.2019.05.075.

[201] Y. Li, N. Grabham, R. Torah, J. Tudor, and S. Beeby, "Textile-Based Flexible Coils for Wireless Inductive Power Transmission," *Applied Sciences*, vol. 8, no. 6, p. 912, 2018. [Online]. Available: https://www.mdpi.com/2076-3417/8/6/912.

[202] N. J. Grabham, Y. Li, L. R. Clare, B. H. Stark, and S. P. Beeby, "Fabrication Techniques for Manufacturing Flexible Coils on Textiles for Inductive Power Transfer," *IEEE Sensors Journal*, vol. 18, no. 6, pp. 2599-2606, 2018, doi: 10.1109/JSEN.2018.2796138.

[203] P. Li *et al.*, "Sensitivity boost of rosette eddy current array sensor for quantitative monitoring crack," *Sensors and Actuators A: Physical*, vol. 246, pp. 129-139, 2016/08/01/ 2016, doi: https://doi.org/10.1016/j.sna.2016.05.023.

[204] S. Jiao, L. Cheng, X. Li, P. Li, and H. Ding, "Monitoring fatigue cracks of a metal structure using an eddy current sensor," *EURASIP Journal on Wireless Communications and Networking*, journal article vol. 2016, no. 1, p. 188, August 18 2016, doi: 10.1186/s13638-016-0689-y.

[205] Z. Sun, D. Cai, C. Zou, W. Zhang, and Q. Chen, "A Flexible Arrayed Eddy Current Sensor for Inspection of Hollow Axle Inner Surfaces," *Sensors (Basel, Switzerland)*, vol. 16, no. 7, p. 952, 2016, doi: 10.3390/s16070952.

[206] G. Y. Tian, Y. Li, and C. Mandache, "Study of Lift-Off Invariance for Pulsed Eddy-Current Signals," *IEEE Transactions on Magnetics*, vol. 45, no. 1, pp. 184-191, 2009, doi: 10.1109/TMAG.2008.2006246.

[207] D. Wen, M. Fan, B. Cao, B. Ye, and G. Tian, "Lift-Off Point of Intersection in Spectral Pulsed Eddy Current Signals for Thickness Measurement," *IEEE Sensors Letters*, vol. 2, no. 2, pp. 1-4, 2018, doi: 10.1109/LSENS.2018.2822296.

[208] M. Lu, L. Yin, A. J. Peyton, and W. Yin, "A Novel Compensation Algorithm for Thickness Measurement Immune to Lift-Off Variations Using Eddy Current Method," *IEEE Transactions on Instrumentation and Measurement*, vol. 65, no. 12, pp. 2773-2779, 2016, doi: 10.1109/TIM.2016.2600918.

[209] G. Y. Tian and A. Sophian, "Reduction of lift-off effects for pulsed eddy current NDT," *NDT & E International*, vol. 38, no. 4, pp. 319-324, 2005/06/01/ 2005, doi: https://doi.org/10.1016/j.ndteint.2004.09.007.

[210] Y. He, M. Pan, F. Luo, and G. Tian, "Reduction of Lift-Off Effects in Pulsed Eddy Current for Defect Classification," *IEEE Transactions on Magnetics*, vol. 47, no. 12, pp. 4753-4760, 2011, doi: 10.1109/TMAG.2011.2160726.

[211] Y. Yu, Y. Yan, F. Wang, G. Tian, and D. Zhang, "An approach to reduce lift-off noise in pulsed eddy current nondestructive technology," *NDT & E International*, vol. 63, pp. 1-6, 2014/04/01/ 2014, doi: https://doi.org/10.1016/j.ndteint.2013.12.012.

[212] M. Fan, B. Cao, G. Tian, B. Ye, and W. Li, "Thickness measurement using liftoff point of intersection in pulsed eddy current responses for elimination of liftoff effect," *Sensors and Actuators A: Physical*, vol. 251, pp. 66-74, 2016/11/01/ 2016, doi: https://doi.org/10.1016/j.sna.2016.10.003.

[213] M. Fan, B. Cao, A. I. Sunny, W. Li, G. Tian, and B. Ye, "Pulsed eddy current thickness measurement using phase features immune to liftoff effect," *NDT & E International*, vol. 86, pp. 123-131, 2017/03/01/ 2017, doi: https://doi.org/10.1016/j.ndteint.2016.12.003.

[214] M. A. Faraj, F. Samsuri, A. N. AbdAlla, D. Rifai, K. Ali, and Y. Al-Douri, "Hybrid GMR/IR probe to reduce the effects of lift-off," *Measurement and Control*, vol. 52, no. 5-6, pp. 588-598, 2019, doi: 10.1177/0020294019827336.

[215] I. D. Adewale, G. Y. Tian, S. H. Dong, G. X. Ting, Y. Zeng, and G. Liu, "Separation of Lift-off and Defect Depth Features in Magnetic Sensor based Pulsed Eddy Current Signals," *Electromagnetic Nondestructive Evaluation (XVIII)*, vol. 40, pp. 211-221, 2015/06/01/ 2015, doi: 10.3233/978-1-61499-509-8-211.

[216] H. A. Wheeler, "Formulas for the Skin Effect," *Proceedings of the IRE*, vol. 30, no. 9, pp. 412-424, 1942, doi: 10.1109/JRPROC.1942.232015.

[217] S. Hosseingholizadeh, T. Filleter, and A. N. Sinclair, "Evaluation of a Magnetic Dipole Model in a DC Magnetic Flux Leakage System," *IEEE Transactions on Magnetics*, vol. 55, no. 4, pp. 1-7, 2019, doi: 10.1109/TMAG.2019.2897669.

[218] X. Chen and X. Liu, "Pulsed Eddy Current-Based Method for Electromagnetic Parameters of Ferromagnetic Materials," *IEEE Sensors Journal*, vol. 21, no. 5, pp. 6376-6383, 2021, doi: 10.1109/JSEN.2020.3038203.

[219] M. Lu *et al.*, "Conductivity Lift-off Invariance and measurement of permeability for ferrite metallic plates," *NDT & E International*, vol. 95, pp. 36-44, 2018/04/01/ 2018, doi: https://doi.org/10.1016/j.ndteint.2018.01.007.

[220] M. Lu, X. Meng, R. Huang, L. Chen, A. Peyton, and W. Yin, "Lift-off invariant inductance of steels in multi-frequency eddy-current testing," *NDT & E International*, vol. 121, p. 102458, 2021/07/01/ 2021, doi: https://doi.org/10.1016/j.ndteint.2021.102458.

[221] B. Helifa, A. Oulhadj, A. Benbelghit, I. K. Lefkaier, F. Boubenider, and D. Boutassouna, "Detection and measurement of surface cracks in ferromagnetic materials using eddy current testing," *NDT & E International*, vol. 39, no. 5, pp. 384-390, 2006/07/01/ 2006, doi: https://doi.org/10.1016/j.ndteint.2005.11.004.

[222] C. N. Owston, "Eddy-current testing at microwave frequencies," *Non-Destructive Testing*, vol. 2, no. 3, pp. 193-196, 1969/08/01/ 1969, doi: https://doi.org/10.1016/0029-1021(69)90111-X.

[223] D. R. Desjardins, T. W. Krause, A. Tetervak, and L. Clapham, "Concerning the derivation of exact solutions to inductive circuit problems for eddy current testing," *NDT & E International*, vol. 68, pp. 128-135, 2014/12/01/ 2014, doi: https://doi.org/10.1016/j.ndteint.2014.07.008.

[224] F. Hughes, R. Day, N. Tung, and S. M. Dixon, "High-frequency eddy current measurements using sensor-mounted electronics," *Insight- Non-Destructive Testing & Condition Monitoring*, vol. 58, no. 11, pp. 596-600, 2016. [Online]. Available: http://wrap.warwick.ac.uk/85800/.

[225] J. O. Fava, L. Lanzani, and M. C. Ruch, "Multilayer planar rectangular coils for eddy current testing: Design considerations," *NDT & E International*, vol. 42, no. 8, pp. 713-720, 2009/12/01/ 2009, doi: https://doi.org/10.1016/j.ndteint.2009.06.005.

[226] K. Maruyama, I. Marinova, and Y. Saito, "Enhance the Sensibility of the Resonance Type Eddy Current Testing," *Materials Science Forum*, vol. 792, pp. 72-77, 2014, doi: 10.4028/www.scientific.net/MSF.792.72.

[227] D. J. Pasadas, A. L. Ribeiro, H. G. Ramos, B. Feng, and P. Baskaran, "Eddy current testing of cracks using multi-frequency and noise excitation," *2018 IEEE International Instrumentation and Measurement Technology Conference (I2MTC)*, pp. 1-6, 14-17 May 2018 2018, doi: 10.1109/I2MTC.2018.8409716.

[228] N. Zhang, S. Wang, S. Ning, and S. Wang, "Study on planar coil with multi-frequency stimulations applied to an eddy current non-destructive testing," in *2017 20th International Conference on Electrical Machines and Systems (ICEMS)*, 11-14 Aug. 2017 2017, pp. 1-4, doi: 10.1109/ICEMS.2017.8056343.

[229] J. Bosse, P.-Y. Joubert, P. Larzabal, and A. Ferréol, "High resolution approach for the localization of buried defects in the multi-frequency eddy current imaging of metallic structures," *NDT & E International*, vol. 43, no. 3, pp. 250-257, 2010/04/01/ 2010, doi: https://doi.org/10.1016/j.ndteint.2009.12.002.

[230] A. Punapung and A. Kaewpoonsuk, "A Design for a Programmable Swept Frequency Module for Eddy Current Testing," in *2018 International Electrical Engineering Congress (iEECON)*, 7-9 March 2018 2018, pp. 1-4, doi: 10.1109/IEECON.2018.8712264.

[231] W. Cheng and H. Hashizume, "Characterization of multilayered structures by swept-frequency eddy current testing," *AIP Advances*, vol. 9, no. 3, p. 035009, 2019, doi: 10.1063/1.5079959.

[232] J. García-Martín, J. Gómez-Gil, and E. Vázquez-Sánchez, "Non-Destructive Techniques Based on Eddy Current Testing," *Sensors (Basel, Switzerland)*, vol. 11, no. 3, pp. 2525-2565, 2011/02/28/ 2011, doi: 10.3390/s110302525.

[233] C. H. Dinh *et al.*, "Real-Time Thickness Measurement Using Resonant Eddy-Current Sensor," *IEEE Transactions on Instrumentation and Measurement*, vol. 70, pp. 1-9, 2021, doi: 10.1109/TIM.2021.3077997.

[234] C. Xiu, L. Ren, and H. Li, "Investigation on Eddy Current Sensor in Tension Measurement at a Resonant Frequency," *Applied Sciences*, vol. 7, no. 6, p. 538, 2017. [Online]. Available: https://www.mdpi.com/2076-3417/7/6/538.

[235] Z. Liu, K. Tsukada, K. Hanasaki, and M. Kurisu, "Two-Dimensional Eddy Current Signal Enhancement via Multifrequency Data Fusion," *Research in Nondestructive Evaluation*, vol. 11, no. 3, pp. 165-177, 1999/01/01 1999, doi: 10.1080/09349849909410029.

[236] M. Morozov, G. Yun Tian, and P. J. Withers, "The pulsed eddy current response to applied loading of various aluminium alloys," *NDT & E International*, vol. 43, no. 6, pp. 493-500, 2010/09/01/ 2010, doi: https://doi.org/10.1016/j.ndteint.2010.05.004.

[237] Y. He, F. Luo, M. Pan, X. Hu, J. Gao, and B. Liu, "Defect classification based on rectangular pulsed eddy current sensor in different directions," *Sensors and Actuators A: Physical*, vol. 157, no. 1, pp. 26-31, 2010/01/01/ 2010, doi: https://doi.org/10.1016/j.sna.2009.11.012.

[238] I. M. Z. Abidin, "Modelling and experimental investigation of eddy current distribution for angular defect characterisation," PhD, School of Electrical, Electronic and Computer Engineering, Newcastle University, unpublished PhD thesis, 2010.

[239] C. Wang, S. Wu, J. Xin, R. He, J. Chen, and D. Wang, "Numerical Simulation of Oil and Gas Pipeline Crack Detection Based on Pulsed Eddy Current Testing Technology," in *2021 4th International Conference on Electron Device and Mechanical Engineering (ICEDME)*, 19-21 March 2021 2021, pp. 46-50, doi: 10.1109/ICEDME52809.2021.00018.

[240] W. Cheng, "Thickness Measurement of Metal Plates Using Swept-Frequency Eddy Current Testing and Impedance Normalization," *IEEE Sensors Journal*, vol. 17, no. 14, pp. 4558-4569, 2017, doi: 10.1109/JSEN.2017.2710356.

[241] R. R. Hughes, Y. Fan, and S. Dixon, "Near electrical resonance signal enhancement (NERSE) in eddy-current crack detection," *NDT & E International*, vol. 66, pp. 82-89, 2014/09/01/ 2014, doi: https://doi.org/10.1016/j.ndteint.2014.04.009.

[242] R. R. Hughes and S. Dixon, "Eddy-current crack detection at frequencies approaching electrical resonance," *AIP Conference Proceedings*, vol. 1581, no. 1, pp. 1366-1373, 2014, doi: 10.1063/1.4864980.

[243] R. R. Hughes and S. Dixon, "Analysis of Electrical Resonance Distortion for Inductive Sensing Applications," *IEEE Sensors Journal*, vol. 18, no. 14, pp. 5818-5825, 2018, doi: 10.1109/JSEN.2018.2841506.

[244] R. R. Hughes and S. Dixon, "Developments in near electrical resonance signal enhancement (NERSE) eddy-current methods," *AIP Conference Proceedings*, vol. 1650, no. 1, pp. 345-352, 2015, doi: 10.1063/1.4914629.

[245] A. Nag, S. C. Mukhopadhyay, and J. Kosel, "Wearable Flexible Sensors: A Review," *IEEE Sensors Journal*, vol. 17, no. 13, pp. 3949-3960, 2017, doi: 10.1109/JSEN.2017.2705700.

[246] A. K. RamRakhyani and G. Lazzi, "On the Design of Efficient Multi-Coil Telemetry System for Biomedical Implants," *IEEE Transactions on Biomedical Circuits and Systems*, vol. 7, no. 1, pp. 11-23, 2013, doi: 10.1109/TBCAS.2012.2192115.

[247] X. Liu, C. Xia, X. Han, Z. Wu, and Z. Liao, "Simultaneous Wireless Power and Information Transmission Based on Harmonic Characteristic of Soft-Switching Inverter," *IEEE Transactions on Industrial Electronics*, pp. 1-1, 2021, doi: 10.1109/TIE.2021.3086710.

[248] A. Triviño, J. M. González-González, and J. A. Aguado, "Wireless Power Transfer Technologies Applied to Electric Vehicles: A Review," (in English), *Energies*, vol. 14, no. 6, p. 1547, 2021-03-18 2021, doi: http://dx.doi.org/10.3390/en14061547.

[249] S. Kuka, K. Ni, and M. Alkahtani, "A Review of Methods and Challenges for Improvement in Efficiency and Distance for Wireless Power Transfer Applications," (in English), no. 0, 2020, doi: https://doi.org/10.2478/pead-2020-0001.

[250] B. D. Truong, "Investigation on power optimization principles for series-configured resonant coupled wireless power transfer systems," *AEU - International Journal of Electronics and Communications*, vol. 106, pp. 67-81, 2019/07/01/ 2019, doi: https://doi.org/10.1016/j.aeue.2019.04.023.

[251] L. Chen, S. Liu, Y. C. Zhou, and T. J. Cui, "An Optimizable Circuit Structure for High-Efficiency Wireless Power Transfer," *IEEE Transactions on Industrial Electronics*, vol. 60, no. 1, pp. 339-349, 2013, doi: 10.1109/TIE.2011.2179275.

[252] J. O. Mur-Miranda *et al.*, "Wireless power transfer using weakly coupled magnetostatic resonators," *2010 IEEE Energy Conversion Congress and Exposition*, pp. 4179-4186, 12-16 Sept. 2010 2010, doi: 10.1109/ECCE.2010.5617728.

[253] Y. Zhang, Z. Yan, J. Zhu, S. Li, and C. Mi, "A review of foreign object detection (FOD) for inductive power transfer systems," *eTransportation*, vol. 1, p. 100002, 2019/08/01/ 2019, doi: https://doi.org/10.1016/j.etran.2019.04.002.

[254] W. Zhang, S. Wong, C. K. Tse, and Q. Chen, "Analysis and Comparison of Secondary Series- and Parallel-Compensated Inductive Power Transfer Systems Operating for Optimal Efficiency and Load-Independent Voltage-Transfer Ratio," *IEEE Transactions on Power Electronics*, vol. 29, no. 6, pp. 2979-2990, 2014, doi: 10.1109/TPEL.2013.2273364.

[255] W. Chwei-Sen, O. H. Stielau, and G. A. Covic, "Design considerations for a contactless electric vehicle battery charger," *IEEE Transactions on Industrial Electronics*, vol. 52, no. 5, pp. 1308-1314, 2005, doi: 10.1109/TIE.2005.855672.

[256] A. Karalis, J. D. Joannopoulos, and M. Soljačić, "Efficient wireless non-radiative mid-range energy transfer," *Annals of Physics*, vol. 323, no. 1, pp. 34-48, 2008/01/01/ 2008, doi: https://doi.org/10.1016/j.aop.2007.04.017.

[257] Z. Bi, T. Kan, C. C. Mi, Y. Zhang, Z. Zhao, and G. A. Keoleian, "A review of wireless power transfer for electric vehicles: Prospects to enhance sustainable mobility," *Applied Energy*, vol. 179, pp. 413-425, 2016/10/01/ 2016, doi: https://doi.org/10.1016/j.apenergy.2016.07.003.

[258] M. Longair, "'...a paper ...I hold to be great guns': a commentary on Maxwell (1865) 'A dynamical theory of the electromagnetic field'," *Philosophical Transactions of the Royal Society A: Mathematical, Physical and Engineering Sciences*, vol. 373, no. 2039, p. 20140473, 2015, doi: doi:10.1098/rsta.2014.0473.

[259] J. R. Nagel, "Induced Eddy Currents in Simple Conductive Geometries: Mathematical Formalism Describes the Excitation of Electrical Eddy Currents in a Time-Varying Magnetic Field," *IEEE Antennas and Propagation Magazine*, vol. 60, no. 1, pp. 81-88, 2018, doi: 10.1109/MAP.2017.2774206.

[260] M. Etemadrezaei, "22 - Wireless Power Transfer," in *Power Electronics Handbook (Fourth Edition)*, M. H. Rashid Ed.: Butterworth-Heinemann, 2018, pp. 711-722.

[261] V. Shevchenko, O. Husev, R. Strzelecki, B. Pakhaliuk, N. Poliakov, and N. Strzelecka, "Compensation Topologies in IPT Systems: Standards, Requirements, Classification, Analysis, Comparison and Application," *IEEE Access*, vol. 7, pp. 120559-120580, 2019, doi: 10.1109/ACCESS.2019.2937891.

[262] W. Chwei-Sen, G. A. Covic, and O. H. Stielau, "Power transfer capability and bifurcation phenomena of loosely coupled inductive power transfer systems," *IEEE Transactions on Industrial Electronics*, vol. 51, no. 1, pp. 148-157, 2004, doi: 10.1109/TIE.2003.822038.

[263] J. Sallan, J. L. Villa, A. Llombart, and J. F. Sanz, "Optimal Design of ICPT Systems Applied to Electric Vehicle Battery Charge," *IEEE Transactions on Industrial Electronics*, vol. 56, no. 6, pp. 2140-2149, 2009, doi: 10.1109/TIE.2009.2015359.

[264] C. Bruschini, "On the low-frequency EMI response of coincident loops over a conductive and permeable soil and corresponding background reduction schemes," *IEEE Transactions on Geoscience and Remote Sensing*, vol. 42, no. 8, pp. 1706-1719, 2004, doi: 10.1109/TGRS.2004.830164.

[265] R. Huang, B. Zhang, D. Qiu, and Y. Zhang, "Frequency Splitting Phenomena of Magnetic Resonant Coupling Wireless Power Transfer," *IEEE Transactions on Magnetics*, vol. 50, no. 11, pp. 1-4, 2014, doi: 10.1109/TMAG.2014.2331143.

[266] H. Nguyen and J. I. Agbinya, "Splitting Frequency Diversity in Wireless Power Transmission," *IEEE Transactions on Power Electronics*, vol. 30, no. 11, pp. 6088-6096, 2015, doi: 10.1109/TPEL.2015.2424312.

[267] Y. Zhang and Z. Zhao, "Frequency Splitting Analysis of Two-Coil Resonant Wireless Power Transfer," *IEEE Antennas and Wireless Propagation Letters*, vol. 13, pp. 400-402, 2014, doi: 10.1109/LAWP.2014.2307924.

[268] L. Xiang, Z. Zhu, J. Tian, and Y. Tian, "Foreign Object Detection in a Wireless Power Transfer System Using Symmetrical Coil Sets," *IEEE Access*, vol. 7, pp. 44622-44631, 2019, doi: 10.1109/ACCESS.2019.2908866.

[269] X. Zhang, Y. Jin, Q. Yang, Z. Yuan, H. Meng, and Z. Wang, "Detection of metal obstacles in wireless charging system of electric vehicle," *2017 IEEE PELS Workshop on Emerging Technologies: Wireless Power Transfer (WoW)*, pp. 89-92, 20-22 May 2017 2017, doi: 10.1109/WoW.2017.7959371.

[270] J. Kim, G. Wei, M. Kim, H. Ryo, P. Ri, and C. Zhu, "A Splitting Frequencies-Based Wireless Power and Information Simultaneous Transfer Method," *IEEE Transactions on Circuits and Systems I: Regular Papers*, vol. 65, no. 12, pp. 4434-4445, 2018, doi: 10.1109/TCSI.2018.2847339.

[271] N. Hatchavanich, A. Sangswang, and M. Konghirun, "Secondary-Side Voltage Control via Primary-Side Controller for Wireless EV Chargers," *IEEE Access*, vol. 8, pp. 203543-203554, 2020, doi: 10.1109/ACCESS.2020.3036542.

[272] D. Seo, "Design Method of Three-Coil WPT System Based on Critical Coupling Conditions," *IEEE Journal of Emerging and Selected Topics in Power Electronics*, pp. 1-1, 2019, doi: 10.1109/JESTPE.2019.2917708.

[273] J. I. Agbinya and H. Nguyen, "Principles and Applications of Frequency Splitting in Inductive Communications and Wireless Power Transfer Systems," *Wireless Personal Communications*, vol. 107, no. 2, pp. 987-1017, 2019/07/01 2019, doi: 10.1007/s11277-019-06313-1.

[274] L. Jianyu, T. Houjun, and G. Xin, "Frequency Splitting Analysis of Wireless Power Transfer System Based on T-type Transformer Model," *Elektronika ir Elektrotechnika*, vol. 19, no. 10, pp. 109-113, 10/12 2013, doi: 10.5755/j01.eee.19.10.5455.

[275] M. Iordache, D. Niculae, L. I. Bobaru, and L. Mandache, "Circuit analysis of frequency splitting phenomena in wireless power transfer systems," in *2015 9th International Symposium on Advanced Topics in Electrical Engineering (ATEE)*, 7-9 May 2015 2015, pp. 146-151, doi: 10.1109/ATEE.2015.7133758.

[276] J. Wang, M. Leach, E. G. Lim, Z. Wang, and Y. Huang, "Investigation of magnetic resonance coupling circuit topologies for wireless power transmission," *Microwave and Optical Technology Letters*, vol. 61, no. 7, pp. 1755-1763, 2019, doi: 10.1002/mop.31803.

[277] Z. Guan, B. Zhang, and D. Qiu, "Influence of Asymmetric Coil Parameters on the Output Power Characteristics of Wireless Power Transfer Systems and Their Applications," *Energies*, vol. 12, no. 7, p. 1212, 2019. [Online]. Available: https://www.mdpi.com/1996-1073/12/7/1212.

[278] T. C. Beh, M. Kato, T. Imura, S. Oh, and Y. Hori, "Automated Impedance Matching System for Robust Wireless Power Transfer via Magnetic Resonance Coupling," *IEEE Transactions on Industrial Electronics*, vol. 60, no. 9, pp. 3689-3698, 2013, doi: 10.1109/TIE.2012.2206337.

[279] M. Hirao and H. Ogi, "Brief Instruction to Build Emats," in *EMATs for Science and Industry: Noncontacting Ultrasonic Measurements*, M. Hirao and H. Ogi Eds. Boston, MA: Springer US, 2003, pp. 69-80.

[280] S. Samanta and A. K. Rathore, "A comparison and performance evaluation of L-C and C-C-L compensation schemes on CSI based inductive WPT application," *2016 IEEE 25th International Symposium on Industrial Electronics (ISIE)*, pp. 817-822, 8-10 June 2016 2016, doi: 10.1109/ISIE.2016.7744995.

[281] P. A. Hoeher, "FSK-Based Simultaneous Wireless Information and Power Transfer in Inductively Coupled Resonant Circuits Exploiting Frequency Splitting," *IEEE Access*, vol. 7, pp. 40183-40194, 2019, doi: 10.1109/ACCESS.2019.2907169.

[282] R. Narayanamoorthi, A. V. Juliet, and B. Chokkalingam, "Frequency Splitting-Based Wireless Power Transfer and Simultaneous Propulsion Generation to Multiple Micro-Robots," *IEEE Sensors Journal*, vol. 18, no. 13, pp. 5566-5575, 2018, doi: 10.1109/JSEN.2018.2838671.

[283] Y. Zhang, Z. Zhao, and K. Chen, "Frequency-Splitting Analysis of Four-Coil Resonant Wireless Power Transfer," *IEEE Transactions on Industry Applications*, vol. 50, no. 4, pp. 2436-2445, 2014, doi: 10.1109/TIA.2013.2295007.

[284] C. Park, S. Lee, G. Cho, and C. T. Rim, "Innovative 5-m-Off-Distance Inductive Power Transfer Systems With Optimally Shaped Dipole Coils," *IEEE Transactions on Power Electronics*, vol. 30, no. 2, pp. 817-827, 2015, doi: 10.1109/TPEL.2014.2310232.

[285] H. Kudo, K. Ogawa, N. Oodachi, N. Deguchi, and H. Shoki, "Detection of a metal obstacle in wireless power transfer via magnetic resonance," *2011 IEEE 33rd International Telecommunications Energy Conference (INTELEC)*, pp. 1-6, 9-13 Oct. 2011 2011, doi: 10.1109/INTLEC.2011.6099728.

[286] J. Zhou, B. Zhang, and D. Qiu, "An investigation on frequency characteristics of wireless power transfer systems with relay resonators," *COMPEL - The international journal for computation and mathematics in electrical and electronic engineering*, vol. 36, no. 6, pp. 1594-1611, 2017/11/06 2017, doi: 10.1108/COMPEL-12-2016-0538.

[287] J. Li and K. Ji, "Frequency splitting research of series-parallel type magnetic coupling resonant wireless power transfer system," in *2018 13th IEEE Conference on Industrial Electronics and Applications (ICIEA)*, 31 May-2 June 2018 2018, pp. 2254-2257, doi: 10.1109/ICIEA.2018.8398085.

[288] Y. Zhang, Z. Zhao, and K. Chen, "Frequency splitting analysis of magnetically-coupled resonant wireless power transfer," in *2013 IEEE Energy Conversion Congress and Exposition*, 15-19 Sept. 2013 2013, pp. 2227-2232, doi: 10.1109/ECCE.2013.6646983.

[289] J. Zhou, B. Zhang, W. Xiao, D. Qiu, and Y. Chen, "Nonlinear Parity-Time-Symmetric Model for Constant Efficiency Wireless Power Transfer: Application to a Drone-in-Flight Wireless Charging Platform," *IEEE Transactions on Industrial Electronics*, vol. 66, no. 5, pp. 4097-4107, 2019, doi: 10.1109/TIE.2018.2864515.

[290] A. de Cheveigné *et al.*, "Multiway canonical correlation analysis of brain data," *NeuroImage*, vol. 186, pp. 728-740, 2019/02/01/ 2019, doi: https://doi.org/10.1016/j.neuroimage.2018.11.026.

[291] S. Mandal, B. T. Gockel, and A. D. Rollett, "Application of canonical correlation analysis to a sensitivity study of constitutive model parameter fitting," *Materials & Design*, vol. 132, pp. 30-43, 2017/10/15/ 2017, doi: https://doi.org/10.1016/j.matdes.2017.06.050.

[292] C. O. Sakar and O. Kursun, "Discriminative Feature Extraction by a Neural Implementation of Canonical Correlation Analysis," *IEEE Transactions on Neural Networks and Learning Systems*, vol. 28, no. 1, pp. 164-176, 2017, doi: 10.1109/TNNLS.2015.2504724.

[293] P. L. LAI and C. FYFE, "KERNEL AND NONLINEAR CANONICAL CORRELATION ANALYSIS," *International Journal of Neural Systems*, vol. 10, no. 05, pp. 365-377, 2000, doi: 10.1142/s012906570000034x.

[294] M. Ishihara, K. Umetani, and E. Hiraki, "Strategy of Topology Selection Based on Quasi-Duality Between Series–Series and Series–Parallel Topologies of Resonant Inductive Coupling Wireless Power Transfer Systems," *IEEE Transactions on Power Electronics*, vol. 35, no. 7, pp. 6785-6798, 2020, doi: 10.1109/TPEL.2019.2956732.

[295] V. X. Thai, G. C. Jang, S. Y. Jeong, J. H. Park, Y. Kim, and C. T. Rim, "Symmetric Sensing Coil Design for the Blind-Zone Free Metal Object Detection of a Stationary Wireless Electric Vehicles Charger," *IEEE Transactions on Power Electronics*, vol. 35, no. 4, pp. 3466-3477, 2020, doi: 10.1109/TPEL.2019.2936249.

[296] Y. He, M. Pan, D. Chen, and F. Luo, "PEC defect automated classification in aircraft multi-ply structures with interlayer gaps and lift-offs," *NDT & E International*, vol. 53, pp. 39-46, 2013/01/01/ 2013, doi: https://doi.org/10.1016/j.ndteint.2012.10.007.

[297] F. Nafiah, A. Sophian, M. R. Khan, S. B. Abdul Hamid, and I. M. Zainal Abidin, "Image-Based Feature Extraction Technique for Inclined Crack Quantification Using Pulsed Eddy Current," *Chinese Journal of Mechanical Engineering*, vol. 32, no. 1, p. 26, 2019/03/25 2019, doi: 10.1186/s10033-019-0341-y.

[298] J. Kim, D. Kim, and Y. Park, "Analysis of Capacitive Impedance Matching Networks for Simultaneous Wireless Power Transfer to Multiple Devices," *IEEE Transactions on Industrial Electronics*, vol. 62, no. 5, pp. 2807-2813, 2015, doi: 10.1109/TIE.2014.2365751.

[299] M. Lu, X. Meng, R. Huang, L. Chen, A. Peyton, and W. Yin, "A high-frequency phase feature for the measurement of magnetic permeability using eddy current sensor," *NDT & E International*, vol. 123, p. 102519, 2021/10/01/ 2021, doi: https://doi.org/10.1016/j.ndteint.2021.102519.